frontiers | Research Topics

# Outstanding advances in veterinary diagnostic ultrasonography: novel milestones in disease detection, prediction, and treatment

**Edited by**
Hussein M. El-Husseiny and Ryou Tanaka

**Published in**
Frontiers in Veterinary Science

ISSN 1664-8714
ISBN 978-2-8325-6920-7
DOI 10.3389/978-2-8325-6920-7

**Generative AI statement**
Any alternative text (Alt text) provided alongside figures in the articles in this ebook has been generated by Frontiers with the support of artificial intelligence and reasonable efforts have been made to ensure accuracy, including review by the authors wherever possible. If you identify any issues, please contact us.

## About Frontiers

Frontiers is more than just an open access publisher of scholarly articles: it is a pioneering approach to the world of academia, radically improving the way scholarly research is managed. The grand vision of Frontiers is a world where all people have an equal opportunity to seek, share and generate knowledge. Frontiers provides immediate and permanent online open access to all its publications, but this alone is not enough to realize our grand goals.

## Frontiers journal series

The Frontiers journal series is a multi-tier and interdisciplinary set of open-access, online journals, promising a paradigm shift from the current review, selection and dissemination processes in academic publishing. All Frontiers journals are driven by researchers for researchers; therefore, they constitute a service to the scholarly community. At the same time, the *Frontiers journal series* operates on a revolutionary invention, the tiered publishing system, initially addressing specific communities of scholars, and gradually climbing up to broader public understanding, thus serving the interests of the lay society, too.

## Dedication to quality

Each Frontiers article is a landmark of the highest quality, thanks to genuinely collaborative interactions between authors and review editors, who include some of the world's best academicians. Research must be certified by peers before entering a stream of knowledge that may eventually reach the public - and shape society; therefore, Frontiers only applies the most rigorous and unbiased reviews. Frontiers revolutionizes research publishing by freely delivering the most outstanding research, evaluated with no bias from both the academic and social point of view. By applying the most advanced information technologies, Frontiers is catapulting scholarly publishing into a new generation.

## What are Frontiers Research Topics?

Frontiers Research Topics are very popular trademarks of the *Frontiers journals series*: they are collections of at least ten articles, all centered on a particular subject. With their unique mix of varied contributions from Original Research to Review Articles, Frontiers Research Topics unify the most influential researchers, the latest key findings and historical advances in a hot research area.

Find out more on how to host your own Frontiers Research Topic or contribute to one as an author by contacting the Frontiers editorial office: frontiersin.org/about/contact

# Outstanding advances in veterinary diagnostic ultrasonography: novel milestones in disease detection, prediction, and treatment

**Topic editors**
Hussein M. El-Husseiny — Tokyo University of Agriculture and Technology, Japan
Ryou Tanaka — Tokyo University of Agriculture and Technology, Japan

**Citation**
El-Husseiny, H. M., Tanaka, R., eds. (2025). *Outstanding advances in veterinary diagnostic ultrasonography: novel milestones in disease detection, prediction, and treatment*. Lausanne: Frontiers Media SA. doi: 10.3389/978-2-8325-6920-7

# Table of contents

frontiers | Frontiers in Veterinary Science

TYPE Editorial
PUBLISHED 16 September 2025
DOI 10.3389/fvets.2025.1675622



OPEN ACCESS

EDITED AND REVIEWED BY
Andres M. Perez,
University of Minnesota Twin Cities,
United States

*CORRESPONDENCE
Hussein M. El-Husseiny
✉ fw1982@go.tuat.ac.jp;
✉ hussien.alhussieny@fvtm.bu.edu.eg
Ryou Tanaka
✉ ryo@vet.ne.jp

RECEIVED 29 July 2025
ACCEPTED 25 August 2025
PUBLISHED 16 September 2025

CITATION
Hayashi R, El-Husseiny HM and Tanaka R (2025) Editorial: Outstanding advances in veterinary diagnostic ultrasonography: novel milestones in disease detection, prediction, and treatment. *Front. Vet. Sci.* 12:1675622.
doi: 10.3389/fvets.2025.1675622



# Editorial: Outstanding advances in veterinary diagnostic ultrasonography: novel milestones in disease detection, prediction, and treatment

Rio Hayashi[1], Hussein M. El-Husseiny[2,3,4]* and Ryou Tanaka[1]*

[1]Veterinary Teaching Hospital, Tokyo University of Agriculture and Technology, Tokyo, Japan, [2]Institute of Global Innovation Research, Tokyo University of Agriculture and Technology, Fuchu-shi, Tokyo, Japan, [3]Department of Surgery, Anesthesiology, and Radiology, Faculty of Veterinary Medicine, Benha University, Toukh, Egypt, [4]Laboratory of Veterinary Physiology, Department of Veterinary Medicine, Tokyo University of Agriculture and Technology, Tokyo, Japan

KEYWORDS

**ultrasonography, veterinary practice, diagnostic imaging, echocardiography, IVPG, 2DTT, VFM**

Editorial on the Research Topic
Outstanding advances in veterinary diagnostic ultrasonography: novel milestones in disease detection, prediction, and treatment

Veterinary diagnostic ultrasonography has long stood as a cornerstone of modern clinical veterinary medicine. Its non-invasive nature, real-time imaging capabilities, and evolving technological sophistication have positioned it as an indispensable tool across species and disciplines. In recent years, advances in ultrasonographic techniques have opened new frontiers, not only in diagnosis but also in disease monitoring, treatment planning, and prognostics (1). Furthermore, ultrasonography could be used efficiently to provide qualitative evaluation and quantitative scoring of the healing following surgeries (2). In addition, color Doppler ultrasonography has been utilized to assess the function of different organs through evaluation of their vascular hemodynamics. Engagement of novel technologies in ultrasonography presented a novel milestone that extended the uses of ultrasonography to early detection and even prediction of many cardiac diseases. That consequently aids in designing and assessing prompt therapeutic protocols and minimizes the possible deaths (3–5). The present Research Topic, *Outstanding Advances in Veterinary Diagnostic Ultrasonography: Novel Milestones in Disease Detection, Prediction, and Treatment*, brings together groundbreaking research that highlights the most innovative applications and conceptual developments in this domain (Figure 1).

The 13 studies collected here illustrate the diversity and dynamic nature of ultrasonography in the veterinary field. These studies span a range of species, including companion animals, livestock, and exotic species, and encompass clinical, translational, and methodological perspectives. A common theme that emerges is the integration of ultrasonography with other diagnostic and computational technologies, marking a shift toward more predictive and individualized veterinary care.

One of the prominent themes across the collected works is the refinement of cardiac imaging. Hamabe et al. presented a compelling application of two-dimensional speckle-tracking echocardiography (2D-STE) in retrievers with dilated cardiomyopathy (DCM), demonstrating that myocardial strain imaging enables earlier and more sensitive detection of ventricular dysfunction than conventional methods. Similarly, Hirose et al. explored diastolic dysfunction using color M-mode Doppler imaging in hypertensive rat models, highlighting how intraventricular pressure gradients (IVPGs) are influenced by mitral inflow patterns and heart rate findings that hold translational value for both experimental and clinical cardiology.

The utility of ultrasonography in pulmonary vascular disease was examined in depth by Graziano et al. who evaluated the left ventricular eccentricity index (EI) as a non-invasive measure to detect moderate-to-severe precapillary pulmonary hypertension (PAH) in dogs. Their multicenter study showed strong inter-observer agreement and provided validated cut-off values, establishing EI as a valuable tool in emergency and critical care settings where rapid point-of-care assessments are critical.

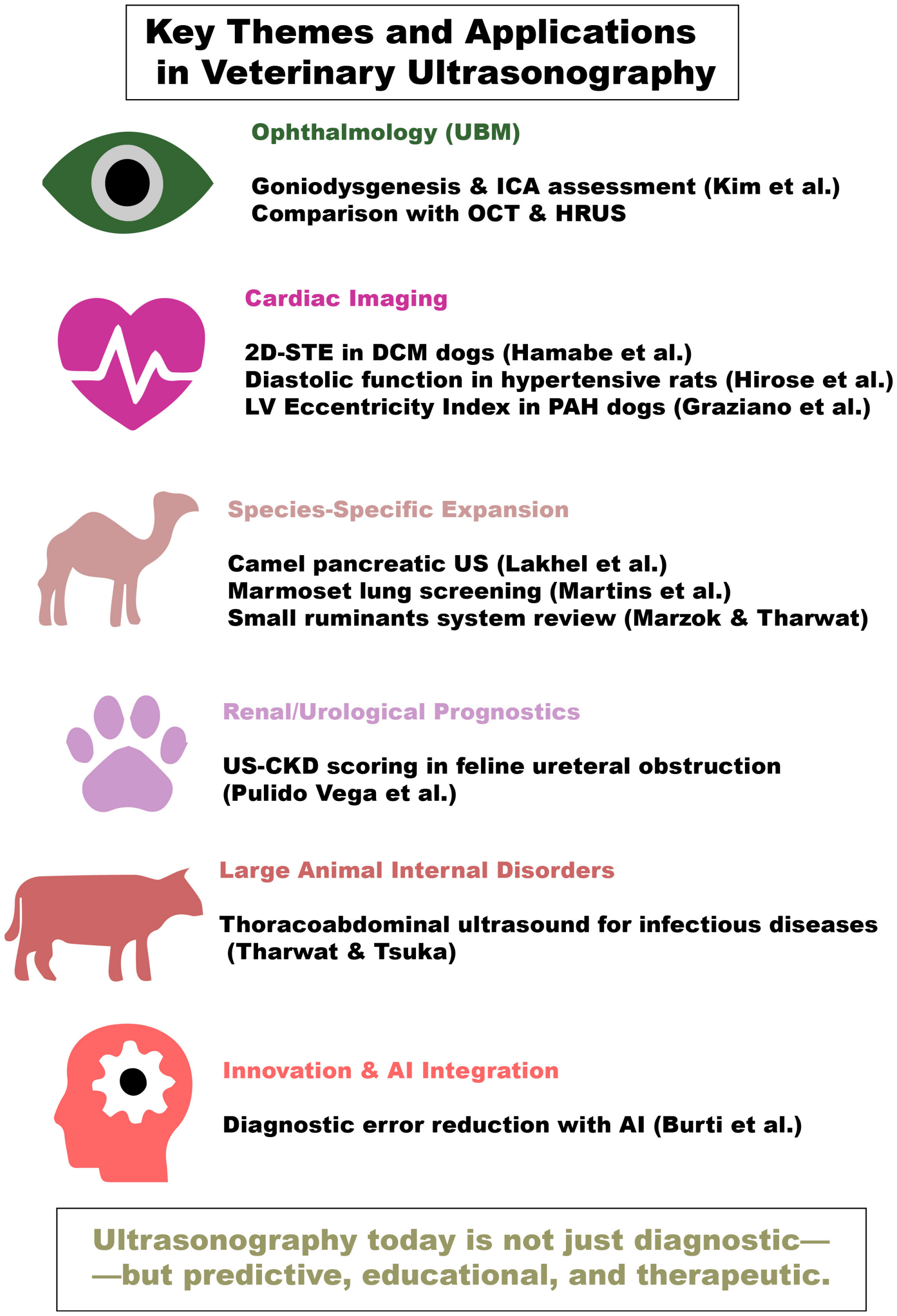


FIGURE 1
Schematic presentation of the outstanding applications of ultrasonography in veterinary practice.

In the realm of nephrology and internal medicine, Pulido Vega et al. investigated contralateral kidney ultrasonographic scoring in cats with unilateral ureteral obstruction. Higher US-CKD scores in the non-obstructed kidney were found to be predictive of poor long-term renal function, demonstrating that structured ultrasonographic evaluation may help inform prognosis and therapeutic strategy in feline urological emergencies.

Ophthalmologic ultrasonography, particularly ultrasound biomicroscopy (UBM), was explored in two complementary articles. First, Kim et al. quantitatively assessed the ciliary cleft and iridocorneal angle in dogs with primary glaucoma and goniodysgenesis, revealing structural predictors of disease. In the second study, Kim et al. outlined the technical advantages of UBM over other imaging modalities such as optical coherence tomography (OCT) and high-resolution ultrasound, supporting UBM's growing role in anterior segment evaluation and screening in canine ophthalmology.

Beyond companion animals, several studies in this Research Topic illustrate the expanding scope of ultrasonography in livestock and exotic species. Lakhel et al. pioneered an ultrasonographic evaluation of the pancreas in dromedary camels, identifying characteristic echogenic patterns across anatomical regions and age groups. Meanwhile, Martins et al. reported on thoracic ultrasound findings in neotropical primates (*Callithrix* spp.), demonstrating that subclinical pneumopathies could be identified using ultrasonography, an important step forward in wildlife medicine and conservation diagnostics.

Tharwat and Tsuka reviewed ultrasonographic features of bacterial and parasitic diseases in ruminants, providing a detailed imaging atlas of thoracic and abdominal pathologies, including reticuloperitonitis and pleuropneumonia. Their work underscores the continuing value of ultrasound in field-based large animal diagnostics. Along similar lines, Marzok and Tharwat presented an illustrated guide to ultrasonographic findings in small ruminants, covering diseases of the digestive, respiratory, urinary, and cardiovascular systems—a practical reference for practitioners in production animal medicine.

Among the technical and clinical innovations highlighted in this Research Topic, the study by Saito et al. offers valuable insights into the therapeutic monitoring of cardiac disease in cats. By evaluating myocardial function before and after carvedilol administration in cats with obstructive hypertrophic cardiomyopathy (HOCM), the authors demonstrated improvements in echocardiographic parameters, including left ventricular fractional shortening and myocardial strain. These findings suggest that ultrasonography can serve not only as a diagnostic tool but also as a non-invasive means of evaluating treatment efficacy and guiding long-term management strategies in feline cardiology.

Education and training in ultrasonography are also undergoing transformation. Guillaumin et al. assessed a hybrid online/in-person POCUS (point-of-care ultrasound) course targeting early-career emergency veterinarians. Their findings indicate that targeted training significantly improves anatomical recognition and confidence in ultrasonographic procedures, supporting the implementation of structured POCUS education in veterinary curricula and continuing professional development.

Finally, the potential of artificial intelligence in veterinary imaging was explored by Burti et al. in their perspective on AI integration for error reduction in diagnostic interpretation. The article not only outlines the challenges of standardization and validation in machine learning but also provides a forward-thinking roadmap for incorporating AI into routine veterinary workflows, including telemedicine and automated image analysis.

Taken together, the articles in this Research Topic present a cohesive and forward-looking view of ultrasonography as a central pillar of veterinary diagnostics. They demonstrate that ultrasound is no longer simply a tool for detection but a predictive, educational, and even interventional platform. By linking imaging findings to outcomes, leveraging emerging technologies, and adapting techniques to underrepresented species and settings, the field is evolving toward a more comprehensive, and integrative diagnostic model.

The road ahead is promising. The continued incorporation of ultrasonography into artificial intelligence systems, point-of-care decision-making tools, and species-specific protocols will further enhance its clinical impact. Equally important is the expansion of ultrasonographic training and credentialing to ensure consistency and competency among practitioners at all levels. As demonstrated by the works in this Research Topic, veterinary ultrasonography is not only keeping pace with modern veterinary practice—it is actively shaping its future.

## Author contributions

RH: Validation, Visualization, Writing – original draft, Writing – review & editing. HE-H: Conceptualization, Supervision, Writing – review & editing. RT: Writing – original draft, Writing – review & editing.

## Acknowledgments

We extend our sincere thanks to the authors, reviewers, and editorial board who contributed to this Research Topic. Their commitment to advancing ultrasonographic knowledge and clinical utility will undoubtedly continue to benefit animal health and veterinary medicine for years to come.

## Conflict of interest

The authors declare that the research was conducted in the absence of any commercial or financial relationships that could be construed as a potential conflict of interest.

## Generative AI statement

The author(s) declare that no Gen AI was used in the creation of this manuscript.

Any alternative text (alt text) provided alongside figures in this article has been generated by Frontiers with the support of artificial intelligence and reasonable efforts have been made to ensure accuracy, including review by the authors wherever possible. If you identify any issues, please contact us.

## Publisher's note



## References

1. Marzok M, Hussen J, Al Dhafiri M, Saleh S, El-Husseiny HM, El-Sherif MW, et al. Ultrasound assessment of botulinum toxin-A (BOTOX) injection into adult Arabian dromedary camels' lips: efficacy in detection and localization. *BMC Vet Res.* (2025) 21:336. doi: 10.1186/s12917-025-04757-1

2. El-Husseiny HM, Mady EA, Usui T, Ishihara Y, Yoshida T, Kobayashi M, et al. Adipose stem cell-seeded decellularized porcine pericardium: a promising functional biomaterial to synergistically restore the cardiac functions post-myocardial infarction. *Vet Sci.* (2023) 10:660. doi: 10.3390/vetsci10110660

3. El-Husseiny HM, Mady EA, Ma D, Hamabe L, Takahashi K, Tanaka R. Intraventricular pressure gradient: a novel tool to assess the post-infarction chronic congestive heart failure. *Front Cardiovasc Med.* (2022) 9:944171. doi: 10.3389/fcvm.2022.944171

4. Yairo A, Mandour AS, Matsuura K, Yoshida T, Ma D, Kitpipatkun P, et al. Effect of loading changes on the intraventricular pressure measured by color m-mode echocardiography in rats. *Diagnostics.* (2021) 11:1403. doi: 10.3390/diagnostics11081403

5. Ma D, Mandour AS, Elfadadny A, Hendawy H, Yoshida T, El-Husseiny HM, et al. Changes in cardiac function during the development of uremic cardiomyopathy and the effect of salvianolic acid B administration in a rat model. *Front Vet Sci.* (2022) 9:905759. doi: 10.3389/fvets.2022.905759

frontiers | Frontiers in Veterinary Science

TYPE Perspective
PUBLISHED 30 August 2024
DOI 10.3389/fvets.2024.1437284



OPEN ACCESS

EDITED BY
Hussein M. El-Husseiny,
Tokyo University of Agriculture and Technology, Japan

REVIEWED BY
Elissa Randall,
Colorado State University, United States
Sofia Alves-Pimenta,
Universidade de Trás-os-Montes e Alto, Portugal

*CORRESPONDENCE
Silvia Burti
✉ silvia.burti@unipd.it

RECEIVED 23 May 2024
ACCEPTED 21 August 2024
PUBLISHED 30 August 2024

CITATION
Burti S, Zotti A and Banzato T (2024) Role of AI in diagnostic imaging error reduction. *Front. Vet. Sci.* 11:1437284.
doi: 10.3389/fvets.2024.1437284



# Role of AI in diagnostic imaging error reduction

Silvia Burti*, Alessandro Zotti and Tommaso Banzato

Department of Animal Medicine, Production and Health, University of Padua, Padua, Italy

The topic of diagnostic imaging error and the tools and strategies for error mitigation are poorly investigated in veterinary medicine. The increasing popularity of diagnostic imaging and the high demand for teleradiology make mitigating diagnostic imaging errors paramount in high-quality services. The different sources of error have been thoroughly investigated in human medicine, and the use of AI-based products is advocated as one of the most promising strategies for error mitigation. At present, AI is still an emerging technology in veterinary medicine and, as such, is raising increasing interest among in board-certified radiologists and general practitioners alike. In this perspective article, the role of AI in mitigating different types of errors, as classified in the human literature, is presented and discussed. Furthermore, some of the weaknesses specific to the veterinary world, such as the absence of a regulatory agency for admitting medical devices to the market, are also discussed.

KEYWORDS

**artificial intelligence, error, machine learning, image quality, radiology—education**

## 1 Introduction

The topic of error mitigation in diagnostic imaging is a relatively unexplored field in the veterinary literature. Indeed, to the best of the authors' knowledge, only two papers investigating such a topic are available (1, 2). Likewise, incidence rates and the overall costs associated with diagnostic imaging errors have been poorly investigated in veterinary medical practice. Indeed, only one study (3) reports the radiologic error rate being comparable to what is reported in human medicine. Instead, an entire set of literature devoted to analyzing the most common causes of diagnostic imaging errors, along with possible solutions, is currently available in human medicine (4, 5). It is important to understand that diagnostic imaging errors are much more intricate than they might seem because they involve a complex interaction between individual psychological (6) environmental, and educational factors (7). A diagnostic error is defined as a "deviation from the expected norm" (8), and the consequences for the patient may vary from no consequences to death. Renfrew et al. (9) first proposed a comprehensive classification of the causes of diagnostic imaging errors, which were subsequently modified by Kim and Mansfield (10). In addition, some authors have approached this complex theme from different perspectives, ranging from the identification of different cognitive biases (6), to the analysis of interpretative errors (4), to the strategies for error reduction (11).

It is important to note at this point that a universally recognized "etiology" of errors in human diagnostic imaging is currently unavailable, and the definitions and the solutions proposed for different scenarios may vary among authors. In recent years, we have witnessed an increased interest in the applications of AI in the veterinary diagnostic imaging field (12, 13). Among other applications, AI is mainly used as a supportive tool to guide the interpretation of medical images in veterinary medicine. Even if AI is reported to have an overall lower error rate than radiologists have both in human (14) and veterinary medicine (15), dealing with such a technology is not as straightforward as it might seem (16, 17). This perspective analysis aims to examine the role of AI in mitigating each source of error in veterinary imaging through the error classification suggested by Kim and Mansfield (10).

# 2 Types of errors and role of AI in mitigation

## 2.1 Complacency

"Complacency refers to over-reading and misinterpretation of findings, a finding is detected but attributed to the wrong cause (false positive-error)" (10). This type of error is reported to be uncommon (0.9%) in human medicine, whilst no data are available in veterinary medicine. In this latter field, a discrepancy between the AI system output and the radiologist's interpretation is likely to occur. AI systems are reported to generate lower error rates (including both false positives and false negatives) than radiologists (at least for some specific findings) (15). Veterinary radiologists should therefore consider reinterpreting findings, taking the AI results into account.

## 2.2 Faulty reasoning

"Error of over-reading and misinterpretation, in which a finding is appreciated and interpreted as abnormal but is attributed to the wrong cause. Misleading information and a limited differential diagnosis are included in this category" (10). At present, the available AI systems only detect specific radiographic findings (15, 18, 19) and are not able to provide differential diagnoses based on the clinical findings. Large language models (LLMs) (20) capable of interpreting the images and generating a list of differentials based on the medical history will soon be available, thus potentially reducing this type of error.

## 2.3 Lack of knowledge

"The finding is seen but is attributed to the wrong cause because of a lack of knowledge on the part of the viewer or interpreter" (10). This type of error is, to the authors' knowledge, particularly relevant in the veterinary scenario, where most radiographic images are not interpreted by a radiologist but by general practitioners. As mentioned earlier, current AI-based systems cannot correlate the imaging findings with a specific list of differentials based on the medical history and therefore, to date, AI has had limited impact in mitigating this type of error.

## 2.4 Under-reading

"The lesion is not detected." According to Kim and Mansfield (10), this alone accounts for 42% of the total diagnostic errors. Under-reading is, most likely, one of the main reasons for implementing AI systems in the day-to-day routine. Indeed, under-reading stands as a very common problem that might arise from both individual and environmental situations (7). The role of AI in mitigating this type of error is, potentially, a game changer as AI systems are not subjected to cognitive biases or environmental contexts (overworking, challenging working environment, distractions, etc.). On the other hand, the final user needs to consider that AI system accuracy is also affected by several factors, such as image quality or lesion rate in the database (21). Lastly, the user needs to be aware that most of the veterinary AI-based systems have a variable reported accuracy in the detection of specific lesions. For instance, accuracy in detecting pleural effusion is usually very high (15, 18, 22) whereas accuracy for pulmonary nodules or masses is significantly lower (18, 23).

## 2.5 Poor communication

"The lesion is identified and interpreted correctly, but the message fails to reach the clinician." Reliable communication of imaging findings is vital for the correct management of patients, both in veterinary and human medicine. Imaging reports use highly specialized terminology, and the accurate interpretation of these terms relies on the expertise of the referring clinician. This type of error is reported to be quite rare (10) as, when a report is unclear, a direct explanation is usually required from the reporting physician. To this end, incorporating large language models (LLMs) (20) within the reporting systems could help in creating more homogeneous reports and therefore improve communication between the clinician and the radiologist.

## 2.6 Prior examination/history

"The finding is missed because of failure to consult prior radiologic studies or reports" and "The finding is missed because of the acquisition of inaccurate or incomplete clinical history." These are among the most common types of errors, and the American College of Radiology recommends that all the patients' previous reports should be available to the radiologist during exam evaluation (10). This type of error is most relevant in teleradiology services since most of these services do not have access to complete patient history. AI-based products guiding radiologists (both in human and veterinary medicine) throughout the reporting process (from image acquisition to final report) could be important in mitigating these errors. For example, using LLMs to promptly summarize the patient's clinical history could provide the radiologist with quick and useful information.

## 2.7 Location

"The finding is missed because the location of a lesion is outside the area of interest on an image, such as in the corner of an image." These errors are fairly common and are possibly related to what is referred to as "intentional" or "tunnel vision bias" (10). These are well-known cognitive biases. In a famous experiment, radiologists were asked to detect pulmonary nodules from CT images. The picture of a gorilla, 10 times larger than the average nodule, was placed in one of the CT images. Surprisingly, 83% of the radiologists did not report seeing the gorilla, despite eye-tracking technologies demonstrating that all the radiologists looked at it (24). In this case, using AI systems to assist the radiologist could help in reducing these types of errors provided that the AI systems themselves do not generate numerous false positives (16). Indeed, as demonstrated by Bernstein et al. (16), a faulty AI decreases radiographers' accuracy especially if the results of the AI are shown in the final report.

## 2.8 Satisfaction of search

"The finding is missed because of the failure to continue to search for additional abnormalities after a first abnormality is found." This is a common situation, especially when advanced imaging modalities, such as CT or MRI, are evaluated (10). To the best of the authors' knowledge, no algorithm for lesion detection in advanced imaging modalities (CT or MRI) has been proposed in the veterinary literature, and, therefore, the usefulness of AI in the reduction of such an error has yet to be established.

## 2.9 Complication

"Complication from a procedure," meaning untoward events that could happen during an invasive examination procedure (9). This is reported to be an uncommon type of error in human medicine (10). The role of AI in the reduction of such an error is similar to that regarding other error types (e.g., prior examination).

## 2.10 Satisfaction of report

"The finding was missed because of the complacency of the report, and over-reliance on the radiology report of the previous examinations." This type of error arises from what is known as alliterative bias, meaning that one radiologist's judgement is influenced by that of another radiologist. To avoid this sort of bias (6), suggest that the radiologist should read previous reports only after rendering the interpretation of findings. This is one of the most dangerous types of errors, as it is perpetuated from one study to the next (10). The authors believe that AI could play a prominent role in reducing these error types. In fact, AI systems are unaware of the results of prior studies and could therefore help the clinician make more factual-based decisions that are devoid of cognitive biases.

# 3 Conclusion

A summary of the error types according to Kim and Mansfield (10) and the possible contribution of AI-based products in their mitigation is reported in Table 1. AI is still a very young technology in veterinary medicine and, despite the increasing number of applications available on the market, is far from being part of most practices' clinical routine. The same is also true, to some extent, in human medicine. Indeed, despite the large investments in and the media impact of AI, the diffusion of AI-based systems is still limited, and actual improvements in healthcare quality related to the widespread adoption of these technologies are still to be demonstrated (25).

TABLE 1 Possible errors according to Kim and Mansfield (10) and role of AI in mitigation.

| Type of error | Role of AI |
|---|---|
| Complacency | Yields lower number of false positives than radiologists do |
| Faulty reasoning | Limited usefulness of AI. Education plays a larger role in mitigating this error type |
| Lack of knowledge | Limited usefulness of AI (LLMs might be more effective) |
| Under-reading | Varies depending on the accuracy for each specific finding |
| Poor communication | Limited usefulness. LLMs could provide a means to homogenize the reports |
| Prior examination/ history | AI-assisted reporting and AI-based tools to create quick summaries of the clinical history could help in mitigating this type of error |
| Location | AI scans the entire image/scan and is not influenced by the position of the lesion |
| Satisfaction of search | AI is unaware of the reasons for the scan/image and checks the entire exam |
| Complication | Similar to prior examination |
| Satisfaction of report | AI-based products are not influenced by this error type and could help in taking more factual-based decisions |

LLMs, large language models.

It is the authors' opinion that AI will likely have different impacts on human and veterinary diagnostic imaging, mostly due to the intrinsic differences that exist between these two disciplines. The number of board-certified radiologists in veterinary medicine is still limited compared to those in human medicine, and therefore it is common practice for veterinary diagnostic images to be interpreted by non-specialists. This poses some questions regarding the effectiveness of these AI-based computer-aided systems in veterinary medicine. In fact, it is reported that AI has a variable accuracy for different radiographic findings (18, 23). If the operator cannot determine the accuracy of the AI system's findings, relying on these systems might lead to misleading outcomes.

In the perspective article presented here, we did not address the importance of AI algorithms in assessing the quality of medical images. This application has been scarcely explored in veterinary medicine, and to date, only two studies highlights these algorithms as a promising tool to enhance the accuracy of interpreting canine radiographs by identifying technical errors (26, 27). Conversely, in human medicine, numerous AI-based algorithms have been developed for evaluating the quality of chest X-ray images, showing promising results (28, 29). This is a field where AI algorithms could again contribute to reducing radiologists' interpretative error rates by automatically screening the quality of diagnostic images before interpretation, similar to what is already happening in human medicine.

In human medicine, new medical devices need to be approved by a regulatory agency, such as the European Medicines Agency in Europe or the Food and Drug Administration in the United States (30). In veterinary medicine, such a regulatory agency does not exist and therefore, to date, there has not been a way to certify vendors' claims regarding the accuracy and stability of the proposed systems (31). It is the authors' opinion that, in such a scenario in veterinary medicine, correct and impartial information to the final users is of vital importance in order to avoid misuse and possible fraud.

## Data availability statement

The original contributions presented in the study are included in the article/supplementary material, further inquiries can be directed to the corresponding author.

## Author contributions

SB: Writing – review & editing. AZ: Writing – review & editing. TB: Writing – original draft, Writing – review & editing.

## Funding

The author(s) declare that financial support was received for the research, authorship, and/or publication of this article. Open Access funding provided by Università degli Studi di Padova|University of Padua, Open Science Committee. The present paper was part of a project funded by a research grant from the Department of Animal Medicine, Production and Health – MAPS, University of Padua, Italy: SID- Banzato 2023 (€20.000).

## Conflict of interest

The authors declare that the research was conducted in the absence of any commercial or financial relationships that could be construed as a potential conflict of interest.

The author(s) declared that they were an editorial board member of Frontiers, at the time of submission. This had no impact on the peer review process and the final decision.

## Publisher's note

All claims expressed in this article are solely those of the authors and do not necessarily represent those of their affiliated organizations, or those of the publisher, the editors and the reviewers. Any product that may be evaluated in this article, or claim that may be made by its manufacturer, is not guaranteed or endorsed by the publisher.

## References

1. Alexander K. Reducing error in radiographic interpretation. *Can Vet J*. (2020) 51:533–536.

2. Lamb CR, Pfeiffer DU, Mantis P. Errors in radiographic interpretation made by veterinary students. *J Vet Med Educ*. (2007) 34:157–9. doi: 10.3138/jvme.34.2.157

3. Cohen J, Fischetti AJ, Daverio H. Veterinary radiologic error rate as determined by necropsy. *Vet Radiol Ultrasound*. (2023) 64:573–84. doi: 10.1111/vru.13259

4. Waite S, Kolla S, Reede D, Gale B, Fuchs T, Scott J. Interpretive error in radiology. *Am J Roentgenol*. (2016) 208:739–49. doi: 10.2214/ajr.16.16963

5. Brady AP. Error and discrepancy in radiology: inevitable or avoidable? *Insights Imaging*. (2017) 8:171–82. doi: 10.1007/s13244-016-0534-1

6. Itri JN, Patel SH. Heuristics and cognitive error in medical imaging. *Am J Roentgenol*. (2018) 210:1097–105. doi: 10.2214/AJR.17.18907

7. Itri JN, Tappouni RR, McEachern RO, Pesch AJ, Patel SH. Fundamentals of diagnostic error in imaging. *Radiographics*. (2018) 38:1845–65. doi: 10.1148/rg.2018180021

8. Brook OR, O'Connell AM, Thornton E, Eisenberg RL, Mendiratta-Lala M, Kruskal JB. Anatomy and pathophysiology of errors occurring in clinical radiology practice. *Radiographics*. (2010) 30:1401–10. doi: 10.1148/rg.305105013

9. Renfrew DL, Franken EA, Berbaum KS, Weigelt FH, Abu-Yousef MM. Error in radiology: classification and lessons in 182 cases presented at a problem case conference. *Radiology*. (1992) 183:145–50. doi: 10.1148/radiology.183.1.1549661

10. Kim YW, Mansfield LT. Fool me twice: delayed diagnoses in radiology with emphasis on perpetuated errors. *AJR Am J Roentgenol*. (2014) 202:465–70. doi: 10.2214/AJR.13.11493

11. Bruno MA, Walker EA, Abujudeh HH. Understanding and confronting our mistakes: the epidemiology of error in radiology and strategies for error reduction. *Radiographics*. (2015) 35:1668–76. doi: 10.1148/rg.2015150023

12. Hennessey E, DiFazio M, Hennessey R, Cassel N. Artificial intelligence in veterinary diagnostic imaging: a literature review. *Vet Radiol Ultrasound*. (2022) 63:851–70. doi: 10.1111/vru.13163

13. Basran PS, Porter I. Radiomics in veterinary medicine: overview, methods, and applications. *Vet Radiol Ultrasound*. (2022) 63:828–39. doi: 10.1111/vru.13156

14. Seah JCY, Tang CHM, Buchlak QD, Holt XG, Wardman JB, Aimoldin A, et al. Effect of a comprehensive deep-learning model on the accuracy of chest x-ray interpretation by radiologists: a retrospective, multireader multicase study. *Lancet Digit Health*. (2021) 3:e496–506. doi: 10.1016/S2589-7500(21)00106-0

15. Boissady E, de La Comble A, Zhu X, Hespel AM. Artificial intelligence evaluating primary thoracic lesions has an overall lower error rate compared to veterinarians or veterinarians in conjunction with the artificial intelligence. *Vet Radiol Ultrasound*. (2020) 61:619–27. doi: 10.1111/vru.12912

16. Bernstein MH, Atalay MK, Dibble EH, Maxwell AWP, Karam AR, Agarwal S, et al. Can incorrect artificial intelligence (AI) results impact radiologists, and if so, what can we do about it? A multi-reader pilot study of lung cancer detection with chest radiography. *Eur Radiol*. (2023) 33:8263–9. doi: 10.1007/s00330-023-09747-1

17. Degnan AJ, Ghobadi EH, Hardy P, Krupinski E, Scali EP, Stratchko L, et al. Perceptual and interpretive error in diagnostic radiology—causes and potential solutions. *Acad Radiol*. (2019) 26:833–45. doi: 10.1016/j.acra.2018.11.006

18. Banzato T, Wodzinski M, Burti S, Osti VL, Rossoni V, Atzori M, et al. Automatic classification of canine thoracic radiographs using deep learning. *Sci Rep*. (2021) 11:3964. doi: 10.1038/s41598-021-83515-3

19. Banzato T, Wodzinski M, Tauceri F, Donà C, Scavazza F, Müller H, et al. An AI-based algorithm for the automatic classification of thoracic radiographs in cats. *Front Vet Sci*. (2021) 8:731936. doi: 10.3389/fvets.2021.731936

20. Mese I, Taslicay CA, Sivrioglu AK. Improving radiology workflow using ChatGPT and artificial intelligence. *Clin Imaging*. (2023) 103:109993. doi: 10.1016/j.clinimag.2023.109993

21. Bradshaw TJ, Huemann Z, Hu J, Rahmim A. A guide to cross-validation for artificial intelligence in medical imaging. *Radiol Artif Intell*. (2023) 5:e220232. doi: 10.1148/ryai.220232

22. Müller TR, Solano M, Tsunemi MH. Accuracy of artificial intelligence software for the detection of confirmed pleural effusion in thoracic radiographs in dogs. *Vet Radiol Ultrasound*. (2022) 63:573–9. doi: 10.1111/vru.13089

23. Pomerantz LK, Solano M, Kalosa-Kenyon E, Leah C, Pomerantz K. Performance of a commercially available artificial intelligence software for the detection of confirmed pulmonary nodules and masses in canine thoracic radiography. *Vet Radiol Ultrasound*. (2023) 64:881–9. doi: 10.1111/vru.13287

24. Drew T, Evans K, Võ MLH, Jacobson FL, Wolfe JM. Informatics in radiology: what can you see in a single glance and how might this guide visual search in medical images? *Radiographics*. (2013) 33:263–74. doi: 10.1148/rg.331125023

25. van Leeuwen KG, de Rooij M, Schalekamp S, van Ginneken B, Rutten MJCM. How does artificial intelligence in radiology improve efficiency and health outcomes? *Pediatr Radiol*. (2022) 52:2087–93. doi: 10.1007/s00247-021-05114-8

26. Banzato T, Wodzinski M, Burti S, Vettore E, Muller H, Zotti A. An AI-based algorithm for the automatic evaluation of image quality in canine thoracic radiographs. *Sci Rep*. (2023) 13:17024. doi: 10.1038/s41598-023-44089-4

27. Tahghighi P, Norena N, Ukwatta E, Appleby RB, Komeili A. Automatic classification of symmetry of hemithoraces in canine and feline radiographs. *J Med Imaging*. (2023) 10:044004. doi: 10.1117/1.JMI.10.4.044004

28. Meng Y, Ruan J, Yang B, Gao Y, Jin J, Dong F, et al. Automated quality assessment of chest radiographs based on deep learning and linear regression cascade algorithms. *Eur Radiol*. (2022):7680–90. doi: 10.1007/s00330-022-08771-x

29. Nousiainen K, Mäkelä T, Piilonen A, Peltonen JI. Automating chest radiograph imaging quality control. *Phys Med*. (2021) 83:138–45. doi: 10.1016/j.ejmp.2021.03.014

30. Darrow JJ, Avorn J, Kesselheim AS. FDA regulation and approval of medical devices: 1976–2020. *JAMA*. (2021) 326:420–32. doi: 10.1001/jama.2021.11171

31. Cohen EB, Gordon IK. First, do no harm. Ethical and legal issues of artificial intelligence and machine learning in veterinary radiology and radiation oncology. *Vet Radiol Ultrasound*. (2022) 63:840–50. doi: 10.1111/vru.13171

TYPE Review
PUBLISHED 02 September 2024
DOI 10.3389/fvets.2024.1435395



OPEN ACCESS

EDITED BY
Hussein M. El-Husseiny,
Tokyo University of Agriculture and Technology, Japan

REVIEWED BY
Ankit Prajapati,
Kamdhenu University, India
Mohamed Zeineldin,
Animal and Plant Health Inspection Service (USDA), United States

*CORRESPONDENCE
Takeshi Tsuka
✉ tsuka@tottori-u.ac.jp

RECEIVED 20 May 2024
ACCEPTED 13 August 2024
PUBLISHED 02 September 2024

CITATION
Tharwat M and Tsuka T (2024) Diagnostic utility of ultrasonography for thoracic and abdominal bacterial and parasitic diseases in ruminants: a comprehensive overview. *Front. Vet. Sci.* 11:1435395.
doi: 10.3389/fvets.2024.1435395



# Diagnostic utility of ultrasonography for thoracic and abdominal bacterial and parasitic diseases in ruminants: a comprehensive overview

Mohamed Tharwat[1] and Takeshi Tsuka[2]*

[1]Department of Clinical Sciences, College of Veterinary Medicine, Qassim University, Buraidah, Saudi Arabia, [2]Department of Veterinary Clinical Medicine, Joint Department of Veterinary Medicine, Faculty of Agriculture, Tottori University, Tottori, Japan

This review article describes the roles of ultrasound in assessing thoracic and abdominal infectious diseases, mainly bacterial and parasitic ones that affect farm animals, including cattle, camels, sheep, and goats. Ultrasonography is a non-invasive imaging technique used to diagnose infectious diseases affecting the cardiovascular, respiratory, digestive, urinary, and hepatobiliary systems. In cases of thoracic and abdominal infections, ultrasound typically reveals abnormalities in echogenicity and echotexture, the presence of unusual artifacts, and mass formation exerting pressure on surrounding structures. Inflammatory and degenerative changes within the viscera can be identified ultrasonographically by comparing the echogenicity of affected areas with that of the surrounding normal parenchyma, such as in fascioliasis. Bacterial and parasitic infections often result in capsular mass lesions with anechoic contents, as observed in hydatid cysts and cysticercosis, or varying echogenic contents, as observed in liver abscesses. Effusions within the pericardium, pleura, and peritoneum are common ultrasonographic findings in infectious thoracic and abdominal diseases. However, these effusions' echogenicity does not always allow for clear differentiation between transudates and exudates. The routine use of ultrasonography in the evaluation of the chest and abdomen in affected or suspected ruminants is highly beneficial for detection, guiding therapeutic decisions, assessing prognosis, and aiding in the eradication of highly contagious diseases that cause significant economic losses.

KEYWORDS

**bacteria, infectious disease, parasitism, ruminant, ultrasonography**

## 1 Introduction

For over 50 years, physicians have been using ultrasonography (US) to aid in diagnosis and guide procedures in day-to-day examinations. US is a simple, safe, and non-invasive tool implemented broadly in general practice (1). There is no doubt that early diagnosis of diseases in animals will affect treatment progress. Therefore, any delay in diagnosis can lead to unwanted complications. From this standpoint, developing new methods to diagnose diseases in their early stages is necessary. Diagnostic imaging modalities, including radiography, computed tomography (CT), and US, are used in veterinary medicine for both diagnosis and therapeutic purposes. However, all modalities except the

US require special precautions, and CT is performed only in fixed sites and more developed countries (2).

In contrast, the US is routinely used in veterinary medicine to investigate various bovine disorders (3–6). The US supplements clinical and laboratory examinations by providing additional information on thoracic and abdominal disorders and verifying antemortem conditions. US is well-tolerated in unsedated animals, allowing serial examinations to monitor disease progression and treatment response or practice scanning techniques. This article reviews the effectiveness of US in assessing infectious diseases, mainly bacterial and parasitic, that affect various ruminants, including cattle, buffaloes, camels, sheep, and goats.

### 1.1 Scanning technique of thoracic and abdominal US

The required US frequency in the transducer used for both sides of the chest is ≤5.0 MHz for adult cattle and buffaloes (7–11) and ≥5.0 MHz for younger calves and small ruminants (2, 12–15), ensuring good quality thoracic US.

US images of the lungs and pleura can be acquired by scanning the intercostal spaces between the 5th and 12th ribs for cattle and between the 3rd and 11th ribs for buffaloes (11, 16). For younger calves, intrathoracic structures on both sides can be scanned between the 3rd and 10th ribs on the left and between the 1st and 10th ribs on the right (14). The anatomical locations to scan the heart include the intercostal spaces between the 3rd and 6th ribs in buffaloes (11), a wider range than the 3rd to 4th intercostal spaces used in cattle (7).

When scanning the abdomen of adult cattle and buffaloes, a lower US frequency between 3.5 and 5.0 MHz is required (8, 9, 11, 17–20). High-quality images can be obtained using a ≥5.0 MHz transducer for the abdominal US in younger calves and small ruminants (19, 21, 22).

The liver can be imaged by US scanning at the right-sided chest region between the 9th and 11th ribs in cattle (18, 23), between the 9th and 12th ribs in buffaloes (11), and between the 7th and 13th ribs in goats and sheep (24–26). In goats and sheep, the liver is observed adjacent to the echogenic line of the diaphragm at the level of the 10th rib (24, 25). The gall bladder is visualized within the liver parenchyma in the US, taken at the 11th to 12th intercostal spaces in buffaloes and at the 9th to 11th intercostal spaces in goats and sheep (11, 24, 25). The common anatomical location to scan the reticulum is the ventral abdominal wall, just caudal to the xiphoid cartilage in cattle and small ruminants (24). In buffaloes, the reticulum can also be examined by US scanning at the ventral thorax aspect on both sides of the sternum within the 6th to 8th intercostal spaces (11). The scanning position for the abomasum in cattle is the ventral midline and paramedian regions of the abdomen at ∼10 cm caudal to the xiphoid process (17). The small intestine can be detected on the abdominal US when scanned on the right side between the 8th rib and pelvis and from the areas of the transverse processes of the vertebrae to the linea alba (17). The intercostal spaces between the 10th and 12th ribs and between the 9th and 12th ribs are the scanning locations allowing visualization of the descending duodenum and the jejunum and ileum in cattle, respectively (17). In adult cattle and buffaloes, transrectal scanning is necessary for US observations of the left kidney and urinary bladder, whereas percutaneous US scanning allows visualization of the right kidney (11, 19, 27–30). Percutaneous US scanning can examine the left kidney at the caudal left paralumbar fossa in some camels, younger calves, and lean adult cattle (28, 30–32). Additionally, percutaneous US can demonstrate the urinary bladder when applying the transducer to the ventral aspect or both flanks of the caudal abdomen in younger calves or small ruminants (33, 34).

## 2 Chest

### 2.1 Pneumonia/pleuropneumonia

Inflammation of the pulmonary parenchyma primarily affects the alveoli and is usually accompanied by inflammation of the bronchioles and often by pleuritis. Clinically, the condition is characterized by cough, abnormal respiratory sounds, polypnea, and changes in the depth and type of respiration (35). It may be caused by viruses, such as respiratory syncytial virus, retroviruses, paramyxovirus, oncogenic beta-retrovirus, capripox virus, and a small ruminant lentivirus group (known as a Maedi-visna); bacteria, such as *Pasteurella multocida* and *Mannheimia haemolytica*; fungi, such as *Cryptococcus neoformans*; parasites, such as *Dictyocaulus filaria, Protostrongylid rufescens*, and *Echinococcus granulosus*; as well as mycoplasma, chlamydia, and rickettsia (35, 36). Infection with *Fusobacterium necrophorum* typically induces chronic suppurative pneumonia, often via various infection entry points such as inhalation and hematogenous spread in younger animals. This occurs when the animals present with chronic weight loss, depression, tachypnea, cough, and mucopurulent nasal discharge. Pleuritis, or pleurisy, is inflammation of the pleura. It is often associated with pulmonary parenchyma inflammation, known as pleuropneumonia (37). Contagious caprine pleuropneumonia is a severe disease of small ruminants, especially goats, found in African and Asian countries (13, 38, 39). The disease is caused by *Mycoplasma capricolum* subsp. *capripneumoniae* infections (13, 38, 39). The acute and subacute forms of the disease are characterized by unilateral fibrinous pleuropneumonia with severe pleural effusion (13, 39, 40).

Although auscultation is considered an important component of veterinary clinical examination, it cannot fully provide diagnostic evidence of pneumonia or pleuropneumonia regarding the severity, extension, and localization of lung pathology (40, 41). Diagnosis of contagious caprine pleuropneumonia relies on clinical and necropsy observations that should be confirmed by laboratory tests (40). Due to the difficulty of isolating this pathogen, molecular techniques are preferred for laboratory confirmations (13). Therefore, ancillary diagnostic approaches are essential to confirm provisional diagnoses from clinical examinations (8).

Thoracic US is very helpful for diagnosing pneumonia due to its ability to distinguish between pathological lung echotextures and the specific US pattern of normal lungs (16, 41–43). Air-filled lung tissues are a strong reflector of US waves, trapping these waves between the lung tissues and the surface of the transducer, generating a reverberation artifact (16, 44). The change in the echotexture of lung structures, resembling that of liver parenchyma, represents pulmonary consolidation (16, 45) (Figure 1). Air-filled small bronchi appear as hyperechoic foci within the hypoechoic echotexture of affected lung structures (16). Detecting consolidation lesions deep within normal air-filled lung structures can be difficult due to reverberation artifacts (16). In cases of severe pneumonia, a US examination reveals hypoechoic zones on the lung surface, representing superficial fluid alveolograms with a comet-tail artifact (45). Accumulating a small amount of effusions within the space between the parietal and visceral pleura can also generate a comet-tail artifact (2, 12, 15). The presence of adhesions between the parietal and visceral pleura can be indicated by the disappearance of the gliding sign, which is the normal sliding movement of the lung within the thoracic cavity during respiration (16). US findings in small ruminants with contagious caprine pleuropneumonia often include the presence of gas echoes within the pleural cavity or abscess formation (13). The mixture of abnormal lung and pleural echotextures is usually detected unilaterally in many caprine cases because the pleural sacs do not communicate; pleural fluid readily transmits sound waves and, therefore, appears anechoic (13) (Figures 2A, B). In cattle, pleuropneumonia is associated with an extension of infectious inflammation over the pleura of the lung, thoracic wall, and diaphragm, mostly affecting one side of the body (37). In camels, US of the thoracic cavity can also detect pleural effusion and aid in determining the prognosis of the diseased animal (45). In severe cases, it shows bilateral heterogeneous pleural effusions with fibrin threads (45). Fibrin appears as filmy and filamentous strands floating in the effusion with loose attachments to the pleural surfaces; pockets of fluid separated by fibrin are commonly imaged (45) (Figures 2C, D). Regarding active phase detection, the use of US appears to be as effective as thoracic radiography (14). The routine use of US may detect the subclinical phase of bovine respiratory disease (43).

## 2.2 Pleural effusion

Pleural effusion is not only a local pleural disease caused by primary pleural infection via local or systemic routes but also a concurrent condition associated with various cardiorespiratory diseases such as pneumonia and pericarditis (45, 46). Pleural effusion is also a non-specific finding associated with heart failure and decreased blood circulation (7). In bovine cases, echogenicity in pleural effusion is hypoechoic, suggesting pleural transudates. An increase in echogenicity suggests empyema, which contains varying amounts of cellular contents, debris, and fibrin (37). The US is useful in guiding thoracocentesis in collecting pleural effusion (37).

## 2.3 Lung cysts

Echinococcosis is one of the most important zoonoses caused by metacestodes of *Echinococcus granulosis* infecting humans and livestock (26, 47, 48). Early detection of this disease is required during the breeding stages. Echinococcosis can induce the formation of single or multiple lung cysts and liver cysts, which are characterized in the US by cavitary masses lined with thin or thick walls containing anechoic to hyperechoic fluids (48). Cystic lesions can be identified within both the lung and liver structures in approximately half of the affected cases (48). Additionally, the US detection sensitivity and specificity for cystic lesions are 88.7 and 75.9%, respectively (47). The severity of respiratory disturbance appears to correlate with the size and multifocal nature of the cystic lesions (48). The US is useful in diagnosing echinococcosis by guiding fine needle aspiration of fluids within the cystic mass, which allows for macroscopic detection of protoscoleces in the germinal cyst layer (48).

## 2.4 Lung and pleural abscessation

Lung abscesses commonly occur in association with the chronic phase of various types of pneumonia. Pleural abscesses can occur due to primary pleural infections from various causes, including trauma or secondary foci extended from lung infections. An abscess can be demonstrated as a well-defined cavitary mass enveloping its contents with variable echogenicity if it develops within the affected lung and pleura (16). The cavitary mass can generate acoustic enhancement (45). The formation of small pulmonary nodules is one common US sign of bronchopneumonia, representing small abscesses and inflamed or necrotic foci (16). Pleural abscesses can cause compression of the peripheral lung structures, depending on their sizes (45) (Figure 3). The echotexture of the visceral pleura helps differentiate this disease from lung abscessation. This is done by observing the line between the affected pleura and the peripheral lung structures, which shows varying degrees of increased echogenicity and thickening.

## 2.5 Pneumothorax

Pneumothorax can be a secondary effect of lung infections, with bovine respiratory syncytial virus being the most common pathogen. This virus can cause bronchopneumonia and interstitial pneumonia, accounting for over 80% of bovine cases. Other causes of pneumothorax include trauma, nutritional deficiency, and toxicity (49, 50). Ruptures of the fragile parts of the affected lung structures and emphysematous bullae are the main sources of air outflow into the thoracic cavity, referred to as a closed pneumothorax (49–51). The air-filled thoracic cavity creates a reverberation artifact, which causes the US to miss deep pulmonary consolidation lesions (Figure 4). The risk of missing such lesions in the US can be reduced by identifying typically unilateral involvement, absence of airway sounds at the dorsal region of the affected thoracic cavity through auscultation, and inducing a ping sound from free air within the thoracic cavity through percussion-auscultation (51).

## 2.6 Pericarditis

Traumatic pericarditis is a common pericardial disease in dairy cattle because the reticulum is a common entry point for infection. The strong peristaltic contractions generated by the reticulum can

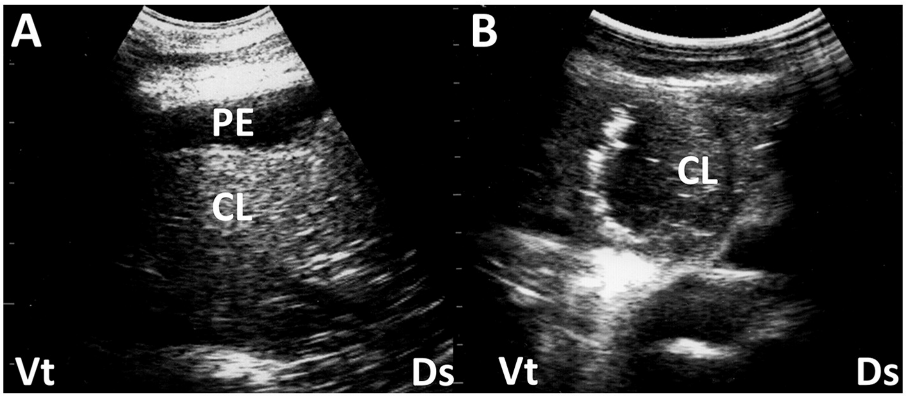


FIGURE 1
Ultrasonograms **(A, B)** of a consolidated lung (CL) in two camel calves with pneumonia. **(A)** Echogenicity in CL is increased heterogeneously. Anechoic pleural effusion (PE) is also evident. **(B)** In a consolidated lung, small pockets of gas often remain, seen as small hyperechoic areas. Ds, dorsal; Vt, ventral (45).

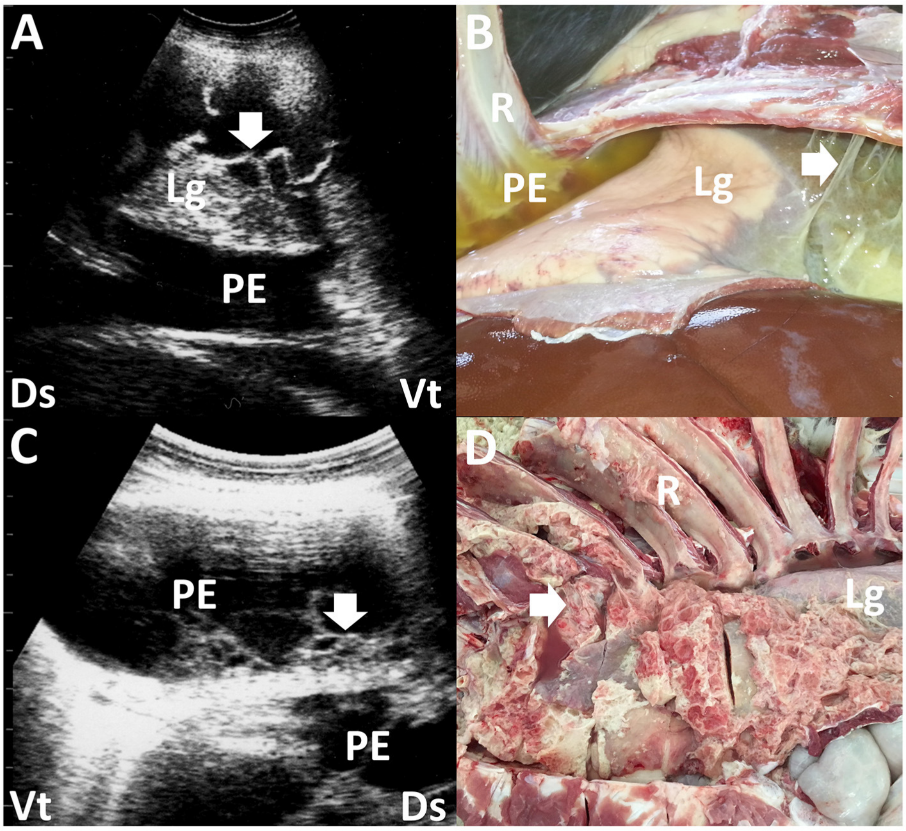


FIGURE 2
Ultrasonograms and macroscopic views show contagious caprine pleuropneumonia in a caprine case **(A, B)** and fibrinous pleuropneumonia in a camel calf **(C, D)**. **(A)** Echogenic fibrinous strands (arrow) are floating within an anechoic pleural effusion (PE). Compressed lung structures are demonstrated as echogenic. Lg, lung; Ds, dorsal; Vt, ventral. **(B)** Fibrinous adhesion (arrow) between the lung (Lg) and pleura and the accumulation of clear yellow pleural effusion (PE) is evident. R, rib (13). **(C)** Webbed fibrinous strands (arrow) are floating within hypoechoic pleural effusion (PE). Ds, dorsal; Vt, ventral. **(D)** Fibrous adhesive scars (arrow) are evident over the surface of the lung (Lg). R, rib (45).

facilitate the perforation of long, sharp foreign bodies from the reticulum itself (52). This can result in injury to the pericardial sac after passing through the peritoneum and diaphragm (7, 46, 52–54). Hematogenous spread of *Pasteurella*, *Salmonella*, coliform, and anaerobic bacteria is also implicated in cases of pericarditis infection (46). This disease is very rare in sheep and goats, including mycoplasmas, especially *Mycoplasma capricolum* subsp. *Capripneumoniae*, and *Mycoplasma mycoides* subsp. *mycoides* may

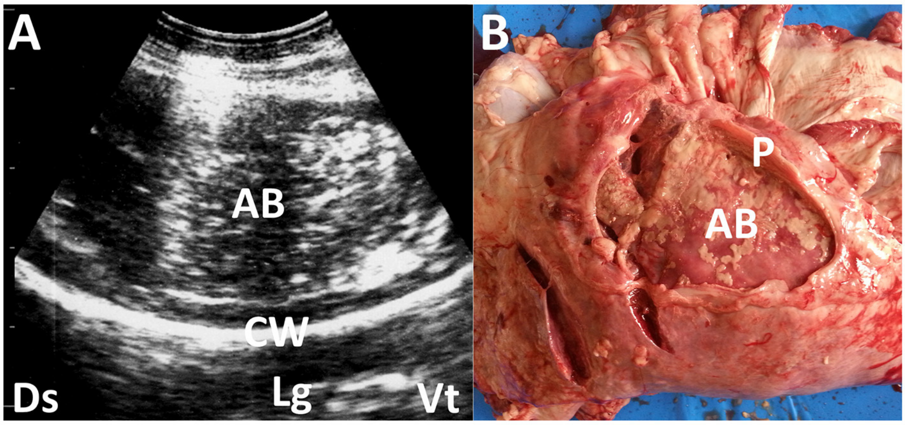


FIGURE 3
Ultrasonogram **(A)** and macroscopic view **(B)** showing pleural abscessation (AB) in a buck. **(A)** The capsular mass with a size of >3 cm includes the heterogeneous, hyperechogenic contents within the hyperechoic capsular wall (CW). Lg, lung; Ds, dorsal; Vt, ventral. **(B)** The AB mass is derived from the thickened pleural walls (P).

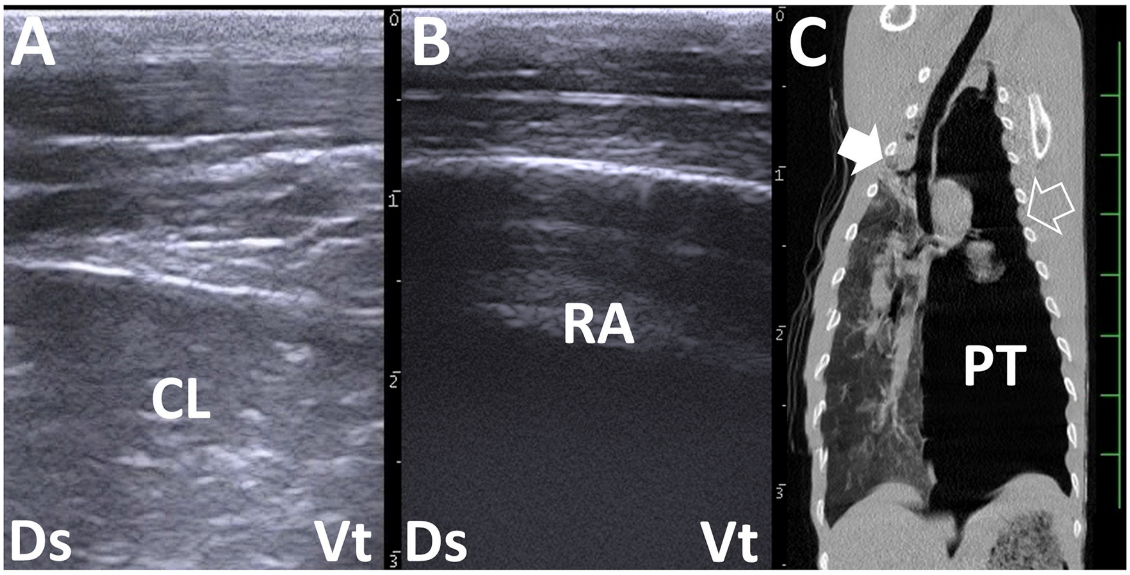


FIGURE 4
Right and left thoracic ultrasonograms **(A, B)** and computed tomography (CT) **(C)** in a bovine calf with left pneumothorax. **(A)** Increased echogenicity in the lung structures represents consolidated lung (CL). **(B)** Reverberation artifact (RA) is demonstrated extensively within the left dorsal thoracic cavity. No pleural sliding is evident. **(C)** Consolidation in the cranial right lung lobe is demonstrated more deeply than the scanning regions of the right chest (filled arrow). At the scanning region of the left chest (empty arrow), the intrathoracic accumulation of air represents pneumothorax (PT). The scale is 50 mm in the CT image.

be the causative agents. It is important to differentiate idiopathic hemorrhagic pericarditis from pericarditis induced by infection, including traumatic pericarditis (7).

The presence of non-inflammatory presternal edema and pulsatile distension of jugular and mammary veins, along with muffled or splashing heart sounds identified through heart auscultation, are noticeable macroscopic findings indicative of pericarditis (46). Thoracic US effectively supports the diagnosis of pericarditis by enabling visualization of the lung, pleura, and heart (46). Pericardial effusion is a specific US finding in pericarditis cases. In buffalos with traumatic pericarditis, pericardial effusion is accompanied by pleural effusion and lung abscessation in ∼50 and 13% of cases, respectively (46, 53). The echogenicity of pericardial effusion is commonly hypoechoic to echogenic (7).

Additionally, fibrin threads are formed that protrude from the epicardium and float in the fluid (7, 11, 46, 53) (Figure 5A). In contrast, idiopathic hemorrhagic pericarditis is commonly found in US and is characterized by an accumulation of anechoic pericardial effusion without fibrin clots (7). This distinction helps differentiate it from frequent pericarditis and in the choice of therapeutic options, such as drainage, given the favorable prognosis associated with idiopathic pericarditis (7). Pericardial hemorrhagic effusion caused by epicardial or pericardial lymphohematopoietic neoplasms resulting from bovine leukosis virus (BLV) infection appears as anechoic fluid on US (55). US-guided collection of pericardial effusion is useful for diagnosing this condition based on cytologic examination of the collected fluids, in which lymphocytes are the predominant cellular components (55). Johne's disease induces an accumulation of anechoic pericardial effusion together with pleural effusion in 31% of previous camel cases (56). Pericardial effusions are associated with trypanosomosis in 20% of previous camel cases (57, 58). Combined thoracic and abdominal US is useful for diagnosing trypanosomosis because it can identify accumulations of anechoic to hypoechoic effusions within the peritoneal and pleural spaces and the pericardium (57). Furthermore, continuous use of US during trypanosomosis treatment is effective for evaluating the positive therapeutic effects based on the disappearance of effusions within multiple spaces as indicated by changes in echotexture (58).

### 2.7 Endocarditis

Bacterial endocarditis is the most common endocardial disease in cattle. The condition is defined as an infection of one or more of the endocardial surfaces of the heart. The pathogenesis of this disease is not clearly defined, but chronic active infection leading to sustained or recurrent bacteremia is believed to be a predisposing factor. Echocardiography provides a valuable means of imaging the cardiac chambers and valves in cattle (3, 59, 60). Without the use of echocardiography, it is difficult to diagnose tricuspid, mitral, or pulmonic vegetative endocarditis accurately. Valvular thickening is one of the most sensitive US findings for diagnosing bacterial endocarditis (Figure 5B), as observed in more than 75% of the examined cases (3, 7, 61). The tricuspid valve is the anatomical part most frequently affected (7). US measurement of valvular thickness can support the diagnosis of this disease based on the critical border thresholds of 0.85, 1.27, 1.06, and 0.82 cm in the tricuspid, mitral, aortic, and pulmonary valves, respectively (60). Thrombus formation is sometimes detectable in the affected tricuspid, mitral, and pulmonary valves (3). Additionally, comprehensive US assessment may allow the detection of concurrent problems such as an enlarged liver, distended hepatic veins, and accumulation of effusion within multiple spaces of the pleura, pericardium, and peritoneum (3). In most cases, echocardiography permits an antemortem diagnosis, which can be especially useful in cases with a poor prognosis to avoid ineffective treatment and animal suffering (61).

## 3 Abdomen

### 3.1 Peritonitis

Peritonitis is a focal or diffuse inflammation of the serosal surface of the abdominal viscera or the wall of the abdomen with adhesions as a natural consequence of an inflamed serosa. The condition is common in cattle and rarely clinically identified in sheep or goats (62). The causes of peritonitis are multiple, including uterine tears, ruptured bladder, gastrointestinal perforation, and injury to the peritoneum and diaphragm due to sharp material perforating from the reticulum, referred to as reticuloperitonitis (5, 52, 54). Reticuloperitonitis induces the formation of a reticular abscess and free fluid and fibrin deposits within the abdominal cavity (54). In camels, gastric or intestinal perforation seems to be the frequent cause of peritonitis (63, 64). The pathogen of peritonitis in a llama was reported to be *Streptococcus equi* subsp. *Zooepidemicus,* which may have been transmitted via hematogenous dissemination from pneumonia (64, 65). The bacteria are also the causative agents of peritonitis and pleuropneumonia in dromedary camels (65). Clinical signs of peritonitis include colic, tense abdomen, stomach atony, ileus, weakness, plus or minus fever, diarrhea, painful movement, and recumbency (62). These clinical signs are reported to apply to all species but are non-specific (62).

US of the peritoneum has been cited as the best method to assess the extent of peritoneal reaction/abscessation in ruminants (17, 53, 57, 62, 63). Intraabdominal abscesses are ultrasonographically characterized by an echogenic capsular mass of varying thickness enveloping the hypoechoic to echogenic contents, sometimes generating acoustic shadowing (17, 18). Intraabdominal accumulations of the peritoneal effusions and abscessation associated with reticuloperitonitis can be identified with US scanning at the paramedian ventral areas within the 6th to 12th intercostal spaces (9, 52). Inflammatory reaction within the abdomen causes the creation of fibrins, represented as hypoechoic to hyperechoic strands, floating into the effusion or forming as septa-like structures, including effusions within the spaces between the peritoneum, greater omentum, and viscera such as the intestines, liver, kidneys, rumen, and spleen (9, 17, 54, 63, 66) (Figures 6A, B). In 50% of camel cases, the formation of fibrin strands into hypoechoic effusions that accumulate between intestinal loops was observed by the US as a complication of intestinal obstruction despite the absence of fibrin strands in 33% of the camel cases (57). Small amounts of effusion can be commonly demonstrated using the US but may be difficult to detect within the adhered mass of the ruptured small intestines as the effusion source (66, 67).

Peritoneal effusion is one of the most sensitive indicators of peritonitis in the US, but it is nonspecific because other diseases can also cause peritoneal effusion (54). Peritonitis can induce local or general accumulations of exudates with varying echogenicity depending on the cell counts and amount of fibrin (66). Anechoic fluids in the US in non-inflammatory abdominal effusions are mainly caused by increased intravascular hydrostatic pressure and/or decreased intravascular colloid osmotic pressure (66). Types of peritoneal effusion associated with fascioliasis vary (23). They include the accumulation of modified transudates or exudates in secondary peritonitis and transudates caused by hypoalbuminemia, leading to decreased intravascular oncotic pressure (66). Trypanosomiasis, caused by *Trypanosoma evansi*, results in Surra, a severe protozoal disease affecting camels in the Middle East, Africa, and Asia (58, 68, 69). Common US characteristics of this disease include massive intraabdominal accumulations of anechoic or hypoechoic fluids (58) (Figures 6C, D). Identification of peritoneal effusion via the US may indicate chronic trypanosomiasis, presenting clinically as chronic weight loss and subcutaneous edema (6, 57, 58, 69). The uroperitoneum

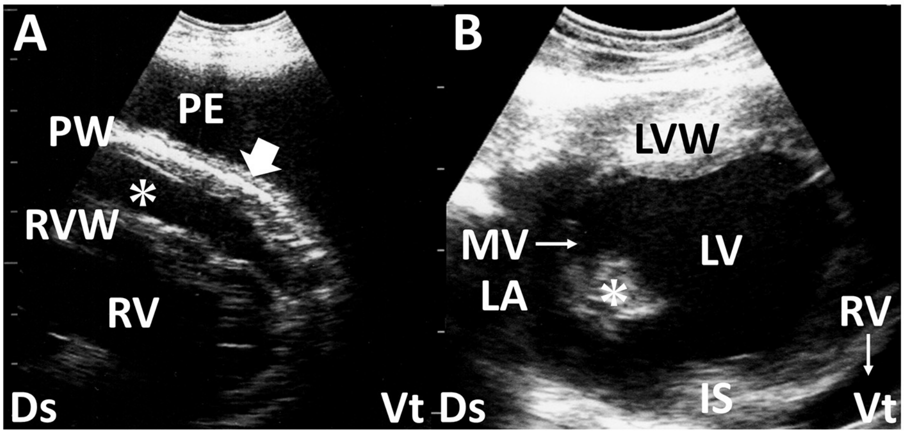


FIGURE 5
Long-axis echocardiograms show fibrinous pericarditis in sheep **(A)** and vegetation of the mitral valve in deer with endocarditis **(B)**. **(A)** Hypoechoic pericardial effusion (asterisk) is seen within the space between the right ventricular wall (RVW) and the thickened pericardium wall (PW), accompanied by the formation of small, corrugated structures (arrow). A large amount of anechoic pleural effusion (PE) is also evident. **(B)** The echogenic vegetative structure of the mitral valve (MV, asterisk), sized 1.0 × 1.4 cm, is seen in the outflow tract between the left atrium (LA) and left ventricle (LV). IS, interventricular septum; LVW, left ventricular wall; RV, right ventricle; Ds, dorsal; Vt, ventral (61).

typically manifests as an anechoic peritoneal effusion, which is distinct from the US findings of peritonitis (11, 19, 28, 34, 57, 70–72). However, the retention of intraabdominal urine can frequently lead to secondary peritonitis, increasing the echogenicity of peritoneal fluids, including strands of hyperechoic fibrin (28). Peritoneal mesotheliomas often present as anechoic patterns of peritoneal effusion in the US (73). This generates transudates with fewer cellular components throughout the abdominal cavity, sometimes leading to anechoic fluid accumulation in the scrotum (73). It is necessary to distinguish between scrotal enlargement associated with massive peritoneal effusion seen in the US vs. enlargement due to orchitis and/or epididymitis, which are mostly associated with brucellosis in rams and bucks (74) (Figure 7). Although the echogenicity of peritoneal effusion is an effective indicator for differentiation between peritonitis and other diseases, it is not diagnostic. Therefore, US-guided abdominocentesis effectively collects peritoneal effusion because laboratory examination is highly sensitive in diagnosing peritonitis (18, 54, 73).

## 3.2 Liver abscessation

Liver abscessation has a major economic impact on the feedlot industry due to liver condemnation and reduced animal performance and carcass yield. It can occur at any age and in any type of cattle, contributing to the greatest economic loss in grain-fed cattle (75). This disease is often diagnosed incidentally during postmortem examination due to difficulty detecting its clinical signs, even when the animals have hundreds of small abscesses or several large abscesses (20). In a retrospective study on isolates from camel liver abscesses, *Staphylococcus* spp., *Corynebacterium* spp., and *Streptococcus* spp. were the predominant pathogens (76). US of liver abscesses can appear as single or multiple formation of masses sized between 3 and 20 cm (11, 77, 78). These US findings appear to change depending on the entry of infection, inflammatory reaction, and chronicity (77, 78). Liver abscesses seldom infiltrate the peripheral liver parenchyma, making it easy to distinguish the lesion's border by US. However, the formation of septa-causing chambers in the mass may indicate partial destruction of liver structures, possibly related to the chronicity of liver abscessation (77). The echogenicity of abscess contents varies from anechoic to hyperechoic (11, 75) (Figure 8).

Additionally, abscess contents can appear heterogeneously or homogeneously, although long-standing liver abscesses tend to have homogeneous contents (77). US is useful for guiding centesis procedures to differentiate liver cysts from tumors and for drainage during treatment (77). US can also provide significant evidence for choosing therapeutic options and assessing prognosis. Identification of multiple liver abscesses by the US indicates an unfavorable outcome, often associated with serious conditions such as sepsis and local spread from infectious foci within the umbilical remnants (77, 78). Evaluating the intrahepatic distribution of lesions by US may help decide whether surgical therapy is necessary for liver abscesses, even if they affect multiple areas (78). This approach was successful in a recent case of liver lobectomy for a calf with multiple liver abscesses (78).

## 3.3 Fascioliasis

Fascioliasis is caused by the infestation of *Fasciola hepatica* into the hepatobiliary system. The acute phase corresponds to the intrahepatic migration of immature parasites through the intestinal mucosa, known as the hepatic stage (11, 79). The chronic phase occurs when adult flukes establish themselves in the biliary ducts, referred to as the biliary stage (79). During the biliary stage, biliary obstruction develops, and plasma protein leaks across the epithelium, leading to hypoalbuminemia. There is also whole blood loss due to the feeding activities of the flukes, exacerbating

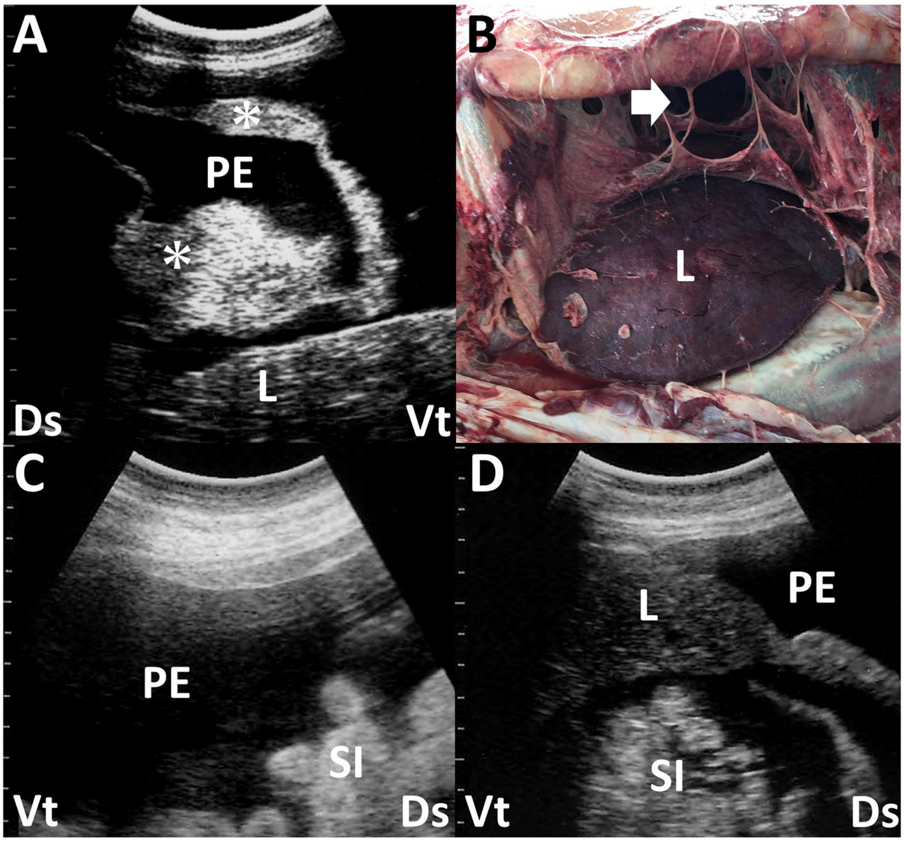


FIGURE 6
Ultrasonogram **(A)** and macroscopic view **(B)** in a dromedary camel with chronic peritonitis. Ultrasonograms **(C, D)** of a female camel with chronic trypanosomiasis. **(A)** Hypoechoic peritoneal effusion (PE) is seen within the abdominal cavity between the abdominal viscera. The echogenic fibrous strands (asterisk) and liver (L) are imaged floating into the PE. Ds, dorsal; Vt, ventral. **(B)** The formation of the fibrin's sept-like strands (arrow) is evident within the abdominal cavity. Discolored liver structure (L) is also seen (63). **(C, D)** Hypoechoic peritoneal effusions (PE) are seen within the abdominal cavity, in which the small intestines (SI) and liver (L) are floating. Ds, dorsal; Vt, ventral (58).

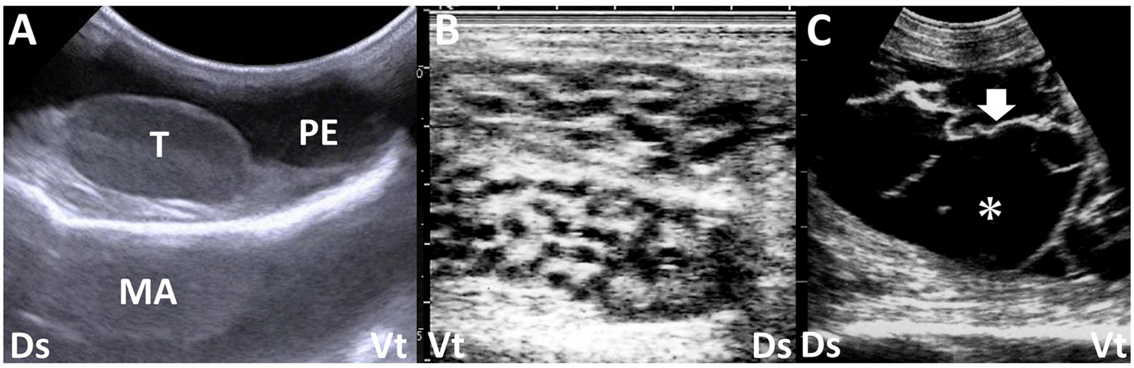


FIGURE 7
Ultrasonograms of the swollen scrotums in a calf with peritoneal mesothelioma **(A)** and two bucks with epididymitis **(B)** and periorchitis **(C)** caused by infections with *Brucella melitensis*. **(A)** Anechoic peritoneal effusion (PE) accumulates around the normal structure of the testis (T) within the scrotum. MA, mirror image artifact (image courtesy of Dr. Yasuhiro Morita, who belongs to Kyushu University). **(B)** Honeycomb-like structures of the epididymis are seen. **(C)** Echogenic fibrous strands (arrow) are seen on the tunics surrounding the atrophied testis and floating within anechoic effusion (asterisk). Dr, dorsal; Vt, ventral.

anemia and hypoalbuminemia (80). As adult worms increase, the likelihood of developing liver fibrosis increases (81). The fibrotic response of the liver to fluke-induced damage varies among hosts and may partly account for differing species' susceptibilities (82).

Based on previous experimental studies using rabbit and ovine models, the US characteristics of fascioliasis may change depending on the development of hepatic and biliary stages (79, 83). These studies initially identified the intrahepatic distribution

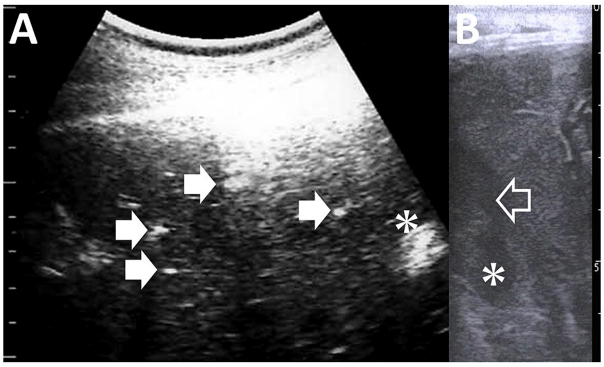


FIGURE 8
Ultrasonograms of liver abscess in a camel **(A)** and in a calf with umbilical vein infection **(B)**. **(A)** A 1-cm-sized abscess (asterisk) is characterized as the capsular mass enveloping the heterogeneous echogenic contents. Arrows in the image point to the calcified bile ducts. **(B)** Anechoic contents are evident within the lumen of the umbilical vein (empty arrow) and the cavity of a 2-cm-sized abscess (asterisk).

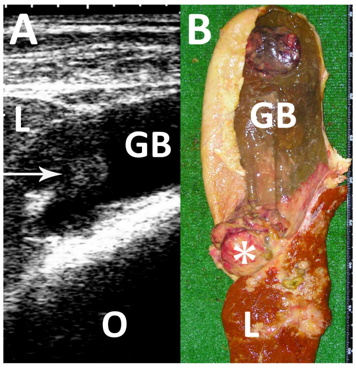


FIGURE 9
Ultrasonogram **(A)** and macroscopic view **(B)** in a Japanese black cow with fascioliasis. **(A)** An echogenic mass (arrow) is seen within the gallbladder (GB). L, liver; O, Omasum. **(B)** A 5-cm cauliflower-like mass (asterisk) is seen between the discolored liver structure (L) and gallbladder (GB) (80).

of hypoechoic to hyperechoic lesions, followed by dilated, tortuous biliary ducts containing active echogenic parasites in their lumens during 7–8 weeks and 9–10 weeks after *Fasciola hepatica* infection, respectively (79, 83). However, naturally infected animals may exhibit a mixture of pathological changes corresponding to the hepatic and biliary stages due to the time lag between *Fasciola hepatica* infection and symptom onset (79). Cattle and buffaloes naturally affected by fascioliasis show heterogeneous echotexture of liver parenchyma in US, with scattered hyperechoic spots, bile duct enlargement, and gallbladder wall thickening (11, 23, 80) (Figure 9). In cases where fascioliasis causes severe cholangiohepatitis and inflammatory liver fibrosis, the liver parenchyma appears heterogeneous. Chronic fascioliasis is the most common cause of bile duct calcification, which, in the US, generates acoustic shadowing distal to the hyperechoic walls of affected bile ducts (11, 23, 77, 80). This manifests as ring-like or tube-like echotexture in US, observed in cross-sectional or longitudinal views (77, 80). In addition to identifying liver lesions, US helps guide cholecystocentesis for detecting liver fluke eggs and facilitates cytological and bacteriological examinations of bile fluids aspirated via a spinal needle introduced percutaneously (77).

## 3.4 Hydatid cysts

The adult tapeworm, *Echinococcus granulosus*, is found in the intestines of carnivores, particularly dogs (84). Eggs are passed in the feces and ingested by sheep, goats, other ungulates, or humans (84). In these intermediate hosts, ingested eggs release oncospheres that enter intestinal venules or lacteals and migrate to the liver or lungs via the circulatory system. The metacestode stage, known as the hydatid cyst, develops in these organs over several months. Hydatid cysts typically average 5–10 cm in diameter, contain a yellowish, serum-like fluid, and may have a granular inner wall with multiple brood capsules (11, 26, 48). Hydatid "sand," which is an accumulation of detached brood capsules, may be observed in the cyst fluid. US examination of sheep with hydatid cysts shows multiple cysts with anechoic content in the abdomen (26, 85). An elongated echogenic structure corresponding to the scolex is typically seen in the center of the cyst. Cysts are most commonly found in the liver, lungs, and spleen (84) (Figure 10). US detection of liver hydatid cysts accounts for 9.2 and 2.5% of examined ovine and caprine cases, respectively (86). US sensitivity and specificity for detecting these lesions at necropsy are 54.4 and 97.6%, respectively (85). The classification criteria for cystic echinococcosis in veterinary fields in the US align with those of the World Health Organization (79, 84, 87). These criteria categorize cystic disease into five types (79, 87). Active and fertile cysts are demonstrated by the intrahepatic formation of rounded, unilocular, anechoic, well-defined nodules with or without septa in the US (79, 87). The formation of the mass appearing with an irregular contour and variable echogenicity indicates the inactive stage in cystic echinococcosis (79, 87).

## 3.5 Cysticercosis

Ovine visceral metacestodiasis is caused by the migration of *Cysticercus tenuicollis*, the intermediate stage of *Taenia hydatigena*, found in the intestines of dogs, coyotes, wolves, and other carnivores, to the liver and lung tissue of intermediate hosts such as sheep, goats, cattle, pigs, and squirrels (88). The adult tapeworm of this larval form is the canine tapeworm *Taenia hydatigena*. Onchospheres released from eggs penetrate the intestine and travel via the portal vein to various tissues, especially the liver, omentum, mesentery, and peritoneum. Migration through the liver causes hemorrhagic tracks, and on reaching the liver surface, the larva develops into a thin-walled, fluid-filled bladder (89). Alternatively, it may degenerate, calcify, or occasionally predispose to black disease (89). The US of the affected liver typically shows a diffuse hyperechoic pattern in the liver parenchyma (88). Acute

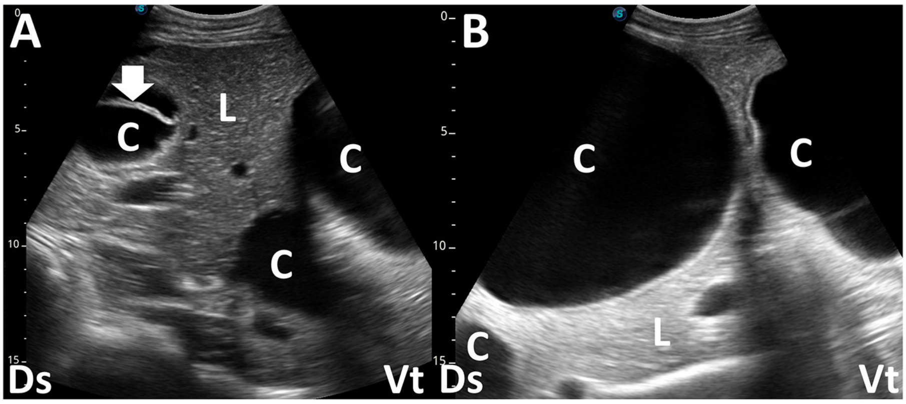


FIGURE 10
Ultrasonograms **(A, B)** in a female camel with liver hydatidosis. **(A)** Three cystic masses (C) enveloping anechoic fluids are evident within the compressed liver parenchymas (L). Thickening in the wall of one mass corresponds to an early daughter cyst (arrow). **(B)** Two large and one small cystic mass (C) are seen within the liver (L). Ds, dorsal; Vt, ventral (84).

cysticercosis is characterized by the presence of tubular, red, blood-filled tracts 2–4 mm in diameter within the liver parenchyma, where cysts may also be present (Figure 11). Similar US findings are common in the mesentery, omentum, and serosal surface of peritoneal viscera.

## 3.6 Pyelonephritis

Pyelonephritis is an infectious renal disease caused by local or systemic infection by less common isolates, including *Escherichia coli*, *Staphylococcus* spp., *Streptococcus* spp., *Enterococcus* spp., *Klebsiella* spp. *Trueperella pyogenes* and *Pseudomonas* spp. (29, 31, 32, 90). According to previous abattoir survey examinations, the prevalence of pyelonephritis may be lower in sheep and goats than in cattle, accounting for between 0.9 and 3.5% (29). Common US characteristics of the affected kidney include a dilated and deformed renal sinus and an unclear echogenicity border between the renal cortex and medulla (6, 27–29, 31, 32, 54, 91) (Figure 12A). Typically, the dilated ureter appears at the location of the renal pelvis outlet. It contains hyperechoic purulent debris, red blood cells, and pus (27, 28, 91). When using US to identify dilation in the renal pelvis and ureter, it is essential to differentiate it from hydronephrosis, which is characterized by dilated renal pelvis and pressure atrophy of the renal parenchyma (30, 71, 72, 90). Echogenic foci generate acoustic shadowing, which is evident if the exudates accumulate and crystal deposits are present within the renal parenchyma (27). The echotexture of the affected kidney shows renal abscessation, characterized by a capsular mass enveloped by a hyperechoic capsular wall and hypoechoic content (30, 32). Regarding the US appearance of other infectious renal diseases, BVD infection can cause glomerulonephritis, appearing as hypoechoic medullary pyramids (28). This appearance contrasts with the increased echogenicity of the renal cortex seen in dilated renal parenchyma, which subsequently decreases in size during the chronic phase (28). Embolic nephritis can occur secondary to septicemia (28). Some affected animals develop endocarditis secondary to systemic bacterial infection (28). US can identify hypoechoic foci formation in the renal cortex, although these lesions are often small and difficult to detect (28). The US is useful for guiding percutaneous centesis of the kidney for aspiration of purulent materials and biopsy, allowing differentiation between various renal diseases (30).

## 3.7 Cystitis

Cystitis is often caused by bacterial infection, resulting in urinary bladder inflammation (28). The US of cystitis identifies diffuse thickening in the bladder walls due to thickened and corrugated mucosa (28, 71). The affected urinary bladder includes multiple echogenic fluid contents swirling within the lumen (28). In some animals with pyelonephritis, the fluid contents within the urinary bladder show increased heterogeneously echogenicity due to the outflow of purulent materials into the lumen (27, 28) (Figure 12B). Therefore, if there is a change in urine echogenicity, the bladder and kidney should be scanned together using US.

## 3.8 Enteritis

Johne's disease is caused by *Mycobacterium avium* subsp. *paratuberculosis* infection, also known as paratuberculosis. The disease is characterized by chronic, contagious enteritis, leading to chronic wasting and fatal development of persistent diarrhea, ultimately resulting in death (56, 92–96). This organism may cause Crohn's disease in humans (97). Therefore, strict isolation and eradication of infected animals are required. The clinical use of US is useful for isolating suspected animals until confirmatory laboratory tests allow a conclusive diagnosis of Johne's disease. US commonly identifies the thickening of the intestinal walls in most affected ruminants, such as cattle, camels, goats, and sheep (56, 94, 98). In caprine cases with Johne's disease, US identifies thickened intestinal walls measuring >2.0 mm, typically including corrugation of the intestinal mucosa (94) (Figures 13A, B). In camels affected with Johne's disease,

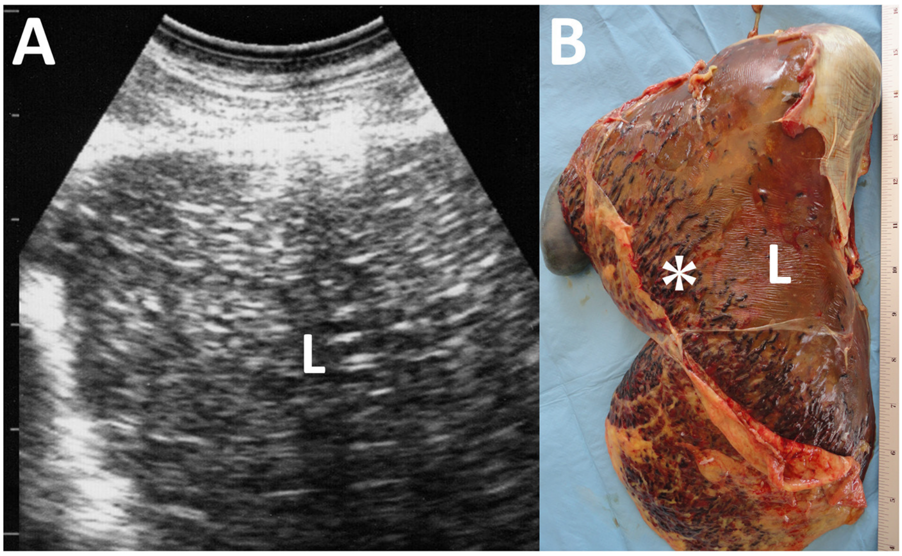


FIGURE 11
Ultrasonogram **(A)** and macroscopic view **(B)** of cysticercosis in the liver of an ovine case. **(A)** The liver parenchyma (L) is demonstrated as heterogeneously hyperechoic. **(B)** Blood-filled tracts (asterisk) are seen within the swollen liver (L) due to the migration of *Cysticercus tenuicollis* (the embryos of *Taenia hydatigena*).

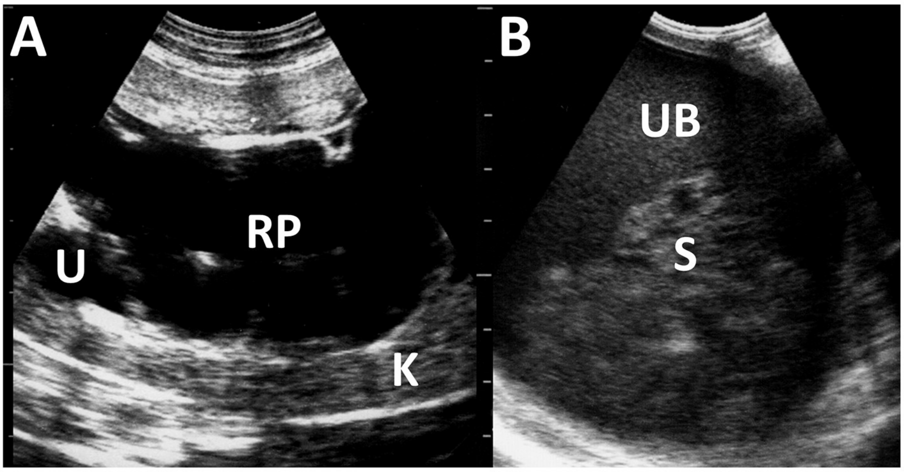


FIGURE 12
Ultrasonograms of pyelonephritis in the kidney of a caprine case **(A)** and the urinary bladder of an ovine case **(B)**. **(A)** The affected kidney (K) has loss of normal echotexture of its parenchyma and increased echogenicity. Dilated renal pelvis (RP) and ureter (U) include anechoic urine. **(B)** The echogenicity of the urine is increased within the lumen of the urinary bladder (UB). Echogenic sediments (S) of cell debris, pus, and red blood cells are also evident.

thickening and corrugation in the intestinal walls are also common US characteristics, identified in 84% of previous cases (56) (Figures 13C, D). The severity of intestinal wall thickness is classified as mild, moderate, or severe based on US measurements (56). Specifically, the values for mild, moderate, and severe are 6.8, 12.8, and 17.5 mm, respectively, compared to the normal value of 3.6 mm (56). In 95% of camel cases, the thickening and corrugation of the intestinal walls identified by US can represent macroscopic changes, such as increased sizes in the folds of the mucous membrane within the lumens of the affected intestinal loops (56, 94, 95). Other US findings include increased hepatic echogenicity, omental edema, and peritoneal, pleural, and pericardial effusions in affected caprine, ovine, and camel cases (6, 56, 94). Additionally, these cases have enlargement of the mesenteric lymph nodes demonstrated ultrasonographically as the hypoechoic cortex and hyperechoic medulla (6, 94). The enlarged lymph nodes are identified as another US finding in which an echogenic capsule envelops anechoic, echogenic, or heterogeneous parenchymas (6, 56). When US identifies intraabdominal swollen masses, it is necessary to differentiate lymphadenopathy associated with infectious gastrointestinal diseases such as Johne's disease from intraabdominal abscess, enzootic bovine leukosis, and fat necrosis (99). BLV-associated lymphadenopathy and fat necrosis are commonly demonstrated as heterogeneous hyperechoic and hypoechoic mass lesions, respectively (4, 99). US helps guide the biopsy of intraabdominal masses, aiding the differential diagnosis (4, 91).

Eosinophilic enteritis is an inflammatory bowel disease caused by infiltration of eosinophils. It occurs idiopathically or secondary to parasitism, among other causes, such as drug reactions, systemic eosinophilic syndrome, and malignancy in ruminants (100). Thickening in the intestinal walls, with a dilated lumen filled with fluid, is a common US characteristic of this disease, representing inflammation of the intestinal mucosa, lamina propria, and submucosa (100).

Hemorrhagic bowel syndrome is an acute necrohemorrhagic enteritis, with *Clostridium perfringens* infection considered the most likely cause (101). The accumulation of heterogeneously echogenic masses of blood clots in the lumen of the small intestine is indicative of this disease, as identified by the US in 19% of affected animals (101, 102). Thickening in the intestinal walls is evident in only 10% of cases (102).

### 3.9 Umbilical remnant infection

Infection in the external stump, or omphalitis, is a macroscopically detectable umbilical infection that induces various degrees of umbilical swelling (103, 104). The umbilical infection can transfer pathogens into the lumens of the internal umbilical remnants, including the umbilical vein, umbilical artery, and urachus, resulting in omphalophlebitis, omphaloarteritis, and urachitis, respectively (33, 104). Palpation cannot always detect umbilical remnant infections despite helping diagnose omphalitis (103). US is an effective imaging tool that provides high-quality images for evaluating intraabdominal involvement during percutaneous scanning (21).

In 50% of the healthy calves aged 3 weeks old, the US detects the umbilical vein as a round anechoic to hypoechoic structure within the abdominal cavity (33, 103). An abnormality in retraction after umbilical cord break is considered if the full length of the umbilical vein is identified in the US at this age (33). US can provide evidence to evaluate the association between the umbilical vein and liver abscess formation (21, 33). During US, a urachal abscess can be identified as a tubular structure with varying wall thickness and echogenic materials. This structure typically enters the liver when scanning from the midline of the ventral abdominal surface toward the right side and moving cranially from the umbilicus (19, 21, 33) (Figure 14). The urachus is a common route for the intraabdominal spread of umbilical infection into the urinary bladder in younger animals, where it can be identified as a tubular structure present at birth (33). The urachal abscess appears in US as an accumulation of echogenic contents with or without small hyperechoic deposits within the extended lumen of the tubular structure (19, 105) (Figure 15). The degree of extension of the affected urachal lumen, including the purulent materials, is a significant factor in surgical decision-making (105). The spread of infection between the umbilical cord and urinary bladder via the umbilical vein can be assessed by the flow of echogenic contents within the umbilical vein toward the lumen of the urinary bladder (33, 70, 105). The umbilical artery may serve as an entry point for systemic infection via the aorta (104). The umbilical artery is detectable when applying US to healthy calves up to 1 month old, but its diameter decreases with age (104). In the US of omphaloarteritis, the diameters of affected umbilical arteries are observed to remain stable but subsequently increase with growth (104). However, the US diagnosis of omphaloarteritis is more difficult than that of omphalophlebitis and urachitis (21).

## 4 Utility of US compared with the other imaging modalities

Thoracic radiography can distinguish lower lung field density, providing good contrast with the hyperdense contours of the heart and diaphragm located in the central and caudal aspect of the thoracic cavity. Abnormal shape and contour of the heart and diaphragm are radiographic evidence suggestive of pericarditis, including an unclear diaphragm line, gas opacity overlapping the caudal contour of the heart, and an enlarged dorso-caudal cardiac silhouette (10). However, radiography has a lower sensitivity to detect this disease, especially in cattle, compared with the use of US (10). On thoracic radiographs, the soft tissue opacity of the lung becomes a good background to highlight various types of pulmonary lesions, such as lung cysts and abscesses appearing as round to oval radiopaque masses, depending on their sizes (48). Radiography can also identify specific cavitary lung lesions, such as gas-forming bacteria-induced lung abscesses, including gas-fluid interfaces and gas-filled masses of emphysematous bullae (36). The radiographic detection sensitivities of lung abscesses and emphysematous bullae are 30 and 38%, respectively, whereas pneumothorax has a sensitivity of 0% (106). This indicates that pneumothorax may be difficult to diagnose using thoracic radiography, identical to thoracic US based on Figure 4. Thoracic radiography helps distinguish between three types of pneumonia classified as alveolar, interstitial, and bronchial patterns (106). However, a mixture of these three patterns is common in ruminants with pneumonia, making it difficult to differentiate among them using radiographs (106). When thoracic radiography reveals hypodense structures of air-filled bronchi enhanced by the diffuse, hyperdense changes of the affected lung structures, referred to as an air bronchogram, this radiographic sign is among the most useful evidence to confirm consolidation (36, 107). This radiographic abnormality mostly appears within the cranioventral lung regions in ruminants (15, 108). However, this region normally overlaps with the opacity of the forelimbs on lateral thoracic radiographs taken in a standing position (108–110). Physical or drug restraints of the examined animals are required to place them in a lateral recumbent position to obtain optimal lateral thoracic radiographs, with their forelimbs pulled cranially to sufficiently evaluate cranioventral lung regions (108, 110). However, forced examination may lead to the progression of weakness and exacerbation of pneumonia in the examined animals (107). Therefore, new radiographic techniques have been developed to provide good views of cranioventral lung fields, such as the two-legged technique, where the examined calf's body is held up with its forelimbs pulled cranially (108), and the three-legged technique,

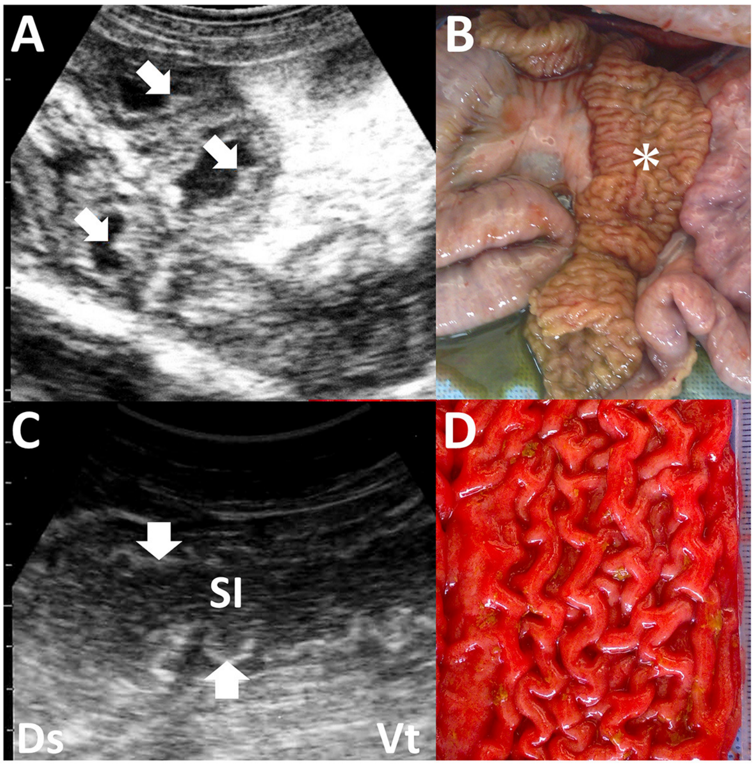


FIGURE 13
Ultrasonograms and macroscopic views of Johne's disease in a caprine case **(A, B)** and camel's case **(C, D)**. **(A)** The corrugated intestinal mucosa (arrows) is visible on the thickened intestinal walls. **(B)** Corrugated changes (asterisk) in the intestinal mucosa are seen extensively (94). **(C)** The longitudinal section of the corrugated intestinal mucosa appears as wavelike lines (arrows) within the dilated lumen of the affected small intestine (SI). **(D)** Corrugation of the intestinal mucosa is evident on the whole surface of the affected intestine (56).

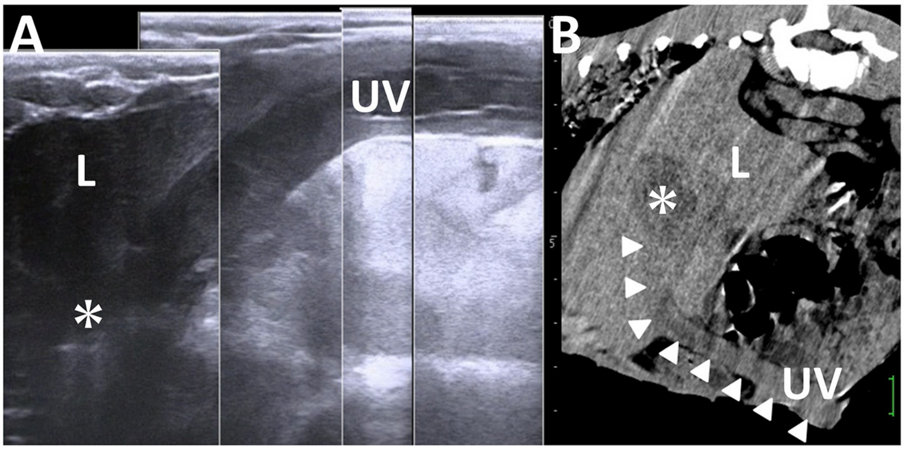


FIGURE 14
Ultrasonogram **(A)** and computed tomography **(B)** of liver abscessation associated with umbilical vein infection in a calf. **(A)** The tubular structure of the umbilical vein (UV), including anechoic contents, runs between the umbilicus and the liver (L) and ends at the capsulated mass (asterisk) within the L. **(B)** The umbilical vein (UV) is demonstrated as the entry of infection (arrowheads) from the umbilicus to the capsulated mass (asterisk) within the liver (L). The scale is 25 mm in the CT image.

where the animal stands on one forelimb and both hindlimbs while lifting the opposite forelimb for lateral thoracic radiography (110). These radiographic techniques may take several attempts due to unexpected movement and faster respiratory motion in struggling animals, making this examination very stressful for both examiners and examined animals (36).

Regarding observation of the cranioventral lung field, thoracic US is not superior to thoracic radiography (110). In the thoracic

US, visualizing thoracic regions between the 1st and 3rd intercostal spaces is very difficult due to the scanning operation to maneuver the transducer into the axillary space (12, 41, 110). Although a previous report described a bovine thoracic US technique that extended scanning areas to the 1st to 2nd intercostal spaces, this technique seems to cause great discomfort in the examined animals. Additionally, this technique may be applicable only to very young calves estimated to be under 12 weeks of age (12, 110). Therefore, despite being more routinely available, thoracic UA cannot completely replace thoracic radiography as a diagnostic technique (110).

The radiopacity on abdominal radiography is mostly homogeneous in the abdominal viscera themselves. In contrast, heterogeneous radiodense structures of the ingesta and radiolucent gas are visible within the lumens of gastrointestinal tracts. Differences in radiodensity between abdominal viscera, omentum, and intraabdominal fat tissues can clarify the contours of the abdominal viscera packed within the abdominal cavity (25). However, the contours of most abdominal viscera, such as the liver, are commonly unclear, limiting the clinical utility of plain abdominal radiography (25). Conversely, lesions and materials generating lower or higher radiodensities can provide good contrast against adjacent abdominal viscera on plain abdominal radiographs. Radiography is superior to the US in identifying metallic foreign bodies causing traumatic reticuloperitonitis, which appear mostly as radiopaque, sharp, linear materials contrasting well with the radiodensities of the thoracoabdominal region, including the reticulum, diaphragm, and heart (17, 48, 53). Full attachment of the magnet with a metallic foreign body and its position partly predicts reticular perforation (53, 111). Despite appearing as a hyperechoic linear structure causing acoustic shadowing on US, US rarely identifies metallic foreign bodies (17, 25). Gas-filled abscesses are detectable as radiolucent structures on abdominal radiographs, providing good contrast to the radiopaque structures of abdominal viscera (53, 111, 112). The formation of a gas-filled or gas-fluid interface mass adjacent to the reticulum is a suggestive radiographic sign of a perforating foreign body (111). Peritoneal effusion makes the contours of abdominal viscera unclear (25). Despite the higher potential of US to distinguish these types of peritoneal effusions, there is no specific radiographic sign to differentiate between transudates, exudates, and modified transudates (25).

Using a positive contrast medium helps distinguish abdominal organs from each other on radiographs of the ruminant abdomen, where the rumen occupies the majority of the space (17). The upper or lower gastrointestinal tracts can be identified radiographically by administering barium sulfate medium via a stomach tube in younger calves and small ruminants (22). However, a disadvantage of this method in ruminants is the time-dependent differences in contrast enhancements in the gastrointestinal tracts; for goats, several minutes to hours are required after oral administration of barium sulfate medium to enhance the forestomach, small intestine and large intestine (22). Additionally, the superimposition of positively enhanced gastrointestinal tracts can result in the images obscuring each other (22). This appears to be why routine abdominal US is replacing gastrointestinal contrast radiography (25). Excretory urography has been previously utilized for small ruminants and young calves, allowing time-dependent, normal contrast enhancement within the renal parenchyma such as the hilus and renal pelvis, followed by contrast medium filling within the lumens of the ureter, and finally, the urinary bladder (112–114). Experimentally induced nephrosis caused the cessation or delay of contrast medium outflow within the urinary tract (113, 114). In a previous case involving a calf with a gas-filled urachal abscess, this technique effectively confirmed no communication between the urinary bladder and the mass (112). Retrograde urethrography and cystography are also available to clarify communication between the urinary bladder and the mass via the persistent urachus (115). These contrast radiographic techniques targeting the urinary tract can complement the limitations of the abdominal US, which sometimes incompletely identifies the urinary tract; the kidney and urinary bladder are partly visible, whereas the ureter is rarely evident.

CT is a valuable imaging modality used for visualizing organs throughout the entire body without superimposition, and it is effective for both for small and large ruminants when available (2, 22, 107, 116). The intravenous injection of contrast medium during CT scanning enhances the ability to distinguish between normal and abnormal structures present within organs (e.g., the liver) by providing differing contrast enhancements between these structures (25, 78, 116). Abdominal CT scanning, combined with gastrointestinal contrast, is particularly useful for evaluating pathological changes within the gastrointestinal lumens (116). For instance, in newborn calves, the umbilical vein can be visualized

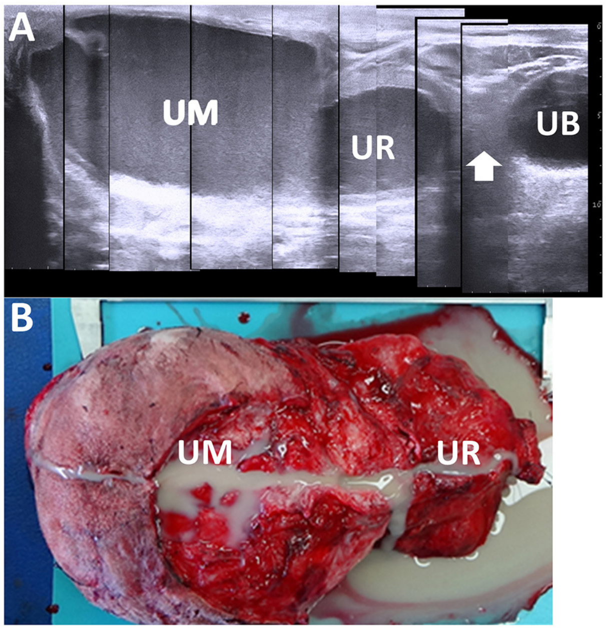


FIGURE 15
Ultrasonogram **(A)** and macroscopic view **(B)** in a calf with abscessation extending between the umbilicus and urachus. **(A)** There are echogenic contents within the extended lumens of the umbilicus (UM) and urachus (UR), sized at ~10 and 5 cm, respectively. The cord-like structure (arrow) is seen between the extended UR and the urinary bladder (UB). **(B)** The extended mass of the umbilicus (UM) and urachus (UR) enveloping the pus is removed surgically after suturing and cutting at the part of the cord-like structure.

running between the umbilical cord and the liver along the ventral abdominal walls (117). It has been observed that the umbilical vein typically disappears on CT around 21 days of age, making this an appropriate time frame to detect remnant umbilical veins (117).

The use of CT in 1-month-old Holstein calves presenting with stifle arthritis allowed the identification of purulent omphalophlebitis extending to a liver abscess, aiding in the prognosis. CT revealed pneumothorax as the unilateral accumulation of gas within the left thoracic cavity, effectively identifying infectious lesions in previous CT scans of the thoracic and abdominal regions (44, 78, 112).

In cases of echinococcosis, CT has revealed the intrahepatic formation of various sizes of round hypoattenuating structures, with changes in the thickened and mineralized cystic walls depending on the developmental stages of the disease (25). Using multi-directional reconstructed and three-dimensional (3D) CT images and basic transverse sections, the extent and severity of lesions formed within the organs, such as lung and liver abscesses, can be evaluated. This approach also allows for the assessment of the spatial relationship between lesions and adjacent organs, as well as any mass effects (44, 73, 116).

There are great technical limitations in each of these imaging modalities in clinical practice. In radiography, the limitation-associated factors include the magnitude of X-ray irradiation power generated from the X-ray machine, the sizes of the animals applicable for radiographic examination, and the number of required examiners (44, 107). High X-ray irradiation is required for X-ray transmission through the large body mass of adult cattle and buffaloes (53). The required X-ray conditions are 85–113 kVp and 50–200 mAs, and 90–115 kVp and 50–70 mAs, when taking thoracic and abdominal radiographs for adult large ruminants, respectively (10, 48, 53). In contrast, the exposure conditions are 45–85 kVp and 2–50 mAs for the chest of small ruminants and younger calves (15, 36, 107, 110). Radiographic limitations are also associated with the difficulty in evaluation using two-directional radiographic views (107). Dorsoventral radiographs are very difficult to take for the thoracic and abdominal regions of adult animals with larger dorsoventral depths of these regions (53, 107). Sedation is commonly required to place animals in dorsal recumbency for proper positioning to take dorsoventral radiographs (25).

US has limited ability to demonstrate lesions presenting at depths >10 cm, even when using a transducer with lower US frequency (2, 36). When scanning large-sized structures, the US can provide fragmented images because the scanning window is too small to scan the whole body (2, 25). Therefore, it is required to visualize the full length of targeted structures based on the sequential US obtained by scanning while moving the transducer gently and slowly across the skin's surface. Successful results from this scanning method depend on the skill levels of the sonographer.

CT has limitations regarding acceptable body sizes and weights in examined animals. Adult cattle are not commonly applicable as the examined target for CT scanning due to their large body mass unless using a specific CT machine with a larger CT gantry and scanning table capable of tolerating heavy body weight (117, 118). Deep anesthesia is commonly required for CT scanning, whereas sedation can sufficiently immobilize an animal for CT scanning when using a multidetector CT machine that allows for shortened scan times (25, 109). Additionally, endotracheal intubation is recommended to control breathing during CT scanning, such as breath-hold techniques, because breath motion can generate motion artifacts and reduce image quality (22, 107, 118), despite previous reports suggesting that motion-associated imaging quality is not usually poor for diagnostic assessment (44).

Therefore, routine use of US should be combined with radiography to enhance sensitivity in detecting infectious lesions within the chest and abdomen (17, 22). CT would be the advanced imaging modality to complement the routine use of US and radiography.

3D US is an advanced imaging technique that can provide various directional axes of organs more accurately than two-dimensional US (119). Previous uses of 3D US aimed to measure bovine mammary glands when scanned percutaneously (120) and fetuses within a gravid uterus when scanned transrectally (119). In terms of the clinical applicability of this method for diagnosing infections and thoracic and abdominal diseases, a freehand manner of moving the transducer slowly along targeted structures may be suitable for demonstrating immovable lesions such as abscess formation within the lung and liver and infectious foci in the urinary tracts and umbilicus (120).

## 5 Conclusion

The combined use of US, radiography, and CT can help overcome the limitations of individual imaging modalities in both large and small ruminants. To further enhance the diagnostic efficacy of these imaging techniques, whether used in routine practice or advanced settings, it is crucial to incorporate 3D or four-dimensional US machines and introduce diagnostic assistance systems, such as artificial intelligence algorithms. Additionally, it is important to recognize that extensive basic data from previous ruminant cases is essential for maximizing the potential of these advanced technologies. Therefore, ongoing integrated research is necessary to continually update and refine the range of abnormal imaging findings associated with both common and rare diseases while exploring newly developed imaging techniques, such as advanced US scanning methods.

## Author contributions

TT: Data curation, Writing – review & editing. MT: Conceptualization, Data curation, Writing – original draft.

## Funding

The author(s) declare that no financial support was received for the research, authorship, and/or publication of this article.

## Conflict of interest

The authors declare that the research was conducted in the absence of any commercial or financial relationships that could be construed as a potential conflict of interest.

## Publisher's note

All claims expressed in this article are solely those of the authors and do not necessarily represent those of their affiliated organizations, or those of the publisher, the editors and the reviewers. Any product that may be evaluated in this article, or claim that may be made by its manufacturer, is not guaranteed or endorsed by the publisher.

## References


1. Andersen CA, Holden S, Vela J, Rathleff MS, Jensen MB. Point-of-Care ultrasound in general practice: a systematic review. *Ann Fam Med.* (2019) 17:61–9. doi: 10.1370/afm.2330

2. Berman J. Literature review of the principal diagnostic tests to detect bovine respiratory disease in pre-weaned dairy and veal calves. *Animals.* (2024) 14:329. doi: 10.3390/ani14020329

3. Mohamed T, Buczinski S. Clinicopathological findings and echocardiographic prediction of the localisation of bovine endocarditis. *Vet Rec.* (2011) 169:180. doi: 10.1136/vr.d4346

4. Tharwat M, Buczinski S. Diagnostic ultrasonography in cattle with abdominal fat necrosis. *Can Vet J.* (2012) 53:41–6.

5. Braun U, Widmer C, Nuss K, Hilbe M, Gerspach C. Clinical, laboratory and ultrasonographic findings in 38 calves with type-4 abomasal ulcer. *Acta Vet Scand.* (2021) 3:38. doi: 10.1186/s13028-021-00601-2

6. Tharwat M. Fundamentals of diagnostic ultrasound in dromedary camel medicine. *Int J Vet Sci.* (2024) 13:1–6. doi: 10.47278/journal.ijvs/2023.057

7. Buczinski S. Cardiovascular ultrasonography in cattle. *Vet Clin North Am Food Anim Pract.* (2009) 25:611–32. doi: 10.1016/j.cvfa.2009.07.010

8. Gouda SM. Ultrasonographic identification of abdominal and thoracic lesions resulting from foreign body syndrome in buffaloes. *Res J Vet Pract.* (2015) 3:41–6. doi: 10.14737/journal.rjvp/2015/3.2.41.46

9. Abdelaal A, Abdelbaset-Ismail A, Gomaa M, Gouda S, Dhama K. Efficacy of ultrasound in diagnosis and management of internal abscessations in Egyptian buffaloes (*Bubalus bubalis*). *Asian J Anim Vet Adv.* (2017) 12:239–46. doi: 10.3923/ajava.2017.239.246

10. Sangwan V, Mohindroo J, Kumar A, Randhawa CS. Clinical, radiographic and ultrasonographic differences in cows and buffaloes suffering with pericarditis. *Int J Livestock Res.* (2018) 8:255–63. doi: 10.5455/ijlr.20170904090349

11. Acorda JA. Applications of ultrasonography for diagnosis of diseases and disorders in dairy buffaloes. *Philipp J Vet Anim Sci.* (2019) 45:153–66.

12. Ollivett TL, Caswell JL, Nydam DV, Duffield T, Leslie KE, Hewson J, et al. Thoracic ultrasonography and bronchoalveolar lavage fluid analysis in Holstein calves with subclinical lung lesions. *J Vet Intern Med.* (2015) 29:1728–34. doi: 10.1111/jvim.13605

13. Tharwat M, Al-Sobayil, F. Diagnostic ultrasonography in goats with contagious caprine pleuropneumonia caused by *Mycoplasma capricolum* subsp capripneumoniae. *BMC Vet Res.* (2017) 13:263. doi: 10.1186/s12917-017-1167-4

14. Berman J, Masseau I, Fecteau G, Buczinski S, Francoz DJ. Comparison of thoracic ultrasonography and thoracic radiography to detect active infectious bronchopneumonia in hospitalized dairy calves. *J Vet Intern Med.* (2021) 35:2058–68. doi: 10.1111/jvim.16157

15. Abdullah SM, El-Sheikh AKR, Mahmoud ARM, Attia NE. Clinical hematobiochemical and radiographical studies of caprine pneumonia. *Slov Vet Res.* (2023) 60:65–74. doi: 10.26873/SVR-1562-2022

16. Babkine M, Blond L. Ultrasonography of the bovine respiratory system and its practical application. *Vet Clin North Am Food Anim Pract.* 25:633–49. doi: 10.1016/j.cvfa.2009.07.001

17. Braun U. Ultrasonography in gastrointestinal disease in cattle. *Vet J.* (2003) 166:112–24. doi: 10.1016/S1090-0233(02)00301-5

18. Mohamed T, Oikawa S. Ultrasonographic characteristics of abdominal and thoracic abscesses in cattle and buffaloes. *J Vet Med A Physiol Pathol Clin Med.* (2007) 54:512–7. doi: 10.1111/j.1439-0442.2007.00989.x

19. Kurt B, Cihan M. Evaluation of the clinical and ultrasonographic findings in abdominal disorders in cattle. *Vet Arh.* (2013) 83:11–21.

20. Abdelaal AM, Gouda S, Tharwat M. Clinico-biochemical, ultrasonographic and pathological findings of hepatic abscess in feedlot cattle and buffaloes. *Vet World.* (2014) 7:306–10. doi: 10.14202/vetworld.2014.306-310

21. O'Brien RT, Forrest LJ. A retrospective study of umbilical sonography in calves. *Vet Radiol Ultrasound.* (1996) 37:63–7. doi: 10.1111/j.1740-8261.1996.tb00815.x

22. Alsafy MAM, El-Gendy SAA, El-Kammar MH, Ismaiel M. Contrast radiographic, ultrasnographic and computed tomographic imaging studies on the abdominal organs and fatty liver infiltration of Zaraibi goat. *J Med Sci.* (2013) 13:316–26. doi: 10.3923/jms.2013.316.326

23. El Damaty HM, Mahmmod YS, Gouda SM, Sobhy NM. Epidemiological and ultrasonographic investigation of bovine fascioliasis in smallholder production system in Eastern Nile Delta of Egypt. *Prev Vet Med.* (2018) 158:35–42. doi: 10.1016/j.prevetmed.2018.07.009

24. Kandeel AE, Omar MSA, Mekkawy NHM, El- Seddawy FD, Gomaa M. Anatomical and ultrasonographic study of the stomach and liver in sheep and goats. *Iraqi J Vet Sci.* (2009) 23:181–91.

25. Stieger-Vanegas SM, McKenzie E. Abdominal imaging in small ruminants: liver, spleen, gastrointestinal tract, and lymph nodes. *Vet Clin North Am Food Anim Pract.* (2021) 37:55–74. doi: 10.1016/j.cvfa.2020.10.001

26. Hussein HA, Elrashidy M. Ultrasonographic features of the liver with cystic echinococcosis in sheep. *Vet Rec Open.* (2014) 1:e000004. doi: 10.1136/vropen-2013-000004

27. Floeck M. Sonographic application in the diagnosis of pyelonephritis in cattle. *Vet Radiol Ultrasound.* (2007) 48:74–7. doi: 10.1111/j.1740-8261.2007.00207.x

28. Floeck M. Ultrasonography of bovine urinary tract disorders. *Vet Clin North Am Food Anim Pract.* (2009) 25:651–67. doi: 10.1016/j.cvfa.2009.07.008

29. Braun U, Nuss K, Wehbrink D, Rauch S, Pospischil A. Clinical and ultrasonographic findings, diagnosis and treatment of pyelonephritis in 17 cows. *Vet J.* (2008) 175:240–8. doi: 10.1016/j.tvjl.2006.12.018

30. Tharwat M. Ultrasonography of the kidneys in healthy and diseased camels (*Camelus dromedaries*). *Vet Med Int.* (2020) 2020:7814927. doi: 10.1155/2020/7814927

31. Tharwat M, Sadan M, El-Shafaey E, Al-Hawas A, Saeed EMA. Unilateral nephrectomy in a female dromedary camel with pyelonephritis caused by *Staphylococcus lugdunensis*. *Pak Vet J.* (2018) 38:116–8. doi: 10.229261/pakvetj/2018.024

32. Tharwat M, Sadan M, El-Shafaey E, Saeed E, Al-Hawas A. Bilateral renal abscessation and chronic active pyelonephritis in a male camel (*Camelus dromedarius*) caused *by Escherichia coli*. *J Vet Med Sci.* (2018) 80:778–83. doi: 10.1292/jvms.17-0484

33. Steiner A, Lejeune B. Ultrasonographic assessment of umbilical disorders. *Vet Clin North Am Food Anim Pract.* (2009) 25:781–94. doi: 10.1016/j.cvfa.2009.07.012

34. Mejia S, McOnie RC, Nelligan KL, Fubini SL. Small ruminant urinary obstruction: decision trees for treatment. *J Am Vet Med Assoc.* (2022) 260:S64–71. doi: 10.2460/javma.22.02.0071

35. Otter A, Brzozowska A. Pneumonia in adult cattle. *Vet Rec.* (2022) 190:191–3. doi: 10.1002/vetr.1551

36. Breuer RM, Riedesel EA, Fowler J, Yaeger MJ, Smith JS, Kreuder AJ. Ultrasonography and digital radiography findings in sheep with clinical disease associated with small ruminant lentivirus infection. *Can Vet J.* (2022) 63:391–9.

37. Braun U, Pusterla N, Flückiger M. Ultrasonographic findings in cattle with pleuropneumonia. *Vet Rec.* (1997) 141:12–7. doi: 10.1136/vr.141.1.12

38. Ahaduzzaman M. Contagious caprine pleuropneumonia (CCPP): a systematic review and meta-analysis of the prevalence in sheep and goats. *Transbound Emerg Dis.* (2021) 68:1332–44. doi: 10.1111/tbed.13794

39. Yatoo IM, Parray OR, Bashir ST, Bhat RA, Gopalakrishnan A, Karthik K, et al. Contagious caprine pleuropneumonia - a comprehensive review. *Vet Q.* (2019) 39:1–25. doi: 10.1080/01652176.2019.1580826

40. Tharwat M. Alterations in acid-base balance, blood gases and hemato-biochemical profiles of whole blood and thoracic fluid in goats with contagious caprine pleuropneumonia. *Vet World.* (2021) 14:1874–8. doi: 10.14202/vetworld.2021.1874-1878

41. Buczinski S, Forté G, Francoz D, Bélanger AM. Comparison of thoracic auscultation, clinical score, and ultrasonography as indicators of bovine respiratory disease in preweaned dairy calves. *J Vet Intern Med.* (2014) 28:234–42. doi: 10.1111/jvim.12251

42. Buczinski S, Ménard J, Timsit E. Incremental value (Bayesian Framework) of thoracic ultrasonography over thoracic auscultation for diagnosis of bronchopneumonia in preweaned dairy calves. *J Vet Intern Med.* (2016) 30:1396–401. doi: 10.1111/jvim.14361

43. Buczinski S, Forté G, Bélanger AM. Ultrasonographic assessment of the thorax as a fast technique to assess pulmonary lesions in dairy calves with bovine respiratory disease. *J Dairy Sci.* (2013) 96:4523–8. doi: 10.3168/jds.2013-6577

44. Fowler JL. *Pulmonary Imaging of Dairy Calves With Naturally Acquired Respiratory Disease*. Oregon State University, Corvallis, OR (2017).

45. Tharwat M, Al-Sobayil F. Ultrasonographic findings in camel calves (*Camelus dromedarius*) with thoracic affections. *J Camel Pract Res.* (2016) 23:287–90. doi: 10.5958/2277-8934.2016.00048.5

46. Mohamed T. Clinicopathological and ultrasonographic findings in 40 water buffaloes (*Bubalus bubalis*) with traumatic pericarditis. *Vet Rec.* (2010) 167:819–24. doi: 10.1136/vr.c3113

47. Dore F, Varcasia A, Pipia AP, Sanna G, Pinna Parpaglia ML, Corda A, et al. Ultrasound as a monitoring tool for cystic echinococcosis in sheep. *Vet Parasitol.* (2014) 203:59–64. doi: 10.1016/j.vetpar.2014.03.016

48. Kumar A, Saini NS, Mohindroo J, Singh BB, Sangwan V, Sood NK. Comparison of radiography and ultrasonography in the detection of lung and liver cysts in cattle and buffaloes. *Vet World.* (2016) 9:1113–20. doi: 10.14202/vetworld.2016.1113-1120

49. Peek SF, Slack JA, McGuirk SM. Management of pneumothorax in cattle by continuous-flow evacuation. *J Vet Intern Med.* (2003) 17:119–22. doi: 10.1111/j.1939-1676.2003.tb01334.x

50. Slack JA, Thomas CB, Peek SF. Pneumothorax in dairy cattle: 30 cases (1990-2003). *J Am Vet Med Assoc.* (2004) 225:732–5. doi: 10.2460/javma.2004.225.732

51. Divers TJ. Respiratory diseases. In: Divers TJ, Peek SF, editors. *Rebhun's Diseases of Dairy Cattle*. 1st ed. Philadelphia, PA: Lippincott Williams & Wilkins (1995). p. 121–2.

52. Pal M, Tayal R. Diagnosis of reticular abscess in buffaloes: a review. *Pharma Innov J.* (2018) 7:697–9.

53. Braun U. Traumatic pericarditis in cattle: clinical, radiographic and ultrasonographic findings. *Vet J.* (2009) 182:176–86. doi: 10.1016/j.tvjl.2008.06.021

54. Muiño R, Hernández J, Castillo C. Acute abdominal disorders in dairy cattle: what can clinicians do under field conditions? *Ruminants.* (2021) 1:46–57. doi: 10.3390/ruminants1010004

55. Peek SF, McGuirk SM, Gaska J, Ravi M, Bell C, Pinkerton MA. Idiopathic hemorrhagic pericardial effusion as a precursor to epicardial lymphosarcoma in three cows. *J Vet Intern Med.* (2012) 26:1069–72. doi: 10.1111/j.1939-1676.2012.00952.x

56. Tharwat M, Al-Sobayil F, Ali A, Hashad M, Buczinski S. Clinical, ultrasonographic, and pathologic findings in 70 camels (*Camelus dromedarius*) with Johne's disease. *Can Vet J.* (2012) 53:543–8.

57. Tharwat M, Al-Sobayil F, Ali A, Buczinski S. Ultrasonographic evaluation of abdominal distension in 52 camels (*Camelus dromedarius*). *Res Vet Sci.* (2012) 93:448–56. doi: 10.1016/j.rvsc.2011.07.009

58. Tharwat M. Ultrasonographic findings in camels (*Camelus dromedarius*) with trypanosomiasis. *J Camel Pract Res.* (2013) 20:283–7.

59. Buczinski S, Tsuka T, Tharwat M. The diagnostic criteria used in bovine bacterial endocarditis: a meta-analysis of 460 published cases from 1973 to 2011. *Vet J.* (2012) 193:349–57. doi: 10.1016/j.tvjl.2012.02.012

60. Buczinski S, Tolouei M, Rezakhani A, Tharwat M. Echocardiographic measurement of cardiac valvular thickness in healthy cows, cows with bacterial endocarditis, and cows with cardiorespiratory diseases. *J Vet Cardiol.* (2013) 15:253–61. doi: 10.1016/j.jvc.2013.08.001

61. Tharwat M, Al-Sobayil F, Al-Hawas A, Buczinski S. Elevated serum concentration of cardiac troponin I in a Dorcas gazelle (*Gazella dorcas*) with mitral vegetation. *Comp Clin Pathol.* (2014) 23:469–73. doi: 10.1007/s00580-013-1847-9

62. Tharwat M, Ahmed AF, El-Tookhy O. Chronic peritonitis in buffaloes and cattle: clinical, hematological, ultrasonographic findings and treatment. *J Anim Vet Adv.* (2012) 15:2775–81. doi: 10.3923/javaa.2012.2775.2781

63. Tharwat M. Chronic peritonitis in dromedary camels: clinical, ultrasonographic and pathologic findings. *J Camel Pract Res.* (2019) 26:169–72. doi: 10.5958/2277-8934.2019.00026.2

64. Hewson J, Cebra CK. Peritonitis in a llama caused by *Streptococcus equi* subsp. *Zooepidemicus*. *Can Vet J.* (2001) 42:465–7.

65. Heller M, Anderson D, Silveira F. Streptococcal peritonitis in a young dromedary camel. *Aust Vet J.* (1998) 76:253–4. doi: 10.1111/j.1751-0813.1998.tb10152.x

66. Braun U. Ascites in cattle: ultrasonographic findings and diagnosis. *Vet Clin North Am Food Anim Pract.* (2016) 32:55–83. doi: 10.1016/j.cvfa.2015.09.004

67. Yoshimura N, Tsuka T, Yoshimura T, Otoi T. Efficacy of abdominal ultrasonography for differentiation of gastrointestinal diseases in calves. *Animals.* (2022) 12:2489. doi: 10.3390/ani12192489

68. Enwezor FNC, Sackey AKB. Camel trypanosomosis—a review. *Vet Arh.* (2005) 75:439–52.

69. Tharwat M. Acid-base balance, blood gases and haematobiochemical profiles in camels (*Camelus dromedarius*) with trypanosomiasis. *J Camel Pract Res.* (2021) 28:143–7. doi: 10.5958/2277-8934.2021.00024.2

70. Braun U, Nuss K, Wapf P, Lischer C. Clinical and ultrasonographic findings in five cows with a ruptured urachal remnant. *Vet Rec.* (2006) 159:780–2. doi: 10.1136/vr.159.22.750

71. Tharwat M, Al-Sobayil F. Ultrasonographic findings in camels (*Camelus dromedarius*) with different urinary affections. *J Camel Pract Res.* (2016) 23:301–8. doi: 10.5958/2277-8934.2016.00050.3

72. Tharwat M. Obstructive urolithiasis in dromedary camels: clinical, ultrasonographic and postmortem findings. *J Camel Pract Res.* (2021) 28:85–93. doi: 10.5958/2277-8934.2021.00013.8

73. Morita Y, Sugiyama S, Tsuka T, Okamoto Y, Morita T, Sunden Y, et al. Diagnostic efficacy of imaging and biopsy methods for peritoneal mesothelioma in a calf. *BMC Vet Res.* (2019) 15:461. doi: 10.1186/s12917-019-2195-z

74. Ali A, Dear R, Osman S, Tharwat M, Al-Sobayil F, Elshahed M. Scrotal enlargement in rams and bucks in Qassim region, central of Saudi Arabia: clinical and ultrasonographic findings and seroprevalence of brucellosis. *Trop Anim Health Prod.* (2019) 51:2109–14. doi: 10.1007/s11250-019-01937-8

75. Tharwat M. Ultrasonography of the liver in healthy and diseased camels (*Camelus dromedaries*). *J Vet Med Sci.* (2020) 82:399–407. doi: 10.1292/jvms.19-0690

76. Aljameel MA, Halima MO, ElTigani-Asil AE, Abdalla AS, Abdellatif MM. Liver abscesses in dromedary camels: pathological characteristics and aerobic bacterial aetiology. *Open Vet J.* (2014) 4:118–23. doi: 10.5455/OVJ.2014.v4.i2.p118

77. Braun U. Ultrasonography of the liver in cattle. *Vet Clin North Am Food Anim Pract.* (2009) 25:591–609. doi: 10.1016/j.cvfa.2009.07.003

78. Sato R, Yamada K, Yokoyama T, Tanimoto K, Takeuchi S, Tatsuzawa N, et al. Partial hepatectomy for treatment of multiple liver abscess in a calf: a case report. *BMC Vet Res.* (2021) 17:67. doi: 10.1186/s12917-021-02750-y

79. Corda A, Corda F, Secchi V, Pentcheva P, Tamponi C, Tilocca L, et al. Ultrasonography of parasitic diseases in domestic animals: a systematic review. *Animals.* (2022) 12:1252. doi: 10.3390/ani12101252

80. Tharwat M. Ultrasonographic findings in cattle and buffaloes with chronic hepatic fascioliosis. *Trop Anim Health Prod.* (2012) 44:1555–60. doi: 10.1007/s11250-012-0105-5

81. Marcos LA, Yi P, Machicado A, Andrade R, Samalvides F, Sánchez J, et al. Hepatic fibrosis and *Fasciola hepatica* infection in cattle. *J Helminthol.* (2007) 81:381–6. doi: 10.1017/S0022149X07850231

82. Van Metre DC, Tennant BC, Whitlock RH. Infectious diseases of the gastrointestinal tract. In: Divers TJ, Peek SF, editors. Rebhun's Diseases of Dairy Cattle. 2nd ed. Philadelphia, PA: Lippincott Williams & Wilkins (2007). p. 200–94.

83. Gonzalo-Orden M, Millán L, Álvarez M, Sánchez-Campos S, Jiménez R, González-Gallego J, et al. Diagnostic imaging in sheep hepatic fascioliasis: Ultrasound, computer tomography and magnetic resonance findings. *Parasitol Res.* (2003) 90:359–64. doi: 10.1007/s00436-003-0866-x

84. Tharwat M, El Moghazy HM, Oikawa S. Ultrasonographic verification of hepatic hydatidosis in a female dromedary camel: a case report. *J Vet Med Sci.* (2023) 85:1286–90. doi: 10.1292/jvms.23-0325

85. Sage AM, Wachira TM, Zeyhle EE, Weber EP, Njoroge E, Smith G. Evaluation of diagnostic ultrasound as a mass screening technique for the detection of hydatid cysts in the liver and lung of sheep and goats. *Int J Parasitol.* (1998) 28:349–53. doi: 10.1016/S0020-7519(97)00187-2

86. Maxson AD, Wachira TM, Zeyhle EE, Fine A, Mwangi TW, Smith G. The use of ultrasound to study the prevalence of hydatid cysts in the right lung and liver of sheep and goats in Turkana, Kenya. *Int J Parasitol.* (1996) 26:1335–8. doi: 10.1016/S0020-7519(96)00124-5

87. Lahmar S, Chéhida FB, Pétavy AF, Hammou A, Lahmar J, Ghannay A, et al. Ultrasonographic screening for cystic echinococcosis in sheep in Tunisia. *Vet Parasitol.* (2007) 143:42–9. doi: 10.1016/j.vetpar.2006.08.001

88. Tharwat M, Al-Hawas A. Liver diseases in sheep and goats: Parallel sonographic and pathologic findings. *Int J Vet Sci.* (2024) 13:284–90. doi: 10.47278/journal.ijvs/2023.094

89. Blazek K, Schimarova J, Hulinska D. Pathology of the migration phase of *Taenia hydatigena* (Palas 1766) larvae. *Folia Parasitol.* (1985) 32:127–37.

90. Tharwat M, Al-Hawas A. Suppurative pyelonephritis in a caprine buck: clinical, laboratory, ultrasonographic and pathologic findings. *Int J Vet Sci.* (2024) 13:479–83. doi: 10.47278/journal.ijvs/2023.097

91. Sparling AM. An unusual presentation of enzootic bovine leukosis. *Can Vet J.* (2000) 41:315–6.

92. Tharwat M, Al-Sobayil F. Ultrasonographic findings in camels (*Camelus dromedarius*) with abdominal disorders. *J Camel Pract Res.* (2016) 23:291–9. doi: 10.5958/2277-8934.2016.00049.7

93. Fecteau M. Paratuberculosis in cattle. *Vet Clin North Am Food Anim Pract.* (2018) 34:209–22. doi: 10.1016/j.cvfa.2017.10.011

94. Tharwat M, Al-Sobayil F, Hashad M, Buczinski S. Transabdominal ultrasonographic findings in goats with paratuberculosis. *Can Vet J.* (2012) 53:1063–70.

95. Tharwat M, Al-Sobayil F, El-Magawry S. Clinicobiochemical and postmortem investigations in 60 Camels (*Camelus dromedarius*) with Johne's disease. *J Camel Pract Res.* (2013) 20:145–9.

96. Tharwat M. Ultrasonography of the abdomen in healthy and diseased camels (*Camelus dromedaries*) – a review. *J Appl Anim Res.* (2020) 48:300–12. doi: 10.1080/09712119.2020.1788035

97. Chamberlin WM, Naser SA. Integrating theories of the etiology of Crohn's disease. On the etiology of Crohn's disease: questioning the hypotheses. *Med Sci Monit.* (2006) 12:RA27–33.

98. Munday K, Mudron P. Abdominal ultrasonography in cattle. *Folia Vet.* (2016) 60:34–40. doi: 10.1515/fv-2016-0005

99. Braun U, Schnetzler C, Dettwiler M, Sydler T, Meyer S, Gerspach C. Ultrasonographic findings in a cow with abomasal lymphosarcoma: case report. *BMC Vet Res.* (2011) 7:20. doi: 10.1186/1746-6148-7-20

100. Fushimi Y, Takagi M, Kawaguchi H, Miyoshi N, Tsuka T, Deguchi E. Three cases of idiopathic eosinophilic enteritis with chronic obstinate diarrhea in Japanese Black fattening cattle. *J Vet Med Sci.* (2015) 77:337–40. doi: 10.1292/jvms.14-0460

101. Dennison AC, VanMetre DC, Callan RJ, Dinsmore P, Mason GL, Ellis RP. Hemorrhagic bowel syndrome in dairy cattle: 22 cases (1997–2000). *J Am Vet Med Assoc.* (2002) 221:686–9. doi: 10.2460/javma.2002.221.686

102. Braun U, Forster E, Steininger K, Irmer M, Gautschi A, Previtali M, et al. Ultrasonographic findings in 63 cows with haemorrhagic bowel syndrome. *Vet Rec.* (2010) 166:79–81. doi: 10.1136/vr.c178

103. Trent AM. Surgical management of umbilical masses in calves. *Bov Pract.* (1987) 22:170–3. doi: 10.21423/bovine-vol0no22p170-173

104. Guerri G, Vignoli M, Palombi C, Monaci M, Petrizzi L. Ultrasonographic evaluation of umbilical structures in Holstein calves: a comparison between healthy calves and calves affected by umbilical disorders. *J Dairy Sci.* (2020) 103:2578–90. doi: 10.3168/jds.2019-16737

105. Hassel DM, Tyler JW, Tucker RL, Sondhof AF. Clinical Vignette: urachal abscess and cystitis in a calf. *J Vet Intern Med.* (1995) 9:286–8. doi: 10.1111/j.1939-1676.1995.tb01083.x

106. Masseau I, Fecteau G, Breton L, Hélie P, Beauregard G, Blond L. Radiographic detection of thoracic lesions in adult cows: a retrospective study of 42 cases (1995–2002). *Can Vet J.* (2008) 49:261–7.

107. Fowler J, Stieger-Vanegas SM, Vanegas JA, Bobe G, Poulsen KP. Comparison of thoracic radiography and computed tomography in calves with naturally occurring respiratory disease. *Front Vet Sci.* (2017) 4:101. doi: 10.3389/fvets.2017.00101

108. Tegtmeier C, Arnbjerg J. Evaluation of radiology as a tool to diagnose pulmonic lesions in calves, for example prior to experimental infection studies. *J Vet Med B Infect Dis Vet Public Health.* (2000) 47:229–34. doi: 10.1046/j.1439-0450.2000.00331.x

109. Cooley SD, Schlipf JW Jr, Stieger-Vanegas SM. Computed tomographic characterization of the pulmonary system in clinically normal alpacas. *Am J Vet Res.* (2013) 74:572–8. doi: 10.2460/ajvr.74.4.572

110. Shimbo G, Tagawa M, Matsumoto K, Tomihari M, Yanagawa M, Ueda Y, et al. Three-legged radiographic view for evaluating cranioventral lung region in standing calves with bovine respiratory disease. *J Vet Med Sci.* (2019) 81:120–6. doi: 10.1292/jvms.18-0333

111. Gugjoo MB, Dar SH, Ahmad RA, Hussain HA, Dar MD, Parrah JUD, et al. Traumatic reticuloperitonitis in cattle and buffalo: recent advances in understanding of etiopathogenesis, diagnosis and treatment. *Indian J Anim Sci.* (2021) 91:895–905. doi: 10.56093/ijans.v91i11.118124

112. Sato R, Yamada K, Shinozuka Y, Ochiai H, Onda K. Gas-filled urachal abscess with a pinging sound in a heifer calf. *Vet Med.* (2019) 64:362–6. doi: 10.17221/61/2019-VETMED

113. Kumar R, Pandey NN, Singh GR, Setia HC. Radiographic evaluation of experimentally induced nephrosis in goats. *Indian J Anim Sci.* (1995) 65:636–9.

114. Ragab GA, Seif MM, Hagag UA. Radiologic and ultrasonographic studies of kidneys in goat. *BS Vet Med J.* (2010) 20:30–7. doi: 10.21608/jvmr.2020.77577

115. Singh CK, Kalita D, Das A, Das S, Kaushik P. Retrograde iohexol urethrography and cystography for diagnosis and surgical management of persistent urachus in a female Sahiwal calf. *Pharma Innov J.* (2023) SP-12:770–2.

116. Stieger-Vanegas SM, Cebra CK. Contrast-enhanced computed tomography of the gastrointestinal tract in clinically normal alpacas and llamas. *J Am Vet Med Assoc.* (2013) 242:254–60. doi: 10.2460/javma.242.2.254

117. Braun U, Schnetzler C, Augsburger H, Müller U, Dicht S, Ohlerth S. Computed tomography of the abdomen of calves during the first 105 days of life: II. Liver, spleen, and small and large intestines. *Schweiz Arch Tierheilkd.* (2014) 156:227–36. doi: 10.1024/0036-7281/a000582

118. Goda Y, Mizutani S, Mizutani Y, Kitahara G, Siswandi R, Wakabayashi K, et al. The usefulness of computed tomography for cryptorchidism in bulls. *J Vet Med Sci.* (2022) 84:1430–6. doi: 10.1292/jvms.22-0124

119. Rotheneder S, González-Grajales LA, Beck H, Bootz F, Bollwein H. Variability of bovine conceptus-related volumes in early pregnancy measured with transrectal 3-dimensional ultrasonography. *J Dairy Sci.* (2022) 105:4534–46. doi: 10.3168/jds.2021-21006

120. Franz S, Hofmann-Parisot MM, Baumgartner W. Evaluation of three-dimensional ultrasonography of the bovine mammary gland. *Am J Vet Res.* (2004) 65:1159–63. doi: 10.2460/ajvr.2004.65.1159

frontiers | Frontiers in Veterinary Science

TYPE Original Research
PUBLISHED 03 December 2024
DOI 10.3389/fvets.2024.1476746

Check for updates

OPEN ACCESS

EDITED BY
Ryou Tanaka,
Tokyo University of Agriculture and Technology, Japan

REVIEWED BY
Howard Dobson,
Invicro, United States
Andras Komaromy,
Michigan State University, United States

*CORRESPONDENCE
Kyung-Mee Park
✉ parkkm@cbu.ac.kr

RECEIVED 06 August 2024
ACCEPTED 08 November 2024
PUBLISHED 03 December 2024

CITATION
Kim D, Kwon H, Hwang J, Jung JS and Park K-M (2024) Quantitative analysis of iridocorneal angle and ciliary cleft structures in canine eyes using ultrasound biomicroscopy.
*Front. Vet. Sci.* 11:1476746.
doi: 10.3389/fvets.2024.1476746



# Quantitative analysis of iridocorneal angle and ciliary cleft structures in canine eyes using ultrasound biomicroscopy

Donghee Kim, Hyun Kwon, Jiyi Hwang, Ji Seung Jung and Kyung-Mee Park*

Laboratory of Veterinary Surgery and Ophthalmology, College of Veterinary Medicine, Chungbuk National University, Cheongju, Republic of Korea

**Introduction:** This study aimed to examine the relationship between the relative opening of the ICA (RO-ICA) and the structure of the ciliary cleft (CC) using Ultrasound Biomicroscopy (UBM).

**Materials and methods:** Clinical data from 31 eyes of 17 dogs at the Veterinary Teaching Hospital of Chungbuk National University, Korea, were analyzed. RO-ICA was categorized as “Slightly Narrow”, “Narrow”, “Open”, and “Wide Open”, with eyes further grouped into “Narrow” (including Slightly Narrow and Narrow) and “Open” (including Open and Wide Open) for analysis. Statistical methods, including linear regression and average comparisons between groups, were employed to explore correlations between RO-ICA and parameters such as ICA, CC width (CCW), CC length (CCL), and CC area (CCA).

**Results:** The distribution showed “Narrow” (3 eyes, 9.7%), “Slightly Narrow” (13 eyes, 41.9%), and “Open” (14 eyes, 45.2%) as the predominant categories. In the Open group, CCL and CCA were significantly larger compared to the Narrow group. A positive correlation was observed between RO-ICA and CCL, and CCA across all groups. Notably, in the Narrow group, RO-ICA demonstrated a particularly significant positive correlation with all assessed parameters, including ICA, CCW, CCL, and CCA. However, no significant correlation was observed between RO-ICA and the assessed parameters in the Open group. In conclusion, while a smaller RO-ICA generally correlates with a smaller CC, a larger RO-ICA does not guarantee a larger CC.

**Conclusion:** Additional UBM examinations are recommended for comprehensive evaluations, particularly in cases where gonioscopy indicates an open iridocorneal angle.

KEYWORDS

**glaucoma, iridocorneal angle, ciliary cleft, ultrasound biomicroscopy, canine**

## 1 Introduction

Glaucoma in dogs is a serious, progressive disease that frequently leads to blindness (1, 2). This condition is characterized by the gradual narrowing and collapse of the iridocorneal angle (ICA), impairing the normal flow of aqueous humor and subsequently increasing intraocular pressure (IOP), a key contributor to vision loss (1, 3). Thorough evaluation of the ICA is critical in managing glaucoma. This integral component of the anterior chamber of the eye is responsible for regulating ocular fluid dynamics and intraocular pressure. Its alterations significantly contribute to the elevation of IOP and the progression of the disease (3–6). Therefore, precise assessment of the ICA and its related structures is imperative for the early detection and effective treatment of glaucoma in dogs.

Clinically, the assessment of the ICA in veterinary practice has predominantly relied on tools like gonioscopy or contact retinal camera (RetCam Shuttle; Clarity Medical Systems, Pleasanton, CA) for visual examination of the ICA's anterior face (7–9). Gonioscopy, when feasible, reveals details such as narrow or closed iridocorneal angles, occasionally accompanied by pectinate ligament dysplasia (PLD) (9–11). However, this method has limitations due to its focus exclusively on the anterior aspect of the ICA, particularly in its inability to accurately measure the angle and evaluate finer structures such as the ciliary cleft (CC) (12). In contrast to gonioscopy, Ultrasound Biomicroscopy (UBM) provides a non-invasive and more precise approach (12, 13). It facilitates detailed imaging of the CC, an internal structure of the ICA, going beyond the capabilities of gonioscopy (14, 15). By providing cross-sectional images of the ICA, UBM emerges as an essential tool for accurate detection and effective management of ocular diseases like glaucoma (16, 17).

The ICA constitutes the peripheral, circumferential part of the anterior chamber, formed where the cornea, sclera, and base of the iris meet (4, 18). The anterior face of the ICA is composed of pectinate ligaments, characterized by slender, branching beams of iris tissue that span across the ICA, creating the iconic pectinate ligament structure (19–21). Posterior to the ICA lies the CC, a peripheral circumferential space extending posteriorly to the pectinate ligaments into the posterior ciliary body. This space, almost virtual in nature, forms a triangular shape with an anterior base (22–24). It serves as a crucial pathway for aqueous humor flow, connecting the radial collector channels that lead to the intrascleral venous plexus in the conventional outflow pathway, and to the porosity of the loose connective tissue and its extracellular matrix in the ciliary body in the unconventional outflow pathway (25–28). Therefore, abnormalities or changes in these structures can lead to pathologies and issues in intraocular pressure regulation (3, 5, 29).

Due to the significance of the ICA in primary angle closure glaucoma (PACG), considerable research has been conducted on the pectinate ligament through gonioscopy. These studies suggest that the narrowing of the ICA and PLD may play a role in PACG (3, 11, 30). In one particular study, the total outflow capacity, as measured by tonography, appeared normal when PLD was observed via gonioscopy. This implies that the condition of the pectinate ligament may present minimal resistance to outflow, especially if flow holes are present to allow aqueous humor access to the CC (29). Such findings highlight a potential discrepancy between the anterior aspect of the ICA, primarily the pectinate ligament as seen through gonioscopy, and its internal structure, the CC (12, 29, 31). Furthermore, this casts doubt on the reliability of using gonioscopy alone as an indicator to estimate total outflow capacity (16, 21, 32). This situation emphasizes the necessity for more in-depth research to investigate the correlation between these structural variances.

In our study, we aim to explore the relationship between the relative opening of the ICA and the structure of the CC using UBM. Our objectives include providing a more precise and quantifiable analysis of these structures. This will enable us to assess the extent to which the CC can be accurately predicted through clinically convenient methods like gonioscopy. This approach is anticipated to deepen our understanding of the interplay between the anterior and internal structures of the ICA, especially in the context of PACG. To our knowledge, this study is the first to quantitatively address the correlation between the relative opening of the ICA and the structure of the CC.

# 2 Materials and methods

## 2.1 Clinical information

This retrospective study utilized clinical data from dogs treated at the Veterinary Teaching Hospital of Chungbuk National University, Chungju, Korea. The data compilation spanned from August 29, 2018, to September 20, 2022, involving 31 eyes from 17 different dogs. Ethical approval for this research was granted by the Institutional Animal Care and Use Committee (CBNUA-1700-22-02). The ophthalmological evaluations were performed by Dr. KM Park, a veterinary medicine faculty member, along with a team of eye care veterinarians. These assessments included various tests, such as slit-lamp biomicroscopy (MW50D, SHIGIYA, Hiroshima, Japan), the Schirmer Tear Test (Schirmer Tear Flow Strips, GuldenOphthalmics, PA), assessments of the menace response, pupillary light reflex, and dazzle reflex, and rebound tonometry (TonoVet plus®, icare, Vantaa, Finland). Additional diagnostic methods encompassed gonioscopy (Ocular Koeppe Diagnostic Lenses, Ocular Instruments.inc), indirect ophthalmoscopy (Pan Retinal® 2.2, VOLK, OH), and UBM (VuPAD®, Sonomed Escalon, Lake Success, NY, United States). In this research, patients exhibiting other ocular diseases aside from incipient cataracts were excluded during the complete ophthalmic examination process.

## 2.2 UBM examination

In this study, UBM examinations were essential to the ophthalmic assessments. To standardize the condition of all subjects with consistent pupil dilation, the dogs underwent topical application of 0.5% tropicamide (Mydriacyl®, Alcon, Geneva, Switzerland). UBM imaging was performed only after confirming full mydriasis. Additionally, 0.5% proparacaine hydrochloride (Alcaine®; Alcon) was applied for topical anesthesia. During the UBM procedure, the dogs' eyelids were gently held open, and the UBM transducer was positioned precisely perpendicular to the corneoscleral limbus in the dorsal quadrant of the eye.

In our research, we adopted a method inspired by Ekesten et al., but specifically adapted for UBM imaging, to assess the relative opening of the iridocorneal angle (RO-ICA) (10, 11). This involved establishing a baseline along the lower edge of the CC, essentially extending the iris root line. Key measurements were taken perpendicular to this baseline: the distance at the point where the pectinate ligaments intersect the sclera (length "a"), and the distance from the anterior surface of the cornea (length "b"). The RO-ICA was then calculated by dividing length "a" by length "b", thereby quantifying the relative opening in terms of proportional lengths, instead of focusing on absolute length measurements (Figure 1A).

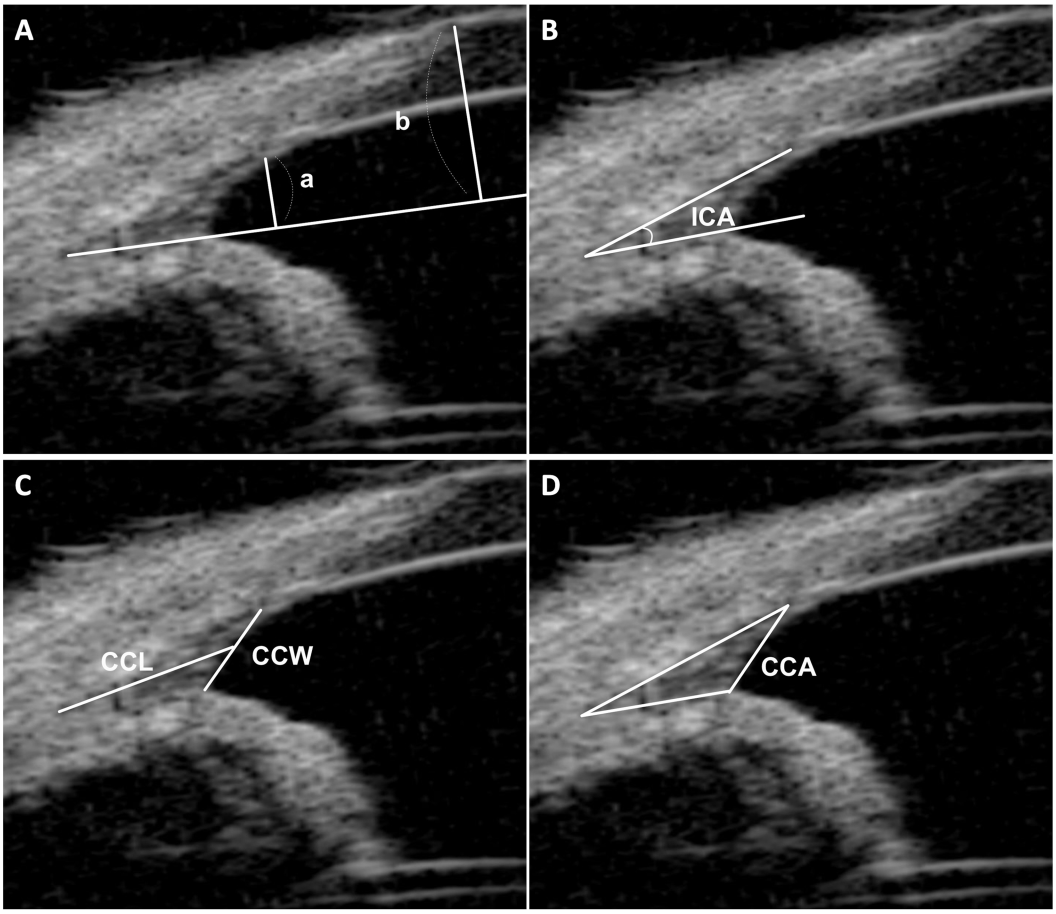


FIGURE 1
UBM measurement method. **(A)** This section illustrates the measurement of the relative opening of the iridocorneal angle (RO-ICA). It involves drawing a baseline from the lower surface of the ciliary cleft, extending the iris root line. Perpendicular lines are then drawn from the junction of the pectinate ligaments and sclera (length "a") and from the anterior surface of the cornea (length "b"). The RO-ICA is calculated by dividing length "a" by length "b". **(B)** Demonstrates the measurement of the Iridocorneal Angle (ICA), defined as the peripheral circumference of the anterior chamber at the convergence point of the sclera, cornea, and iris base. **(C)** Details the measurements of the ciliary cleft width (CCW) and length (CCL), with the CCW being the distance from the iris root to the corneoscleral, and the CCL measured from the angle recess to the midpoint of the CCW. **(D)** Describes the measurement of the Ciliary Cleft Area (CCA), which is the area enclosed by the ciliary cleft.

The evaluation of the CC in each eye included four parameters based on established research (22–24): (a) the geometric Iridocorneal Angle (ICA), the angle formed between the plane of the iris root and the posterior corneoscleral limbus; (b) the width of the entrance to the CC (CCW); (c) the length of the CC (CCL); and (d) the area of the CC as manually measured (CCA). These assessments allowed for a detailed analysis of the CC's anatomical structure and its potential implications for canine ocular health (Figures 1B–D).

## 2.3 Grading of the relative opening of the iridocorneal angle

In our study, the grading of the RO-ICA was conducted using the numerical grade scale established by Ekesten et al. (10). The grading system categorizes the RO-ICA into five distinct classes based on specific numerical intervals. These are as follows: "Closed" for an RO-ICA of $X \leq 0.15$, "Narrow" for $0.15 < X \leq 0.30$, "Slightly narrow" for $0.30 < X \leq 0.45$, "Open" for $0.45 < X \leq 0.55$, and "Wide Open" for $X \geq 0.55$. The X was calculated by dividing the distance at the intersection of the pectinate ligaments and the sclera (length "a") by the distance from the anterior surface of the cornea (length "b").

For further analysis in our study, the categories of "Narrow" and "Slightly Narrow" within the grading of the RO-ICA were combined to form the "Narrow Group". Similarly, the "Open" and "Wide Open" categories were grouped together to constitute the "Open Group".

## 2.4 Statistical analysis

In this study, we conducted our statistical analyses using SPSS software (version 17.0; SPSS Inc., Chicago). To assess differences in breed, sex, and weight among the groups, we utilized the Chi-squared ($\chi^2$) test. The Shapiro–Wilk test was initially applied to evaluate the normality of our data. Upon confirming data normality, we then employed the *t*-test to compare the mean values between groups. This method was specifically used for analyzing the differences between the narrow and open groups categorized under the RO-ICA classification. Furthermore, to investigate the relationship between RO-ICA measurements and various parameters assessed in the study, a single linear regression analysis was performed. The interpretation of the correlation was standardized as follows: R = 0.00–0.10, negligible correlation; R = 0.10–0.39, weak correlation; R = 0.40–0.69, moderate correlation; R = 0.70–0.89, strong correlation; R = 0.90–1.00, very strong correlation. We established levels of statistical significance at $p < 0.05$ represented as * in our study. For ease of interpretation in the figures, asterisks are used, whereas the actual $p$-values are explicitly detailed in the text of the study, ensuring comprehensive and clear communication of our statistical findings.

# 3 Results

## 3.1 The distribution of the relative opening of the iridocorneal angle

In the evaluation of the iridocorneal angles among the canine subjects, a variation in the RO-ICA grades was observed. The "Narrow" category comprised 3 eyes, accounting for 9.7% of the total. A significant portion, 41.9%, fell into the "Slightly Narrow" category, involving 13 eyes. The majority of the eyes, 14 in number, representing 45.2%, were classified as "Open". The "Wide Open" category was the least represented, with only 1 eye, constituting 3.2% of the sample.

## 3.2 Canine characteristics

In the Narrow group, consisting of 16 eyes from 8 dogs, the breeds most commonly observed were Poodles and Malteses. The gender distribution favored males, with 5 males compared to 3 females. The mean age of the dogs in this group was 9.46 ± 4.21 years (range, 1.5–15 years), and the mean weight was recorded at 4.87 ± 1.60 kg (range, 2.85–9.80 kg). The IOP in this group was 16.69 ± 2.18 mmHg (range, 13.00–20.00 mmHg).

The Open group included 15 eyes from 10 dogs, with breeds such as Poodles and Shih Tzus being predominant. This group had a larger number of female dogs, with 6 females and 4 males. The mean age in this group was 7.90 ± 3.19 years (range, 4.0–15.0 years), and the mean weight was 5.60 ± 2.08 kg (range, 3.5–9.7 kg). The IOP in this group was 15.93 ± 2.25 mmHg (range, 12.00–20.00 mmHg).

Statistical analysis revealed no significant differences in terms of sex, weight, age or IOP between the Narrow and Open groups, indicating a similar distribution of these characteristics across both groups (Supplementary Tables 1, 2).

## 3.3 Comparative analysis of ICA, CCW, CCL, and CCA between narrow and open groups

In this study, the values of the ICA, CCW, CCL, and CCA were compared between the Narrow and Open groups. The mean ICA in the Narrow group was 20.68 ± 7.12°, while in the Open group, it was 18.03 ± 6.36°. This difference was not statistically significant, with a $p$-value of 0.284 (Figure 2A). Similarly, the CCW did not show a significant difference between groups, with mean values of 0.58 ± 0.18 mm in the Narrow group and 0.62 ± 0.14 mm in the Open group ($p = 0.464$) (Figure 2B). However, significant differences were observed in CCL and CCA measurements; the Narrow group exhibited a mean CCL of 0.99 ± 0.14 mm and CCA of 0.22 ± 0.04 $mm^2$, whereas the Open group showed a mean CCL of 1.12 ± 0.18 mm and CCA of 0.26 ± 0.04 $mm^2$ ($p < 0.05$, $p < 0.05$ respectively). These findings indicate that while the ICA and CCW do not significantly differ between the two groups, both CCL and CCA are notably larger in the Open group compared to the Narrow group (Figures 2C,D).

## 3.4 Regression analysis outcomes across combined narrow and open groups

The regression analysis for the ICA yielded interesting insights. A positive correlation was observed between RO-ICA and ICA, but this association was not statistically significant. The regression model accounted for only 3.316% of the variance in ICA ($p = 0.3269$) (Figure 3A). Regarding the CCW, the analysis revealed a positive correlation with RO-ICA. However, the relationship was not statistically significant, with the model explaining 12.30% of the variance in CCW ($p = 0.0531$) (Figure 3B). For the CCL, the regression analysis showed a weak positive association with RO-ICA. This correlation was statistically significant, with the model accounting for 16.07% of the variance in CCL ($p < 0.05$) (Figure 3C). Lastly, in the case of the CCA, the regression analysis indicated a significant weak positive correlation with RO-ICA. The model explained a considerable 26.84% of the variance in CCA, and the association was statistically significant ($p < 0.01$) (Figure 3D).

## 3.5 Regression analysis outcomes in narrow groups

The regression analysis for the ICA yielded significant insights. A moderate positive correlation was found between the RO-ICA and ICA, with the regression model explaining 33.76% of the variance in ICA. This association was statistically significant ($p < 0.05$), suggesting a strong linear dependence of ICA on RO-ICA (Figure 4A). Similarly, a weak positive correlation was observed with the CCW. The model accounted for 30.80% of the variance in CCW, and this relationship was statistically significant ($p < 0.05$), indicating a notable association between RO-ICA and CCW (Figure 4B). The CCL also showed a statistically significant weak positive association with RO-ICA, with the model explaining 27.94% of the variance in CCL ($p < 0.05$) (Figure 4C). Lastly, for the CCA, a significant weak positive correlation with RO-ICA was indicated. The model accounted for 26.50% of the variance in CCA, with this association being statistically significant ($p < 0.05$) (Figure 4D).

## 3.6 Regression analysis outcomes in open groups

In the Open group, the regression analysis for the ICA revealed that the association between RO-ICA and ICA was not statistically

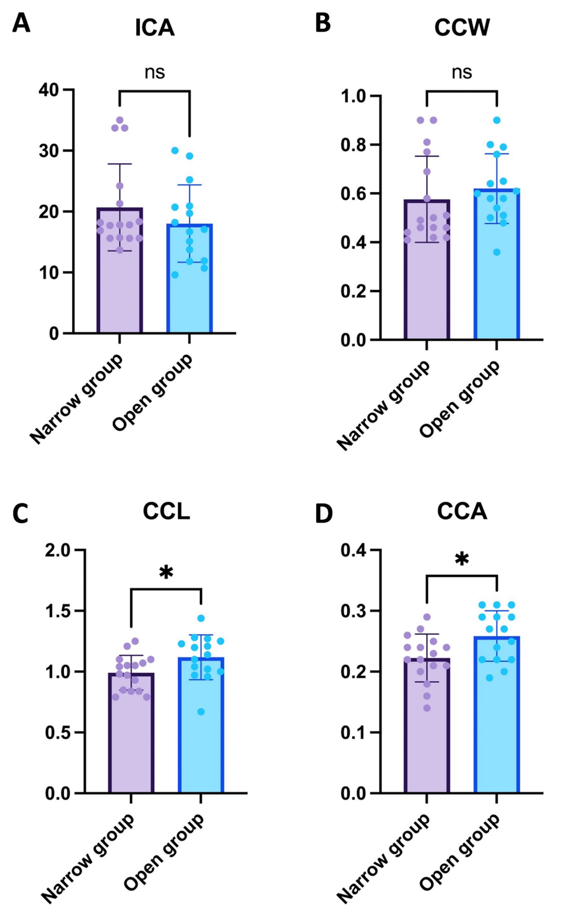


FIGURE 2
Comparative analysis of ICA, CCW, CCL, and CCA between narrow and open groups. **(A)** ICA Comparison in the Narrow group with 16 eyes showed a mean ICA of 20.68 ± 7.12°, in contrast to the Open group with 15 eyes at 18.03 ± 6.36°, with no statistically significant difference observed ($p$ = 0.284). **(B)** CCW Comparison revealed mean values of 0.58 ± 0.18 mm in the narrow group of 16 eyes compared to 0.62 ± 0.14 mm in the open group of 15 eyes, without a significant difference ($p$ = 0.464). **(C)** CCL Comparison indicated a significant difference, with the narrow group of 16 eyes showing a mean of 0.99 ± 0.14 mm and the open group of 15 eyes at 1.12 ± 0.18 mm ($p$ < 0.05). **(D)** CCA Comparison also displayed a significant variation; the narrow group with 16 eyes had a mean CCA of 0.22±0.04mm$^2$ compared to 0.26±0.04mm$^2$ in the Open group of 15 eyes ($p$<0.05). For clarity in interpreting our findings, levels of statistical significance in the study are denoted as follow: $p$<0.05 (*).

significant, with the model accounting for only 0.39% of the variance in ICA ($p$ = 0.8242). This suggests a negligible linear dependence between RO-ICA and ICA (Figure 5A). Similarly, the CCW showed a non-significant relationship with RO-ICA, with the regression model explaining just 3.42% of the variance in CCW ($p$ = 0.5096) (Figure 5B). For the CCL, the regression analysis indicated an equally minimal relationship, accounting for merely 2.38% of the variance in CCL ($p$ = 0.5832), pointing to no strong linear correlation between RO-ICA and CCL (Figure 5C). Lastly, the analysis for the CCA also demonstrated a very weak linear relationship with RO-ICA, as the model accounted for only 1.48% of the variance in CCA ($p$ = 0.6663) (Figure 5D).

# 4 Discussion

In this study, our goal was to investigate the correlation between the RO-ICA and the structure of the CC using UBM We aimed to provide a detailed, quantitative analysis of these structures, enabling a more accurate prediction of CC characteristics through methods like gonioscopy.

This study was conducted retrospectively, including all patients who visited during the specified period. During patient selection, those with ophthalmic diseases other than incipient cataracts were excluded, and no specific selection criteria were applied regarding breed. For cases in which both eyes met the measurement criteria, each eye was treated as an independent data point; for cases with only one eye meeting the criteria, only that eye was included in the analysis.

Previous studies have established a relationship between the progressive narrowing of the ICA and the development of glaucoma (3, 11). It has also been demonstrated that the risk of developing PACG is significantly higher in dogs with a narrowed or closed CC (29, 33). Our study sought to clarify the relationship between these two factors, which are considered critical. Overall, we found a positive correlation between the RO-ICA and the CC. However, we also demonstrated that, even in cases categorized as "Open" gonioscopically, there can still be a presence of a narrowed CC despite a relatively larger opening of the ICA. This finding challenges some of the traditional understandings of the relationship between ICA opening and CC in canine eyes (12).

The method used for measuring the RO-ICA in this study was developed through modifications of the techniques previously described by Ekesten et al. (10) and Bjerkås et al. (11). Unlike previous studies that relied on gonioscopy to observe and measure only the anterior face of the ICA, our research utilized UBM to examine sectioned images of the ICA. Additionally, we adopted the criteria for evaluating the measurement values directly from Ekesten et al.'s study (10). In contrast to previous research, where the percentages of Slightly Narrow, Narrow, Open, and Wide Open were 6.4, 25, 55.9, and 9.3% respectively, our study found these categories to be 9.7, 41.9, 45.2, and 3.2%. Notably, in our study, the proportion of eyes classified in the narrow group was higher than that in previous research. This difference could be attributed to the fact that the earlier study focused on Samoyeds, a single breed, while our study included a variety of breeds. Predominantly, breeds like Poodles and Shih Tzus, known to be prone to glaucoma due to structural reasons, were part of our research, which might explain the relatively higher proportion of the narrow group in our findings (34, 35).

Numerous risk factors for PACG have been identified in previous studies. Notably, female dogs are reported to have approximately twice the risk of developing PACG compared to males (36, 37). One theory suggests that gender differences in ICA morphology may contribute to this increased risk (16, 38, 39). Additionally, there has been an observation of progressive narrowing of the ICA with age, a finding that is significant as it implies that the width of the ICA may be a dynamic feature, changing as the dog ages, which could influence the risk of developing glaucoma (10, 21). There has also been a noted positive correlation between age and the severity of PLD (11, 21, 32). However, our study observed no significant differences in terms of sex, weight, age, and breed between the Narrow and Open groups.

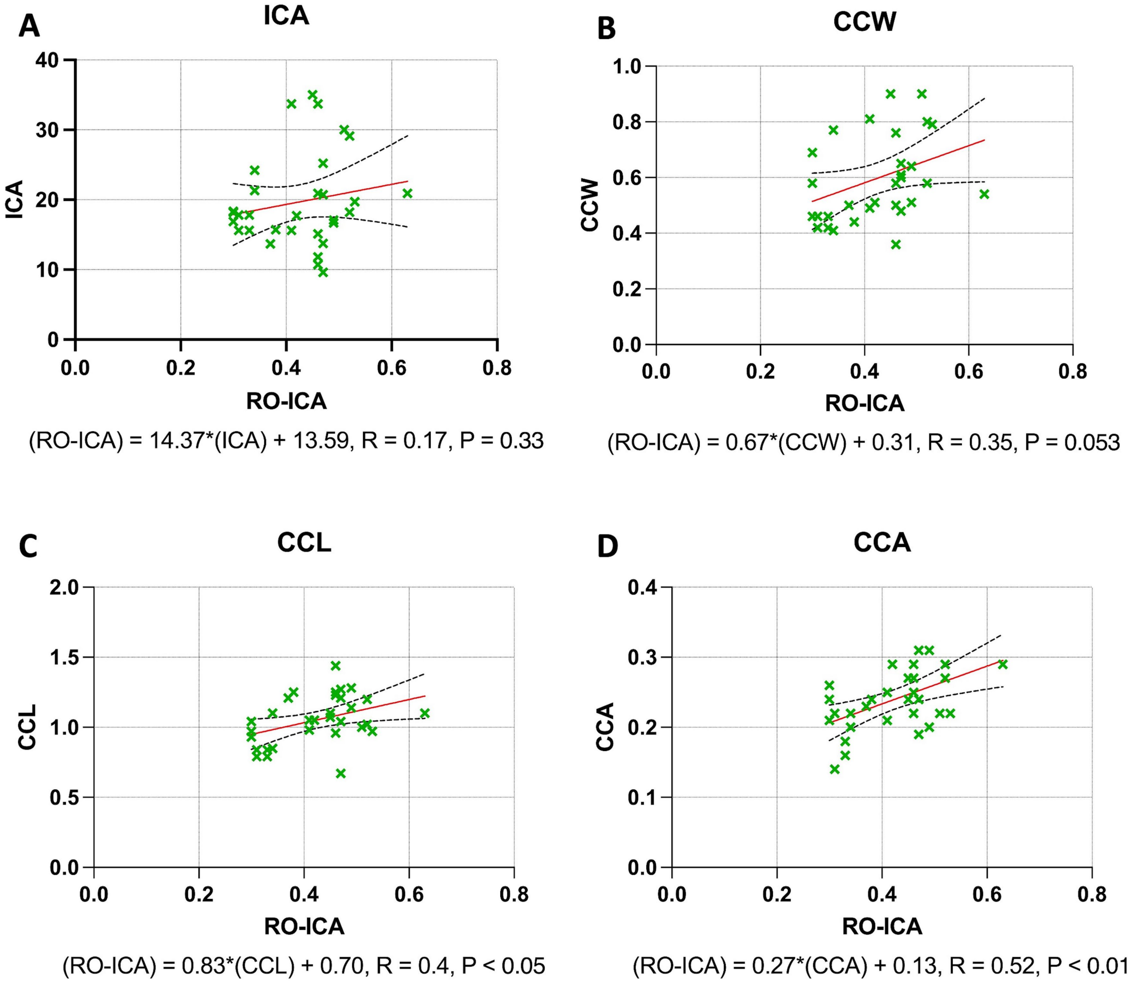


FIGURE 3
Regression analysis outcomes across combined narrow and open groups. **(A)** The linear regression model examining the relationship between RO-ICA and ICA in 31 eyes, described by the equation Y = 14.37X + 13.59, shows a weak linear correlation with an $R^2$ value of 0.03316. Analysis of the slope and y-intercept, including standard errors and 95% confidence intervals, reveals no significant linear relationship ($p = 0.3269$). **(B)** The analysis of RO-ICA versus CCW in 31 eyes demonstrates a modest correlation using the equation Y = 0.6666X + 0.3144, resulting in an $R^2$ of 0.1230. The confidence interval for the slope ranges from −0.009422 to 1.343, with a marginal slope significance ($p = 0.0531$), suggesting a weak linear relationship. **(C)** The linear regression model for RO-ICA versus CCL in 31 eyes, given by Y = 0.8282X + 0.7013, indicates a substantial correlation with an $R^2$ of 0.1607. The slope is significantly non-zero ($p < 0.05$), confirming a significant linear relationship. Detailed confidence intervals for both slope and y-intercept are provided. **(D)** In assessing RO-ICA against CCA in 31 eyes, the model Y = 0.2698X + 0.1255 shows a moderate correlation with an $R^2$ of 0.2684. A significant slope ($p < 0.01$) signifies a notable linear relationship. Standard errors and confidence intervals for both slope and y-intercept are included. Levels of statistical significance in the study are categorized as $p < 0.05$, $p < 0.01$, $p < 0.001$, and $p < 0.0001$ for clarity.

Based on the results of this study, it was observed that the CCL and CCA were statistically significantly smaller in the Narrow group compared to the Open group. Additionally, when conducting regression analysis regardless of the group, both CCL and CCA demonstrated a positive correlation with the RO-ICA. This correlation was more pronounced when the ICA's relative opening was smaller, particularly in the Narrow group. Here, all factors, including ICA, CCW, CCL, and CCA, showed a positive correlation with RO-ICA. In essence, this suggests that a smaller RO-ICA is likely to be associated with a smaller CC. These findings are in line with previous results that showed no significant difference between UBM-derived CC grades and subjective gonioscopic grades, further reinforcing the consistency and validity of these measures (12).

However, in the Open group, despite the CCL and CCA being significantly larger compared to the Narrow group, there was no observed correlation with the RO-ICA. This outcome contrasts with previous studies that found no differences between UBM-derived CC grades and subjective gonioscopic grades when the CC depicted on UBM images was graded as open (12). This result suggests that a large RO-ICA does not necessarily correlate with a large CC. This discovery holds substantial clinical importance, indicating that even if the ICA is assessed as open through gonioscopy, there could still be a predisposition to PACG. The findings also imply the potential necessity of evaluating the CC using UBM examinations.

Previous studies have recognized the CC as an essential anatomical structure in the formation of IOP. Research by Dubin

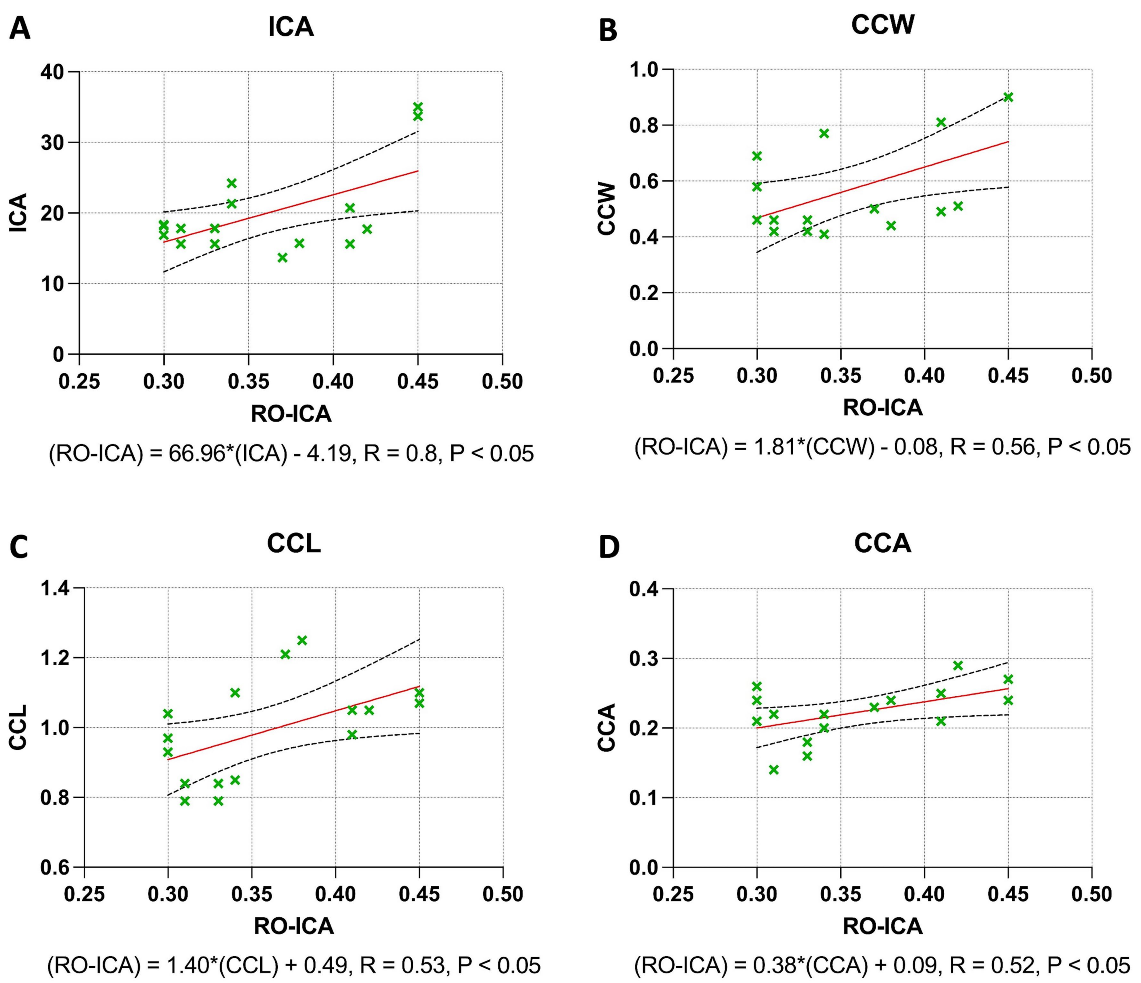


FIGURE 4
Regression analysis outcomes in narrow groups. **(A)** The regression model between RO-ICA and ICA for 16 eyes, represented by Y = 66.96X – 4.193, shows a moderate correlation with an $R^2$ value of 0.3376. A significant slope ($p < 0.05$) supports a notable linear relationship. Standard errors and confidence intervals are provided for both slope and y-intercept. **(B)** In examining RO-ICA against CCW for 16 eyes, the equation Y = 1.816X – 0.07650 results in a correlation coefficient ($R^2$) of 0.3080. The slope, significantly different from zero ($p < 0.05$), suggests a meaningful linear relationship. Confidence intervals for both slope and y-intercept are included. **(C)** The relationship between RO-ICA and CCL in 16 eyes is depicted by the linear model Y = 1.396X + 0.4894, demonstrating a fair correlation ($R^2 = 0.2794$). The slope is significantly non-zero ($p < 0.05$), indicating a significant linear association. Detailed confidence intervals for the slope and y-intercept are provided. **(D)** The regression model for RO-ICA versus CCA in 16 eyes, given by Y = 0.3759X + 0.08741, exhibits a correlation of $R^2 = 0.2650$. The significant slope ($p < 0.05$) implies a significant linear relationship. Standard errors and confidence intervals for both the slope and y-intercept are included in the figure. Levels of statistical significance in the study are categorized as $p < 0.05$, $p < 0.01$, $p < 0.001$, and $p < 0.0001$ for clarity.

et al. highlighted that a narrowed or closed CC in dogs significantly increases the risk of developing PACG by 20 times. Their findings also revealed that, despite the angle index assessed through gonioscopy providing a subjective estimate of outflow capacity through the iridocorneal angle, the pectinate ligament might not be the critical factor in restricting the flow of aqueous humor through the iridocorneal angle (33). Additionally, other studies have indicated that even in cases with PLD, if the CC remains open, the overall outflow capacity may still be normal (2, 29). Further research, particularly studies on goniotomy which involves widening the CC, has demonstrated an increase in the flow of aqueous humor, underscoring the CC's importance in IOP regulation and its pivotal role in the pathogenesis of PACG (40).

One of the parameters studied in our research, the ICA, overall, did not exhibit a correlation with the RO-ICA. However, in the Narrow group, a positive correlation was observed, indicating that a smaller RO-ICA tends to correspond with a smaller ICA. Since gonioscopy cannot evaluate the internal structure of the ICA, making it an imperfect marker, there has been research attempting to understand their relationship (21). In previous studies, the ZibWest angle index, which comprehensively evaluates the grade of ICA and PLD, was used to assess the correlation with ICA. These studies revealed that when ICA measurements were conducted using SD-OCT, they showed significant correlations with gonioscopic ZibWest angle indices (41). Although PLD was not evaluated in our study, a similar outcome was observed in terms of the correlation between ICA grade and ICA, aligning with these prior findings.

This study has several limitations that should be acknowledged. A primary limitation is the small sample size,

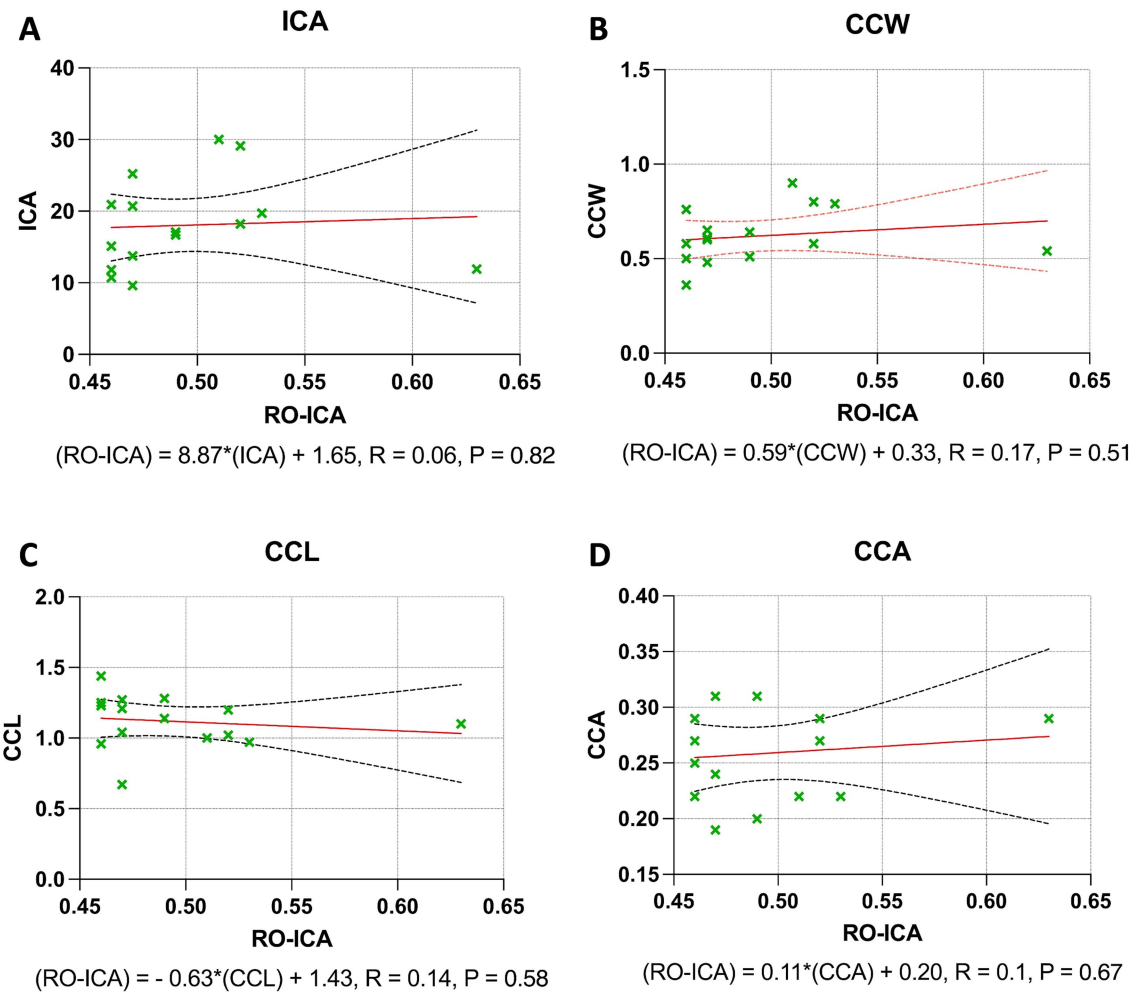


FIGURE 5
Regression analysis outcomes in open groups. **(A)** The linear regression model between RO-ICA and ICA for 15 eyes is represented by Y = 8.867X + 13.65, showing a very weak correlation with an $R^2$ value of 0.003936. The large confidence intervals for the slope, ranging from −75.65 to 93.39, and y-intercept, from −28.26 to 55.56, demonstrate a high level of uncertainty. The slope's insignificance ($p = 0.8242$) suggests no meaningful linear relationship. **(B)** For RO-ICA against CCW in 15 eyes, the regression equation Y = 0.5853X + 0.3308 results in a low correlation coefficient ($R^2 = 0.03416$). The wide confidence interval of the slope, spanning from −1.279 to 2.450, and its non-significance ($p = 0.5096$) indicate a lack of significant linear relationship. **(C)** The relationship between RO-ICA and CCL in 15 eyes is depicted by Y = −0.6319X + 1.431, indicating a negligible correlation ($R^2 = 0.02378$). The slope's confidence interval, ranging from −3.058 to 1.794, along with its non-significance ($p = 0.5832$), implies no significant linear association. **(D)** The linear model for RO-ICA versus CCA in 15 eyes, given by Y = 0.1121X + 0.2033, exhibits minimal correlation ($R^2 = 0.01475$). The slope, not significantly non-zero ($p = 0.6663$), with a confidence interval from −0.4370 to 0.6612, suggests a non-significant linear relationship. Levels of statistical significance in the study are categorized as $p < 0.05$, $p < 0.01$, $p < 0.001$, and $p < 0.0001$ for clarity.

which may restrict the generalizability of our findings. While a pre-study power analysis was not conducted, we consider this study an initial observational effort to investigate the relationship between the relative opening of the iridocorneal angle (RO-ICA) and the ciliary cleft (CC) structure. A larger sample size would be necessary to confirm these findings and potentially identify broader correlations between RO-ICA and CC. Additionally, the method we used to calculate RO-ICA was originally developed for gonioscopy images. Consequently, there may be some differences when compared to cross-sectional imaging. This also applies to the standard values used for interpretation, which could vary. Despite these potential discrepancies, this study made a concerted effort to measure RO-ICA in a consistent and standardized manner. Furthermore, our study included cases of incipient cataract. While some research suggests that cataracts may influence the size of the ciliary cleft, we did not observe significant differences between normal eyes and those with incipient cataracts (24). As a result, we included these cases in our study results, considering them relevant to our overall findings.

In conclusion, a smaller RO-ICA can generally be associated with a smaller CC. However, a larger RO-ICA does not necessarily indicate a larger CC. Therefore, in clinical settings, when an open ICA is observed using gonioscopy, the possibility of a smaller CC should always be considered (Figure 6). Consequently, additional UBM examinations are recommended for a more comprehensive assessment.

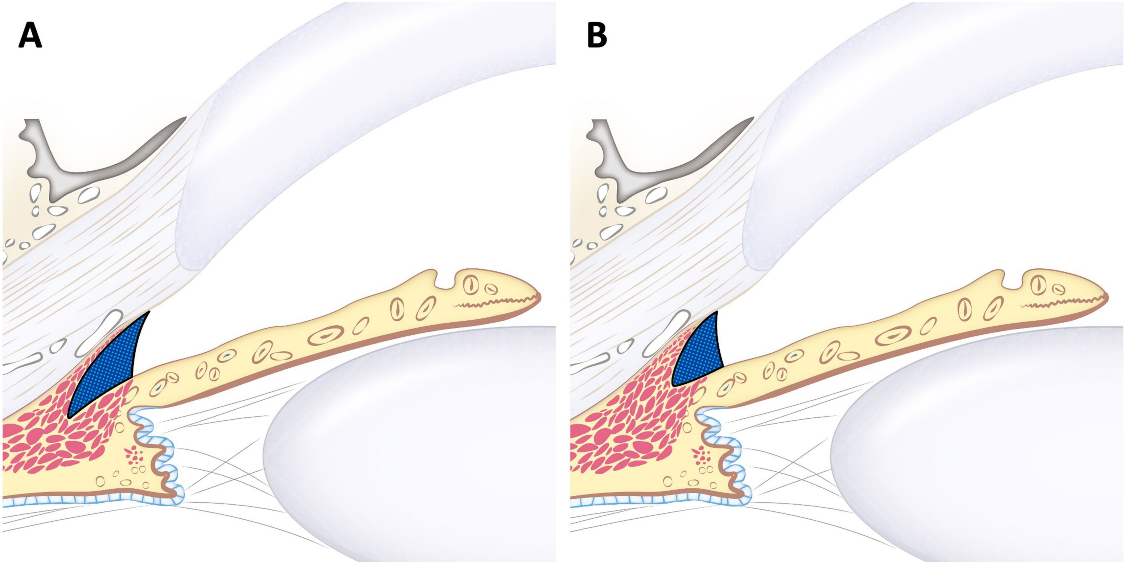


FIGURE 6
Schematic image of large RO-ICA with varying sizes of the ciliary cleft. This figure illustrates the different ciliary clefts in the same larger RO-ICA. Although **(A)** and **(B)** have the same relatively large RO-ICA, **(B)** shows that CCW, CCL, and CCA are all smaller compared to **(A)**. This indicates that even with the same relative opening, the ciliary cleft can vary in size.

## Data availability statement

The original contributions presented in the study are included in the article/supplementary material, further inquiries can be directed to the corresponding author.

## Ethics statement

The animal studies were approved by Institutional Animal Care and Use Committee. The studies were conducted in accordance with the local legislation and institutional requirements. Written informed consent was obtained from the owners for the participation of their animals in this study.

## Author contributions

DK: Writing – original draft, Writing – review & editing. HK: Formal analysis, Validation, Writing – review & editing. JH: Project administration, Validation, Visualization, Writing – review & editing. JJ: Project administration, Resources, Validation, Writing – review & editing. K-MP: Funding acquisition, Writing – review & editing.

## Funding

The author(s) declare that financial support was received for the research, authorship, and/or publication of this article. This work was supported by the National Research Foundation of Korea (NRF) grant funded by the Korea government. MSIT (RS-2024-00344226), "Regional Innovation Strategy (RIS)" through the National Re-search Foundation of Korea (NRF) funded by the Ministry of Education (MOE) (2021 RIS-001) and the Basic Research Lab Program (2022R1A4A1025557) funded by the Ministry of Science and ICT.

## Conflict of interest

The authors declare that the research was conducted in the absence of any commercial or financial relationships that could be construed as a potential conflict of interest.

## Publisher's note

All claims expressed in this article are solely those of the authors and do not necessarily represent those of their affiliated organizations, or those of the publisher, the editors and the reviewers. Any product that may be evaluated in this article, or claim that may be made by its manufacturer, is not guaranteed or endorsed by the publisher.

## Supplementary material

The Supplementary material for this article can be found online at: https://www.frontiersin.org/articles/10.3389/fvets.2024.1476746/full#supplementary-material

# References


1. Miller PE, Bentley E. Clinical signs and diagnosis of the canine primary Glaucomas. *Vet Clin North Am Small Anim Pract*. (2015) 45:1183–1212, vi. doi: 10.1016/j.cvsm.2015.06.006

2. Pizzirani S. Definition, classification, and pathophysiology of canine Glaucoma. *Vet Clin North Am Small Anim Pract*. (2015) 45:1127–57, v. doi: 10.1016/j.cvsm.2015.06.002

3. Grozdanic SD, Kecova H, Harper MM, Nilaweera W, Kuehn MH, Kardon RH. Functional and structural changes in a canine model of hereditary primary angle-closure glaucoma. *Invest Ophthalmol Vis Sci*. (2010) 51:255–63. doi: 10.1167/iovs.09-4081

4. Freddo TF, Civan M, Gong H. Aqueous humor and the dynamics of its flow: mechanisms and routes of aqueous humor drainage. In: Albert DM, Jakobiec F, editrs. *Principles and Practice of Ophthalmology*. Cham: Springer International Publishing (2022) 1989–2033.

5. Park S, Casanova MI, Bannasch DL, Daley NL, Kim S, Kuchtey J, et al. Ocular morphologic traits in the American cocker spaniel may confer primary angle closure glaucoma susceptibility. *Sci Rep*. (2022) 12:18980. doi: 10.1038/s41598-022-23238-1

6. Goel M, Picciani RG, Lee RK, Bhattacharya SK. Aqueous humor dynamics: a review. *Open Ophthalmol J*. (2010) 4:52–9. doi: 10.2174/1874364101004010052

7. Turner G, Groth A, Hii C, O'Reilly A, Volk H, Hardman C. Statistical agreement of gonioscopy performed as a puppy and as an adult in the Samoyed dog. *Vet Ophthalmol*. (2023) 27:228–37. doi: 10.1111/vop.13138

8. Bedford P. A simple method of gonioscopy for the dog and cat. *J Small Anim Pract*. (2008) 26:407–10. doi: 10.1111/j.1748-5827.1985.tb02216.x

9. Zibura AE, Robertson JB, Westermeyer HD. Gonioscopic iridocorneal angle morphology and incidence of postoperative ocular hypertension and glaucoma in dogs following cataract surgery. *Vet Ophthalmol*. (2021) 24:50–62. doi: 10.1111/vop.12802

10. Ekesten B, Narfström K. Correlation of morphologic features of the iridocorneal angle to intraocular pressure in Samoyeds. *Am J Vet Res*. (1991) 52:1875–8. doi: 10.2460/ajvr.1991.52.11.1875

11. Bjerkås E, Ekesten B, Farstad W. Pectinate ligament dysplasia and narrowing of the iridocorneal angle associated with glaucoma in the English springer spaniel. *Vet Ophthalmol*. (2002) 5:49–54. doi: 10.1046/j.1463-5224.2002.00213.x

12. Gibson TE, Roberts SM, Severin GA, Steyn PF, Wrigley RH. Comparison of gonioscopy and ultrasound biomicroscopy for evaluating the iridocorneal angle in dogs. *J Am Vet Med Assoc*. (1998) 213:635–8. doi: 10.2460/javma.1998.213.05.635

13. Pavlin CJ, Foster FS. Ultrasound biomicroscopy. High-frequency ultrasound imaging of the eye at microscopic resolution. *Radiol Clin North Am*. (1998) 36:1047–58. doi: 10.1016/S0033-8389(05)70230-X

14. Pavlin CJ, Harasiewicz K, Sherar MD, Foster FS. Clinical use of ultrasound biomicroscopy. *Ophthalmology*. (1991) 98:287–95. doi: 10.1016/S0161-6420(91)32298-X

15. Bentley E, Miller PE, Diehl KA. Use of high-resolution ultrasound as a diagnostic tool in veterinary ophthalmology. *J Am Vet Med Assoc*. (2003) 223:1617–1622, 1599. doi: 10.2460/javma.2003.223.1617

16. Boillot T, Rosolen SG, Dulaurent T, Goulle F, Thomas P, Isard PF, et al. Determination of morphological, biometric and biochemical susceptibilities in healthy Eurasier dogs with suspected inherited glaucoma. *PLoS One*. (2014) 9:e111873. doi: 10.1371/journal.pone.0111873

17. Hasegawa T, Kawata M, Ota M. Ultrasound biomicroscopic findings of the iridocorneal angle in live healthy and glaucomatous dogs. *J Vet Med Sci*. (2016) 77:1625–31. doi: 10.1292/jvms.15-0311

18. Pizzirani S, Gong H. Functional anatomy of the outflow facilities. *Vet Clin North Am Small Anim Pract*. (2015) 45:1101–1126, v. doi: 10.1016/j.cvsm.2015.06.005

19. Bedford PGC. Gonioscopy in the dog. *J Small Anim Pract*. (1977) 18:615–29. doi: 10.1111/j.1748-5827.1977.tb05830.x

20. Bedford PGC, Grierson I. Aqueous drainage in the dog. *Res Vet Sci*. (1986) 41:172–86. doi: 10.1016/S0034-5288(18)30595-2

21. Pearl R, Gould D, Spiess B. Progression of pectinate ligament dysplasia over time in two populations of flat-coated retrievers. *Vet Ophthalmol*. (2015) 18:6–12. doi: 10.1111/vop.12098

22. Kawata M, Tsukizawa H, Nakayama M, Hasegawa T. Rectification of width and area of the ciliary cleft in dogs. *J Vet Med Sci*. (2010) 72:533–7. doi: 10.1292/jvms.09-0507

23. Choi K-H, Choo SW, Jeong S-w, Kim JY. Ultrasound biomicroscopy studies to evaluate ciliary cleft parameters in healthy eyes of American cocker spaniels. *Pak Vet J*. (2019) 39:66–70. doi: 10.29261/pakvetj/2019.002

24. Kim D, Goh Y-S, Kim H, Park S-E, Hwang J, Kang N, et al. Evaluation of ciliary cleft changes after phacoemulsification using ultrasound biomicroscopy in dogs with cataracts. Frontiers in veterinary. *Science*. (2023) 10:10. doi: 10.3389/fvets.2023.1247127

25. Swaminathan SS, Oh DJ, Kang MH, Rhee DJ. Aqueous outflow: segmental and distal flow. *J Cataract Refract Surg*. (2014) 40:1263–72. doi: 10.1016/j.jcrs.2014.06.020

26. Johnstone MA. CHAPTER 3 – aqueous humor outflow system overview. In: RL Stamper, MF Lieberman and MV Drake, editors. Becker-Shaffer's diagnosis and therapy of the Glaucomas. *Eighth* ed. Edinburgh: Mosby (2009). 25–46.

27. Johnson M, McLaren JW, Overby DR. Unconventional aqueous humor outflow: a review. *Exp Eye Res*. (2017) 158:94–111. doi: 10.1016/j.exer.2016.01.017

28. Alm A, Nilsson SFE. Uveoscleral outflow – a review. *Exp Eye Res*. (2009) 88:760–8. doi: 10.1016/j.exer.2008.12.012

29. Rühli MB, Spiess BM. Goniodysplasia in the Bouvier des Flandres. *Schweiz Arch Tierheilkd*. (1996) 138:307–11.

30. Read RA, Wood JL, Lakhani KH. Pectinate ligament dysplasia (PLD) and glaucoma in flat coated retrievers. I. Objectives, technique and results of a PLD survey. *Vet Ophthalmol*. (1998) 1:85–90. doi: 10.1046/j.1463-5224.1998.00019.x

31. van der Linde-Sipman JS. Dysplasia of the pectinate ligament and primary glaucoma in the Bouvier des Flandres dog. *Vet Pathol*. (1987) 24:201–6. doi: 10.1177/030098588702400301

32. Oliver JA, Ekiri A, Mellersh CS. Prevalence and progression of pectinate ligament dysplasia in the welsh springer spaniel. *J Small Anim Pract*. (2016) 57:416–21. doi: 10.1111/jsap.12497

33. Dubin AJ, Bentley E, Buhr KA, Miller PE. Evaluation of potential risk factors for development of primary angle-closure glaucoma in Bouviers des Flandres. *J Am Vet Med Assoc*. (2017) 250:60–7. doi: 10.2460/javma.250.1.60

34. Gelatt KN, MacKay EO. Prevalence of the breed-related glaucomas in pure-bred dogs in North America. *Vet Ophthalmol*. (2004) 7:97–111. doi: 10.1111/j.1463-5224.2004.04006.x

35. Kato K, Sasaki N, Matsunaga S, Nishimura R, Ogawa H. Incidence of canine glaucoma with goniodysplasia in Japan: a retrospective study. *J Vet Med Sci*. (2006) 68:853–8. doi: 10.1292/jvms.68.853

36. Slater MR, Erb HN. Effects of risk factors and prophylactic treatment on primary glaucoma in the dog. *J Am Vet Med Assoc*. (1986) 188:1028–30.

37. Vajaranant TS, Nayak S, Wilensky JT, Joslin CE. Gender and glaucoma: what we know and what we need to know. *Curr Opin Ophthalmol*. (2010) 21:91–9. doi: 10.1097/ICU.0b013e3283360b7e

38. Tsai S, Bentley E, Miller PE, Gomes FE, Vangyi C, Wiese A, et al. Gender differences in iridocorneal angle morphology: a potential explanation for the female predisposition to primary angle closure glaucoma in dogs. *Vet Ophthalmol*. (2012) 15:60–3. doi: 10.1111/j.1463-5224.2011.00956.x

39. Narayanaswamy A, Sakata LM, He MG, Friedman DS, Chan YH, Lavanya R, et al. Diagnostic performance of anterior chamber angle measurements for detecting eyes with narrow angles: an anterior segment OCT study. *Arch Ophthalmol*. (2010) 128:1321–7. doi: 10.1001/archophthalmol.2010.231

40. Morrison JC, Van Buskirk EM. The canine eye: pectinate ligaments and aqueous outflow resistance. *Invest Ophthalmol Vis Sci*. (1982) 23:726–32.

41. Kim SA, Shim J, Kang S, Seo K. Inter-device agreement between spectral domain optical coherence tomography, ultrasound biomicroscopy, and gonioscopy in evaluating the iridocorneal angle in normotensive dogs. *J Vet Sci*. (2023) 24:e34. doi: 10.4142/jvs.22241

frontiers | Frontiers in Veterinary Science

TYPE Original Research
PUBLISHED 05 December 2024
DOI 10.3389/fvets.2024.1462437

Check for updates

OPEN ACCESS

EDITED BY
Hakyoung Yoon,
Jeonbuk national University, Republic of Korea

REVIEWED BY
Ana Patrícia Fontes-Sousa,
University of Porto, Portugal
Ashley Walker,
VCA Bay Area Veterinary Specialists,
United States

*CORRESPONDENCE
Ryou Tanaka
✉ ryo@vet.ne.jp

†These authors have contributed equally to this work

RECEIVED 10 July 2024
ACCEPTED 15 October 2024
PUBLISHED 05 December 2024

CITATION
Hamabe L, Shimada K, Hirose M, Hasegawa M, Takeuchi A, Yoshida T, Azakami D, Mandour AS and Tanaka R (2024) Assessment of myocardial function in Retrievers with dilated cardiomyopathy using 2D speckle tracking echocardiography: a pilot study.
*Front. Vet. Sci.* 11:1462437.
doi: 10.3389/fvets.2024.1462437



# Assessment of myocardial function in Retrievers with dilated cardiomyopathy using 2D speckle tracking echocardiography: a pilot study

Lina Hamabe[1†], Kazumi Shimada[1†], Miki Hirose[1], Mizuki Hasegawa[1], Aki Takeuchi[1], Tomohiko Yoshida[2], Daigo Azakami[1], Ahmed S. Mandour[1,3] and Ryou Tanaka[1]*

[1]Department of Veterinary Medicine, Faculty of Agriculture, Tokyo University of Agriculture and Technology, Tokyo, Japan, [2]Department of Clinical Veterinary Medicine, Obihiro University of Agriculture and Veterinary Medicine, Obihiro, Hokkaido, Japan, [3]Department of Animal Medicine (Internal Medicine), Faculty of Veterinary Medicine, Suez Canal University, Ismailia, Egypt

Early diagnosis of canine dilated cardiomyopathy (DCM) is complicated by the presence of a prolonged asymptomatic phase, for which a comprehensive evaluation of myocardial function is essential. This pilot study was conducted to evaluate the myocardial function in dogs with DCM using two-dimensional speckle tracking echocardiography (2D-STE). Nine client-owned Retrievers with DCM and twelve client-owned clinically normal Retrievers were comparatively evaluated using standard echocardiography and 2D-STE. Dogs with DCM were characterized by significant dilation of the left ventricle (LV), thinning of the LV wall, and myocardial hypokinesis when compared to clinically normal dogs. The global strain analysis showed a significant reduction of strain in both radial and circumferential directions, and the regional strain analysis revealed a greater degree of myocardial dysfunction at the LV free wall in the circumferential direction in dogs with DCM. The regional strain analysis also demonstrated a difference in the pattern of contraction between dogs with DCM and clinically normal dogs. The results of this study illustrate the ability of 2D-STE to evaluate both global and regional myocardial function in dogs with DCM and show differences between dogs with DCM and clinically normal dogs.

KEYWORDS

**2D-STE, canine dilated cardiomyopathy, dog, echocardiography, Retrievers, strain analysis**

## 1 Introduction

Canine dilated cardiomyopathy (DCM) is the most common form of cardiomyopathy in dogs (1, 2). It is characterized by progressive ventricular dilation resulting from the loss of myocardial contractility in the absence of any other cardiac, pulmonary, or systemic disease that may lead to similar characteristics (1–3). While there are different phenotypes of DCM in dogs, idiopathic DCM is often considered breed-specific and is most often seen in large and giant breed dogs (1–3). There is a prolonged duration of the disease's asymptomatic, pre-clinical phase without any associated clinical signs, which is known to last for months to years (1, 2). Gradual progression eventually leads to the symptomatic clinical phase, which is associated with the presence of congestive heart failure (CHF) or sudden death (1, 4). While the importance of early disease detection is well acknowledged, identifying this pre-clinical phase has proven difficult (1, 4).

Standard echocardiography is a widely accepted method for evaluating myocardial function. It has commonly been used to assess myocardial changes observed with DCM, and the diagnosis is made based on echocardiographic evidence of left ventricular (LV) dilation, myocardial hypokinesis, and increased sphericity (1, 2, 5, 6). LV fractional shortening (FS) is the most commonly used echocardiographic measurement of systolic function; however, it does not reflect the true systolic function because it only assesses myocardial movements in locally restricted segments (6, 7). Additionally, FS is affected by the loading conditions and the presence of mitral insufficiency, which further limits its usefulness (6, 8). Simpson's method of discs is another method that can assess myocardial changes, which uses two-dimensional measurements to estimate volume measurements (9). While it may provide more accurate volume measurements, it does not allow regional assessment. Similarly, E-point to septal separation, which measures the distance between the maximal early diastolic motion (E-point) of the septal mitral valve leaflet to the interventricular septum (IVS), is another commonly used parameter of systolic function. However, its measurement is restricted to a local segment and is influenced by the presence of mitral stenosis and aortic regurgitation (4, 8). Since quantitative assessment of regional myocardial function cannot be adequately made, standard echocardiography may not be particularly sensitive in detecting subtle myocardial changes observed in the early asymptomatic phase of DCM nor in monitoring mild disease progression (5).

Two-dimensional speckle tracking echocardiography (2D-STE) is an advanced echocardiographic technique that assesses myocardial function by quantifying myocardial deformation (10). Strain, the parameter of 2D-STE, quantifies the myocardial deformation as the percentage change in the length of the myocardium relative to its original length during systole and diastole, and it allows quantitative evaluation of both global and regional myocardial function (10, 11). LV myocardium is divided into segments, where regional strain is the average value within each segment, and global strain is the average value of all segments, representing the overall myocardial function (10, 12). In addition, segmental analysis allows the quantification of LV synchronicity by identifying variability between the segments (10, 13). In humans, reduced strain values are seen in patients with DCM, and 2D-STE has been shown to be useful in predicting the outcome of heart transplantation and cardiac resynchronization therapy in patients with DCM (14–17).

This pilot study aimed to illustrate the ability of 2D-STE to comprehensively evaluate the myocardial function in dogs with DCM by quantifying both global and regional myocardial function and determining whether it allows distinction from clinically normal dogs.

# 2 Materials and methods

## 2.1 Study population

Client-owned Retrievers diagnosed with DCM (DCM group) and clinically normal Retrievers (control group) were recruited for enrollment in this study. DCM group consisted of nine Retrievers presented at the Tokyo University of Agriculture and Technology Animal Medical Centre for the diagnosis and treatment of DCM and was diagnosed as clinical DCM with or without the presence of symptoms of CHF. Diagnosis was made based on echocardiographic evidence of LV dilation (LVIDdN >1.7), increased sphericity, and depressed systolic function (FS < 25%), and with the presence of at least one of the following conditions: (1) radiographic evidence of left-sided or biventricular cardiac enlargement, (2) radiographic evidence of pulmonary oedema or pleural effusion, and (3) electrocardiographic (ECG) evidence of arrhythmia including atrial fibrillation, ventricular premature complexes and ventricular tachycardia (1, 5, 18). Comprehensive cardiovascular examinations including echocardiography, radiography, ECG, and oscillometric blood pressure measurements were performed to exclude any congenital or acquired cardiac disease and systemic hypertension in addition to DCM. Blood tests consisting of a complete blood count, serum biochemistry, and thyroid panel, including serum thyroxine, serum free thyroxine, and endogenous canine thyrotropin concentrations, were performed to exclude any concurrent systemic disease that may affect cardiac function, unless the referring veterinarians had done them within two-weeks of referral. Owners were questioned regarding dietary history to exclude the possibility of grain-free diet, metabolic deficiencies and history of use of drugs known to affect cardiac function. Dogs with echocardiographic data from the previous examinations that allowed a definitive diagnosis of DCM were allowed to enroll during the medical treatment.

Clinically normal Retrievers included 12 dogs with an unremarkable history and normal physical examination, with no evidence of congenital or acquired cardiac disease seen with standard echocardiographic examination. Dogs in the control group were selected based on breed, sex, age, and bodyweight to match the DCM group.

## 2.2 Study protocol

The study was carried out in compliance with the guidelines established by the Tokyo University of Agriculture and Technology Animal Medical Center, with informed consent obtained from all owners. Echocardiographic evaluations, including standard echocardiography and 2D-STE, were performed using either of the ultrasonography units: ALOKA prosound $\alpha$ 10 equipped with a 3–8 MHz phased array transducer probe (UST-52108) (Hitachi Aloka Medical, Ltd., Japan) and LISSENDO 880LE equipped with a 9–12 MHz phase array transducer probe (S31) (Fujifilm Ltd., Japan). A mean of at least three measurements was obtained from consecutive cardiac cycles in sinus rhythm for each parameter. The investigators were aware of the clinical status of the dogs as evaluations took place in a clinical setting. None of the dogs were sedated during the echocardiography.

## 2.3 Standard echocardiography

The examination was performed in accordance with the published methodology in veterinary literature (6). The dimensions of the LV chamber were measured using M-mode from the right parasternal short-axis view. The measurements included LV internal dimension at end-diastole (LVIDd) and at end-systole (LVIDs), interventricular septal (IVS) thickness at end-diastole (IVSd) and at end-systole (IVSs) and LV free-wall (LVFW) thickness at end-diastole (LVFWd) and at end-systole (LVFWs), measured at the level of the papillary muscle. Diastolic and systolic LVID normalized to body weight (LVIDdN and

LVIDsN, respectively) were calculated as reported by Cornell et al. (18). LV systolic function was evaluated using FS and systolic time intervals. FS was calculated using the following equation: FS (%) = LVIDd-LVIDs/LVIDd x 100. Peak pulmonary blood flow velocity (PA Vmax) and peak aortic blood flow velocity (Ao Vmax) were obtained using the spectral Doppler from the right parasternal short-axis view at the level of the pulmonary artery and left parasternal apical five-chamber view, respectively. Systolic time intervals, which are the ratio of pre-ejection period and ejection time (PEP:ET) and stroke volume (SV), were measured from spectral Doppler aortic velocity. LV diastolic function was assessed by trans-mitral rapid ventricular filling (E) and atrial contraction (A), and E to A ratio (E/A) obtained from the trans-mitral flow profile at the left parasternal apical four-chamber view. The left parasternal apical four-chamber view was used for the pulse-wave tissue Doppler imaging (TDI) assessment to measure the mitral annular tissue velocities. Systolic (S′) and early (E′) diastolic myocardial velocities were obtained at IVS and LVFW, and the corresponding ratio between E and E′ (E/E′) at IVS and LVFW was calculated.

## 2.4 Two-dimensional speckle tracking echocardiography

Right parasternal short axis view at the level of the papillary muscle with the frame rate of 70–110 frames/s was acquired, which was then analyzed offline (DAS-RS1 software 6.0v, Hitachi Aloka Medical, Ltd., Japan). Firstly, the endocardial and epicardial borders of the LV were manually traced at end-systole by placing several regions of interest (ROIs), which were then automatically tracked on a frame-by-frame basis by the software. Strain measurements were taken in the radial and circumferential directions. Six-segment model was used for the regional analysis, where the LV was divided into six segments (anterior (AN), lateral (LT), posterior (PS), inferior (IN), septal (SP), and anterior septal (AS)). LV synchrony was assessed by calculating the synchrony time index (STI), which is the difference in timing of peak strains from the earliest to the latest segments. Strain parameters were obtained, including global peak strain in the radial and circumferential directions (GRS and GCS), regional strains at the six segments in both directions, and STI in the radial direction.

## 2.5 Statistical analysis

Statistical analysis was performed using statistical software (Prism 8.0v, GraphPad Software Inc., USA). Normal distribution was graphically inspected and tested using the Shapiro–Wilk test. Significant differences between the DCM and control groups were evaluated using unpaired Student's t-test for normally distributed parameters and Mann–Whitney test for parameters not normally distributed. A significant difference was defined as $p < 0.05$.

# 3 Results

## 3.1 Study population

Dogs in the DCM group ($n = 9$) consisted of three Golden and six Labrador Retrievers, of which three were male and six were female. The average age and bodyweight for the DCM group were 11.33 ± 2.35 years old (range 6–14 years old) and 25.88 ± 4.88 kg (range 16.00–32.15 kg). The control group ($n = 12$) consisted of six Golden and six Labrador Retrievers, four of which were male and eight of which were female. The average age and bodyweight for the control group were 9.50 ± 1.83 years old (range 6–12 years old) and 26.90 ± 5.53 kg (range 18.30–38.60 kg). There was no statistical difference with age ($p = 0.06$) and bodyweight ($p = 0.66$) between the groups.

While four dogs were asymptomatic, the remaining five dogs from the DCM group were presented with one or more of the following clinical signs of CHF: cough ($n = 2$), exercise intolerance ($n = 4$), and ascites ($n = 2$). ECG abnormality of isolated ventricular premature beats was observed in two dogs. Among five dogs presented with clinical signs, four dogs were already being treated with one or a combination of the following agents: angiotensin converting enzyme inhibitor ($n = 3$), furosemide ($n = 3$), pimobendan ($n = 3$), and taurine ($n = 1$).

## 3.2 Standard echocardiography

Table 1 shows the results of standard echocardiography of Retrievers with DCM and clinically normal Retrievers. Standard echocardiographic evaluation of the control group revealed all parameters to be within the reference range (6, 19–22). On the other hand, in the DCM group, LVIDd was above, and FS was below the reference range (6, 19–22). Compared to the control group, the DCM group showed statistically significant dilation of LV (LVIDs $p = 0.0009$) and thinning of LV walls (IVSs $p = 0.0114$, LVFWd $p = 0.0173$, LVFWs $p = 0.0088$), except for IVSd and LVIDd. LVIDdN and LVIDsN also revealed significant differences between the groups ($p = 0.0269$ and $p = 0.0024$, respectively). Additionally, significant reductions in FS ($p < 0.0001$) and S′ IVS ($p = 0.0002$), and an increase in Ao PEP/ET (0.0210) were observed in the study group compared to the control group, suggestive of impaired systolic function in the DCM group. A significant reduction in Ao Vmax ($p = 0.0210$) and SV ($p = 0.0441$) in the DCM group was also observed. Moreover, mitral valve regurgitation secondary to mitral annulus dilation was observed in three dogs in the DCM group that also showed signs of CHF. The average heart rate during the echocardiographic examination was 104.40 ± 19.80 beats per minute (bpm) (range 80.00–134.00 bpm) for the DCM group and 108.90 ± 14.05 bpm (range 84.00–130.00 bpm) control group, showing no significant differences between the groups ($p = 0.57$).

## 3.3 Two-dimensional speckle tracking echocardiography

Table 2 shows the results of 2D-STE of Retrievers with DCM and clinically normal Retrievers, and Figure 1 shows examples of radial and circumferential strains for Retrievers with DCM and clinically normal Retrievers. Comparison of 2D-STE values between groups revealed global strain values to be significantly lower in the DCM group in both radial and circumferential directions (GRS $p = 0.0401$, GCS $p = 0.0026$). Regionally, significantly lower strain values were observed with the DCM group at the anterior septal and posterior segments in radial

TABLE 1 Standard echocardiographic parameters of Retrievers with DCM and clinically normal Retrievers.

| | DCM ($n$ = 9) | Control ($n$ = 12) | $p$-Value |
|---|---|---|---|
| IVSd (mm) | 8.67 ± 2.01 | 9.74 ± 1.39 | 0.165 |
| IVSs (mm) | 11.05 ± 2.74 | 14.03 ± 2.15 | 0.0114 |
| LVIDd (mm) | 49.21 ± 12.92 | 40.69 ± 3.77 | 0.0722 |
| LVIDs (mm) | 37.00 (28.50–70.06) | 27.18 (21.33–31.56) | 0.0009 |
| LVFWd (mm) | 8.07 ± 1.21 | 9.96 ± 1.91 | 0.0173 |
| LVFWs (mm) | 11.10 ± 1.44 | 13.61 ± 2.24 | 0.0088 |
| LVIDdN | 1.90 ± 0.49 | 1.55 ± 0.12 | 0.0269 |
| LVIDsN | 1.44 ± 0.46 | 0.98 ± 0.08 | 0.0024 |
| FS (%) | 19.35 ± 6.05 | 32.47 ± 4.54 | <0.0001 |
| PA Vmax (cm/s) | 56.75 ± 18.95 | 69.50 ± 16.92 | 0.1325 |
| Ao Vmax (cm/s) | 64.67 ± 21.34 | 99.25 ± 31.86 | 0.0210 |
| Ao PEP:ET | 0.43 ± 0.09 | 0.29 ± 0.07 | 0.0025 |
| SV (ml) | 8.10 (5.80–17.00) | 11.52 (8.30–24.00) | 0.0441 |
| E (cm/s) | 53.55 ± 25.78 | 56.36 ± 8.79 | 0.7308 |
| A (cm/s) | 40.52 ± 7.84 | 48.32 ± 9.58 | 0.0862 |
| E/A | 1.35 ± 0.62 | 1.22 ± 0.31 | 0.5602 |
| S′ IVS (cm/s) | 5.31 ± 1.71 | 10.51 ± 2.55 | 0.0002 |
| E/E′ IVS | 10.45 (6.06–29.10) | 7.06 (5.13–11.55) | 0.0831 |
| S′ LVFW (cm/s) | 8.66 ± 3.27 | 10.43 ± 1.51 | 0.1577 |
| E/E′ LVFW | 8.93 ± 4.42 | 5.43 ± 1.35 | 0.0245 |

DCM, dilated cardiomyopathy; SD, standard deviation; IVSd, interventricular septal thickness at end-diastole; IVSs, interventricular septal thickness at end-systole; LVIDd, left ventricular internal diameter at end-diastole; LVIDs, left ventricular internal diameter at end-systole; LVFWd, left ventricular free wall thickness at end-diastole; LVFWs, left ventricular free wall thickness at end-systole; LVIDdN, diastolic left ventricular internal diameter normalized to body weight; LVIDsN, systolic left ventricular internal diameter normalized to body weight; FS, fractional shortening; PA Vmax, peak pulmonary blood flow velocity; Ao Vmax, peak aortic blood flow velocity; Ao PEP/ET, aortic pre-ejection period to left ventricular ejection time ratio; SV, stroke volume; E, rapid ventricular filling; A, atrial contraction; E/A, ratio of rapid ventricular filling to atrial contraction; S′ IVS, systolic myocardial velocity at interventricular septum; E/E′ IVS, ratio of rapid ventricular filling to rapid diastolic motion at interventricular septum; S′ LVFW, systolic myocardial velocity at left ventricular posterior wall; E/E′ LVPW, ratio of rapid ventricular filling to rapid diastolic motion at left ventricular free wall.

TABLE 2 Two-dimensional speckle-tracking echocardiographic parameters of Retrievers with DCM and clinically normal Retrievers expressed as mean ± SD.

| | DCM ($n$ = 9) | Control ($n$ = 12) | $p$-Value |
|---|---|---|---|
| Global radial strain (%) | 21.62 ± 9.46 | 32.24 ± 11.88 | 0.0401 |
| Regional radial anterior septal strain (%) | 19.55 ± 13.14 | 31.64 ± 9.43 | 0.0236 |
| Regional radial anterior strain (%) | 22.90 ± 12.76 | 27.60 ± 14.46 | 0.4479 |
| Regional radial lateral strain (%) | 22.50 ± 12.56 | 33.33 ± 16.56 | 0.1181 |
| Regional radial posterior strain (%) | 20.01 ± 10.57 | 36.33 ± 12.62 | 0.005 |
| Regional radial inferior strain (%) | 21.52 ± 10.52 | 32.48 ± 15.93 | 0.09 |
| Regional radial septal strain (%) | 23.24 ± 7.45 | 32.04 ± 14.37 | 0.1114 |
| Global circumferential strain (%) | −8.60 ± 2.92 | −12.34 ± 2.04 | 0.0026 |
| Regional circ. anterior septal strain (%) | −10.35 ± 5.18 | −13.52 ± 4.13 | 0.1351 |
| Regional circ. anterior strain (%) | −8.54 ± 4.55 | −10.62 ± 3.02 | 0.2228 |
| Regional circ. lateral strain (%) | −8.20 ± 3.93 | −12.15 ± 3.50 | 0.0252 |
| Regional circ. posterior strain (%) | −9.34 ± 4.86 | −13.90 ± 3.02 | 0.0157 |
| Regional circ. inferior strain (%) | −7.17 ± 2.79 | −10.55 ± 3.57 | 0.0118 |
| Regional circ. septal strain (%) | −8.11 ± 2.17 | −13.44 ± 3.20 | 0.0004 |
| STI (ms) | 45.37 ± 18.80 | 47.52 ± 19.50 | 0.8021 |

DCM, dilated cardiomyopathy; SD, standard deviation; STI, synchrony time index.

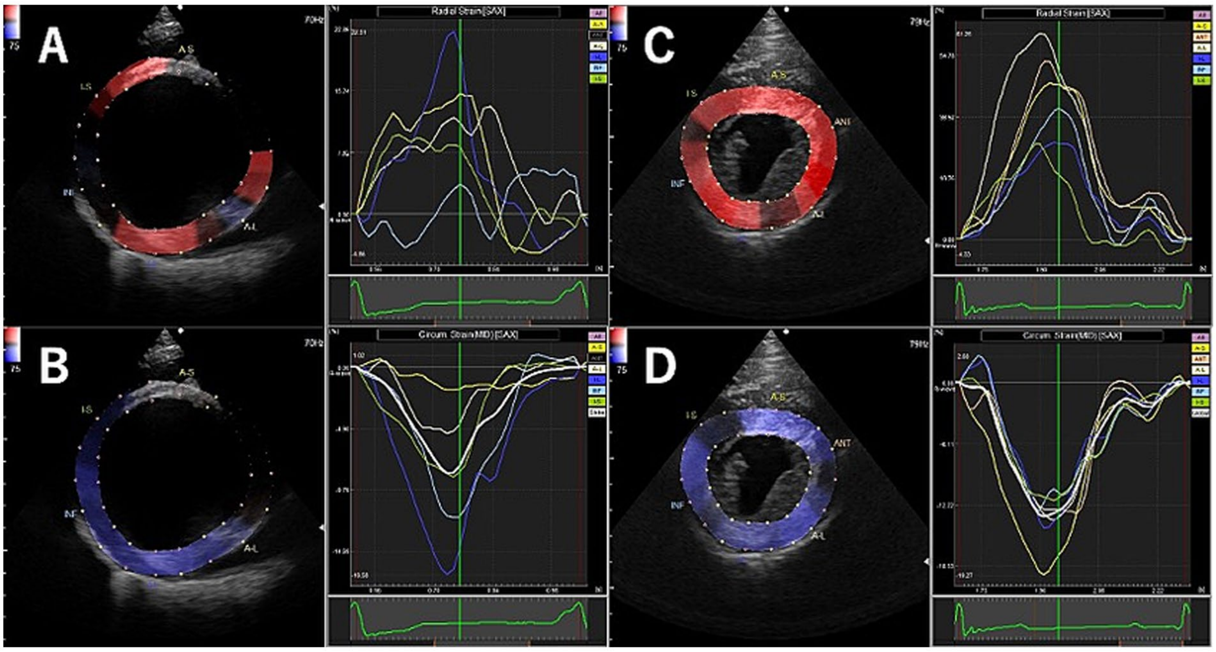


FIGURE 1
Examples of radial and circumferential strain profiles obtained from right parasternal short axis view at the level of the papillary muscle using two-dimensional tissue tracking in Retrievers with DCM (A: radial, B: circumferential) and clinically normal Retrievers (C: radial, D: circumferential).

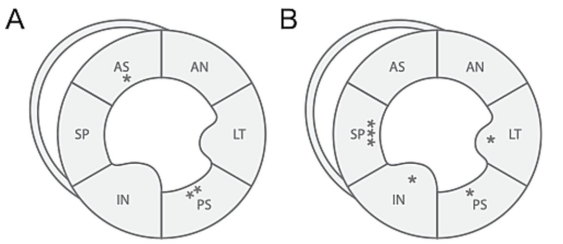


FIGURE 2
Illustration of differences in regional strain values between Retrievers with DCM and clinically normal Retrievers observed in (A) radial and (B) circumferential directions. *$p < 0.05$, **$p < 0.005$, ***$p < 0.001$. AN, anterior; LT, lateral; PS, posterior; IN, inferior; SP, septal; AS, anterior septal.

direction (AS $p = 0.0236$, PS = 0.0054), and at lateral, posterior, inferior and septal segments in circumferential directions (LT $p = 0.0252$, PS $p = 0.0157$, IN $p = 0.0118$, SP $p = 0.0004$) (Figure 2). Evaluation of the time to peak for each myocardial segment at the radial direction showed a homogenous pattern of contraction with the earliest time to peak at the septal segment in the control group. In contrast, the DCM group showed heterogenous pattern of contraction with the earliest time to peak at the lateral segment (Figure 3). Lastly, there was no significant difference in STI between groups.

## 4 Discussion

This pilot study illustrated the difference in myocardial function between nine Retrievers with DCM and 12 clinically normal Retrievers with comparable sex, age, and body weight. In this study, Golden and Labrador Retrievers were collectively grouped as Retrievers as they are known to be closely related based on genetic and phenotypic breed grouping (23).

Both standard echocardiography and 2D-STE analysis revealed significant differences between the DCM and the control groups, even though the DCM group included asymptomatic dogs and dogs already receiving medical treatment. In standard echocardiography, dogs with DCM showed significant dilation and thinning of the LV and myocardial hypokinesis, illustrated by the significant increase in LVIDs, LVIDdN and LVIDsN, and significant reduction in LV wall thickness and parameters of systolic function in comparison to the clinically normal dogs. The lack of significant difference in LVIDd between the groups is thought to be due to the small sample size and the greater variability among the DCM group. Three dogs in the DCM group had mild to moderate mitral valve regurgitation secondary to the mitral annulus dilation in association with the dilation of LV. Additionally, dogs with DCM showed a significantly higher value of E/E' at the LVFW, which was suggestive of volume overload, as E/E' is known to be a good indicator of increased LA pressure (24).

Strain analysis is based on deformation imaging where strain parameters are calculated from 2D displacement of the myocardium (10, 11). Therefore, unlike the tissue-Doppler analysis, 2D-STE is considered angle-independent, allowing the myocardial function to be evaluated from various spatial orientations (10, 11). A comparison of global analysis between the groups showed significantly lower strain values in dogs with DCM in both radial and circumferential directions, indicating significant myocardial dysfunction. Myocardial contractility occurs in both radial and circumferential directions, and radial and circumferential strains are sensitive indicators of myocardial contractility in dogs (10, 25). It is known that radial deformation

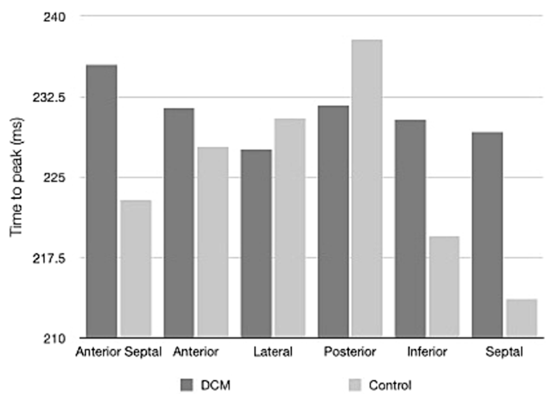


FIGURE 3
Time to peak values for the regional myocardial segments in radial direction illustrating the pattern of contraction of Retrievers with DCM and clinically normal Retrievers.

indicates transmural dysfunction, whereas circumferential deformation indicates subendocardial and subepicardial dysfunction (26). Therefore, the results of this study suggest that the myocardial dysfunction of DCM involves the entire myocardium. Previous studies in humans and dogs have reported that myocardial contractility primarily occurs in the radial and circumferential directions, and that deformation in these directions may serve as a sensitive indicator of myocardial contractility (25, 27, 28).

One of the major advantages of 2D-STE includes the ability to allow simultaneous evaluation of the global and regional myocardial function (10, 11). Regional analysis of 2D-STE revealed that in the circumferential directions, significantly lower strain values were focused around the LVFW (including the lateral, posterior, inferior and septal segments). Such result suggests that at least in the endocardium or the epicardium of the LV, LVFW is more susceptible to myocardial dysfunction associated with DCM. In normal LV, contraction occurs in homogenous pattern with the septal segment contracting slightly earlier than the lateral and posterior segments (14). A similar result was observed in the clinically normal dogs, where on average the septal segment was the first and lateral and posterior segments were the last to reach peak strain. In contrast, on average, in dogs with DCM, the lateral segment was the first and the anterior septal segment was the last to reach peak strain, showing heterogeneous pattern of contraction. It is known that a heterogeneous pattern of contraction ultimately results in reduced SV (14). In this study, a significant reduction of SV was observed in the dogs with DCM, which suggests that the heterogeneous pattern of contraction may indicate myocardial dysfunction, resulting in reduced SV. This point should further be studied under a condition of increased myocardial demands, for example using an exercise intolerance test. DCM has a prolonged period of asymptomatic phase during which myocardial hypokinesis may be the only detectable evidence (1, 2, 5). Therefore, the evaluation of the pattern of contraction may be used as additional criteria for the evaluation of DCM.

In human medicine, LV mechanical dyssynchrony is an important prognostic factor in patients with DCM (14). The orientation of the cardiac motion is largely radial and circumferential, and a reduction in systolic function is associated with increased radial mechanical dyssynchrony in patients with DCM (14, 17). However, this study did not show any significant difference in STI between groups, regardless of the demonstration of heterogeneous pattern of contraction in dogs with DCM. The proposed normal range for the STI in dogs is 0–45 ms (29). Interestingly, in this study, the STI value for the control group was just above the proposed normal range of STI, and for the DCM group, it was in the upper range. A similar study with clinically healthy Retrievers also showed a higher STI value in comparison to the proposed STI values (22). The higher STI values for the control and DCM groups in this study may be due to the sample population's older age compared to the population of the proposed STI values, whose mean age was 3.1 years old. A study by Lopez-Alvarez has also evaluated the mechanical synchrony in Doberman Pinschers with DCM using TDI, which failed to show differences between the normal dogs and dogs with DCM, a result similar to this study (30). Mechanical dyssynchrony may be less evident in dogs with DCM.

The radial and circumferential strains can be evaluated in parasternal short-axis views at the basal, papillary muscles and apex level of the LV. In both humans and dogs, strain values appear greater at the apex in comparison to the base creating an apex to base gradient (31–33). In a case with dogs with pre-clinical DCM, a study by Predo et al. showed that, while overall decrease in radial and circumferential strains were observed at all three levels of the LV, the greatest difference was observed at level of the papillary muscles (30). Based on such finding, in this study, strain analysis was only performed at the level of the pupillary muscle, none the less, a further study including the analysis at all three level should be conducted.

There are several limitations to this study. As this study was a pilot study, the total number of dogs included in the study was small, and although the difference was statistically insignificant, the average age of DCM group was slightly older than the control group. Additionally, the DCM group included dogs with both asymptomatic and symptomatic DCM. In order to evaluate the true potential of 2D-STE to diagnose DCM at an early stage, ideally, the study should consist of three groups, including clinically normal dogs, dogs with asymptomatic DCM and symptomatic DCM. Further studies need to be conducted on a larger scale. Furthermore, some of the dogs that exhibited symptoms were already receiving medications including angiotensin converting enzyme inhibitor, furosemide and pimobendan. While these medications are essential for managing DCM, they may influence the myocardial function, particularly by improving systolic function and may later strain parameters. This presents a potential limitation of the study, as controlling for the effects of treatment on echocardiographic evaluation was not feasible. One of the advantages of 2D-STE is that it is angle-independent and can be analyzed in multiple spatial orientations. Since this study only included the analysis in radial and circumferential directions, longitudinal analysis should also be performed. Lastly, 2D-STE analysis has its own limitations, such as the additional cost of the software and the expertise and time required to perform the analysis after examinations.

This study evaluated the myocardial function using 2D-STE, and demonstrated that the strain parameters differed between dogs with DCM and clinically normal dogs. The results of global strain analysis indicate that dogs with DCM are associated with a significant reduction of strain values in both radial and circumferential directions. Regional strain analysis suggested the possibility of increased susceptibility of the LVFW to circumferential myocardial dysfunction. Moreover, dogs with DCM showed a heterogeneous pattern of contraction, which may be associated with the progression of myocardial dysfunction. Irrespective of the heterogeneous pattern of contraction in dogs with DCM, significant mechanical dyssynchrony was not observed.

2D-STE Evaluation of myocardial function using 2D-STE provides valuable information on both global and regional myocardial function and to quantify myocardial synchronicity, which is not readily possible with standard echocardiography. Additional information provided by the 2D-STE analysis allows for a comprehensive and accurate evaluation of myocardial function, which is essential for diagnosing myocardial dysfunction and monitoring treatment and may serve as a prognostic indicator.

## Data availability statement

The original contributions presented in the study are included in the article/supplementary material, further inquiries can be directed to the corresponding author.

## Ethics statement

Ethical review and approval were waived for this study, since it only included echocardiographic examination, which is considered non-invasive, and informed consent was obtained from all owners of the subjects involved in the study.

## Author contributions

LH: Conceptualization, Methodology, Formal Analysis, Investigation, Writing-original draft. KS: Formal analysis, Investigation, Methodology, Writing – review & editing. MHi: Software, Validation, Visualization, Writing – review & editing. MHk: Software, Validation, Visualization, Writing – review & editing. AT: Investigation, Writing – review & editing. TY: Investigation, Writing – review & editing. DA: Data curation, Writing – review & editing. AM: Resources, Writing – review & editing. RT: Conceptualization, Supervision, Writing – review & editing.

## Funding

The author(s) declare that no financial support was received for the research, authorship, and/or publication of this article.

## Conflict of interest

The authors declare that the research was conducted in the absence of any commercial or financial relationships that could be construed as a potential conflict of interest.

## Publisher's note



## References

1. Dukes-McEwan J, Borgarelli M, Tidholm A, Vollmar AC, Häggström J. Proposed guidelines for the diagnosis of canine idiopathic dilated cardiomyopathy. *J Vet Cardiol*. (2003) 5:7–19. doi: 10.1016/S1760-2734(06)70047-9

2. Tidholm A, Häggström J, Borgarelli M, Tarducci A. Canine idiopathic dilated cardiomyopathy. Part I: Aetiology, clinical characteristics, epidemiology and pathology. *Vet J*. (2001) 162:92–107. doi: 10.1053/tvjl.2001.0571

3. Wess G, Domenech O, Dukes-McEwan J, Häggström J, Gordon S. European Society of Veterinary Cardiology screening guidelines for dilated cardiomyopathy in Doberman pinschers. *J Vet Cardiol*. (2017) 19:405–15. doi: 10.1016/j.jvc.2017.08.006

4. Bonagura JD, Visser LC. Echocardiographic assessment of dilated cardiomyopathy in dogs. *J Vet Cardiol*. (2022) 40:15–50. doi: 10.1016/j.jvc.2021.08.004

5. Oyama MA. Chapter 7- canine cardiomyopathy In: LP Tilley, FWK Smith, MA Oyama and MM Sleeper, editors. Manual of canine and feline cardiology. *Fourth* ed. Saint Louis: W.B. Saunders (2008). 139–50.

6. Boon JA. Veterinary echocardiography. *2nd ed*. ed. New Jersey: John Wiley & Sons (2011).

7. Fuentes VL. Chapter 4- echocardiography and Doppler ultrasound In: LP Tilley, FWK Smith, MA Oyama and MM Sleeper, editors. Manual of canine and feline cardiology. *Fourth* ed. Saint Louis: W.B. Saunders (2008). 78–98.

8. Wess G. Screening for dilated cardiomyopathy in dogs. *J Vet Cardiol*. (2022) 40:51–68. doi: 10.1016/j.jvc.2021.09.004

9. Wess G, Mäurer J, Simak J, Hartmann K. Use of Simpson's method of disc to detect early echocardiographic changes in Doberman pinschers with dilated cardiomyopathy. *J Vet Intern Med*. (2010) 24:1069–76. doi: 10.1111/j.1939-1676.2010.0575.x

10. Hamabe L, Mandour AS, Shimada K, Uemura A, Yilmaz Z, Nagaoka K, et al. Role of two-dimensional speckle-tracking echocardiography in early detection of left ventricular dysfunction in dogs. *Animals*. (2021) 11:2361. doi: 10.3390/ani11082361

11. Cameli M, Mandoli GE, Sciaccaluga C, Mondillo S. More than 10 years of speckle tracking echocardiography: still a novel technique or a definite tool for clinical practice? *Echocardiography*. (2019) 36:958–70. doi: 10.1111/echo.14339

12. Voigt JU, Pedrizzetti G, Lysyansky P, Marwick TH, Houle H, Baumann R, et al. Definitions for a common standard for 2D speckle tracking echocardiography: consensus document of the EACVI/ASE/industry task force to standardize deformation imaging. *Eur Heart J Cardiovasc Imaging*. (2015) 16:1–11. doi: 10.1093/ehjci/jeu184

13. Delgado V, Ypenburg C, van Bommel RJ, Tops LF, Mollema SA, Marsan NA, et al. Assessment of left ventricular dyssynchrony by speckle tracking strain imaging comparison between longitudinal, circumferential, and radial strain in cardiac resynchronization therapy. *J Am Coll Cardiol*. (2008) 51:1944–52. doi: 10.1016/j.jacc.2008.02.040

14. Friedberg MK, Slorach C. Relation between left ventricular regional radial function and radial wall motion abnormalities using two-dimensional speckle tracking in children with idiopathic dilated cardiomyopathy. *Am J Cardiol*. (2008) 102:335–9. doi: 10.1016/j.amjcard.2008.03.064

15. Jasaityte R, Dandel M, Lehmkuhl H, Hetzer R. Prediction of short-term outcomes in patients with idiopathic dilated cardiomyopathy referred for transplantation using standard echocardiography and strain imaging. *Transplant Proc*. (2009) 41:277–80. doi: 10.1016/j.transproceed.2008.10.083

16. Carasso S, Rakowski H, Witte KK, Smith P, Carasso D, Garceau P, et al. Left ventricular strain patterns in dilated cardiomyopathy predict response to cardiac resynchronization therapy: timing is not everything. *J Am Soc Echocardiogr*. (2009) 22:242–50. doi: 10.1016/j.echo.2008.12.003

17. Labombarda F, Blanc J, Pellissier A, Stos B, Gaillard C, Bajolle F, et al. Health-e-child project: mechanical dyssynchrony in children with dilated cardiomyopathy. *J Am Soc Echocardiogr*. (2009) 22:1289–95. doi: 10.1016/j.echo.2009.07.026

18. Cornell CC, Kittleson MD, Della Torre P, Häggström J, Lombard CW, Pedersen HD, et al. Allometric scaling of M-mode cardiac measurements in normal adult dogs. *J Vet Intern Med*. (2004) 18:311–21. doi: 10.1892/0891-6640(2004)18<311:asomcm>2.0.co;2

19. Morrison SA, Moise NS, Scarlett J, Mohammed H, Yeager AE. Effect of breed and body weight on echocardiographic values in four breeds of dogs of differing somatotype. *J Vet Intern Med*. (1992) 6:220–4. doi: 10.1111/j.1939-1676.1992.tb00342.x

20. Gugjoo MB, Hoque M, Saxena AC, Shamsuz Zama MM, Dey S. Reference values of M-mode echocardiographic parameters and indices in conscious Labrador retriever dogs. *Iran J Vet Res*. (2014) 15:341–6.

21. Saini N, Uppal SK, Randhawa CS. Echocardiographic parameters and indices in healthy Labrador retriever dogs. *Israel J. Vet. Med*. (2017) 72:28–34.

22. Hamabe L, Shimada K, Mandour AS, Yoshida T, Hirose M, Hendawy H, et al. Evaluation of left ventricular function in healthy retrievers using standard and 2D speckle-tracking echocardiography. *Vet Sci*. (2022) 9:529. doi: 10.3390/vetsci9100529

23. Vonholdt BM, Pollinger JP, Lohmueller KE, Han E, Parker HG, Quignon P, et al. Genome-wide SNP and haplotype analyses reveal a rich history underlying dog domestication. *Nature*. (2010) 464:898–902. doi: 10.1038/nature08837

24. Ishikawa T, Fukushima R, Suzuki S, Miyaishi Y, Nishimura T, Hira S, et al. Echocardiographic estimation of left atrial pressure in beagle dogs with experimentally-induced mitral valve regurgitation. *J Vet Med Sci*. (2011) 73:1015–24. doi: 10.1292/jvms.10-0141

25. Ro WB, Kang MH, Park HM. Serial evaluation of cardiac biomarker NT-pro BNP with speckle tracking echocardiography in a 6-year-old Golden retriever dog with subaortic stenosis and dilated cardiomyopathy. *Vet Q*. (2020) 40:77–82. doi: 10.1080/01652176.2020.1727992

26. Geyer H, Caracciolo G, Abe H, Wilansky S, Carerj S, Gentile F, et al. Assessment of myocardial mechanics using speckle tracking echocardiography: fundamentals and clinical applications. *J Am Soc Echocardiogr*. (2010) 23:351–69. doi: 10.1016/j.echo.2010.02.015

27. Kouzu H, Yuda S, Muranaka A, Doi T, Yamamoto H, Shimoshige S, et al. Left ventricular hypertrophy causes different changes in longitudinal, radial, and circumferential mechanics in patients with hypertension: a two-dimensional speckle tracking study. *J Am Soc Echocardiogr*. (2011) 24:192-9. doi: 10.1016/j.echo.2010.10.020

28. Suzuki R, Matsumoto H, Teshima T, Koyama H. Clinical assessment of systolic myocardial deformations in dogs with chronic mitral valve insufficiency using two-dimensional speckle-tracking echocardiography. *J Vet Cardiol*. (2013) 15:41–9. doi: 10.1016/j.jvc.2012.09.001

29. Chetboul V, Serres F, Gouni V, Tissier R, Pouchelon JL. Radial strain and strain rate by two-dimensional speckle tracking echocardiography and the tissue velocity based technique in the dog. *J Vet Cardiol*. (2007) 9:69–81. doi: 10.1016/j.jvc.2006.11.002

30. López-Alvarez J, Fonfara S, Pedro B, Stephenson H, Cripps PJ, Dukes-McEwan J. Assessment of mechanical ventricular synchrony in Doberman pinschers with dilated cardiomyopathy. *J Vet Cardiol*. (2011) 13:183–95. doi: 10.1016/j.jvc.2011.05.003

31. Westrup U, McEvoy FJ. Speckle tracking echocardiography in mature Irish wolfhound dogs: technical feasibility, measurement error and reference intervals. *Acta Vet Scand*. (2013) 55:41. doi: 10.1186/1751-0147-55-41

32. Tsugu T, Postolache A, Dulgheru R, Sugimoto T, Tridetti J, Nguyen Trung ML, et al. Echocardiographic reference ranges for normal left ventricular layer-specific strain: results from the EACVI NORRE study. *Eur Heart J Cardiovasc Imaging*. (2020) 21:896–905. doi: 10.1093/ehjci/jeaa050

33. Pedro B, Stephenson H, Linney C, Cripps P, Dukes-McEwan J. Assessment of left ventricular function in healthy great Danes and in great Danes with dilated cardiomyopathy using speckle tracking echocardiography. *J Vet Cardiol*. (2017) 19:363–75. doi: 10.1016/j.jvc.2017.06.002

frontiers | Frontiers in Veterinary Science

TYPE Original Research
PUBLISHED 17 December 2024
DOI 10.3389/fvets.2024.1450104



OPEN ACCESS

EDITED BY
Ryou Tanaka,
Tokyo University of Agriculture and Technology, Japan

REVIEWED BY
Howard Dobson,
Invicro (United States), United States
Andresa Guimarães,
Federal Rural University of Rio de Janeiro, Brazil

*CORRESPONDENCE
Cidéli de Paula Coelho
✉ cpcoelho@prof.unisa.br

RECEIVED 16 June 2024
ACCEPTED 30 November 2024
PUBLISHED 17 December 2024

CITATION
Martins JA, de Souza Balbueno MC, Málaga SK, da Costa LD and de Paula Coelho C (2024) Thoracic ultrasound for diagnosing pneumopathies in neotropical primates.
*Front. Vet. Sci.* 11:1450104.
doi: 10.3389/fvets.2024.1450104



# Thoracic ultrasound for diagnosing pneumopathies in neotropical primates

Jéssica Amancio Martins[1], Melina Castilho de Souza Balbueno[1], Soraya Kezam Málaga[1], Leonardo Dourado da Costa[2] and Cidéli de Paula Coelho[1]*

[1]University of Santo Amaro, São Paulo, Brazil, [2]L&M Veterinária, Belo Horizonte, Brazil

Lung ultrasound can be useful for the early diagnosis and treatment of respiratory complications. The combination of air and soft tissue confirms imaging artefacts that can contribute to differentiation between healthy and deteriorated lung tissue. Although non-human primates are often chosen as research models due to their anatomical and physiological similarity to humans, there is a lack of data on the use of lung ultrasound in these individuals. The aim of this study was to evaluate the contribution of ultrasound examinations of the thoracic region of *Callithrix* sp. for diagnosing pneumopathy. Parameters were obtained from 166 new world non-human primates of both sexes, aged between 1 and 15 years and weighing between 128 g and 680 g kept under human care at the Mucky Project in Itu, São Paulo. Thoracic ultrasound examinations were carried out using a LOGIQe—R7 device (GE, United States), with a 10–22 MHz linear transducer, at four points on the left and right antimeres. Among these 166 individuals, 72 had some kind of pulmonary alteration. Forty-one of the animals with pulmonary alterations diagnosed on ultrasound died and underwent necropsy. Histopathological examination showed that in half of the samples the lung tissue was compatible with some form of pneumopathy. Considering these cases, the pulmonary alterations diagnosed through thoracic ultrasound examination in *Callithrix* sp. can be correlated with the occurrence of pneumopathy, which is often asymptomatic. Lung ultrasound is an important tool for use in clinics to detect and monitor respiratory diseases and can save lives by enabling early treatment.

KEYWORDS

**respiratory disease, *Callithrix* sp., lobar consolidation, lung, ultrasound**

## 1 Introduction

Chest ultrasound examinations can be useful for the early detection and treatment of respiratory complications such as pneumonia, atelectasis and pleural effusion. They are of great value in both human and veterinary medicine, even in critically ill patients (1).

Non-human primates are widely used in anatomy and physiology research due to their similarities to humans, however, deforestation, habitat fragmentation, hunting for pets and hybridization are anthropogenic factors that can favour the population decline of NHP species, the lack of standardization in NHP species kept in captivity, makes it necessary to establish normal and pathological standards (2).

The lung parenchyma has a spongiform appearance. Its porosity and lung density result from a combination of elasticity and performance that allow remodeling of the air spaces, inflation, deflation, recruitment of peripheral air spaces and even thickening of the interalveolar septa (3). The bronchi, pulmonary bronchioles, ducts and alveolar sacs are components of the peripheral airspace. Their surface is protected by a thin continuous layer of surfactant, which is responsible for organizing the bubbles that fill the distal air spaces and provides structure and support, so that aeration of the lung parenchyma occurs properly (3, 4). Any pathological or functional situation that leads to a loss of porosity and lung density interferes with the relationship between air and tissue. This alteration can contribute to understanding lung ultrasound findings (3).

In healthy lung tissue, there is a large amount of air and little water. The normal lung pattern is visualized as parallel lines in a horizontal direction starting in the subpleural region and extending to the distal field, in ultrasound this finding is denominated line A (Figure 1A) (3).

The thickened pulmonary septum located in the subpleural region has very small dimensions, making it impossible to visualize it on ultrasound (approximately 1 mm). However, when there is significant thickening, the beam becomes disorganized and this results in a difference in acoustic impedance in the image, compared with the adjacent area composed of air (5).

The liquid in the lung parenchyma produces an image of a small anechoic structure. Its resolution is lower than that of the ultrasound beam due to the difference in acoustic impedance caused by the presence of air. This causes reverberating vertical artefacts called B lines (Figure 1B), which would be found not under normal conditions but, rather, in alveolar-interstitial syndromes (5).

Air bronchograms are frequently seen on lung ultrasound and are characterized by hyperechoic spots or lines within the consolidated area. There are two types of air bronchogram: dynamic and static. Dynamic bronchograms are so called because they involve a centrifugal inspiratory movement that accompanies the patient's respiratory movement. They are related to the irrigation capacity of the consolidated lung tissue through the airways and, for this reason, are often found in situations of pneumonia (Figure 1C). Static bronchograms are observed when there is no air inside the consolidation, due to a resorption process that contributes to reducing the volume of the consolidation (Figure 1D). This finding can be observed in late cases of atelectasis caused by reabsorption (6, 7).

Pulmonary consolidations are observed as delimited areas that resemble hepatic parenchyma (pulmonary hepatization), with well-defined regular or irregular outlines. Their acoustic impedance is high, due to the presence of multiple B lines or acoustic shadows over them (8).

Consolidations may be associated with alveolar impregnation caused by exudate, transudate, blood, fibrin or any other substance that replaces air (8). In the consolidated area, there is a loss of aeration, which forms a hypoechoic area located in the subpleural or tissue region (9).

Consolidations can be focal, partial or lobar (10). According to the appearance and location, it is possible to differentiate pneumonia from atelectasis due to tissue resorption. In patients with atelectasis due to tissue resorption, loss of pleural gliding is observed as an early sign, which differs from the presence of dynamic air bronchograms that glide in synchrony with respiratory movements. In 98.5% of cases, acute alveolar consolidations are in contact with the visceral pleural region. In late cases of atelectasis due to reabsorption, it will only be possible to visualize them when there is reabsorption of the gas content and a decrease in the volume of the consolidation, which is confirmed by a static bronchogram image (5).

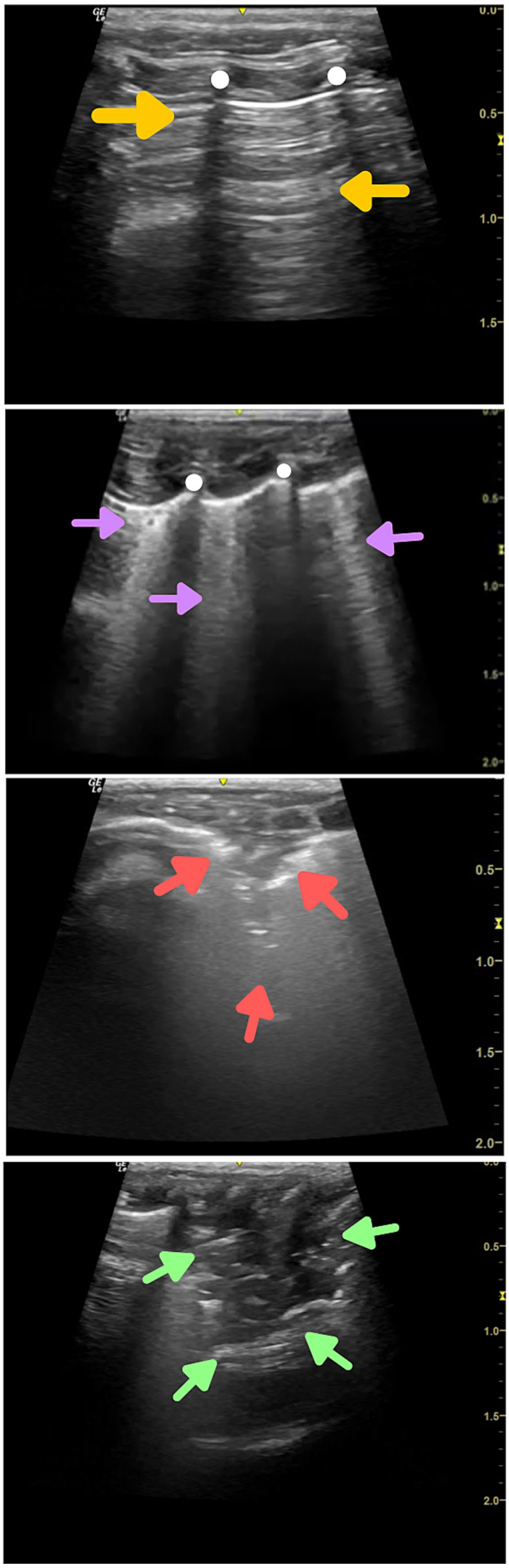

FIGURE 1
Thoracic ultrasound findings from *Callithrix* sp. **(A)** Healthy lung parenchyma, with the presence of parallel horizontal lines starting in

*(Continued)*

FIGURE 1 (Continued)
the subpleural region and extending to the distal field (lines A—profile A) (yellow arrowheads). **(B)** Presence of parallel vertical hyperechoic artefacts starting in the subpleural region and extending to the distal field (lines B—profile B) (purple arrowheads). **(C)** Presence of consolidation with air bronchograms, represented by a hypoechoic area in the subpleural region, with poorly delimited outlines and the presence of vertical hyperechoic lines within the area described (profile C) (red arrowheads). **(D)** Presence of consolidation with static bronchogram, represented by a triangular-shaped hypoechogenic area, without vertical hyperechogenic lines inside the area described (green arrowheads).

When bronchopneumonia develops and compromises peripheral areas, there is a loss of aeration and the following ultrasound characteristics are observed: in patients with incipient infections involving interstitial inflammation, foci of B lines with irregular intervals are observed; and in cases of focal bronchopneumonia, small, consolidated areas are observed in the subpleural or lobar region, along with larger lobar consolidations. The presence of secretions and air in the bronchial region is observed on ultrasound as hyperechoic lines within the consolidated area, which move along in synchrony with breathing (5, 11).

The aim of this study was to assess the contribution of ultrasound examination of the thoracic region of individuals of *Callithrix* sp. to making the diagnosis of pulmonary abnormalities.

## 2 Methodology

All the procedures described in this study were authorized by the Ethics Committee for the Use of Animals (CEUA) at the University of Santo Amaro, Brazil, and the project was filed under the number 57/2021. The project was also authorized by SISBIO (Authorization for Activities for Scientific Purposes of the Brazilian Ministry of the Environment) under the number 78874-1. The letter of consent to carry out this study was then given to and countersigned by the person in charge of the Mucky Project, where the animals were living. The methodology involved evaluating the influence of factors such as sex, age, and body mass on ultrasound findings in marmosets, as well as statistically comparing the frequency of key findings between different species.

Thoracic ultrasonogram examinations were carried out using a LOGIQe - R7 device (GE, United States), with a 10–22 MHz linear transducer and with the aid of an acoustic gel. Images were obtained through the left and right parasternal windows.

The patients were sedated with isoflurane, induced via mask, and this was maintained at a rate of 1 to 3%, with 100% oxygen, for the duration of the examination, which lasted a maximum of 20 min (12). Before the examination, a four-hour water-and-food fast was imposed. The animals remained in a supine position during the examination and were assessed at four points on each antimere (Figure 2).

Thoracic sonographic findings were compared with histopathological results obtained from 10 animals that died during the study period.

## 3 Results

This observational study used a convenience sample made up of 166 individuals of *Callithrix* sp. (males and females), aged between 1 and 15 years (5.32 ± 3.76 years) and with an average weight of 128 g to 680 g (0.33 ± 0.07 kg). They were living within the premises of the NGO Mucky Project, in the municipality of Itu, São Paulo, Brazil, and the assessments were carried out between November 2, 2021, and January 24, 2022.

FIGURE 2
Image showing the points on *Callithrix* sp. that were assessed using the thoracic transducer.

As regards the gender of the animals: 20 (12.04%) were *C. aurita* species [13 (65%) males and 7 (35%) females], 69 (41.5%) were *C. jacchus* species [34 (49.27%) males and 35 (50.72%) females], 30 (18.07%) were of the *C. penicilatta* species [13 (18.07%) males and 35 (50.72%) females] and 47 (28.31%) were *Callithrix* sp. hybrids [28 (59.57%) males and 19 (40.42%) females].

We sampled 166 marmosets (*Callithrix* spp.) with a mass of 0.33 ± 0.07 kg (0.13–0.68) and an age of 5.39 ± 3.21 years (0.70–15.00).

The species did not differ significantly in terms of mass ($H = 5.24$, df = 3, $p = 0.155$), but they did in terms of age ($H = 43.69$, df = 3, $p < 0.001$).

The sex ratio was 53% males to 47% females, which did not differ significantly from an equal sex ratio ($z = -0.774$, $p = 0.439$).

Among the 166 individuals assessed, 43 (25.90%) had B lines, located as follows, 20 (12.04%) had a static bronchogram (SBC) and 43 (25.90%) had dynamic bronchograms (DBC) (Table 1). The distribution of the lesions is shown in a mosaic (Figure 3).

Regarding concomitant findings, 30 animals had more than one type of pulmonary artefact, the occurrence of B-lines associated with

TABLE 1 Frequency of ultrasound findings (number of animals and percentage per species) from the thorax of neotropical primates of the genus *Callithrix*.

| Taxon | Line A | Line B | SBC | DBC | *N* |
|---|---|---|---|---|---|
| *Callithrix aurita* | 20 (100%) | 5 (25%) | 2 (10%) | 7 (35%) | 20 |
| *Callithrix jacchus* | 69 (100%) | 12 (17%) | 9 (13%) | 12 (17%) | 69 |
| *Callithrix penicillata* | 30 (100%) | 11 (37%) | 4 (13%) | 10 (33%) | 30 |
| *Callithrix* sp. | 47 (100%) | 15 (32%) | 5 (11%) | 14 (30%) | 47 |
| Total | 166 (100%) | 43 (26%) | 20 (12%) | 43 (26%) | 166 |

Source: The author, 2022.

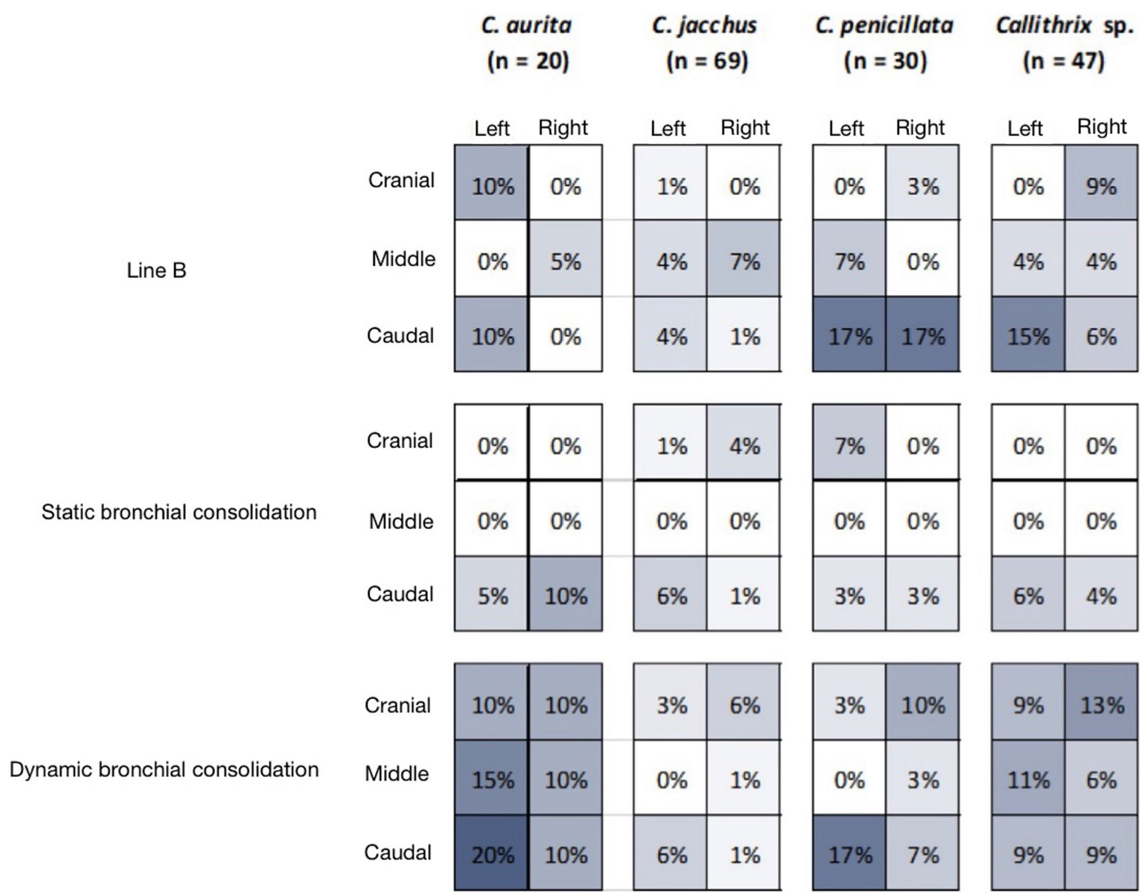


FIGURE 3
Visual representation of the frequency of anatomical distribution of ultrasound findings from the thorax of neotropical primates of the genus *Callithrix* sp.

consolidation, together with a dynamic bronchogram, was observed in 17 animals, with higher prevalence in the left caudal window, in 8 animals B-lines associated with consolidation, together with a static bronchogram, with higher prevalence in the left caudal window, in 1 animal B-lines associated with consolidation, together with a static bronchogram, and consolidation together with a dynamic bronchogram, the occurrence of consolidation with a static bronchogram, in association with consolidation with a dynamic bronchogram, was observed in 4 animals, with higher prevalence in the right cranial and right caudal windows.

Line A was found in all the animals evaluated, while line B was found in 26% of the marmosets (43/166). Static bronchial consolidation (SBC) was seen in 12% of the marmosets (20/166) and dynamic bronchial consolidation (DBC) was seen in 26% of the marmosets (43/166). Table 1 the frequency of these findings among the species analyzed. No significant differences were detected between the marmoset species, regarding the frequencies of line B ($\chi^2 = 5.309$, df = 3, $p = 0.151$), SBC ($\chi^2 = 0.279$, df = 3, $p = 0.964$) and DBC ($\chi^2 = 4.699$, df = 3, $p = 0.195$) (Figures 3, 4).

The occurrence of SBC was heterogeneous in relation to the incidence of line B ($p = 0.014$), such that it was more frequent in animals in which line B was present (22%) than in those in which line A was absent (8%). Similarly, the incidence of SBC was also heterogeneous in relation to the incidence of line A ($p = 0.005$), such

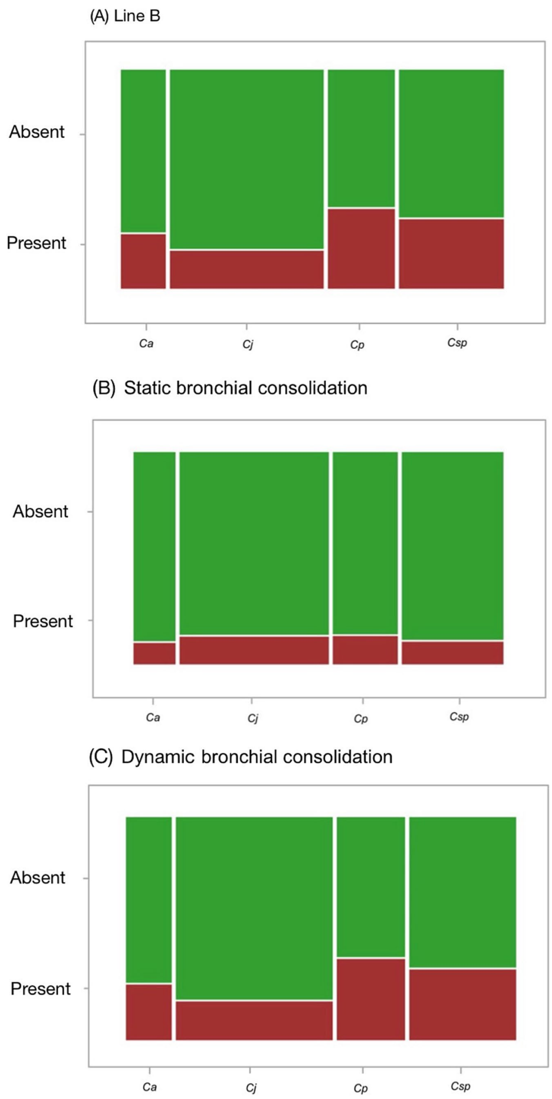


FIGURE 4
Mosaic graph of the frequency of ultrasound findings from the thorax of neotropical primates of the genus *Callithrix*. The height of the bars represents the relative frequency of ultrasound findings, and the width represents the sampling effort for each species. **(A)** shows the frequency of artefact lines B, in **(B)** the frequency of consolidations with static bronchograms and in **(C)** the frequency of consolidations with dynamic bronchograms. Key: Ca, *Callithrix aurita*; Cj, *Callithrix jacchus*; Cp, *Callithrix penicillata*; Csp, *Callithrix* sp.

that it was less frequent in animals in which line B was present (40%) than in those in which line B was absent (19%). On the other hand, there was no significant heterogeneity regarding the incidence of SBC and DBC ($p = 1$) (13).

The ultrasound findings were not influenced by the sex, age or mass of the animals. The frequency of the main findings was not statistically different between the marmoset species.

Three animals that died from bronchopneumonia, marked by necrotic neutrophils in the bronchial and bronchiolar lumen, had dynamic bronchograms and one of them had associated SBC. These sonographic findings were seen in cases of bacterial suppurative origin and also aspiration origin, this may indicate that dynamic bronchograms may be associated with bronchopneumonia, three animals presented the B-line sonographic finding in association with alveolar oedema and congestion, as reported in dogs and humans, three animals presented SBC associated with a congestive process, and one animal presented DBC associated with a congestive process (Supplementary material).

## 4 Discussion

Until now, there had been no research on use of thoracic ultrasound among non-human primates, which was why it was necessary to make correlations with studies conducted on humans and on dogs and cats.

Pulmonary auscultation in *Callithrix* sp. is difficult to perform because of the sounds emitted by these animals when they are not under sedation. However, thoracic ultrasound can be performed on awake animals that are manually restrained and can provide important pulmonary assessment parameters, the animals in this study with pathologies were submitted to treatment and ultrasound monitoring without sedation.

For dogs and cats, ultrasound and radiography have proved to be satisfactory methods for both detecting and classifying alveolar-interstitial syndrome. These two techniques show topographical conformity of the alterations, although radiography enables greater detection of involvement of the caudal windows and ultrasound enables greater detection of involvement of the cranial windows. Patients with alveolar-interstitial syndrome and respiratory distress from various causes were analyzed. The animals with cardiogenic pulmonary edema showed a diffuse pattern, while those with pneumonia showed a unilateral pattern, which may suggest that use of a complementary diagnostic method may be useful (14).

In the present study, only lung ultrasound was used, and the animals assessed as exhibiting evidence of lung pathological conditions showed focal alterations (B-lines in 24% of the animals studied, consolidation with static bronchogram in 11% of the animals studied and consolidation with static bronchogram in 24% of the animals studied). Occurrence of consolidations with static or dynamic bronchograms was associated with the presence of the B-line artefact, which suggests that these ultrasound findings are influenced by a common physiological or anatomical process.

One question that needs to be considered regarding this finding is that the individuals evaluated did not show any clinical respiratory signs.

During the study period, some of the animals with lobar consolidations detected through ultrasound died and were sent for necropsy. The macroscopic and histopathological findings indicated the presence of suppurative pneumonia.

In a study carried out to detect pneumonia in children, the location where consolidations were most frequently found was the lower regions of the chest (15). In dogs with bacterial pneumonia, the window most affected was the right cranial window, but involvement of the right and left middle windows was also observed. The fragment sign (consolidation) was evident in the left middle window, right middle window and right cranial window (16). In the animals sampled in this study, the presence of consolidations was observed predominantly in the caudal windows, as previously observed and reported in humans.

Pinpimai et al. (17), isolated *Klebsiella pneumoniae* through a phylogenetic study on the tissues of four marmosets with no previous clinical symptoms that had been found dead in their enclosure, with foamy content in the oral cavity. At necropsy, multilobe pneumonia was observed, and microscopy showed mild suppurative pneumonia with pulmonary edema, emphysema and extramedullary hematopoiesis. Rod-shaped bacteria were detected inside the alveoli.

In Brazil, *Klebsiella pneumoniae* was found in the tissues of 11 marmosets that had been kept at an institution in the state of São Paulo, and histological findings compatible with hyperacute septicemia were observed. In the lungs, the presence of interstitial pneumonia and hemorrhage was reported, highlighting the importance of surveillance of this pathogen due to its emerging nature and its ability to produce resistance to antibiotics and the possibility of infecting human and non-human reservoirs (18).

In a retrospective study on pneumopathies in 638 marmosets diagnosed through necropsy, only 39 did not show pulmonary alterations. The most prevalent inflammatory lung disease was interstitial pneumonia, observed in 206 marmosets. The presence of bacteria was minimal in marmosets with interstitial pneumonia, and these were isolated by means of culture: *Escherichia coli*, *Streptococcus* spp., *Erysipelothrix rhusiopathiae*, *Klebsiella pneumoniae* and *Pseudomonas aeruginosa*. Other forms of pneumonia were rare and included lobar pneumonia in 9 animals, suppurative bronchopneumonia in 6 animals and broncho interstitial pneumonia in 2 animals. Lobar pneumonia was observed and divided according to the type of exudate (purulent or fibrinopurulent). In eight out of nine cases of lobar pneumonia and in all suppurative bronchopneumonia, the classifications were moderate to severe and acute to subacute. These conditions were the main causes of illness or death in most cases. *Streptococcus* spp., with or without association with *Bordetella bronchiseptica*, was isolated in the individuals affected by suppurative bronchopneumonia. *Bordetella bronchiseptica* was also isolated in one animal with fibrinopurulent pleuropneumonia. *Enterococcus* spp. and *Klebsiella pneumoniae* ssp. were also isolated. Circulatory disorders such as edema, hemorrhage and hyaline membrane formation were reported (19).

In pneumopathies caused by SARS-CoV in marmosets, multifocal to coalescent interstitial pneumonitis was reported, with mild infiltrate with a high number of neutrophils in the inter-alveolar septa 2 days after infection. On the fourth day after infection, the intestinal infiltrate was predominantly mononuclear, with an increase in the number of alveolar macrophages and exudates. On the seventh day after infection, the inflammatory condition improved, but edema was reported, with irregular distribution (20). Thoracic radiographic monitoring in ventro-dorsal and latero-lateral projections of nine male marmosets infected with the MERS-CoV virus revealed diffuse interstitial infiltration ranging from mild to severe, with greater involvement of the caudal lobes (21).

In a retrospective study on free-ranging *Callithrix* individuals that died due to *Toxoplasma gondii*, histopathological analysis revealed pneumonia with many intra-alveolar foamy macrophages and fibrin deposition. The pneumonia was interstitial and bronchointerstitial, mild to moderate, with or without multifocal areas of necrosis, and with edema and mild to severe alveolar hemorrhage (22). In the present study, the lungs were found to have an intense infiltrate of necrotic neutrophils in the bronchiolar and bronchial lumens, interspersed between bacterial clusters (rods and cocci). Edema, congestion and thickening of the interalveolar septa were also observed, but it was not possible to isolate the agent. In the present study, the animals submitted to post-mortem histopathological analysis with results compatible with pulmonary oedema associated or not with congestion on thoracic ultrasound showed line B, one animal had an associated B-line and static bronchogram. Meanwhile, animals with post-mortem histopathological analysis compatible with suppurative bronchopneumonia and aspiration bronchopneumonia showed associations of dynamic and static bronchograms on ultrasound evaluation.

Among the individuals that presented alterations on examination, 50 had been kept at an institution in the state of São Paulo at which a fire occurred 2 years before the start of the research of the present study (47 out of these 50 were present at the time of the fire), which may have influenced the findings of the examinations. This was the first study using ultrasound to detect pulmonary pathological conditions in non-human primates. Further research is therefore necessary to determine the frequency of lesions and their most likely topographical locations.

Throughout the study, 41 individuals died, of which 19 had pulmonary alterations. These individuals were sent for necropsy and histopathological analysis, which showed that 10 had alterations in the lung tissue, including suppurative pneumonia and pulmonary congestion, which in some cases was associated with oedema. In the sample, 8 individuals showed alterations suggestive of congestion and pulmonary oedema and on ultrasound the B-line artefact was observed in 6 of these individuals, which corroborates findings already reported in humans and domestic animals.

Regarding the 9 animals that showed no alterations on histopathological examination, one hypothesis is that they died between 6 and 18 months after the date of the ultrasound assessment and as there was no serial monitoring, there is no way of determining their evolution. Further research is needed involving other imaging techniques such as radiography and computed tomography, in order to assess the sensitivity and specificity of these different techniques for these species.

Lung ultrasound combined with chest radiography has proved to be a sensitive method for diagnosing small lobar consolidations and for the early detection of pleural effusion, although, some practical limitations in using ultrasound techniques have been reported in their use among humans, including the impossibility of assessing the retro-scapular region, difficulty relating to overlapping structures, need for an experienced operator (23). And the presence of subcutaneous emphysema and dressings, which can compromise the quality of the examination (24).

In neotropical primates, the retro-scapular region has been assessed without difficulty due to the anatomy of these species. However, the operator's level of experience is fundamental for identifying image alterations, and care must be taken not to confuse the liver parenchyma and presence of gastric contents with alterations in the dorso-caudal pulmonary windows.

## 5 Conclusion

Thoracic ultrasound is a useful tool in the clinical routine for assessing wild animals. It has good applicability due to its low cost, quick execution time and non-invasive nature. It has shown good sensitivity for diagnosing pathological lung conditions. The pulmonary patterns observed are similar to those found in human medicine, in terms of the appearance and localization of the alterations. In this study, it was possible to correlate the frequency of pulmonary consolidations identified through thoracic ultrasound and histopathological findings with occurrences of pneumonia, and to correlate the presence of the B-line artefact, with or without association with pulmonary consolidation, with congestion, which may or may not be associated with oedema in *Callithrix* sp.

## Data availability statement

The original contributions presented in the study are included in the article/Supplementary material, further inquiries can be directed to the corresponding author.

## Ethics statement

The animal study was approved by Ethics Committee for the Use of Animals (CEUA) at the University of Santo Amaro, Brazil, and the project was filed under the number 57/2021. The project was also authorized by SISBIO (Authorization for Activities for Scientific Purposes of the Brazilian Ministry of the Environment) under the number 78874-1. The study was conducted in accordance with the local legislation and institutional requirements.

## Author contributions

JM: Methodology, Writing – original draft, Writing – review & editing. MS: Writing – original draft, Writing – review & editing. SM: Methodology, Writing – review & editing. LC: Methodology, Writing – review & editing. CP: Supervision, Writing – review & editing.

## Funding

The author(s) declare that financial support was received for the research, authorship, and/or publication of this article.

## Acknowledgments

We would like to thank the *Coordenação de Aperfeiçoamento de Pessoal de Nível Superior* (CAPES)—Programa de Suporte à Pós-Graduação de Instituições de Ensino Particulares (PROSUP)—Brazil for financial support. All the team members from Project Mucky, Itu—São Paulo—Brazil, for allowing us to assess your precious non-human primates. We would like to express our very great appreciation to L&M Veterinarian.

## Conflict of interest

The authors declare that the research was conducted in the absence of any commercial or financial relationships that could be construed as a potential conflict of interest.

## Publisher's note

All claims expressed in this article are solely those of the authors and do not necessarily represent those of their affiliated organizations, or those of the publisher, the editors and the reviewers. Any product that may be evaluated in this article, or claim that may be made by its manufacturer, is not guaranteed or endorsed by the publisher.

## Supplementary material

The Supplementary material for this article can be found online at: https://www.frontiersin.org/articles/10.3389/fvets.2024.1450104/full#supplementary-material

## References

1. Mojoli F, Bouhemad B, Mongodi S, Lichtenstein D. Lung ultrasound for critically ill patients. *Am J Resp Crit Care Med*. (2019) 199:701–14. doi: 10.1164/rccm.201802-0236CI

2. Valle RR, Ruiz-Miranda CR, Pereira DG, Rímoli J, Bicca-Marques JC, Jerusalinsky L, et al. (2021). *Callithrix penicillata* (amended version of 2018 assessment). Available at: https://dx.doi.org/10.2305/IUCN.UK.2021-1.RLTS.T41519A191705321.en. (Accessed on September 27, 2021)

3. Soldati G, Smargiassi A, Inchingolo R, Sher S, Nenna R, Valente S, et al. Lung ultrasonography may provide an indirect estimation of lung porosity and airspace geometry. *Respiration*. (2014) 88:458–68. doi: 10.1159/000368086

4. Scarpelli EM. The alveolar surface network: a new anatomy and its physiological significance. *Anat Rec*. (1998) 251:491–527. doi: 10.1002/(SICI)1097-0185(199808)251:4<491::AID-AR8>3.0.CO;2-V

5. Lichtenstein D, Mezière G, Biderman P, Gepner A, Barré O. The comet-tail artifact. *Am J Resp Crit Care Med*. (1997) 156:1640–6. doi: 10.1164/ajrccm.156.5.96-07096

6. Lichtenstein D, Mezière G, Seitz J. The dynamic air bronchogram. *Chest*. (2009) 135:1421–5. doi: 10.1378/chest.08-2281

7. Inchingolo R, Copetti R, Smargiassi A, Gerardi RE, Conte EG, Corbo GM, et al. Air bronchogram integrated lung ultrasound score to monitor community-acquired pneumonia in a pilot pediatric population. *J Ultrasound*. (2021) 24:191–200. doi: 10.1007/s40477-020-00547-7

8. Soldati G. Sonographic findings in pulmonary diseases. *Radiol Med*. (2006) 111:507–15. doi: 10.1007/s11547-006-0046-z

9. Staub LJ, Biscaro RRM, Maurici R. Accuracy and applications of lung ultrasound to diagnose ventilator-associated pneumonia: a systematic review. *J Intensive Care Med*. (2017) 33:447–55. doi: 10.1177/0885066617737756

10. Lin CH, Lo PY, Lam MC, Wu HD. Usefulness of chest ultrasonography in predicting diagnosis in non-emergency small animal patients with lung parenchymal and pleural disease. *Front Vet Sci*. (2020) 7:16882. doi: 10.3389/fvets.2020.616882

11. Mongodi S, Via G, Girard M, Rouquette I, Misset B, Braschi A, et al. Lung ultrasound for early diagnosis of ventilator-associated pneumonia. *Chest*. (2016) 149:969–80. doi: 10.1016/j.chest.2015.12.012

12. Carpenter JW, Marion C. Exotic animal formulary. *5th* ed. Amsterdam: Elsevier (2017). 776 p.

13. GitHub. (2020). GitHub—atahk/pscl: political science computational laboratory. Available at: https://github.com/atahk/pscl. (Accessed June 15, 2024)

14. Ward JL, Lisciandro GR, DeFrancesco TC. Distribution of alveolar-interstitial syndrome in dogs and cats with respiratory distress as assessed by lung ultrasound versus thoracic radiographs. *J Vet Emerg Crit Care*. (2018) 28:415–28. doi: 10.1111/vec.12750

15. Milliner BHA, Tsung JW. Lung consolidation locations for optimal lung ultrasound scanning in diagnosing pediatric pneumonia. *J Ultrasound Med*. (2017) 36:2325–8. doi: 10.1002/jum.14272

16. Ward JL, Lisciandro GR, Ware WA, Miles KG, Viall AK, DeFrancesco TC. Lung ultrasonography findings in dogs with various underlying causes of cough. *J Am Vet Med Assoc*. (2019) 255:574–83. doi: 10.2460/javma.255.5.574

17. Pinpimai K, Banlunara W, Roe WD, Dittmer K, Biggs PJ, Tantilertcharoen R, et al. Genetic characterization of hypervirulent *Klebsiella pneumoniae* responsible for acute death in captive marmosets. *Front Vet Sci*. (2022) 9:940912. doi: 10.3389/fvets.2022.940912

18. Guerra JM, NCCA F, Morales Dos Santos AL, JSP B, BSS P, Milanelo L, et al. Hypervirulent *Klebsiella pneumoniae* as unexpected cause of fatal outbreak in captive marmosets, Brazil. *Emerg Infect Dis*. (2020) 26:3039–43. doi: 10.3201/eid2612.191562

19. Bleyer M, Kunze M, Gruber-Dujardin E, Mätz-Rensing K. Spontaneous lung pathology in a captive common marmoset colony (*Callithrix jacchus*). *Primate Biol*. (2017) 4:17–25. doi: 10.5194/pb-4-17-2017

20. Greenough TC, Carville A, Coderre J, Somasundaran M, Sullivan JL, Luzuriaga K, et al. Pneumonitis and multi-organ system disease in common marmosets (*Callithrix jacchus*) infected with the severe acute respiratory syndrome-associated coronavirus. *Am J Pathol*. (2005) 167:455–63. doi: 10.1016/S0002-9440(10)62989-6

21. Falzarano D, de Wit E, Feldmann F, Rasmussen AL, Okumura A, Peng X, et al. Infection with MERS-CoV causes lethal pneumonia in the common marmoset. *PLoS Pathog*. (2014) 10:e1004250. doi: 10.1371/journal.ppat.1004250

22. Rodrigues A, Ritter JM, Santos D, Pizzolato F, Aquino S, Parente T, et al. Pathology and epidemiology of fatal toxoplasmosis in free-ranging marmosets (*Callithrix* spp.) from the Brazilian atlantic forest. *PLoS Negl Trop Dis*. (2022) 16:e0010782. doi: 10.1371/journal.pntd.0010782

23. Ianniello S, Piccolo CL, Buquicchio GL, Trinci M, Miele V. First-line diagnosis of paediatric pneumonia in emergency: lung ultrasound (LUS) in addition to chest-X-ray (CXR) and its role in follow-up. *Br J Radiol*. (2016) 89:20150998. doi: 10.1259/bjr.20150998

24. Lichtenstein DA. Lung ultrasound in the critically ill. *Ann Intensive Care*. (2014) 4:1. doi: 10.1186/2110-5820-4-1

frontiers | Frontiers in Veterinary Science

TYPE Original Research
PUBLISHED 22 January 2025
DOI 10.3389/fvets.2025.1518713



OPEN ACCESS

EDITED BY
Hussein M. El-Husseiny,
Tokyo University of Agriculture and Technology, Japan

REVIEWED BY
Howard Dobson,
Invicro, United States
Adeline Decambron,
Hopia Veterinary Clinic, France

*CORRESPONDENCE
Diego Pulido Vega
✉ diego.pulido-vega@vet-alfort.fr

RECEIVED 28 October 2024
ACCEPTED 08 January 2025
PUBLISHED 22 January 2025

CITATION
Pulido Vega D, Ficheroulle J, Manassero M, Mortier J and Maurey C (2025) Association of preoperative ultrasonographic parameters of the contralateral kidney with long-term serum creatinine in cats treated for unilateral ureteral obstruction.
*Front. Vet. Sci.* 12:1518713.
doi: 10.3389/fvets.2025.1518713



# Association of preoperative ultrasonographic parameters of the contralateral kidney with long-term serum creatinine in cats treated for unilateral ureteral obstruction

Diego Pulido Vega[1]*, Jérémie Ficheroulle[1,2], Mathieu Manassero[3], Jeremy Mortier[1] and Christelle Maurey[4]

[1]Service of Diagnostic Imaging, DEPEC, École Nationale Vétérinaire d'Alfort, Maisons-Alfort, France, [2]Teaching and Clinical Department of Companion Animal, Faculty of Veterinary Medicine, Fundamental and Applied Research for Animals and Health, University of Liège, Liège, Belgium, [3]Service of Small Animal Surgery, École Nationale Vétérinaire d'Alfort, Maisons-Alfort, France, [4]Laboratoire de Santé Animale, Service of Internal Medicine, École Nationale Vétérinaire d'Alfort, INRAE, ANSES, UMR Virology, Maisons-Alfort, France

**Introduction:** Prediction of renal recovery after surgical management of feline unilateral ureteral obstruction (UO) is crucial to guide therapeutic decisions, but predictors of this outcome are still lacking. Despite the functional importance of the contralateral kidney, there is currently no precise description of its ultrasonographic (US) features. In addition, US parameters of both the renal collecting system and the renal parenchyma have been identified in human medicine as prognostic factors in the case of UO but have not been described in veterinary medicine. The aim of this study was to evaluate an association between preoperative structural US renal parameters and long-term International Renal Interest Society (IRIS) stage after successful renal decompression with subcutaneous ureteral bypass (SUB) device in cats with unilateral UO.

**Methods:** This retrospective study included 60 cats with unilateral UO and evaluated preoperative US parameters of both kidneys, including measurements of parenchymal and pelvic areas as well as a renal score. Cats were divided according to their serum creatinine at 3 months postoperatively into group A (IRIS stages I and II) and group B (IRIS stages III and IV).

**Results:** A higher US chronic kidney disease (US-CKD) score of the kidney contralateral to the UO was associated with long-term IRIS stages III and IV. It also appeared as a fair discriminator of long-term IRIS stage IV, with an area under the curve of 0.74. The optimal cutoff value for accurately identifying cats with long-term IRIS stage IV was a US-CKD score > 7, with a specificity of 98%, a sensitivity of 25%, and a positive likelihood ratio of 12.75. No preoperative US parameters regarding the obstructed kidney, including parenchymal and pelvic areas, were significantly associated with long-term creatinine.

**Conclusion:** Ultrasonographic scoring of contralateral chronic kidney disease abnormalities is associated with IRIS stage following treatment of feline unilateral UO with a SUB device and serves as a specific indicator of cats presenting with long-term IRIS stage IV.

KEYWORDS

**sub, ureterolithiasis, ureteral calculi, kidney, ureter**

## 1 Introduction

Ureteral obstruction (UO) is a common cause of acute azotemia in cats, frequently occurring concurrently with chronic kidney disease (CKD) (1–3). Its most common etiology is ureterolithiasis, which is predominantly composed of calcium oxalate (4–11). Treatment of UO is challenging, and a subcutaneous ureteral bypass (SUB) device placement is considered an effective therapeutic strategy, with a low postoperative death rate and an excellent outcome (3, 12). However, this technique comes with high costs for the owners, a demanding follow-up, and a significant rate of long-term complications. In addition, postoperative renal function often remains impaired after the acute episode, reflecting not only the effects of concurrent CKD but also the sequelae of UO, with half of cats having a serum creatinine (SCr) greater than 3.2 mg/dL 6 months after surgery (3, 12–14).

In this context, the identification of prognostic factors is crucial to assist clinicians and pet owners in the surgical decision-making process. In two previous studies (9, 15), no preoperative clinical, biochemical, or ultrasonographic (US) finding was found predictive of long-term renal recovery, although the focus was on the imaging characteristics of the obstructed kidney alone. The McEntee et al. study (15) introduced a ratio of pelvic dilation to overall renal size which was not predictive of long-term SCr. Similar parameters assessing areas, rather than lengths, of both the renal parenchyma and the pelvic dilation have been described in human medicine. For instance, the parenchyma-to-hydronephrosis area ratio (PHAR) has proved to be predictive of renal function recovery after surgery in the context of ureteropelvic junction obstruction (16, 17), but it has not been studied in the context of UO in veterinary medicine.

To the best of the author's knowledge, the US description of feline unilateral UO only focuses on the obstructed kidney, with no mention other than the size of the contralateral kidney (15, 18–22). Given that azotemia remains undetected until 75% of the renal function has been lost (23), unilateral UO does not result in azotemia if the contralateral kidney is functioning well. However, in cats, UO occurs in the course of a CKD, possibly fostered through repeated asymptomatic ureteral obstructive episodes (5), contributing to pre-existing renal damage within the contralateral kidney and explaining why UO becomes clinically relevant (24). This pathophysiological sequence underlines the need for a careful assessment of the contralateral kidney.

The aims of this study were (1) to assess the replicability of the research of McEntee et al. (15) performed on the obstructed kidney with a focus on additional novel US parameters and (2) to extend their work by evaluating ultrasonographically the contralateral kidney with the hypothesis that some parameters would show an association with the long-term renal recovery after pelvic decompression with a SUB device.

## 2 Materials and methods

### 2.1 Selection of cases

Medical and US records of all cats treated with a SUB device (Norfolk Vet Products) between December 2013 and January 2021 at the National Veterinary School of Alfort were retrospectively reviewed. Cats were included in the study if they presented a benign unilateral UO, renal preoperative US images and were followed for at least 3 months postoperatively with ultrasonographic evidence of renal pelvic decompression and patency of the device. Cats that died from renal causes during the 3-month follow-up were also included. Ureteral obstruction was diagnosed based on clinical signs, the presence of azotemia, and US findings such as pelvic dilation, diverticular dilation, ureteral dilation, intraluminal obstructive lesion, or some combination of these. Cats were treated in accordance with the standard surgical and perioperative management protocols, as previously described (3). Long-term follow-up was determined as the first follow-up occurring more than 3 months postoperatively. Additional data were collected and reviewed on a case-by-case basis, by a board-certified veterinary specialist in internal medicine (CM), to identify cats presenting with an acute or chronic kidney disease at the time of the long-term follow-up. This was based on a combination of criteria such as an increase in SCr higher than 20% above the last SCr measurement, acute onset of clinical signs (e.g., anorexia, lethargy, and vomiting), US images at the time of long-term follow-up compared with previous examinations, urine culture, and serum amyloid A protein (SAA) when available. For these cats, the long-term follow-up date was determined as the first follow-up in which the acute or chronic kidney event was resolved. Cats with bilateral UO, ureteral rupture, and UO of neoplastic origin, cats treated as part of a second surgery for UO, with incomplete medical records, lost to follow-up, or deceased from unknown or non-renal cause before long-term follow-up were excluded.

### 2.2 Clinical and biological data

Preoperative standardized clinical data were gathered from all cats including age, sex, breed, weight, nature, and duration of clinical signs. Blood samples and chemistry were collected. During surgery, pelvic urine from the obstructed kidney was collected for bacterial culture. Postoperative data included SCr follow-up for at least 3 months.

### 2.3 Ultrasonographic findings

The US examinations were performed using different ultrasound machines over the study time (IU22, Philips; Affinity 50, Philips) and by various experienced ultrasonographers. A multifrequency (5–8 MHz) microconvex or a multifrequency (5–18 MHz) linear transducer was used for ultrasound examination. Preoperative abdominal US still images were blindly reviewed by a veterinary radiology resident (JF). Measurements were performed for each kidney using the National Institutes of Health image software (Image J 1.53 k). Renal length was determined as the maximum longitudinal dimension in a sagittal plane. Pelvic diameter was measured in sagittal and transverse planes from one pelvic margin to another (Figure 1). Renal parenchymal thickness was defined as the distance between the renal sinus fat to the renal capsule in a sagittal plane. Renal cortical thickness was determined in a sagittal plane as the distance from the corticomedullary interface to the renal capsule. Cranial ureteral diameter was measured just caudally to the ureteropelvic junction, in the transverse plane. Ureteral diameter upstream of the obstruction site was measured in the sagittal plane, if an obstruction site was identified (Figure 2). The total renal area and pelvic area were determined by outlining the kidney and the pelvis on a sagittal plane as previously described (Figure 3) (25–28). The renal parenchymal area (RPA) was calculated by subtracting the pelvic area from the total renal area. Total RPA was defined as the sum of the RPA of both kidneys. Parenchyma-to-hydronephrosis area ratio (PHAR) was calculated by dividing the RPA by the pelvic area, only for obstructed kidneys.

To grade the severity of the CKD on US images, we proposed a US-CKD score. This score allowed a semi-quantitative US description of the kidneys based on the presence of findings reportedly associated with CKD including corticomedullary differentiation attenuation, medullary rim sign, irregular renal margination, renal infarcts, and renal cysts (29–32). A sub-score was assigned to each US finding according to their presence or severity as described in Table 1. The ultrasonographic CKD score was defined as the sum of each sub-score for one kidney (ranging from 0 to 8), and the total US-CKD score was defined as the sum of the US-CKD score of both kidneys.

## 2.4 Groups

Cats were divided into two groups based on their long-term renal recovery. Group A included cats with SCr ⩽ 2.8 mg/dL, corresponding to stages I and II of the International Renal Interest Society (IRIS) classification (33). Group B included cats with SCr > 2.8 mg/dL and cats that died from renal causes during the 3-month follow-up period. The SCr cutoff was based on survival analysis of existing data: Median survival time was superior to 2,250 days in stage IRIS stages I and II cats, while it was 608 and 67 days in IRIS stages III and IV cats, respectively, based on their SCr measured 3 months postoperatively in one study (3).

## 2.5 Data analysis and statistics

Statistical analysis was performed using a statistical package (BiostaTGV, Pierre Louis Institute of Epidemiology and Public Health UMR S 1136). Quantitative descriptive results are presented as medians with ranges. Dichotomous variables are presented as percentages and associated with the number of cases included. Association between US features and groups was assessed using the Mann–Whitney U-test for continuous data and either the $\chi^2$ test or Fisher's exact test for categorical data. The Wilcoxon signed-rank test was used for comparison between the change in SCr between the preoperative period and long-term follow-up. Receiver operating characteristic (ROC) curves were used to assess the diagnostic utility of quantitative US parameters that differed significantly between groups. The generalized Youden index was used to identify optimal cutoff values. An AUC of >0.9 was interpreted as excellent, 0.8 to 0.89 as good, 0.7 to 0.79 as fair, 0.6 to 0.69 as poor, and 0.5 to 0.59 as failure (34), and values are accompanied by their respective 95% confidence intervals (CIs). The level of statistical significance selected was set at a $p$-value of <0.05.

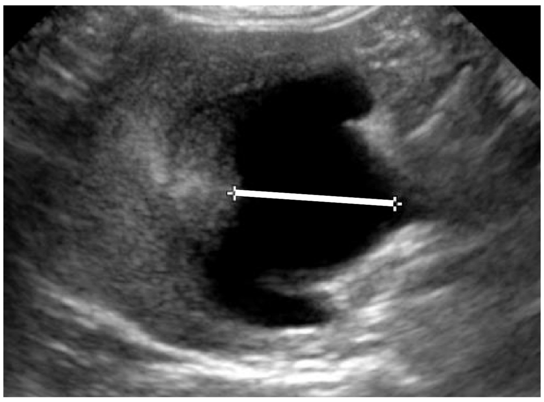

FIGURE 1
Ultrasonographic image of an obstructed kidney, in a transverse plane. The white line indicates the pelvic dilatation, spanning from one edge of the pelvis to the other, with a width of 7 mm.

# 3 Results

## 3.1 Study population

Ninety-eight cats were treated with an SUB device between December 2013 and January 2021 and recruited for the study. Thirty-eight cats were excluded as follows: 25 due to admission criteria and 13 due to follow-up criteria (see Supplementary Figure S1). Fifteen cats presented a bilateral UO, six cats presented a ureteral rupture, and four cats were treated as part of a second surgery on UO. During the follow-up period, one cat presented a contralateral UO, two cats presented an obstruction of the SUB device, and four cats were lost to follow-up. One cat was excluded because of truncated US images. Three cats died of unknown reasons after discharge, and two cats died from non-renal causes: One presented with respiratory distress and signs of congestive heart failure, and the second presented a resolution of azotemia after treatment but died after a blood transfusion. The remaining 60 cats were included in the study, of which four cats died or were euthanized due to persistent marked azotemia and did not survive discharge (range 2–8 days postoperatively). These cats were part of group B, along with cats presenting a long-term SCr > 2.8 mg/dL.

## 3.2 Clinical data

Descriptive statistics on the study population are summarized in Table 2. Of the 60 cats, 38 (63%) were females and 22/60 (37%) were males, of which 31/38 (82%) and 19/22 (86%) were neutered. The median age at presentation was 6.1 years (range 1.5–15.7 years). On admission, median packed cell volume (PCV) was 30% (range 17–45%), and median SCr was 5.9 mg/dL (range 1.4–18.1) with 59/60 (98%) cats being azotemic. Other biochemical abnormalities included anemia (42%, $n = 25/59$), hyperphosphatemia (36%, $n = 9/25$), hyperkalemia (20%, $n = 12/59$), and ionized hypercalcemia (10%, $n = 5/50$). Urine culture obtained by pyelocentesis at the time of SUB placement was positive in 11/59 (18.6%) cats. The median long-term follow-up was 4 months (range 3–8 months). The median long-term SCr was 2.3 mg/dL (range 1.2–5.4 mg/dL), which was significantly lower than preoperative values ($p < 0.001$) and associated with a median decrease in SCr of 3 mg/dL (range 0.1–16.4 mg/dL). Among the 60 cats included, 43 (72%) presented a long-term SCr ⩽ 2.8 mg/dL and were part of group A. The remaining 17 cats (28%) were part

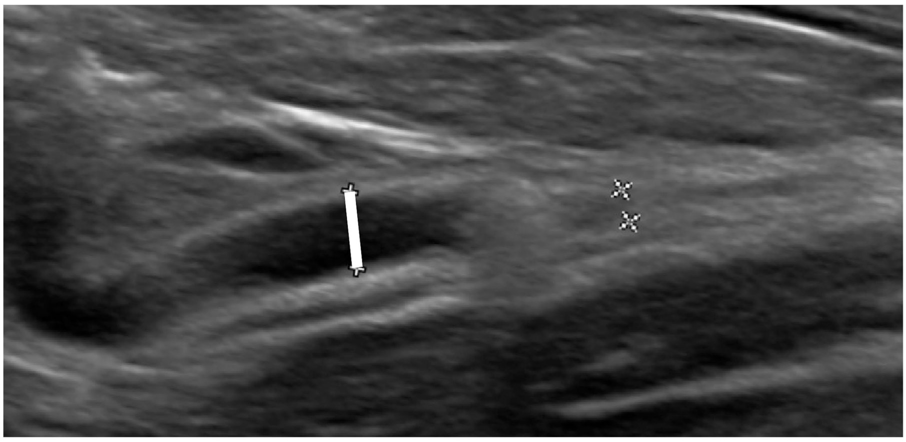

FIGURE 2
Ultrasonographic image of a ureter with intraluminal calculi. The ureter is dilated upstream of the calculi, and its diameter is indicated with the white line (measuring 2.3 mm), with no downstream dilation.

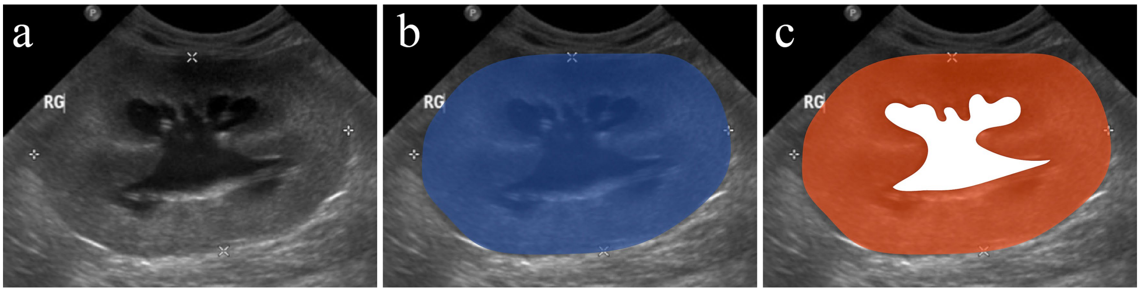


FIGURE 3
Parenchyma-to-hydronephrosis area ratio (PHAR) measurement on an ultrasonographic image of a kidney with hydronephrosis. Sagittal image of a hydronephrotic kidney **(A)**. The blue area **(B)** corresponds to the total renal area. The white area **(C)** corresponds to the pelvic area. The renal parenchymal area (RPA) was calculated by subtracting the pelvic area from the total renal area and corresponds to the orange area **(C)**. The PHAR was calculated by dividing the RPA by the pelvic area.

of group B and included 12 cats with long-term SCr > 2.8 mg/dL and 5 cats that died of renal causes, as described above. Eleven cats presented bacteriuria on urine collected from the SUB device at the time of long-term follow-up. Of these cats, one presented an acute or chronic kidney disease suspected to be pyelonephritis, based on the elevation of SCr, bacteriuria, evocative US findings, and increased SAA. In this case, the long-term follow-up date was set 1.5 months later, when the acute or chronic kidney event had resolved (SCr = 2.5 mg/dL and normalization of SAA). The remaining cats were asymptomatic, and none were suspected of presenting an acute kidney injury at this time based on clinical signs, biological data, and evaluation of serial postoperative SCr values at follow-up. Female cats were significantly more frequent in group A than in group B (72% vs. 41%; $p = 0.03$). The remaining clinical data were not significantly different between groups (Supplementary Table S1).

## 3.3 Ultrasonographic findings

Preoperative US data are summarized in Tables 3, 4. Thirty-five cats were obstructed on the right side (58%) and 25 on the left side (42%). Obstructed kidneys had a median length of 4.4 cm (range 2.3–6 cm) and presented a median pelvic diameter in the transverse plane of 7.2 mm (range 1.4–20.1 mm). Ipsilateral nephroliths were identified in 35 (58%) cats. Peri-renal effusion, peri-renal fat hyperechogenicity, attenuation of the corticomedullary distinction, and renal infarcts were identified in 10 (17%), 14 (23%), 40 (67%), and 32 (53%) cats, respectively. The median US-CKD score was 3 (range 0–7). Median cranial ureteral diameter and upstream obstruction site were 4.8 mm (range 1.5–14 mm) and 3 mm (range 1.6–19.3 mm), respectively. The contralateral kidney had a median length of 3.1 cm (range 1.2–4.9 cm). The most frequent structural abnormalities of this kidney were attenuation of the corticomedullary distinction, renal infarcts, moderately to markedly irregular margination, and pelvic mineralization in 53 (90%), 49 (83%), 44 (75%), and 40 (68%) cats, respectively. The median US-CKD score was 5 (range 0–8) which was significantly higher than in the obstructed kidney ($p < 0.01$; $n = 59$). Nephroliths were identified in 40 (68%) contralateral kidneys.

The median US-CKD score of the contralateral kidney was significantly higher in group B (median, 5 in group A; median, 6 in group B; $p = 0.01$). Through ROC curve analysis, the US-CKD score of the contralateral kidney was a fair discriminator between groups A

10.3389/fvets.2025.1518713

and B (AUC = 0.71, $p < 0.01$, 95% CI: 0.57–0.85). The optimal cutoff to correctly identify group B was a US-CKD score > 6 (specificity: 90.5%; sensitivity: 29.4%) and was associated with a likelihood ratio of 3.1 (95% CI: 0.94–4.94). Higher US-CKD score of the contralateral kidney was also significantly associated with cats presenting long-term CKD IRIS stage IV disease (median, 5 in IRIS stages I–III; median, 6 in stage IV; $p = 0.028$). The US-CKD score of the contralateral kidney was still a fair discriminator to distinguish cats presenting long-term CKD IRIS stage IV disease from others (AUC = 0.74; $p = 0.02$, 95% CI: 0.54–0.94). The optimal cutoff to correctly identify cats presenting long-term CKD IRIS stage IV disease was a US-CKD score > 7 (specificity: 98%; sensitivity: 25%) and was associated with a likelihood ratio of 12.75 (95% CI: 1.30–124.88). US-CKD score of the obstructed kidney was not significantly different among groups (median, 3 in each group; $p = 0.56$). Median total US-CKD score was higher in group B than in group A, but no statistical significance was reached (median, 8 in group A; median, 9 in group B; $p = 0.08$). No other preoperative US parameter, including RPA and PHAR, was significantly associated with long-term SCr (Table 5; Supplementary Table S2).

TABLE 1 Ultrasonographic characteristics assessed to calculate the ultrasonographic chronic kidney disease score (US-CKD score).

| Parameter | Sub-score | |
|---|---|---|
| Corticomedullary differentiation | 0 | Good |
| | 1 | Poor |
| | 2 | Absent |
| Medullary rim sign | 0 | Absent or ⩽ 2 mm |
| | 1 | Present and > 2 mm |
| Irregular renal margination | 0 | Absent |
| | 1 | Mild |
| | 2 | Moderate |
| | 3 | Marked |
| Renal infarcts | 0 | Absent |
| | 1 | Present |
| Renal cysts | 0 | Absent |
| | 1 | Present |

## 4 Discussion

This retrospective study is the first to focus on the preoperative US appearance of the contralateral kidney to predict renal function recovery after surgical treatment of feline unilateral ureteral obstruction. A higher US-CKD score of the contralateral kidney was significantly associated with a poor outcome (SCr > 2.8 mg/dL) at 3 months postoperatively. A cutoff score of >6 discriminated these cats with a specificity of 90.5% and a sensitivity of 29.4%. These results suggest that the potential for renal recovery after unilateral SUB device placement should be discussed with owners in light of the US aspect of the contralateral kidney.

Despite its importance, the ultrasonographic description of the kidney contralateral to unilateral UO is scarce (15, 18–21) and limited to its size, reported as a mean of 6 mm smaller than the obstructed kidney (22). This phenomenon is referred to as "big kidney, little kidney" and results from repeated subclinical obstructive episodes leading to nephron loss and fibrosis (5, 19). To further characterize the contralateral kidney and to grade the US abnormalities associated with CKD, a US-CKD score was proposed. This score is based on the semi-quantitative evaluation of US structural indicators that are reportedly associated with CKD (28–32). In the present study, a higher preoperative contralateral US-CKD score was associated with long-term IRIS stages III and IV (group B). This is likely to have clinical implications as the latter are associated with median survival times of 608 days and 67 days, respectively, compared to more than 2,250 days in stage IRIS stages I and II, based on SCr measured 3 months postoperatively in one study (3). However, there is still a significant difference in median survival time within cats in group B. Therefore, we decided to identify a specific cutoff value to discriminate cats with long-term IRIS stage IV from others, and the value of US-CKD >7 showed a specificity of 98% and a sensitivity of 25%. This cutoff was also associated with an excellent likelihood ratio of 12.75 (95% CI: 1.30–124.88). Assuming that the pre-test probability of reaching IRIS stage IV in the long-term is similar to its prevalence in our study population (15%), this means that identifying preoperatively a US-CKD >7 in the contralateral kidney would substantially raise its post-test probability from 15 to 69% (35). It should be noted that this cutoff value is not sensitive and is primarily intended to

TABLE 2 Descriptive statistics in cats with unilateral ureteral obstruction treated with a SUB device.

| | Median | Inter-quartile range | Number of cats | Reference interval |
|---|---|---|---|---|
| Age (years) | 6.1 | 4.5–8 | 60 | |
| Weight (kg) | 3.6 | 3.3–4.4 | 60 | |
| Duration of clinical signs (days) | 10 | 7–23 | 53 | |
| Total follow-up duration after surgery (years) | 1.4 | 0.7–2.6 | 60 | |
| Preoperative PCV (%) | 30 | 25.5–32.2 | 59 | 29–48 |
| Preoperative creatinine (mg/dL) | 5.9 | 3.4–9.1 | 60 | 0.52–1.78 |
| Preoperative phosphorus (mmol/L) | 69 | 55–97 | 25 | 32–78 |
| Preoperative ionized calcium (mmol/L) | 1.27 | 1.20–1.33 | 50 | 1.10–1.40 |
| Preoperative potassium (mmol/L) | 4.6 | 4.0–5.4 | 59 | 3.6–5.5 |
| Long-term creatinine (mg/dL) | 2.3 | 1.8–2.7 | 56 | 0.52–1.78 |
| Long-term follow-up duration (months) | 4 | 3–5 | 56 | |

SUB = subcutaneous ureteral bypass; PCV = packed cell volume.

10.3389/fvets.2025.1518713

TABLE 3 Ultrasonographic parameters of the obstructed kidney in cats with unilateral ureteral obstruction.

| | Median | Inter-quartile range | Number of cats |
|---|---|---|---|
| Renal length (cm) | 4.4 | 3.9–4.6 | 60 |
| Pelvic diameter in transverse plane (mm) | 7.2 | 4.9–9.8 | 59 |
| Pelvic diameter in sagittal plane (mm) | 10.1 | 8.7–12.6 | 58 |
| Renal cortical thickness (mm) | 4.2 | 3.6–5 | 49 |
| Renal parenchymal thickness (mm) | 8.3 | 7–10.2 | 60 |
| Cranial ureteral diameter (mm) | 4.8 | 3.4–6.4 | 59 |
| Ureteral diameter upstream obstruction site (mm) | 3 | 2.2–3.6 | 52 |
| RPA ($cm^2$) | 7.66 | 4.74–8.99 | 60 |
| PHAR ($cm^2$) | 3.65 | 1.9–5.59 | 58 |
| US-CKD score | 3 | 2–5 | 60 |

RPA = renal parenchymal area; PHAR: parenchyma-to-hydronephrosis area ratio; US-CKD = ultrasonographic chronic kidney disease.

TABLE 4 Ultrasonographic parameters of the kidney contralateral to the ureteral obstruction in cats with unilateral ureteral obstruction.

| | Median | Inter-quartile range | Number of cats |
|---|---|---|---|
| Renal length (cm) | 3.1 | 2.5–3.6 | 59 |
| Renal cortical thickness (mm) | 3.4 | 2.9–4.1 | 46 |
| Renal parenchymal thickness (mm) | 7.4 | 5.7–8.8 | 58 |
| RPA ($cm^2$) | 4.73 | 3.29–6.13 | 59 |
| US-CKD score | 5 | 4–6 | 59 |

RPA = renal parenchymal area; US-CKD = ultrasonographic chronic kidney disease.

TABLE 5 Evaluation of the association between long-term serum creatinine and ultrasonographic parameters of the kidney contralateral to ureteral obstruction in included cats.

| | Group A | Group B | *P*-value |
|---|---|---|---|
| Total renal area ($cm^2$) | 5 [3.8–6.7] | 3.9 [3.3–6.7] | 0.31 |
| Renal parenchymal area: RPA ($cm^2$) | 5.0 [3.6–6.1] | 3.7 [3.3–5.2] | 0.17 |
| Renal length (cm) | 3.2 [2.5–3.6] | 2.8 [2.5–3.6] | 0.75 |
| Renal cortical thickness (mm) | 3.4 [2.9–4.2] | 3.4 [3.1–3.7] | 0.81 |
| Renal parenchymal thickness (mm) | 7.8 [5.8–8.9] | 6.7 [4.7–7.7] | 0.05 |
| US-CKD score | 5 [3–6] | 6 [5–7] | 0.01 |

Values are medians, and values in brackets represent the interquartile range. US-CKD = ultrasonographic chronic kidney disease.

identify cats that are at a high risk of poor renal recovery following surgery. Further research is required to validate prospectively the use of the US-CKD score in alternative contexts and more specifically to correlate its value with basal SCr values. Among other US parameters studied, the median parenchymal thickness of the contralateral kidney was lower in cats of group B (7.8 mm in group A; 6.7 mm in group B) even though this parameter did not reach statistical significance ($p = 0.05$). This is in accordance with a previous study that reported a decrease in renal cortical thickness in cats with impaired renal function (36). These findings highlight the importance of the contralateral kidney in the overall renal function following surgical intervention and advocate for its preoperative US assessment to aid in the surgical decision-making process.

In human medicine, area measurements have been developed to provide a more accurate and objective assessment of hydronephrotic kidneys with ultrasonography. The renal parenchymal area is highly and positively correlated with the renal volume measured by magnetic resonance imaging, with no effect of hydronephrosis on this correlation (37, 38) and serves as an early marker to predict future renal deterioration in infants with posterior urethral valves (39). The parenchyma-to-hydronephrosis area ratio is another parameter that combines the value of the parenchymal area with an objective measure of hydronephrosis. It is used to identify patients who are more suitable for surgery in the context of ureteropelvic junction obstruction as it has been found to predict postoperative renal function in humans undergoing pyeloplasty (16, 17, 38). In this study, it was hypothesized that these preoperative US structural parameters would correlate with nephron mass and serve as surrogate markers of functional renal reserve in cats with ureteral obstruction. However, parenchymal and hydronephrosis area measurements did not allow to predict renal recovery in this study, and one explanation could be that feline UO occurs in the context of CKD, in contrast to humans. Similarly, other regularly measured US parameters of the obstructed kidney did not correlate with long-term SCr, which aligns with the previous results of a recent study (15). These data support the argument that identification of US features such as severe hydronephrosis or thin parenchyma on the obstructed kidney should not deter surgical decompression in cats presenting with unilateral UO as there is no evidence to suggest that these features adversely impact long-term renal recovery.

Our study has a number of limitations. The sample size is moderate owing to the exclusion of a large number of cases, and this might have underpowered the statistical analyses. The long-term follow-up was set at a minimum of 3 months, and a longer period could have helped to better characterize renal recovery. This may only have little impact as other studies suggested overall stability of SCr after 3 months postoperatively (9, 12, 40). As acute events on CKD are part of this disease and may impact long-term outcomes, such cases were included in the study to avoid selection bias. This happened for one case of suspected pyelonephritis, and the long-term follow-up SCr was set when the acute event had resolved. Bacteriuria was detected in 11 cats at the date of follow-up, including the case of suspected pyelonephritis. The remaining cases presenting bacteriuria showed no clinical signs and an overall stability of SCr concentration at the date of long-term follow-up. A previous study reported that postoperative asymptomatic bacteriuria was not associated with survival and that no increase of SCr was observed in these cats (12). In our population, there was no significant difference in the proportion of cats presenting with long-term bacteriuria between the two groups ($p = 1$; $n = 48$). Owing to the retrospective nature of the study, preoperative US was performed by different ultrasonographers. To limit inter-observer variability, all measurements were taken by a single observer. The assessment of some criteria (e.g., cortical thickness) was sometimes challenging as it relied on retrospectively acquired still US images. Standardized prospective evaluation of the US-CKD score, which may also be useful in the follow-up of CKD alone, is required in a larger cohort and with multivariable analysis to confirm our results and draw causal inferences.

## 5 Conclusion

Evaluation of US findings consistent with CKD on the kidney contralateral to UO is beneficial to assess the postoperative evolution of SCr in cats treated unilaterally with an SUB device. In particular, the identification of severe signs of CKD in the contralateral kidney is associated with long-term IRIS stage IV with high specificity. However, measurements of renal parenchymal and hydronephrosis areas were not useful in predicting long-term renal recovery in cats after surgical decompression.

## Data availability statement

The raw data supporting the conclusions of this article will be made available by the authors, without undue reservation.

## Ethics statement

Ethical approval was not required for the studies involving animals in accordance with the local legislation and institutional requirements because the study only involved retrospectively collected clinical data. Written informed consent was obtained from the owners for the participation of their animals in this study.

## Author contributions

DP: Conceptualization, Data curation, Formal analysis, Investigation, Methodology, Resources, Visualization, Writing – original draft, Writing – review & editing. JF: Data curation, Investigation, Methodology, Resources, Writing – review & editing. MM: Methodology, Resources, Supervision, Writing – review & editing. JM: Conceptualization, Investigation, Methodology, Resources, Supervision, Validation, Writing – review & editing. CM: Conceptualization, Investigation, Methodology, Project administration, Resources, Supervision, Validation, Writing – original draft, Writing – review & editing.

## Funding

The author(s) declare that no financial support was received for the research, authorship, and/or publication of this article.

## Conflict of interest

The authors declare that the research was conducted in the absence of any commercial or financial relationships that could be construed as a potential conflict of interest.

## Generative AI statement

The author(s) declare that no Generative AI was used in the creation of this manuscript.

## Publisher's note



## Supplementary material

The Supplementary material for this article can be found online at: https://www.frontiersin.org/articles/10.3389/fvets.2025.1518713/full#supplementary-material

## References


1. Kopecny L, Palm CA, Drobatz KJ, Balsa IM, Culp WTN. Risk factors for positive urine cultures in cats with subcutaneous ureteral bypass and ureteral stents (2010-2016). *J Vet Intern Med*. (2019) 33:178–83. doi: 10.1111/jvim.15343

2. Kyles AE, Stone EA, Gookin J, Spaulding K, Clary EM, Wylie K, et al. Diagnosis and surgical management of obstructive ureteral calculi in cats: 11 cases (1993-1996). *J Am Vet Med Assoc*. (1998) 213:1150–6. doi: 10.2460/javma.1998.213.08.1150

3. Berent AC, Weisse CW, Bagley DH, Lamb K. Use of a subcutaneous ureteral bypass device for treatment of benign ureteral obstruction in cats: 174 ureters in 134 cats (2009–2015). *J Am Vet Med Assoc*. (2018) 253:1309–27. doi: 10.2460/javma.253.10.1309

4. Wormser C, Phillips H, Aronson LR. Retroperitoneal fibrosis in feline renal transplant recipients: 29 cases (1998-2011). *J Am Vet Med Assoc*. (2013) 243:1580–5. doi: 10.2460/javma.243.11.1580

5. Cohen L, Shipov A, Ranen E, Bruchim Y, Segev G. Bilateral ureteral obstruction in a cat due to a ureteral transitional cell carcinoma. *Can Vet J*. (2012) 53:535–8.

6. Johnson CM, Culp WTN, Palm CA, Zacuto AC. Subcutaneous ureteral bypass device for treatment of iatrogenic ureteral ligation in a kitten. *J Am Vet Med Assoc*. (2015) 247:924–31. doi: 10.2460/javma.247.8.924

7. Westropp J, Ruby A, Bailiff N, Kyles A, Ling V. Dried solidified blood calculi in the urinary tract of cats. *J Vet Intern Med*. (2006) 20:828–34. doi: 10.1111/j.1939-1676.2006.tb01793.x

8. Zaid MS, Berent AC, Weisse C, Caceres A. Feline ureteral strictures: 10 cases (2007–2009). *J Vet Intern Med*. (2011) 25:222–9. doi: 10.1111/j.1939-1676.2011.0679.x

9. Horowitz C, Berent A, Weisse C, Langston C, Bagley D. Predictors of outcome for cats with ureteral obstructions after interventional management using ureteral stents or a subcutaneous ureteral bypass device. *J Feline Med Surg*. (2013) 15:1052–62. doi: 10.1177/1098612X13489055

10. Kyles AE, Hardie EM, Wooden BG, Adin CA, Stone EA, Gregory CR, et al. Clinical, clinicopathologic, radiographic, and ultrasonographic abnormalities in cats with ureteral calculi: 163 cases (1984-2002). *J Am Vet Med Assoc*. (2005) 226:932–6. doi: 10.2460/javma.2005.226.932

11. Cannon AB, Westropp JL, Ruby AL, Kass PH. Evaluation of trends in urolith composition in cats: 5,230 cases (1985–2004). *J Am Vet Med Assoc*. (2007) 231:570–6. doi: 10.2460/javma.231.4.570

12. Wuillemin F, Vachon C, Beauchamp G, Dunn M. Subcutaneous ureteral bypass device placement in 81 cats with benign ureteral obstruction (2013-2018). *J Vet Intern Med*. (2021) 35:2778–86. doi: 10.1111/jvim.16280

13. Vrijsen E, Devriendt N, Mortier F, Stock E, Van Goethem B, de Rooster H. Complications and survival after subcutaneous ureteral bypass device placement in 24 cats: a retrospective study (2016–2019). *J Feline Med Surg*. (2020) 23:759–69. doi: 10.1177/1098612X20975374

14. Kulendra NJ, Borgeat K, Syme H, Dirrig H, Halfacree Z. Survival and complications in cats treated with subcutaneous ureteral bypass. *J Small Anim Pract*. (2020) 62:4–11. doi: 10.1111/jsap.13226

15. McEntee EP, Berent AC, Weisse C, Le Roux A, Lamb K. Evaluation of preoperative ultrasonographic parameters to predict renal recovery in long-term survivors after treatment of feline ureteral obstructions: 2012–2019. *J Feline Med Surg*. (2021) 24:328–36. doi: 10.1177/1098612X211023645

16. Han JH, Song SH, Lee JS, Nam W, Kim SJ, Park S, et al. Best ultrasound parameter for prediction of adverse renal function outcome after pyeloplasty. *Int J Urol*. (2020) 27:775–82. doi: 10.1111/iju.14299

17. Li X-D, Wu Y-P, Wei Y, Chen S-H, Zheng Q-S, Cai H, et al. Predictors of recoverability of renal function after Pyeloplasty in adults with Ureteropelvic junction obstruction. *Urol Int*. (2018) 100:209–15. doi: 10.1159/000486425

18. Lamb CR, Cortellini S, Halfacree Z. Ultrasonography in the diagnosis and management of cats with ureteral obstruction. *J Feline Med Surg*. (2018) 20:15–22. doi: 10.1177/1098612X17694253

19. Clarke DL. Feline ureteral obstructions part 1: medical management. *J Small Anim Pract*. (2018) 59:324–33. doi: 10.1111/jsap.12844

20. Fages J, Dunn M, Specchi S, Pey P. Ultrasound evaluation of the renal pelvis in cats with ureteral obstruction treated with a subcutaneous ureteral bypass: a retrospective study of 27 cases (2010-2015). *J Feline Med Surg*. (2018) 20:875–83. doi: 10.1177/1098612X17732900

21. Wormser C, Reetz JA, Drobatz KJ, Aronson LR. Diagnostic utility of ultrasonography for detection of the cause and location of ureteral obstruction in cats: 71 cases (2010–2016). *J Am Vet Med Assoc*. (2019) 254:710–5. doi: 10.2460/javma.254.6.710

22. Bua A-S, Dunn ME, Pey P. Respective associations between ureteral obstruction and renomegaly, urine specific gravity, and serum creatinine concentration in cats: 29 cases (2006-2013). *J Am Vet Med Assoc*. (2015) 247:518–24. doi: 10.2460/javma.247.5.518

23. Braun J-P, Lefebvre HP. Chapter 16—kidney function and damage In: JJ Kaneko, JW Harvey and ML Bruss, editors. Clinical biochemistry of domestic animals. *Sixth* ed. San Diego: Academic Press (2008). 485–528.

24. Bartges J, Polzin D, Segev G. Diseases of the ureter In: Diseases of the ureter in nephrology and urology of small animals. Ames, Iowa, USA: John Wiley & Sons (2011). 583–90.

25. Cost GA, Merguerian PA, Cheerasarn SP, Shortliffe LM. Sonographic renal parenchymal and pelvicaliceal areas: new quantitative parameters for renal sonographic followup. *J Urology*. (1996) 156:725–9. doi: 10.1016/S0022-5347(01)65798-7

26. Rodriguez L, Lock J, Kennedy W, Shortlife L. Evaluation of sonographic renal parenchymal area in the management of hydronephrosis. *J Urology*. (2001) 165:548–51. doi: 10.1097/00005392-200102000-00066

27. Fischer K, Li C, Wang H, Song Y, Furth S, Tasian GE. Renal parenchymal area growth curves for children 0 to 10 months old. *J Urology*. (2016) 195:1203–8. doi: 10.1016/j.juro.2015.08.097

28. Debruyn K, Haers H, Combes A, Paepe D, Peremans K, Vanderperren K, et al. Ultrasonography of the feline kidney: technique, anatomy and changes associated with disease. *J Feline Med Surg*. (2012) 14:794–803. doi: 10.1177/1098612X12464461

29. Pollard R, Philips K. Diagnostic imaging of the urinary tract In: BSAVA manual of canine and feline nephrology and urology. Gloucester: British Small Animal Veterinary Association (2017)

30. Ferreira A, Marwood R, Batchelor D, Maddox T, Mortier JR. Prevalence and clinical significance of the medullary rim sign identified on ultrasound of feline kidneys. *Vet Rec*. (2020) 186:533–3. doi: 10.1136/vr.105619

31. Lamb C, Dirrig H, Cortellini S. Comparison of ultrasonographic findings in cats with and without azotaemia. *J Feline Med Surg*. (2018) 20:948–54. doi: 10.1177/1098612X17736657

32. Cordella A, Pey P, Dondi F, Dunn M, Caramazza C, Cipone M, et al. The ultrasonographic medullary "rim sign" versus medullary "band sign" in cats and their association with renal disease. *Vet Int Med*. (2020) 34:1932–9. doi: 10.1111/jvim.15878

33. IRIS Kidney—Guidelines—IRIS staging of CKD. Available at: http://www.iris-kidney.com/guidelines/staging.html (Accessed December 19, 2024)

34. Nahm FS. Receiver operating characteristic curve: overview and practical use for clinicians. *Korean J Anesthesiol*. (2022) 75:25–36. doi: 10.4097/kja.21209

35. McGee S. Simplifying likelihood ratios. *J Gen Intern Med*. (2002) 17:647–50. doi: 10.1046/j.1525-1497.2002.10750.x

36. Yan G, Chen K, Wang H, Ma T, Chen K. Relationship between ultrasonographically determined renal dimensions and international renal interest society stages in cats with chronic kidney disease. *Vet Int Med*. (2020) 34:1464–75. doi: 10.1111/jvim.15814

37. Wong IY-Z, Copp HL, Clark CJ, Wu H-Y, Shortliffe LD. Quantitative ultrasound renal parenchymal area correlates with renal volume and identifies reflux nephropathy. *J Urol*. (2009) 182:1683–7. doi: 10.1016/j.juro.2009.03.075

38. Rickard M, Lorenzo AJ, Braga LH. Renal parenchyma to Hydronephrosis area ratio (PHAR) as a predictor of future surgical intervention for infants with high-grade prenatal Hydronephrosis. *Urology*. (2017) 101:85–9. doi: 10.1016/j.urology.2016.09.029

39. Odeh R, Noone D, Bowlin PR, Braga LHP, Lorenzo AJ. Predicting risk of chronic kidney disease in infants and young children at diagnosis of posterior urethral valves: initial ultrasound kidney characteristics and validation of parenchymal area as forecasters of renal reserve. *J Urol*. (2016) 196:862–8. doi: 10.1016/j.juro.2016.03.137

40. Berent AC, Weisse CW, Todd K, Bagley DH. Technical and clinical outcomes of ureteral stenting in cats with benign ureteral obstruction: 69 cases (2006–2010). *J Am Vet Med Assoc*. (2014) 244:559–76. doi: 10.2460/javma.244.5.559

frontiers | Frontiers in Veterinary Science

TYPE Original Research
PUBLISHED 05 February 2025
DOI 10.3389/fvets.2025.1495606



OPEN ACCESS

EDITED BY
Hussein M. El-Husseiny,
Tokyo University of Agriculture and Technology, Japan

REVIEWED BY
Aris Pourlis,
University of Thessaly, Greece
Hassan Ainani,
Mohammed VI Polytechnic University, Morocco

*CORRESPONDENCE
El Hassania Lakhel
✉ mogadorvet@yahoo.fr

RECEIVED 12 September 2024
ACCEPTED 09 January 2025
PUBLISHED 05 February 2025

CITATION
Lakhel EH, El Allali K, Achaâban MR and Azrib R (2025) Preliminary ultrasonography study of the pancreas in the dromedary camel (*Camelus dromedarius*).
*Front. Vet. Sci.* 12:1495606.
doi: 10.3389/fvets.2025.1495606



# Preliminary ultrasonography study of the pancreas in the dromedary camel (*Camelus dromedarius*)

El Hassania Lakhel[1]*, Khalid El Allali[1], Mohamed Rachid Achaâban[1] and Rahma Azrib[2]

[1]Comparative Anatomy Unit, Department of Veterinary Biological and Pharmaceutical Sciences, Hassan IInd Agronomy and Veterinary Medicine Institute, Rabat, Morocco, [2]Equine and Canine Unit, Department of Reproduction Medicine and Surgery, Agronomy and Veterinary Institute, Rabat, Morocco

**Introduction:** Pancreatic lesions in camels can lead to significant economic losses. They are practically undetectable, as clinical signs alone are insufficient for specific diagnosis. Ultrasonography is a valuable diagnostic tool for evaluating the pancreas. However, ultrasonographic reference patterns of the pancreas in the camel are yet to be established. This study aimed to define the ultrasonographic appearance, reference values, location, and acoustic window for evaluating the pancreas in healthy camels.

**Methods:** Eight adult and 14 young Moroccan camels were investigated by ultrasonography using a micro-convex probe with SIUI CTS-900 V and Samsung MH70A Doppler ultrasound scanners at 3.5 MHz.

**Results:** The body of the pancreas was scanned just below the right kidney, behind the 12th rib; an ultrasonographic pattern of pancreatic parenchyma appeared as a hyperechoic elongated band, including the portal vein, with a Doppler flow response. The average thickness of the body was 3.60 ± 0.24 cm ($n$ = 14) in young camels significantly lower than in adult camels 4.61 ± 0.26 cm ($n$ = 8). The right lobe was scanned on the right side, adjacent to the duodenal ampulla and abomasum, beneath the liver along the 11th, 10th, and 9th intercostal spaces. The ultrasonographic pattern of parenchyma appeared as a hyperechoic triangle compared to the liver, including portal and duodenal-pancreatic veins, showing a Doppler flow response. The corresponding parenchyma thickness within the three intercostal spaces was 3.93 ± 0.33 cm, 4.40 ± 0.20 cm, and 3.46 ± 0.39 cm in the young camels (n = 14), and 4.99 ± 0.46 cm, 5.90 ± 0.27 cm, and 4.11 ± 0.68 cm in the adults (n = 8), respectively. The pancreatic major duct was seen as an anechoic circle with a hyperechoic wall, with a maximum diameter of 1 cm, and the left lobe scanned beneath the cranial extremity of the spleen; its ultrasonographic pattern showed an irregular hypoechoic band with a mean thickness of 2.32 ± 0.32 cm ($n$ = 14) in young camels and 3.08 ± 0.52 cm ($n$ = 8) in the adults, including a small splenic vein.

**Conclusion:** Ultrasonography combined with Doppler techniques provides valuable information on pancreatic health, blood flow, and tissue perfusion, aiding early detection of pancreatic diseases and, consequently, minimizing economic losses in camel husbandry.

KEYWORDS

**dromedary, camel, pancreas, anatomy, ultrasonography, reference patterns**

# 1 Introduction

Camel husbandry is known to be economically important in desert environments. Indeed, this species shows special adaptive peculiarities to cope with harsh climate conditions at a lower cost than other species, especially cattle and small ruminants (1). In addition, camels constitute a source of meat and dairy products (2).

The dromedary camel is also involved in agricultural vocations, such as transporting crops and diverse tourist activities. However, camel husbandry suffers from significant economic losses, mainly due to parasites, viral, and other diseases (3).

The prevalence of various diseases in camels, as highlighted by Hegazy and Fahmy (4) in their atlas of camel diseases, underscores significant clinical implications. In particular, pancreatic lesions are often overlooked in these publications despite their clear visibility during post-mortem examinations in slaughterhouses. In live camels, however, identifying pancreatic abnormalities remains challenging, as these conditions typically occur without pathognomonic clinical symptoms. This absence of overt signs complicates early diagnosis and emphasizes the urgent need for enhanced diagnostic protocols to detect pancreatic lesions in living animals, ultimately improving herd health management.

In this context, ultrasonography as a diagnostic tool in veterinary medicine has gained prominence recently (5). This non-invasive technique is rapid, safe, informative, and well-tolerated by animals, making it particularly suitable for camel use. Ultrasonography has been applied to explore various parts of the body, including the genital tract (6) and the digestive tract (7, 8). In Morocco, abdominal ultrasound investigations in camels have been conducted as part of academic veterinary theses, further demonstrating the growing recognition of role of ultrasonography in enhancing camel health diagnostics. This evolution in diagnostic practices may facilitate earlier detection of pancreatic lesions and contribute to better overall herd health management.

However, the existing literature has not adequately addressed ultrasonography of the pancreas in camels. For the first time, this study aimed to perform an ultrasonographic investigation of the pancreas in young and adult healthy dromedary camels. This investigation seeks to provide veterinary practitioners with referential ultrasonographic images of this organ and detailed descriptions of the examination protocols used.

# 2 Materials and methods

## 2.1 Animals

This study was conducted on 22 healthy dromedary camels, comprising 14 young camels under 2 years of age (seven males and seven females) and eight adult camels (four males and four females) under 10 years old.

Young camels had an average weight of 330.7 ± 23.4 kg, issued from farms in the southern region of Agadir (Latitude: 30°3′60″N; Longitude: 9°3′60″W). They had unlimited access to grazing and received supplements made of straw and barley. The camels were destined for slaughtering at the Sidi Bibi abattoir (region of Agadir, Southern Morocco). They were selected because, according to veterinary inspectors, most young dromedaries sacrificed for human consumption rarely show lesions in their carcasses and organs, and, therefore, increases the likelihood of obtaining ultrasound patterns without anomalies.

The four adult male dromedaries, weighing 585 ± 11 kg, originated from the Kaouki region of Essaouira, Morocco (Latitude: 31°21′20″N; Longitude: 9°47′50″W). They were used by nomads for tourism purposes and were clinically healthy. They have unrestricted access to grazing and receive straw and barley-based supplements.

The four adult female camels had an average weight of 575 ± 20 kg, were clinically healthy and kept in the sheepfold of the Comparative Anatomy Unit at the Hassan II Agronomy and Veterinary Medicine Institute in Rabat, Morocco (Latitude: 34.00492°N; Longitude: −6.8553°W). They were fed a special camelid industrial diet (Maraa, Alf Sahel, Morocco) and offered sufficient quantities of straw.

All experimental protocols were approved by the local ethics committee for animal science and health and veterinary public health (CESASPV) of the Hassan II Agronomic and Veterinary Medicine Institute, BP 6202, Rabat-Institutes, Morocco (ethical authorization number: CESASPV_2024_A17).

## 2.2 Methods

All the 22 clinically healthy camels, including 14 young camels (seven females and seven males), four adult females, and four adult males were assessed for the liver, kidney, and pancreatic functions to ensure their biochemical healthy statute. Blood samples were collected from all animals to measure urea, creatinine, AST, ALT, and amylase parameters. The results confirmed that all animals were within normal reference values. Following this confirmation, ultrasound examinations of the pancreas were performed. Young camels and adult males were examined using the SIUI CTS-900 V ultrasound scanner, while adult females underwent additional imaging with the Samsung MH70A Doppler ultrasound scanner.

The young camels ($n = 14$) were slaughtered for public consumption of the meat. They had previously been utilized for ultrasonographic examinations. A comprehensive examination of the carcasses was subsequently conducted, which revealed no abnormalities. Following this examination, a gross anatomical study of the pancreas was performed on these young camels.

All examinations of blood tests were conducted on a Mindray machine, using different kits for each parameter. Urea analyses were performed with urea kits that employed the urease-glutamate dehydrogenase method (UV). Creatinine levels were analyzed using a creatinine kit that utilized the sarcosine oxidase method. AST was measured with an aspartate amino-transferase kit (UV assay) following IFCC (International Federation of Clinical Chemistry and Laboratory Medicine) guidelines without pyridoxal phosphate activation. Similarly, ALT was assessed using an alanine amino-transferase kit (UV assay) according to IFCC standards, also without pyridoxal phosphate activation.

## 2.3 Gross anatomical study

The gross anatomical study was realized on the pancreas of the young camels ($n = 14$) and was conducted after the camels were slaughtered. The objective was to explore the external conformation, topography, and relationships with neighboring organs (Figures 1A,B), which may help in interpreting ultrasound images. Subsequently, specific attention was given to the pancreas, which was anatomically studied to reveal its major macroscopic characteristics. The pancreas was carefully extracted to ensure its integrity, and the surrounding adipose tissue was removed to optimize the visualization of all pancreatic components and the external conformation (Figure 1B). Macroscopic measurements (width, length, and thickness) and the weight of the organ were also obtained.

## 2.4 Ultrasound examination

The ultrasound examinations were performed using an SIUI CTS-900 V ultrasound scanner in B-mode (brightness mode), a common imaging technique that provides two-dimensional images of internal structures (9), allowing for a detailed assessment of the pancreas.

Four adult female camels underwent two separate ultrasonography sessions, using both the SIUI CTS-900 V ultrasound scanner and the Samsung MH70A Doppler ultrasound scanner in order to distinguish vascular structures from other anatomical components using color flow. This dual approach aimed to enhance the visualization and assessment of vascular structures.

Despite the presence of experienced restraint technicians, an adult female camel exhibited excessive agitation during the ultrasound examinations, highlighting the challenges of performing such procedures on large and adult animals. Consequently, sedation has been used via intravenous injection of xylazine (Rompun® 2%) at a dose of 0.25–0.5 mg per kg body weight. The same restraint method was applied during the injection, and the ultrasound examination was performed as part of the standard handling procedures for equines.

A 12-h restricted diet was not absolute but necessary to obtain superior quality images. Each animal was examined on an area of both sides, extending from the angle of the hip to the fourth rib dorsally and from the xiphoid to the stifle ventrally. All this area was correctly shaved. After generously applying transmission gel to the probe and the entire sheared area, ultrasonographic exploration was performed using a 3.5–7-MHz micro-convex and convex probe. Machine gain, depth, and frequency parameters were adjusted throughout the examination to ensure high-quality images.

On the right side, the pancreatic body was scanned by positioning the probe behind the 12th rib in the para-lumbar fossa, directed cranially (Figure 2A), allowing for multiple scans; while, ultrasonography of the right lobe of the pancreas was performed using three acoustic windows corresponding to the last three intercostal spaces 11th, 10th, and 9th. Each space was examined from top to bottom, relying on the anatomical references, specifically by locating the liver parenchyma.

On the left side, the left lobe was scanned by positioning the probe below the last transverse processes of the lumbar vertebrae; ventrally to the spleen (Figure 2B).

This careful approach facilitated a thorough evaluation of all lobes of the pancreas and their anatomical relationships.

Measurements performed during ultrasonography examination included the thickness of different parts of the pancreas (body and lobes), the diameter of the portal vein on longitudinal and transversal scans, and the diameter of the pancreatic duct. All measurements were presented as mean ± standard deviation (SD), and the statistical analysis was performed using SPSS version 25.0 (2017; SPSS, Armonk, NY, United States).

A two-way analysis of variance (ANOVA), followed by the Holm–Sidak *post-hoc* test, was used to evaluate the existence of significant differences in ultrasonographic measurements between adult and

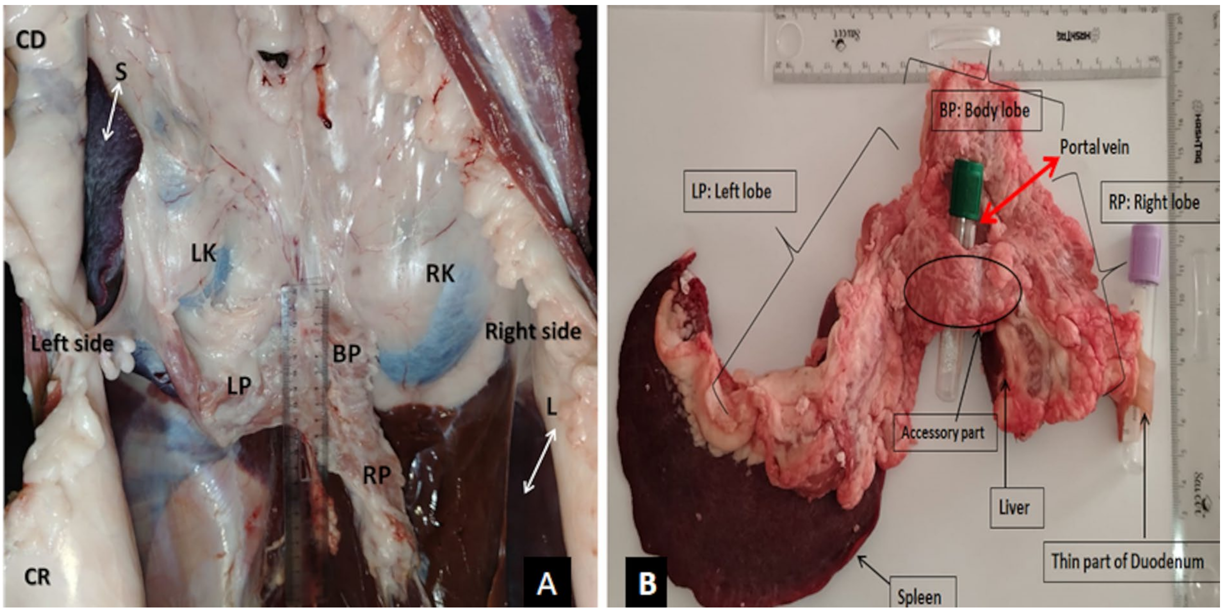


FIGURE 1
**(A)** Topography of the pancreas on the carcass of slaughtered camel (ventral view); **(B)** macroscopic conformation of the pancreas of the dromedary camel (dorsal view). RK, Right kidney; LK, left kidney; L, liver; S, spleen; LP, the left lobe of the pancreas; RP, the right lobe of pancreas; BP,: body lobe of the pancreas; CR, cranial; CD, caudal.

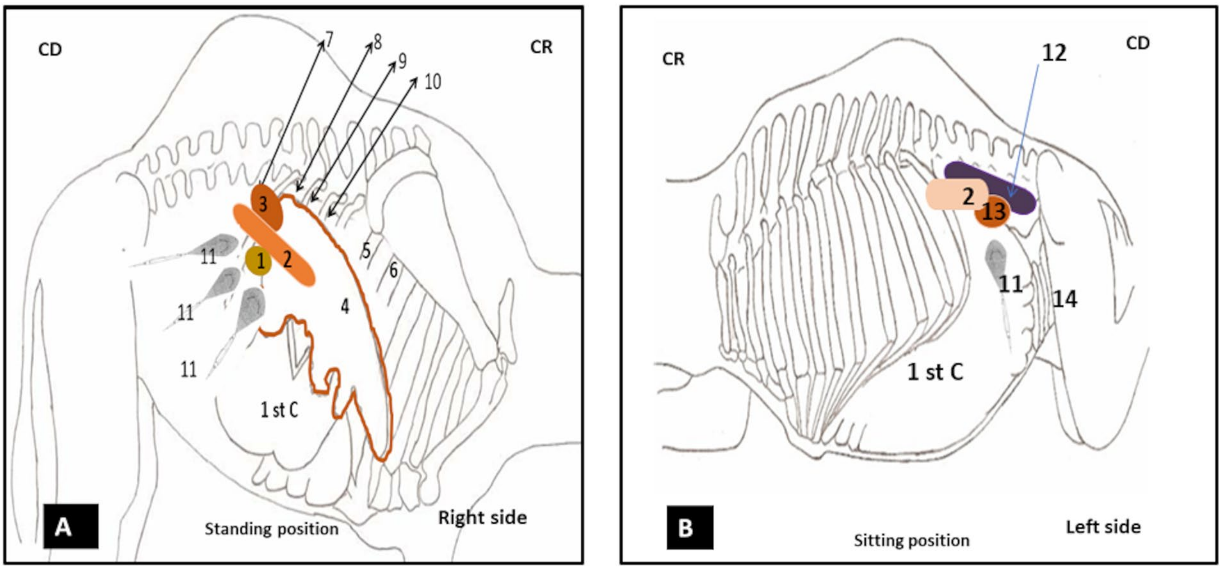


FIGURE 2
**(A)** Illustration of the positions of the probe for ultrasonography of the pancreas on the right side at a standing position. **(B)** Illustration of the position of the probe for ultrasonography of the pancreas on the left side at sitting position. 1: duodenal ampulla; 2: pancreas; 3: right kidney; 4: liver; 5: the 7th intercostal space; 6: the 6th intercostal space; 7: below the 11th intercostal space; 8: the 11th intercostal space; 9: the 10th intercostal space; 10: the 9th intercostal space; 11: probe; 12: spleen; 13: left kidney; 14: spiral colon; C1: first stomach compartment.

young and between females and males categories. A $p$-value of $\leq 0.05$ was deemed to be statistically significant for all tests conducted.

# 3 Results

## 3.1 Gross anatomy of the pancreas

The pancreas in camels is characterized by the development of its left lobe and a relatively reduced right lobe. It generally consists of a body, two lobes, and an accessory part; with an average weight of 124.5 ± 49.1 g (see Figure 1B). The pancreas exhibits similar shape and size in both females and males.

The pancreatic body (*Corpus pancreatic*) in camels is located below the first and second lumbar vertebrae. It is in contact with the portal vein, the caudate hepatic lobe, and the diaphragm. It is also related to the transverse colon and kidney. The width, length, and thickness are approximately 4.8 ± 0.5 cm, 7.6 ± 1.1 cm, and 1.5 ± 0.2 cm, respectively.

The right pancreatic lobe (*Lobus pancreatis dexter*) is prismatic in shape and projects backward and to the right. It is related to the second duodenal flexure and is contained in the meso-duodenum. The width, length, and thickness average 2.1 ± 0.2 cm, 6.9 ± 0.4 cm, and 0.7 ± 0.1 cm, respectively.

The left pancreatic lobe *(Lobus pancreatis sinister)* is larger than the right lobe and is positioned obliquely between the folds of the greater omentum. Anatomically, it is associated with several structures, including the first stomach compartment (rumen), transverse colon, descending colon, spleen, left kidney, and adrenal gland. The average dimensions of the left lobe are as follows: a width of 2.9 ± 1.1 cm, a length of 21.7 ± 7.5 cm, and a thickness of 1 ± 0.3 cm.

The accessory part *(Processus uncinatus)* unites the right and left lobes, forming an annular pancreas around the portal vein; the width, length, and thickness are, on average, 2.5 ± 0.4 cm, 1.3 ± 0.2 cm, and 0.4 ± 0.1 cm, respectively.

## 3.2 Animal examination and laboratory findings

All the examined camels were clinically healthy, showing no signs of pathology. Vital parameters, such as body temperature, respiratory rate, heart rate, and rumination, were within normal limits, indicating good overall health. The blood parameters analyses conducted on the 22 camels to assess kidney function revealed levels of 2.0 ± 0.6 mg/100 mL for urea and 1.04 ± 0.3 mg/100 mL for creatinine, both of which were within normal limits. These values were consistent with the reference ranges established by Bengoumi (10), indicating urea levels between 2 and 4 mg/100 mL and creatinine levels below 2 mg/100 mL.

Additionally, parameters assessing liver function showed levels of 93.4 ± 16.2 u/l for AST and 18.27 ± 4.4 u/l for ALT, both of which were within normal limits. These values were consistent with the reference ranges established by Bengoumi (10), both being lower than the thresholds of 115u/l for AST and 24u/l for ALT.

Finally, the measured levels of amylase activity 854.74 ± 321.27 u/l were within the normal range but lower than the threshold of 2,325 u/l as reported by Mura et al. (11).

## 3.3 Ultrasonographic appearance of the pancreas

The ultrasonographic exploration of the pancreas was performed on a total of 22 camels using a SIUI CTS-900 V ultrasound scanner equipped with micro-convex and convex probes (3.5–7 MHz).

Multiple trials showed that the micro-convex probe at a frequency of 3.5 MHz yielded the highest quality images, despite the complex anatomy of the pancreas and limited access in the intercostal spaces.

Following the anatomical and morphological structure of the pancreas, which is composed of three parts (the body, the right lobe, and the left lobe; see Figure 1B), the ultrasonographic examination was performed using different acoustic windows (Figure 2) for exploration, encompassing all three components.

On four adult female camels, ultrasonography was performed using both the SIUICTS-900 V ultrasound scanner and the Samsung MH70A Doppler ultrasound scanner at 3.5 MHz to assess vascularization. The results confirmed active vascularization observed with the macroscopic examination, identifying the portal vein and pancreatico-duodenal vein among the observed vessels.

The ultrasonography of the pancreatic body was performed on the right flank by positioning the micro-convex probe, just below the transverse processes of the first and second lumbar vertebrae behind the upper third 12th rib. The right kidney was initially identified and localized, and then, the probe was directed cranio-ventrally toward it. The ultrasound frequency was set to 3.5 MHz, with a depth of 14.2 cm and a gain of approximately 50%. The ultrasonographic pattern of pancreatic parenchyma of the body appears hyperechoic, elongated, and irregular in shape, located closely to the anterior visceral surface of the kidney, caudal to the ventral surface of the liver (Figure 3A). The average thickness observed was 3.58 ± 0.22 cm in longitudinal scans of young male camels (Figure 3B), which is quite similar to the 3.63 ± 0.28 cm found in young female camels. However, this thickness was significantly higher ($p < 0, 0001$) in adults than in young camels, 4.64 ± 0.31 cm ($n = 4$), and 4.58 ± 0.24 cm ($n = 4$), respectively, for adult camels males and females. No significant differences were observed between males and females within young and adult categories.

The average thickness of the body was 3.60 ± 0.24 cm ($n = 14$) in young camels, significantly lower than in adult camels 4.61 ± 0.26 cm ($n = 8$).

Furthermore, the position of the animal may affect the pancreas, whereas the thickness remained consistent across standing and sitting positions as well as transverse and longitudinal scans. In the sitting position, the body lobe of the pancreas was identified via ultrasonography in the upper third of the 12th rib. In contrast, in the standing position, it was located behind the middle third of the 12th rib.

The pancreatic parenchyma of the body contains a single large vessel running through it, representing the portal vein, which exhibits a clear color flow Doppler. In longitudinal scans, this vessel appears as an anechoic channel (Figure 3A), with a mean diameter of 1.83 ± 0.19 cm ($n = 14$) in young camels, statistically lower than that observed in adult camels 3.08 ± 0.15 cm ($n = 8$). In transverse scans, it appears as an anechoic circle (Figure 3B). Similar significant differences in the diameter of the portal vein were observed between young and adult camels on a transversal scan 1.80 ± 0.19 cm ($n = 14$) vs. 3.14 ± 0.18 cm ($n = 8$), respectively.

Ultrasonography of the right pancreatic lobe was performed through three distinct acoustic windows to ensure optimal visualization, guided by anatomical reference points.

*The first acoustic window, located at the 11th intercostal space*, identified the proximal margin of the liver from the midline due to the pancreas proximal to the liver. This margin was found to be, on average, 45.25 ± 6.4 cm in adult camels and 39.42 ± 3.2 cm in young camels, whereas no significant differences were found between males and females. The probe was oriented ventrally toward this margin, where the pancreatic parenchyma of the right lobe appeared hyperechoic compared to the liver. It is located caudo-ventrally, intercalated by the duodenal ampulla (Figures 4A,B).

In the standing position, the pancreatic parenchyma was scanned starting from the middle third of the 11th intercostal space, whereas in the sitting position, it was scanned from the upper third, remaining closely adjacent to the duodenal ampulla. The thickness was slightly smaller in the sitting position, particularly when the duodenal ampulla was full (Figures 5A,B).

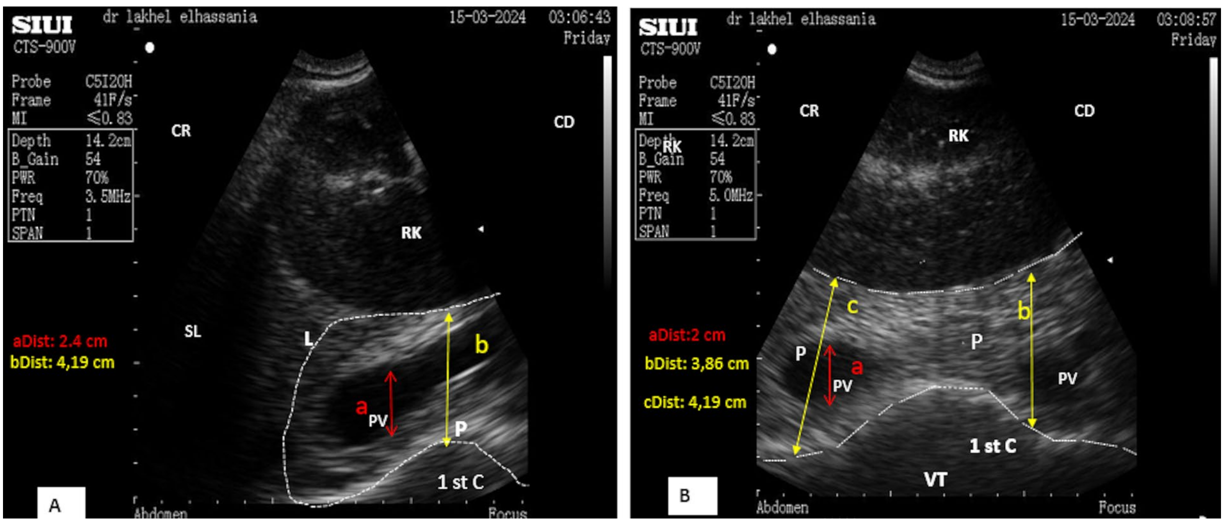


FIGURE 3
**(A)** Longitudinal scan of the body lobe of the pancreas caudally to the upper third of the 12th rib. **(B)** Transverse scan of the body lobe of the pancreas caudally to the upper third of the 12th rib. RK, Right kidney; PV, portal vein; 1st C, first stomach compartment; P, pancreas; L, liver; SL, shadow of the lung; VT, ventral; (aDist), diameter of portal vein; (bDist) and (cDist), thickness of pancreatic body; CR, cranial; CD, caudal; VT, ventral.

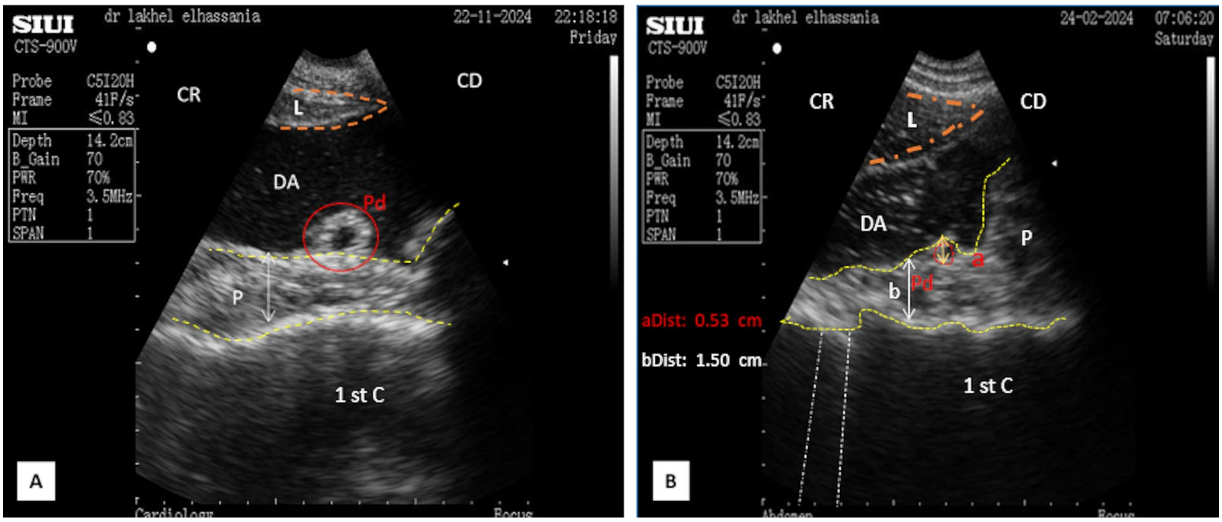


FIGURE 4
**(A)** Transverse scan of the right lobe of the pancreas in the middle third of the 11th intercostal space. **(B)** Identification of structures on the ultrasound image. 1st C, (first stomach compartment); P, pancreas (yellow dotted outline); L, liver (orange dotted outline); DA, duodenal ampulla; Pd, pancreatic duct (red circle); (aDist), diameter of pancreatic duct; (aDist), thickness of the right lobe of the pancreas; CR, cranial; CD, caudal.

In the middle third of the 11th intercostal space, the ultrasonographic pattern of the parenchyma of the right lobe displayed an elongated, irregular band-shaped structure, particularly when the scan did not reveal the portal vein. The thickness of the pancreatic parenchyma of the right lobe was significantly smaller in young camels, measuring 1.61 ± 0.15 cm ($n = 14$), and 2.15 ± 0.24 cm ($n = 8$) in adult camels during transverse scans, regardless of sex (Figure 4B). Additionally, the major pancreatic duct was visible, with a mean width of 0.67 ± 0.05 cm ($n = 14$) for young camels and 0.79 ± 0.05 cm ($n = 8$) for adult camels. No statistical differences were observed for this parameter, regarding age and sex (Figure 4A). In contrast, when the portal vein was included in transverse scans, the pattern appeared triangular, with a thickness of 3.03 ± 0.35 cm ($n = 14$) for young camels and 4.77 ± 0.54 cm ($n = 8$) for adults. In longitudinal scans, the parenchyma appeared irregular and trapezoid-shaped measuring 3.93 ± 0.33 cm for young camels and 4.99 ± 0.43 cm for adults (Figures 5A,B).

The portal vein and the duodenal-pancreatic vein appeared as anechoic channels in longitudinal scans and as anechoic circles in transverse scans, which was confirmed by color flow Doppler ultrasonography. The average diameter of the portal vein was 1.52 ± 0.12 cm for young camels and 3.12 ± 0.45 cm for adults, regardless of sex (Figure 6).

*In the second window, the scan starts from the upper to the lower area in the 10th intercostal space*, identifying the proximal margin of the liver from the dorsal midline at 48.12 ± 4.0 cm for adult camels and 44.14 ± 3.9 cm for young camels, with no significant differences regarding sex. In the standing position, the pancreatic parenchyma was scanned starting from the middle third of the 10th intercostal space, while in the sitting position, the right lobe was pushed upward, and therefore, it was scanned from the upper third.

After directing the probe ventrally toward this margin, it appeared hyperechoic compared to the liver, ventro-caudally to the duodenal ampulla. Its shape was triangular during the resting phase (Figure 6A) and took on a prism-like appearance during the contracting phase of digestion (Figure 6B), as observed when using both the SIUI CTS-900 V and Samsung MH70A ultrasound scanners (Figures 7, 8).

Placing the probe in the middle third of the 10th intercostal space allowed an optimal view of the right lobe. The pancreatic parenchyma was wider than observed in previous positions, with the pancreatic duct visible and having a similar dimension as that observed in the 11th intercostal space (Figures 6, 9A). The average thickness of the parenchyma was 4.40 ± 0.20 cm ($n = 14$) for young camels and 5.90 ± 0.25 cm ($n = 8$) for adults. The portal vein was identified in the center (Figures 6A,B), along with the pancreatico-duodenal vein, which responded to color flow Doppler ultrasonography (Figures 8A,B). In the transversal scan, the portal vein diameter averaged 1.83 ± 0.14 cm ($n = 14$) in young camels and 3.23 ± 0.51 cm ($n = 8$) in the adults.

By moving the probe ventrally in the lower part of the 10th intercostal space, the pancreatic parenchyma of the right lobe, along with the portal vein and pancreatico-duodenal vein, was still observed, but with lesser thickness than previous probe positions (Figure 9B).

*In the third window, the scan starts from the upper to the lower area in the 9th intercostal* space, identifying the proximal margin of the liver from the dorsal midline at 52.1 ± 4.1 cm for adult camels and 47.6 ± 3.5 cm for young camels, with no significant differences regarding sex. However, in the standing position, the pancreatic parenchyma was scanned from the middle third of the 9th intercostal space, adjacent to the abomasum and the first compartment of the stomach (rumen). In the sitting position, it was scanned from the upper third.

The mean thickness of the pancreatic parenchyma in longitudinal scans averages 3.46 ± 0.39 cm ($n = 14$) in young camels and 4.11 ± 0.68 cm ($n = 8$) in the adults. This area includes only the portal vein, which shows a larger width: 1.67 ± 0.35 cm ($n = 14$) in young camels and 2.95 ± 0.18 cm ($n = 8$) in adults.

In the upper third of the 9th intercostal space, the scan shows a triangular-shaped ultrasonographic pattern in the upper third of the 9th intercostal space, which becomes prism-like during contraction. However, in the middle third, it appears as an irregular shape (Figure 10A).

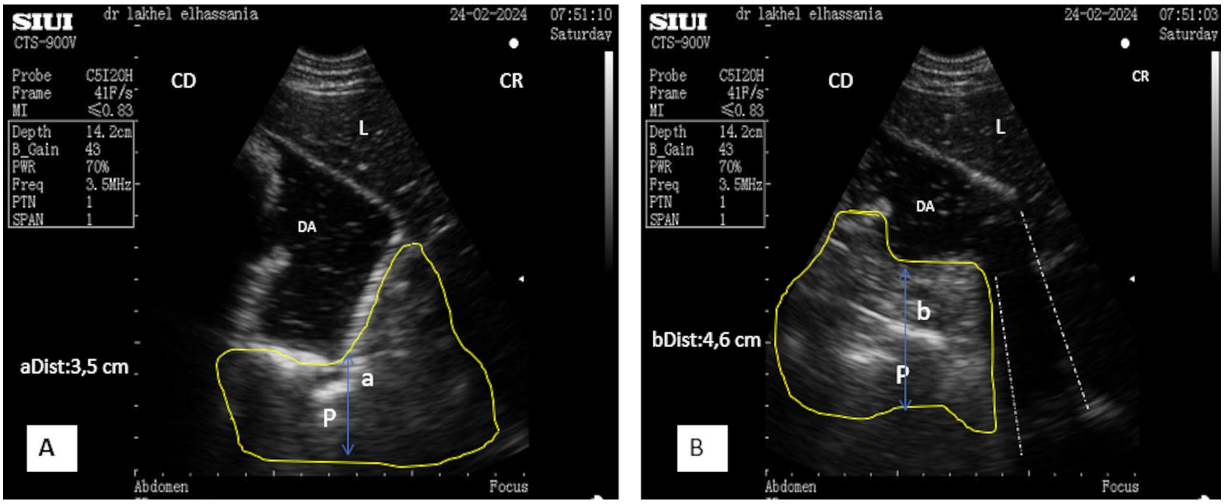


FIGURE 5
**(A)** Longitudinal scan of the right lobe of the pancreas in the middle of the 11th intercostal space in a resting phase. **(B)** Longitudinal scan of the right lobe of the pancreas in the middle of the 11th intercostal space in the contracting phase. L, liver; DA, duodenal ampulla; P, pancreas (yellow outline); (aDist), thickness of the right lobe in resting phase; (bDist), thickness of the right lobe of the pancreas in contraction phase; (White dotted line), acoustic shadow; CR, cranial; CD, caudal.

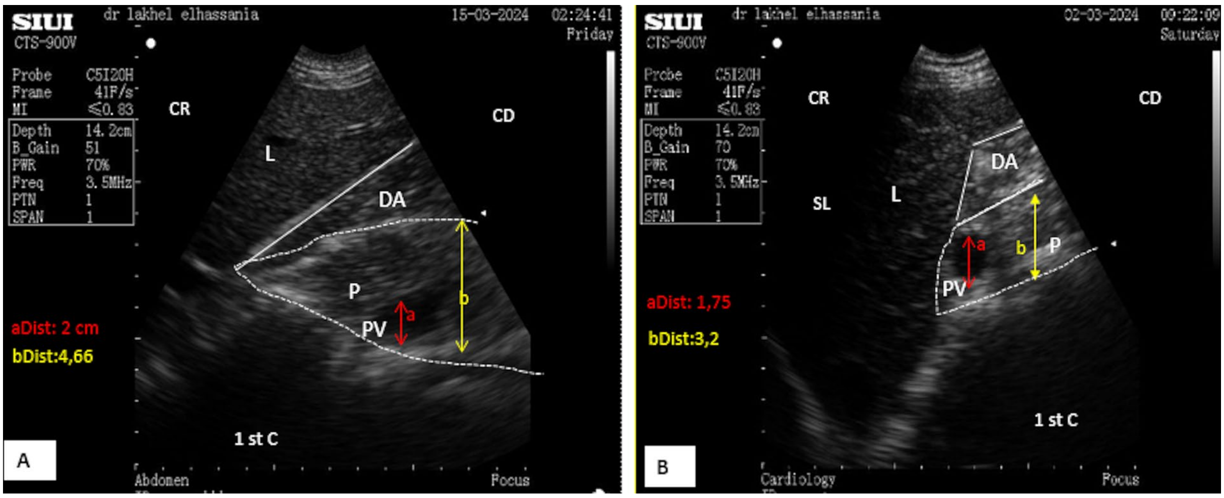


FIGURE 6
**(A)** Transverse scan of the right lobe of the pancreas in the middle of the 10th intercostal space. **(B)** Transverse scan of the right lobe of the pancreas in the upper third of the 10th intercostal space. PV, Portal vein; 1st C, (first stomach compartment); P, pancreas (white dotted outline); L, liver; DA, duodenal ampulla; SL, shadow of the lung; (aDist), diameter of portal vein; (bDist), thickness of pancreatic of the right lobe of the pancreas; CR, cranial; CD, caudal.

In contrast, the thickness is less in the lower third (Figure 10B), resembling a small band compared to previous spaces during the resting phase of ruminal contraction and in the sitting position.

Ultrasonography of the left lobe of the pancreas proved challenging. Based on anatomical and topographical references seen in slaughtered animals (Figure 1A); the probe was positioned in a region defined cranially by the last rib, caudally by the fifth transverse processes of the lumbar vertebra and the left kidney, ventrally by the first stomach compartment "rumen," and dorsally by the spleen. The ultrasound frequency was also set to 3.5 MHz, with a depth of 14.2 cm and a gain of approximately 70%. After identifying the left kidney and the cranial part of the spleen, the probe was directed cranially and ventrally toward the anterior extremity of the spleen. The pancreatic parenchyma appeared as a small hyperechoic band compared to the kidney and slightly hypoechoic compared to the spleen, situated above the first stomach compartment (Figure 11). Because of its elongated form averaging 21.7 ± 7.5 cm in young camels, the left lobe, like the right lobe and body of the pancreas, cannot be fully visualized in a single scan and, therefore, multiple scans are necessary to the entire imaging of its caudal end. These scans should begin by placing the probe ventrally to the surface of the spleen and gradually moving it caudally until reaching the fifth lumbar vertebra.

The parenchyma of the left lobe has an average thickness of 2.32 ± 0.32 cm ($n$ = 14) in young camels and significantly higher

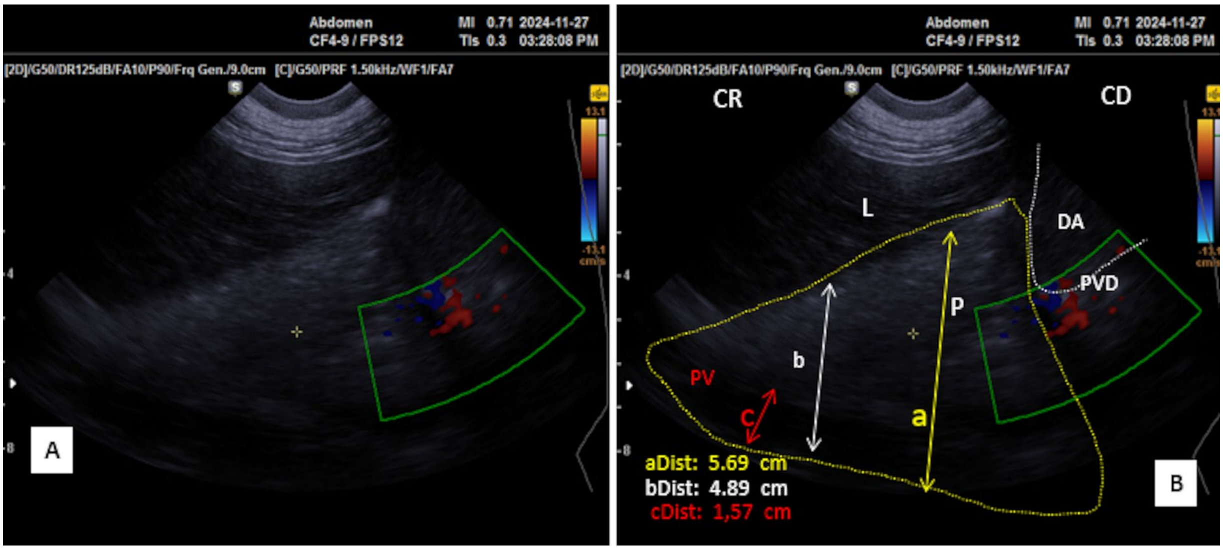


FIGURE 7
Transverse scan of the right lobe of the pancreas in the middle third of the 10th intercostal space **(A)**. **(B)** Identification of structures on the ultrasound image. P, pancreas (yellow dotted outline); L, liver; DA, duodenal ampulla (white dotted outline); PV, portal vein; PDV, pancreatico-duodenal vein; PD, pancreatic duct; (aDist) and (bDist), thickness of pancreatic of the right lobe of the pancreas; (cDist), diameter of portal vein; CR, cranial; CD, caudal.

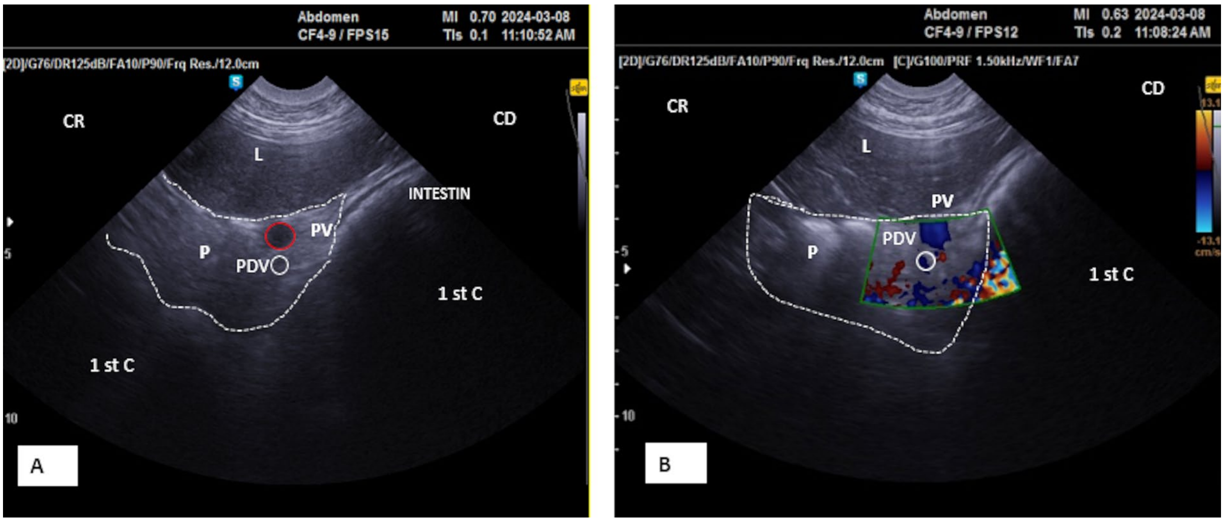


FIGURE 8
**(A)** Transverse scan of the right lobe of the pancreas of the middle third of the 10th. **(B)** Transverse scan of the right lobe of the pancreas of the middle third of the 10th using Doppler mode. P, Pancreas (white dotted outline); PV, portal vein (red circle); PDV, pancreatico-duodenal vein (white circle); L, liver; 1st C, (first stomach compartment); CR, cranial; CD, caudal.

($p < 0.0001$) in adult camels: 3.08 ± 0.52 cm ($n = 8$). The pancreatic parenchyma appears hyperechoic compared to the kidney and slightly hypoechoic compared to the spleen (Figure 11). The portal vein is absent in this area; however, the splenic vein is visible, when using Doppler color flow (Figure 12), and appears as a small anechoic channel on longitudinal scans (Figure 11) and as an anechoic circle on transversal scans (Figure 13).

Ultrasonography can be a challenge to delineate the accessory lobe. However, as it forms the pancreatic annulus around the portal vein, Doppler imaging helps define the vein and, therefore, can visualize the surrounding structures (Figure 8).

Ultrasound examination of non-fasted dromedaries showed acoustic shadows from solid food boluses in the duodenal ampulla, obscuring the pancreatic parenchyma (Figure 14). In contrast, food deprivation for 12 h eliminates this phenomenon (Figure 9). However, the thickness of the pancreatic parenchyma was reduced during the contraction phase of digestion in all animals, even after fasting (Figures 6A, 9A). Additionally, a comet tail artifact from the contractions of the distended rumen was observed above the left lobe,

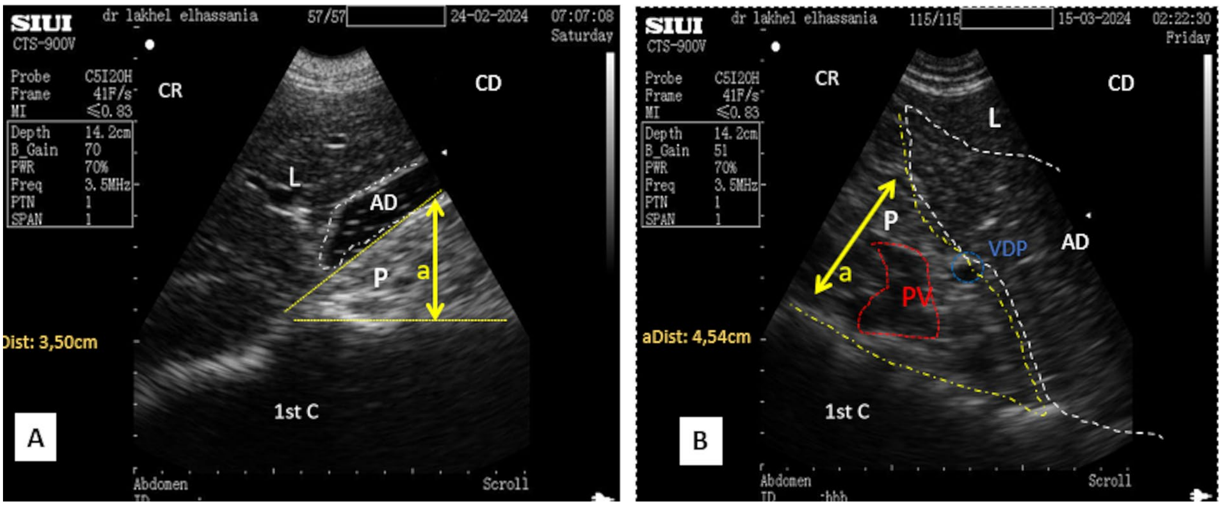


FIGURE 9
**(A)** Transverse scan of the right lobe of the pancreas in the middle third of the 10th intercostal space. **(B)** Transverse scan of the right lobe of the pancreas in the lower third of the 10th intercostal space; 1st C, (first stomach compartment); P, pancreas (yellow dotted outline); L, liver; AD, duodenal ampulla (white dotted outline); PV, portal vein (red dotted outline); (aDist), thickness of pancreatic of the right lobe of the pancreas; CR, cranial; CD, caudal.

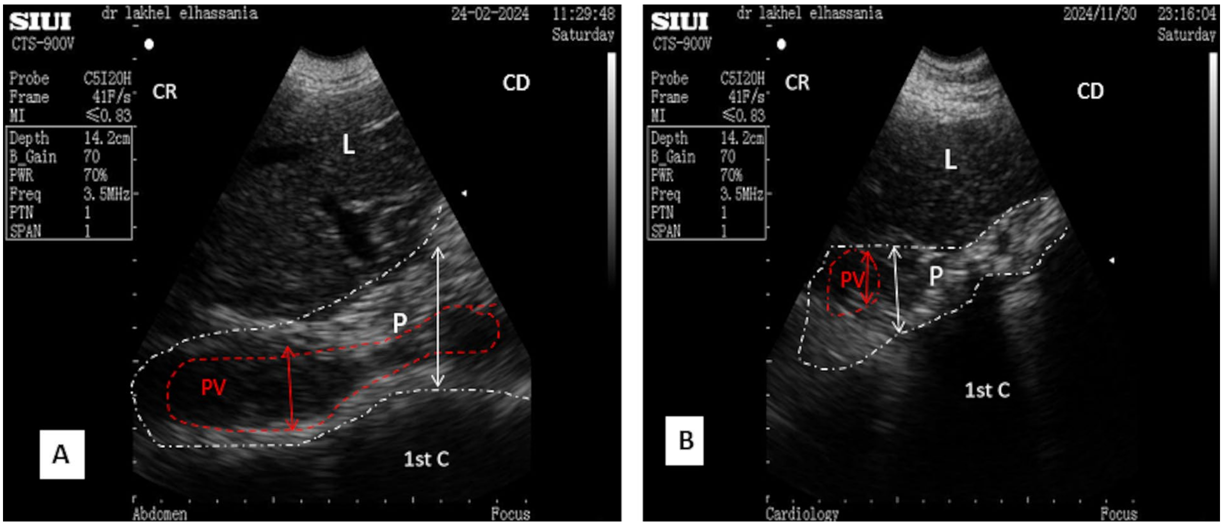


FIGURE 10
**(A)** Longitudinal scan of the right lobe of the pancreas in the middle third of the 9th intercostal space. **(B)** Transversal scan of the right lobe of the pancreas in the middle third of the 9th intercostal space; 1st C, (first stomach compartment); P, pancreas (white dotted outline); L, liver; PV, portal vein (red dotted outline); CR, cranial; CD, caudal.

further complicating the interpretation of the ultrasonographic patterns (Figure 15).

## 4 Discussion

In the camel, ultrasonography has not yet been used as a basic diagnostic tool for abdominal viscera disorders, particularly those of the pancreas. In the present study, ultrasonography was used to explore the pancreas in healthy camels, combined with a detailed inspection of camel carcasses to enable direct assessment of the conformation and topography of the organ.

The results of the macroscopic anatomy and topographic investigation of the pancreas are consistent with previous findings in this species (12–16).

Furthermore, the pancreas differs from that of the ox by the development of the left lobe and the reduction in the right lobe as well as by the absence of the accessory pancreatic duct (14).

Despite its deep position, the pancreas is closely related to adjacent organs, fitting within the spaces between them (17). Ultrasound examination can effectively visualize the pancreas through various acoustic windows. The acquired anatomical observations from slaughtered animal carcasses provide valuable insights that can be reflected in the ultrasound images.

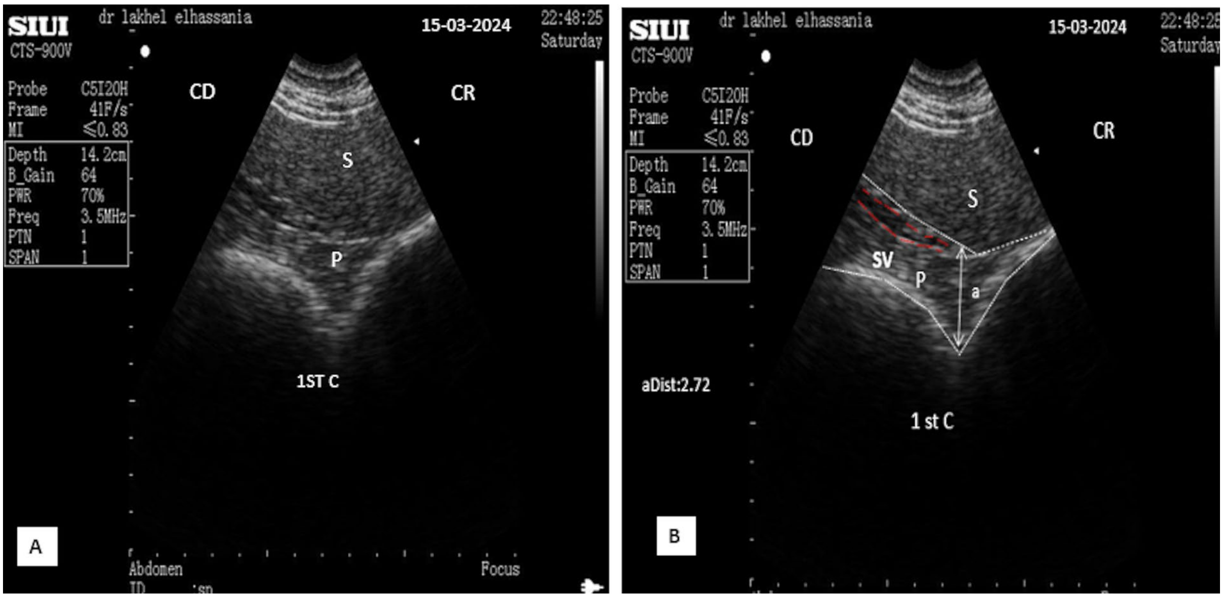


FIGURE 11
**(A)** Longitudinal scan of the left lobe of the pancreas ventrally to the anterior extremity of the spleen under 4th transverse process of the lumbar vertebra in the left flank. (**B**: Identification of structures on the ultrasound image). S, Spleen; P, pancreas (white dotted outline); SV, splenic vein (red dotted outline); (aDist), thickness of the left lobe of the pancreas; CR, cranial; CD, caudal.

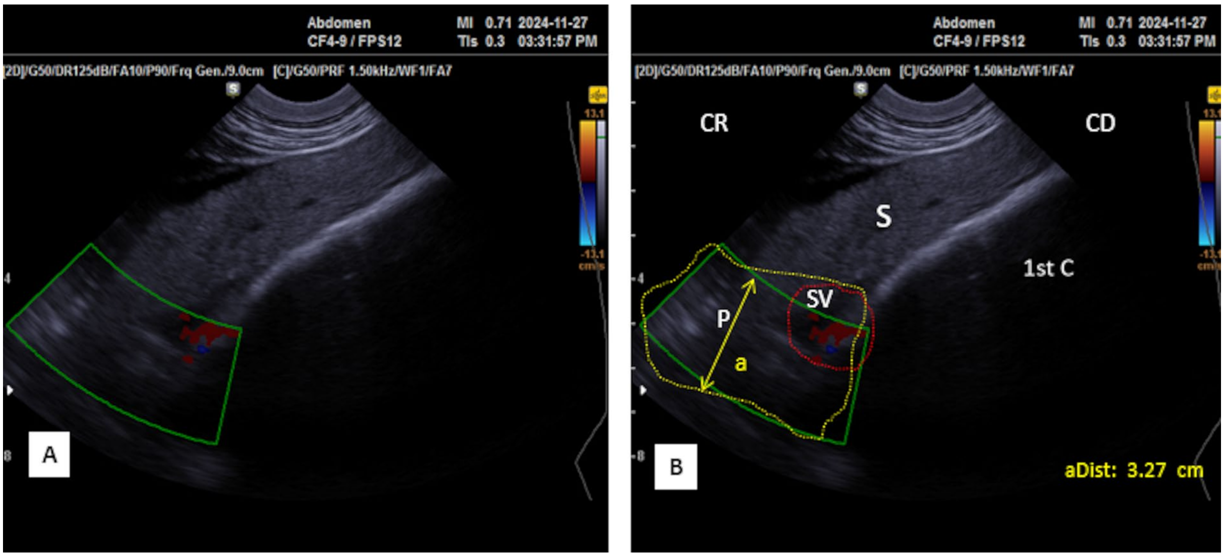


FIGURE 12
**(A)** Transversal scan of the left lobe of the pancreas ventrally to the anterior extremity of the spleen under third transverse process of the lumbar vertebra in the left flank Samsung MH70A Doppler ultrasound scanner. (**B**: Identification of structures on the ultrasound image). S, Spleen; P, pancreas (yellow outline); SV, splenic vein (red dotted circle); (aDist), thickness of the left lobe of the pancreas; 1st C, (first stomach compartment); CR, cranial; CD, caudal.

The ultrasonographic evaluation and measurement of the pancreas in young and adult camels were primarily conducted using the SIUI CTS-900 V ultrasound scanner, which demonstrated effective imaging capabilities for the pancreas. Various transducers were assessed, but the 3.5 MHz micro-convex probe was retained for its optimal ease of use, particularly in intercostal spaces. However, as the SIUI CTS-900 V ultrasound scanner does not incorporate Doppler functionality, a Samsung MH70A Doppler ultrasound scanner, a 3.5-MHz micro-convex probe, was also used for ultrasound examination in four females to visualize and assess the associated vessels.

The pancreatic body parenchyma was visualized by positioning the probe at the level of the portal hepatic incisure. This finding corroborates the descriptions provided by Mostafa et al. (12), as well as our anatomical observations on the carcasses of four young camels, confirming its position below the first and second lumbar vertebrae and behind the upper third of the 12$^{th}$ rib. Mostafa et al. (18) and


FIGURE 13
**(A)** Transverse scan of the left lobe of the pancreas under 3rd transverse process of the lumbar vertebra in the left flank. **(B)** Transverse scan ventrally to the anterior extremity of the spleen under 2nd transverse process of the lumbar vertebra in the left flank. S, Spleen; Lk, left kidney; P, pancreas (white outline); SV, splenic vein (red dotted circle); (aDist), thickness of the left lobe of the pancreas; 1st C, (first stomach compartment); CR, cranial; CD, caudal.

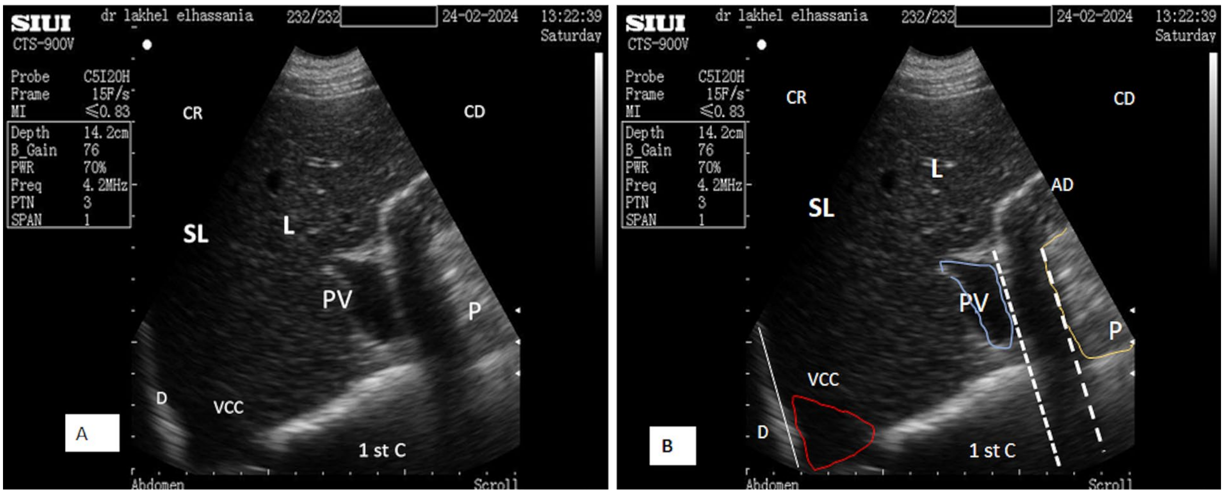


FIGURE 14
**(A)** Transverse scan of the right lobe of the pancreas in the upper third of the 10th intercostal space in the contraction phase. **(B)** Identification of structures on the ultrasound image. SL, shadow of the lung; L, liver; AD, duodenal ampulla; P, pancreas (yellow line); white dotted line, acoustic shadow; PV, portal vein (blue outline); VCC, caudal vena cava (red outline); D, diaphragm; 1st C, (first stomach compartment); CR, cranial; CD, caudal.

Barone (17) also describe the accessory lobe surrounding the portal vein, forming the pancreatic annulus. This structure appears as an anechoic pattern in ultrasonographic imaging and is confirmed by color Doppler ultrasonography. However, distinguishing the accessory lobe as a separate part remains a challenge.

The diameter of the portal vein observed in the body lobe is higher in adults but similar for both sexes. In transversal scans, it averages $1.8 \pm 0.19$ cm in young camels and $3.14 \pm 0.18$ cm in adults.

Furthermore, in camels, the ultrasonographic pattern of the pancreatic body appears hyperechoic, elongated, and irregular in shape, whereas imaging in cows reveals a triangular shape, as noted by Pusterla and Braun (19) and confirmed by Tharwat et al. (20); this triangular structure is related to liver, portal vein, right kidney, and duodenum. In cows, the ultrasonographic pattern of the body lobe is either isoechoic or slightly more echogenic than the reference ultrasonographic pattern of the liver.

The ultrasonography of the pancreatic right lobe of the camel revealed variations in shape and thickness across three acoustic windows. The parenchyma appeared elongated or trapezoid in the 11th intercostal space, triangular to prism-like in the 10th, and irregular or

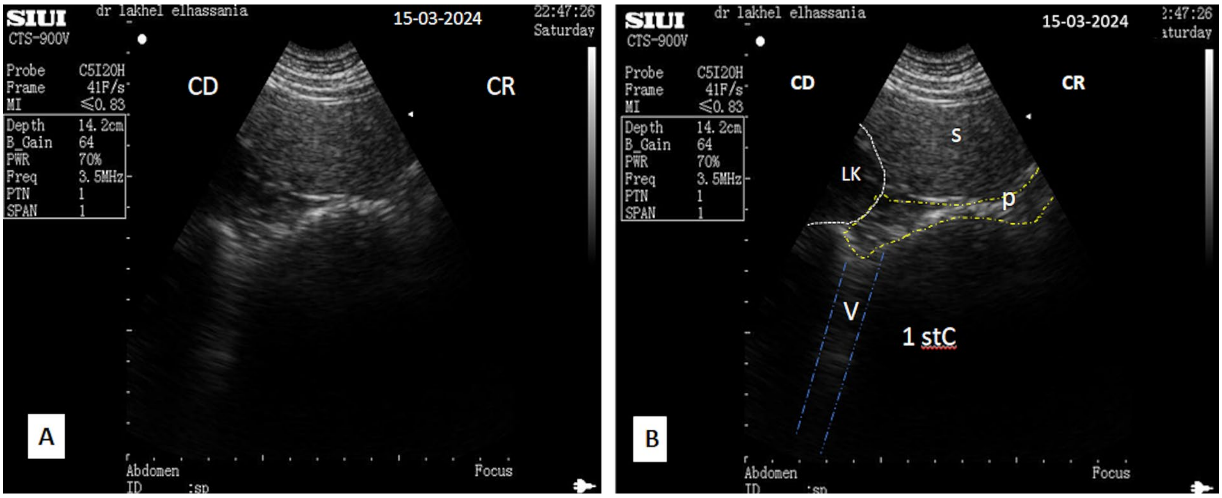


FIGURE 15
**(A)** Transverse scan of the left lobe of the pancreas ventrally to the anterior extremity of the spleen under second transverse process of the lumbar vertebra in the left flank in the contraction phase and (**B**, identification of structures on the ultrasound image); S, spleen; P, pancreas (yellow dotted line); LK, left kidney; 1st C, (first stomach compartment); V, vibration artifact or tail artifact (blue dotted line); CR, cranial; CD, caudal.

band-like in the 9th. It appears close to the duodenal ampulla in the 10th and 11th intercostal spaces, but it is near the abomasum and first stomach compartment in the 9th intercostal space. In contrast, according to Pusterla and Braun (19), the right lobe of the pancreas, in cows, is triangular and generally isoechoic or slightly more echogenic.

The thickness of the pancreatic parenchyma of the right lobe differed across the three acoustic windows; the lowest measurements were obtained in the 9th intercostal space, whereas the highest were in the 10th and a slightly reduced in the 11th. In all windows, the thickness was consistently greater in adults than in young camels. In contrast, the portal vein showed gradual widening across the windows.

Similar to cows (19) and dogs (21), the pancreatic ducts are visible in camels. In particular, the major pancreatic duct is present within the right lobe, as seen in cows, but is very clear in ultrasonographic patterns when scanned in the middle third of the 11th intercostal space (Figure 4). The mean diameter observed was 0.67 ± 0.05 cm (n = 14) for young camels and 0.79 ± 0.05 cm (n = 8) for adult camels, which is consistent with the macroscopic structure noted by Mostafa et al. (12). However, the accessory pancreatic duct is absent, which aligns with anatomical data.

The left lobe was successfully visualized by placing the probe in the left flank, specifically in the region defined cranially by the last rib, caudally by the left kidney, ventrally by the first stomach compartment (rumen), and dorsally by the spleen, which corroborates the description of Mostafa et al. (12). In contrast, the left lobe of the pancreas is not visible in cows, according to Tharwat et al. [19] and Pusterla and Braun (19).

The measurements of the pancreatic parenchyma were conducted through the intercostal spaces using both transversal and longitudinal scanning planes. The probe was oriented in multiple directions to ensure a comprehensive examination of the entire parenchyma, covering the different lobes of the pancreas, which sometimes allows measurements of length, width, and thickness. Imprecision may arise from the irregularity of the organ and its complex anatomical location. Therefore, specific measurements may not necessarily reflect the accurate macroscopic dimensions of the pancreas.

According to the macroscopic study of the pancreas of 14 young camels slaughtered at Sidi Bibi abattoir, the weight of the organ is nearly identical in females and males, which is 113.7 ± 14.9 g. Adult camels were not slaughtered in this abattoir, but according to Mostafa et al. (12), the weight of the pancreas can vary between 300 and 500 g. This finding explains the greater thickness of the pancreatic parenchyma of the body in the adults, measuring 4.05 ± 0.34 cm, and 3.60 ± 0.26 cm in young camels. Regarding the left lobe, it measured 2.32 ± 0.31 cm in adults and 3.08 ± 0.52 cm in young camels. Additionally, in the 10th intercostal space, the thickness of the right lobe was 5.9 ± 0.25 cm in the adult camels and 4.40 ± 0.20 cm in young camels.

Several pancreatic lesions have been described in cattle; in particular, pancreatic atrophy is associated with nutritional deficiencies, pancreatic lithiasis, and tumors (22). Because pancreatic diseases often elude clinical animal evaluation, veterinarians must rely on diagnostic tools that complement the patient's history, clinical signs, and laboratory results, such as ultrasonography (19).

For example, in Denmark, cases of pancreatic calculi have been observed in slaughtered cattle over a 3-month period, with a frequency of 0.43% (23). Using ultrasound technology has been proven to be particularly valuable in diagnosing pancreatic calculi in cows exhibiting non-specific symptoms such as fever, anorexia, and weight loss. Ultrasonographic examination of the pancreas showed a distortion of its reference triangular shape, with a tendency toward a hypoechoic pattern and the presence of pancreatic stones accompanied by distal acoustic shadowing (24). In addition, the ultrasonographic patterns of experimentally induced pancreatitis in cattle showed that patchy hypoechoic foci developed within the pancreatic parenchyma (22).

The pancreatic pseudocysts are another example. One or more circular cystic structures with more or less well-defined contours within the pancreas were observed during ultrasound examinations in dogs. These structures are often wall-less and contain hypoechoic or even anechoic content; these structures typically lack walls and may contain hypoechoic or anechoic content, sometimes with hyperechoic debris dispersed throughout (25).

In addition, in the case of pancreatic abscesses in dogs, the pancreas shows a mass effect, and its echogenicity is variable: a hyperechoic mass with hypoechoic areas corresponding to fluid accumulations can be observed (26).

Pancreatic abnormalities in camels have not yet been described by ultrasound technique. Furthermore, reference models for the normal ultrasonographic appearance of the pancreas are not available, making the present study particularly valuable by providing essential data for the ultrasound examination in this species. However, pancreatic abnormalities have been well-defined in other species, which may be used as a reference for ultrasound examinations of pancreatic lesions in dromedary camels while pending the implementation of such examinations.

Pancreatic lesions represent a subtle and often overlooked pathological case in animals. They manifest as progressive weight loss, affecting the fattening process, leading to reduced meat yield and significant economic losses for farmers. This case underscores the importance of incorporating ultrasonography, which may help in detecting pancreatic lesions and implementing appropriate treatment.

In addition to the challenges associated with ultrasonography in camels compared to other species, such as the need for experienced handlers for restraint, animal preparation time is also crucial. It includes meticulous shaving to ensure better contact between the abdominal wall and probe and generous gel application. The frequent agitation of camels can disrupt the ultrasound trial by displacing the organs and altering their stability. Therefore, light sedation or anesthesia may be necessary, as it helps slow down respiratory movements and ruminal contractions, which is beneficial for obtaining more explicit ultrasound images.

Ultrasound can be performed in either a standing or sitting position. Sometimes, the sitting position is the only option when the animal cannot be anesthetized or is too agitated, but it is essential to take into account the displacement of organs. It is recommended that the animal be deprived of food to prevent interference from ruminal overload. Movements caused by ruminal contractions and respiration can create artifacts and disrupt organ visualization. Consequently, synchronizing the examination with the respiratory phase may help optimize image quality.

Finally, a micro-convex probe is ideal for pancreatic ultrasonography. It facilitates exploration and a better visualization of the organ through narrow intercostal spaces with a frequency of 3.5 MHz reaching a minimum depth of 14 cm, especially as the organ is anatomically deep. The Samsung MH70 ultrasound scanner stands out for its superior resolution and advanced tools, including the Doppler function, which provides valuable information about vascularization. In contrast, the SIUI CTS-900 V ultrasound scanner is effective for routine examinations but is limited by its requirement for Doppler capability. Consequently, the choice of ultrasound machine will depend on the specific needs of the veterinarian and the available budget.

## 5 Conclusion

Ultrasonography is a reliable and non-invasive diagnostic modality for the assessment of the pancreas in various species, including the dromedary camel, despite the deep anatomical positioning of the organ. This study aimed to elucidate the ultrasonographic characteristics of the pancreatic tissue in dromedary camels, thereby advocating for its incorporation into routine veterinary practice. Establishing a reference database for normal pancreatic ultrasonographic patterns and values will enable veterinarians to identify abnormalities, facilitating early detection of pancreatic lesions, particularly in cases where clinical symptoms are non-specific.

Early diagnosis and prompt intervention in pancreatic disorders are crucial for mitigating potential complications, enhancing clinical outcomes, and ultimately reducing economic losses for camel husbandry. Given the increasing challenges posed by climate change, improving the health and productivity of camel livestock through advanced diagnostic techniques is imperative. The findings of this study underscore the significance of ultrasonography as a vital tool for the veterinary assessment of pancreatic health in dromedary camels, contributing to both animal welfare and agricultural sustainability.

## Data availability statement

The original contributions presented in the study are included in the article/supplementary material, further inquiries can be directed to the corresponding authors.

## Ethics statement

The animal study was approved by Committee of Institute of Agronomy and Veterinary Medicine. The study was conducted in accordance with the local legislation and institutional requirements.

## Author contributions

EL: Conceptualization, Formal analysis, Funding acquisition, Investigation, Methodology, Resources, Visualization, Writing – original draft, Writing – review & editing, Software. KE: Conceptualization, Data curation, Formal analysis, Investigation, Methodology, Validation, Visualization, Writing – review & editing. MA: Conceptualization, Data curation, Funding acquisition, Investigation, Methodology, Software, Supervision, Validation, Visualization, Writing – review & editing. RA: Conceptualization, Funding acquisition, Investigation, Methodology, Resources, Software, Supervision, Validation, Visualization, Writing – review & editing.

## Funding

The author(s) declare that no financial support was received for the research, authorship, and/or publication of this article.

## Acknowledgments

The authors wish to express their sincere gratitude to Mohamed Cherrat Ikbal, the head of the veterinary service at ONSSA of Chtouka Ait Baha, and El Malki Rachid, the veterinary technician, for their valuable support in facilitating access to the slaughterhouse, as well as to the butchers who own the animals involved in this study. The authors also want to thank Baroudi Abdelmonim, owner and manager of the El Khattabi Laboratory in Essaouira, for graciously conducting blood parameters analyses. The authors would like to thank Professor Farssi Hicham for his expertise and invaluable assistance in the statistical analysis of this study. Finally, the authors thank the Unit of Comparative Anatomy staff and the Unit of Equine PMC, Hassan IInd Agronomy and Veterinary Institute, Rabat, Morocco, for their valuable collaboration and continuous support throughout this study.

## Conflict of interest

The authors declare that the research was conducted in the absence of any commercial or financial relationships that could be construed as a potential conflict of interest.

The author(s) declared that they were an editorial board member of Frontiers, at the time of submission. This had no impact on the peer review process and the final decision.

## Publisher's note



## References

1. Kandil HM, Wassif IM, Rabee A, Khidr RE, Shoukry MM, Askar AR. Camel, the animal of food security and climate change. *Egypt J Camel Sci*. (2023) 1:1–8. doi: 10.21608/ejcs.2023.220447.1008

2. Askar A. R., Ehdaa R., Rawia D. (2021). Effects of concentrate supplement level on camel-calves growing performance under semi-intensive production system. International Conference for Nature and Natural Resources Conservation- Towards 2030 and Beyond, Sharm El cheikh, Egypt, 87.

3. Al Jassim R, Veerasamy S. Review paper: climate change and camel production: impact and contribution. *J Camel Sci*. (2015) 8:1–17. doi: 10.1016/0300-9629(85)90718-2

4. Hegazy A. A. AND Fahmy Lotfia S. (2007). Atlas of camel diseases. Academy of Scientific Research and Technology, Egypt.

5. Schmitz DG. Understanding the principles of equine ultrasonography. *Vet Medi*. (1991) 52:748–52.

6. Summant V, Purohit GN, Parrek PK, Sahani MS. Ultrasonographic imaging to monitor early pregnancy in the camel (*Camelus dromedarius*). *Revue ElevMed VétPays Trop*. (2002) 55:241–5.

7. Tharwat M, Al Sobayil F, Ali A, Buczinski S. Transabdominal ultrasonographic appearance of the gastrointestinal viscera of healthy camels (*Camelus dromedaries*). *Res Vet Sci*. (2012) 93:1015–20. doi: 10.1016/j.rvsc.2011.12.003

8. Binici C, Baron VON König U, Weber J. Diagnosis of hepatic diseases in ruminants and camelids with a special focus on sonographic examination. *Schweiz Arch Tierheilkd*. (2021) 163:397–408. doi: 10.17236/sat00304

9. Moran CM, Thomson AJW. Preclinical ultrasound imaging. A review of techniques and imaging applications. *Front Phys*. (2020) 8:124. doi: 10.3389/fphy.2020.00124

10. Bengoumi M (1992). Clinical biochemistry of the dromedary and mechanisms of its adaptation to dehydration. PhD thesis of sciences. I.A.V. Hassan II, Rabat, Morocco.

11. Mura U, Mohamed AS, Osman AM, Ipata PL. A comparative study of serum and organ alpha-amylases of the camel (*Camelus dromedarius*). *Comp Biochem Physiol A*. (2005) 82:141–4.

12. Mostafa MS, Aly MA, Ammar S, Aly AE. Topography, morphology and duct system of pancreas of the camel. *Assiut Vet Med*. (1983) 10.2:8–13. doi: 10.21608/avmj.1983.191139

13. Smuts MMSAND, Bezuidenhout AJ. Anatomy of the dromedary. Oxford: Clarendon Press (1987).

14. Ouhsine A. Study of the topography of the abdominal viscera in the dromedary in sternal decubitus position. *Revue Élev Méd Vét Pays trop*. (1989) 42:73–8.

15. Taha AAM, Abdel-Magiede M. Anatomy of the pancreas of the one-humped camel (*Camelus dromedarius*). *J Camel Pract Res*. (1998) 5:57–61.

16. Sultan H.S. (1999). Some morphological studies on the pancreas of the camel (*Camelus dromedarius*). M. Sc. Thesis, University of Khartoum.

17. Barone R. Comparative anatomy of domestic mammals. Volume 4. Splanchnology II. *2nd* ed. Paris: Vigot (1990).

18. Mostafa MS, Aly MA, Ammar S, Aly AE. Blood vessels and nerfs of pancreas of the camel. Assiut. *Vet Med*. (1983) 10.2:14–9. doi: 10.21608/avmj.1983.191140

19. Pusterla N, Braun U. Ultrasonic examination of the pancreas in healthy cows. *Vet Radiol Ultrasound*. (1997) 38:63–8. doi: 10.1111/j.1740-8261.1997.tb01605.x

20. Tharwat M, Sato H, Kurosawa T, Oikawa S. Transcutaneous ultrasound-guided pancreatic biopsy in cattle and its safety: a preliminary report. *Vet J*. (2003) 166:188–93. doi: 10.1016/S1090-0233(03)00027-3

21. Penninck DG, Zeyen Taeymans ON, Cynthia R, Webster CR. Ultrasonographic measurement of the pancreas and pancreatic duct in clinically normal dogs. *AJVR*. (2013) 74, 74:433–7. doi: 10.2460/ajvr.74.3.433

22. Tharwat M, Sato H, Kurosawa T, Oikawa S, Nitanai A. Ultrasonographic imaging of experimentally induced pancreatitis in cattle. *Vet J*. (2003) 165:314–24. doi: 10.1016/S1090-0233(02)00179-X

23. Velling K. Bovine pancreolithiasis in Denmark. *Acta Vet Scand*. (1975) 16:327–40. doi: 10.1186/BF03546651

24. Tharwat M, Abdelaal AM, Selim H, El Magawry S, Floeck M. Ultrasonographic identification of pancreolithiasis in a Holstein cow: a case report. *Vet Med Aust*. (2013) 100:19–23.

25. Vanenkevort B, O'Brien R, Young K. Pancreatic pseudocysts in 4 dogs and 2 cats: ultrasonographic and clinic pathologic findings. *J Vet Intern Med*. (1999) 1999:309–13.

26. Kolb H., Testault I. (2013). Ultrasound of pancreatic diseases in cats and dogs. France: Le Point Vétérinaire.

Frontiers in Veterinary Science

TYPE Original Research
PUBLISHED 19 February 2025
DOI 10.3389/fvets.2025.1507817

Check for updates

OPEN ACCESS

EDITED BY
Mindaugas Tamosiunas,
University of Latvia, Latvia

REVIEWED BY
Zeki Yilmaz,
Faculty of Veterinary Medicine, Türkiye
Vaida Vaskeliene,
Kaunas University of Technology, Lithuania

*CORRESPONDENCE
Ryou Tanaka
ryo@vet.ne.jp
Lina Hamabe
linahamabe@go.tuat.ac.jp

RECEIVED 08 October 2024
ACCEPTED 07 January 2025
PUBLISHED 19 February 2025

CITATION
Hirose M, Ma D, Shimada K, Yoshida T, Matsuura K, Kitpipatkun P, Hatanaka A, Zhao Y, Takahashi K, Tanaka R and Hamabe L (2025) Effects of trans-mitral flow patterns and heart rate on intraventricular pressure gradients and E/E' in the early stage of a rat model of hypertensive cardiomyopathy.
*Front. Vet. Sci.* 12:1507817.
doi: 10.3389/fvets.2025.1507817



# Effects of trans-mitral flow patterns and heart rate on intraventricular pressure gradients and E/E' in the early stage of a rat model of hypertensive cardiomyopathy

Miki Hirose[1], Danfu Ma[2], Kazumi Shimada[1], Tomohiko Yoshida[3], Katsuhiro Matsuura[4], Pitipat Kitpipatkun[1], Akari Hatanaka[1], Yanbing Zhao[2], Ken Takahashi[5], Ryou Tanaka[1]* and Lina Hamabe[6]*

[1]Veterinary Teaching Hospital, Veterinary Medicine, Tokyo University of Agriculture and Technology, Tokyo, Japan, [2]College of Veterinary Medicine, Nanjing Agricultural University, Nanjing, China, [3]Department of Small Animal Medical Centre, Obihiro University of Agriculture and Veterinary Medicine, Obihiro, Japan, [4]Department of Small Animal Clinical Sciences, University of Florida, Gainesville, FL, United States, [5]Department of Pediatrics and Adolescent Medicine, Juntendo University Graduate School of Medicine, Tokyo, Japan, [6]Department of Veterinary Clinical Oncology, Tokyo University of Agriculture and Technology, Tokyo, Japan

**Background:** The mitral inflow spectral is expressed as two separate waves: early diastolic trans-mitral flow velocity (E) and late diastolic trans-mitral flow velocity (A) waves. When the heart rate (HR) increases and the diastolic time diminishes, the mitral flow pattern changes from EA-separation to EA-fusion. The E wave provides information about preload and diastolic function. Tissue Doppler imaging (TDI) and non-invasive intraventricular pressure gradient (IVPG) based on color-M-mode echocardiography are two techniques established in recent years with good repeatability in cardiac function evaluation, especially diastolic.

**Hypothesis/objective:** We hypothesize that IVPG and E/E' are differentially influenced by mitral inflow patterns.

**Animals:** A total of 66 hypertensive cardiomyopathy (HTN-CM) induced by abdominal aorta coarctation and 33 sham-operated rats were divided into 6 groups according to trans-mitral flow patterns.

**Methods:** Conventional echocardiography, TDI, and IVPG sampling were performed on rats under general anesthesia with 2.5% isoflurane at 3 weeks after the operation. After code EA-separation = 1, EA-half-separation = 2, and EA-fusion = 3, Pearson's correlation tests were performed.

**Results:** Both E and E' in EA-fusion (1.04 ± 0.13 and 7.65 ± 0.84) are higher than the EA-separation pattern in all rats (0.91 ± 0.10 and 5.51 ± 0.78, $p < 0.001$). The preload change has more impact on E' than E (0.443 vs. 0.218, $p < 0.001$, respectively), which leads to decreased E/E' in EA-fusion. Total IVPG and basal IVPG positively correlated with the mitral inflow pattern (0.265 and 0.270, $p < 0.001$), while mid-to-apical IVPG was not (0.070, $p = 0.281$).

**Conclusion:** The mitral inflow pattern positively correlates with basal IVPG, E, and E'. Mid-to-apical IVPG was independent of mitral inflow patterns, while E/E' tended to be lower when the mitral inflow pattern changed from EA-separation to EA-fusion.

KEYWORDS

**diastolic function, echocardiography, heart rate, hypertensive cardiomyopathy, intraventricular pressure gradient, rat model**

## Introduction

Hypertension was the leading risk factor for the world's disease burden (1). Hypertensive cardiomyopathy (HTN-CM), a structural cardiac disorder resulting from hypertension, is characterized by left ventricle (LV) hypertrophy and diastolic dysfunction and is considered a silent killer with irreversible characteristics (2–4). It is crucial to diagnose HTN-CM at the early stage since morbidity and mortality synergistically increase with progressed HTN-CM (2). Although conventional echocardiography can evaluate diastolic function through mitral inflow, it is necessary to distinguish pseudo-normal patterns. The Valsalva maneuver is performed to differentiate between normal and pseudo-normal mitral flow patterns, but it is not used in small animals due to the difficulty in managing their breathing. As a result, assessing diastolic function in animals remains challenging (5, 6). The invasive catheterization test is the only method to accurately evaluate diastolic function (7). Nevertheless, the catheterization test is not useful in clinical settings because of its invasiveness, unrepeatability, time-consuming, and laborious; therefore, scientists have developed novel echocardiography technologies to monitor cardiac function non-invasively.

Elevated heart rate (HR) is a risk factor for cardiovascular morbidity and mortality in HTN-CM patients (8). In addition to the aggravation of the patient's condition, high HR also affects the diagnosis of cardiac diseases. For instance, when the HR is elevated, diastasis is encroached or even disappears during the diastolic phase, which leads to a change of trans-mitral inflow pattern to EA-fusion (Figure 1A) or EA-half-separation (Figure 1B) from EA-separation (Figure 1C). EA-half-separation is defined as early diastole in which the atrial contraction is partially merged into the mitral inflow or myocardium movement. This pattern is regarded as the midterm status between EA-separation and EA-fusion.

Meanwhile, in the EA-fusion pattern, the early diastolic phase is completely merged with atrial contraction, such that atrial contraction is the only LV filling period (9). The early diastolic phase plays an indispensable role in LV filling because not only does it have the greatest filling volume but also the status of the early diastolic phase explains the diastolic function. Although sometimes performing echocardiography after patients calm down could avoid EA-fusion, the EA-fusion pattern is still especially common in cats and human patients (8, 10); in this scenario, conventional echocardiography, intraventricular pressure gradient (IVPG), and E/E' are hard to judge by the veterinary clinician in EA-fusion.

Tissue Doppler imaging (TDI) is a useful tool for the quantitative assessment of systolic and diastolic function through the evaluation of the myocardium movement velocities during the cardiac cycle. However, the angle-dependent character diminishes its accuracy, and the steep learning curve for TDI data analysis limits its availability (11).

The IVPG creates a suction force that drives blood from the left atrium (LA) to the LV during early diastole. This mechanism plays a crucial role in diastole because early diastole fills approximately 80% of the ventricle volume. Therefore, IVPG is considered a diastolic indicator *in vivo*. Non-invasive IVPG measurement from color-M-mode echocardiography (CMME) using the Euler equation is well correlated with the gold standard of diastolic function parameter tau, which refers to the LV diastolic time constant (12–14). Moreover, IVPG can be used

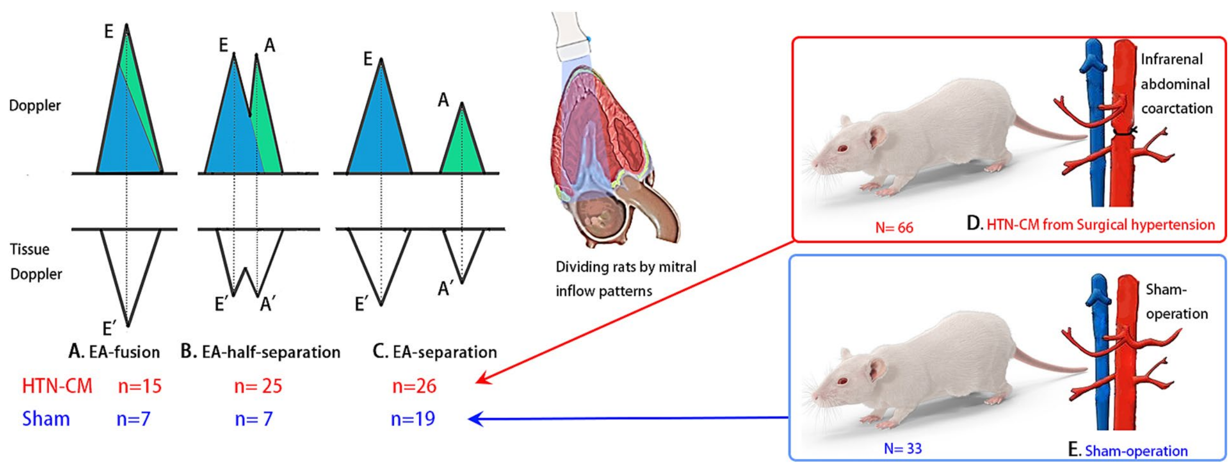


FIGURE 1
Experiment design and mitral inflow patterns: The blue color in the Doppler image indicates the volume of early diastole, and the green color represents the volume of atrial contraction. **(A)** EA-fusion pattern, indicating mixed early diastole and atrial contraction, **(B)** EA-half-separation, **(C)** EA-separation, **(D)** HTN-CM from abdominal aorta coarctation, **(E)** Sham-operation.

for serial assessment of diastolic function in healthy and HTN-CM animals as well as humans from infant to adult (4, 15). Thus, IVPG could easily grade HTN-CM patients using the diastolic function (4).

A previous study proved that IVPG was useful in evaluating diastolic function in hypertensive cardiomyopathy in rats (16). However, the relationship between the mitral inflow pattern and IVPG and E/E' measurements is still unknown. Therefore, this study aimed to determine whether IVPG and E/E' are affected by mitral inflow patterns or not and to find out the relationship between IVPG and mitral inflow patterns in HTN-CM rat models. We hypothesize that IVPG and E/E' are differentially influenced by mitral inflow patterns.

# Materials and methods

## Animal preparation and experimental protocol

The present study was approved by the Animal Care and Use Committee of the Tokyo University of Agriculture and Technology (Approval number: 30-56), and the study was conducted under the National Guide for the Care and Use of Laboratory Animals (1994). A total of 99 healthy 10-week-old female Sprague Dawley rats (Kitayama Labes, Nagao, Japan) weighing 220–250 grams (average ± SD) were included in the study. Rats were given water and food ad libitum and kept in an air-conditioned room at 21°C under a 12-h light/dark cycle. Animals were randomly assigned to two groups: the hypertensive cardiomyopathy group (HTN-CM group, $n = 66$), created by abdominal aorta constriction, and the sham-operated control group (control group, $n = 33$).

For the HTN-CM group, an abdominal aorta coarctation operation was performed as previously described (16). The rats were anesthetized with 40 mg/kg intraperitoneal pentobarbital sodium and were placed in the dorsal position under an operating microscope (Leica M60, Wetzlar, Germany). The abdominal aorta was exposed and dissected from the caudal vena cava (above/below the renal artery) using a cotton swab. The abdominal aorta was ligated using a 3–0 silk suture with a 21-gage needle placed along the side of the aorta to avoid complete ligation (Figure 1D). The needle was removed, and after confirming blood flow had returned to the hind limb without cyanosis, the abdominal incision was closed. Rats in the control group underwent the same procedure without the ligation of the aorta (Figure 1E).

Three weeks postoperatively, blood pressure measurements, conventional echocardiography, and CMME were performed on all rats. In the HTN-CM group, hypertensive cardiomyopathy was confirmed based on the increased LV mass and elevated blood volume (3).

## Blood pressure

The non-invasive blood pressure measurement was obtained using the oscillometric method from the tail (BP monitor for rats, Muromachi, Japan), while the rats were placed in a small cage to limit their movements. Three consecutive measurements were taken, and the average of systemic systolic, diastolic, and mean arterial blood pressure was reported.

## Conventional echocardiography

To minimize the influence of anesthesia and environmental stimulation on the mitral inflow pattern and HR, rats were anesthetized with a set protocol of 2.5% isoflurane with 1 L/min oxygen supply delivered through a mask, and echocardiographic examination was carried out after the stabilization of the HR. Under general anesthesia, rats were positioned in right lateral recumbency, and an echocardiographic examination was performed in accordance with the methodology described by the European Society of Cardiology (6). The morphologic parameters, including left ventricle internal diameter in end-diastole (LVIDd) and left ventricle internal diameter in end-systole (LVIDs), were obtained from the M-mode at the right parasternal short axis view. Early diastolic trans-mitral flow velocity (E) and late diastolic trans-mitral flow velocity (A) were obtained using pulse-wave Doppler mode at the left parasternal apical four-chamber view. All measurements were taken from five consecutive heart cycles, and the average of the obtained parameters was used.

Left ventricle mass (LVM) was calculated with the formula below (6):

$$\mathrm{LVM} = 1.04\left[\left(\mathrm{LVIDd} + \mathrm{IVSd} + \mathrm{LVFWd}\right)^3 - \mathrm{LVIDd}^3\right] \times 0.8 + 0.6 \quad (1)$$

Tissue Doppler imaging (TDI) was performed from the left parasternal apical four-chamber view. The left ventricular free wall and interventricular septal mitral annular tissue velocities were measured with a sample volume of 0.5 mm. The mitral annular tissue velocity profile, which includes early diastolic tissue velocity (E') and late diastolic tissue velocity (A') at the interventricular septum (IVS) and left ventricular posterior wall (LVFW), was obtained.

E/E' was calculated by the below formula:

$$E / E' = \left(\frac{E}{E'\text{at IVS}} + \frac{E}{E'\text{at LVFW}}\right) \Big/ 2 \quad (2)$$

LV end-diastolic pressure (LVEDP) and LV diastolic pressure at the onset of the a-wave (Pre-A LVDP) were calculated by the linear regression equation from invasive catheterization and E/E' (17).

$$\mathrm{LVEDP} = 17.1 + 0.19 * \frac{E'}{E} \quad (3)$$

$$\mathrm{Pre-A\ LVDP} = 6.97 + 0.3 * \frac{E'}{E} \quad (4)$$

## Color-M-mode echocardiography for assessment of IVPG

CMME was performed from the left parasternal apical four-chamber view under the left recumbence gesture. The sample volume was parallel to the mitral inflow in the apical view (Figure 2A) using an ultrasound system (Hitachi Aloka Medical ProSound Premier 75CV, Japan), which supports the CMME (Figure 2B) with a 12-MHz probe.

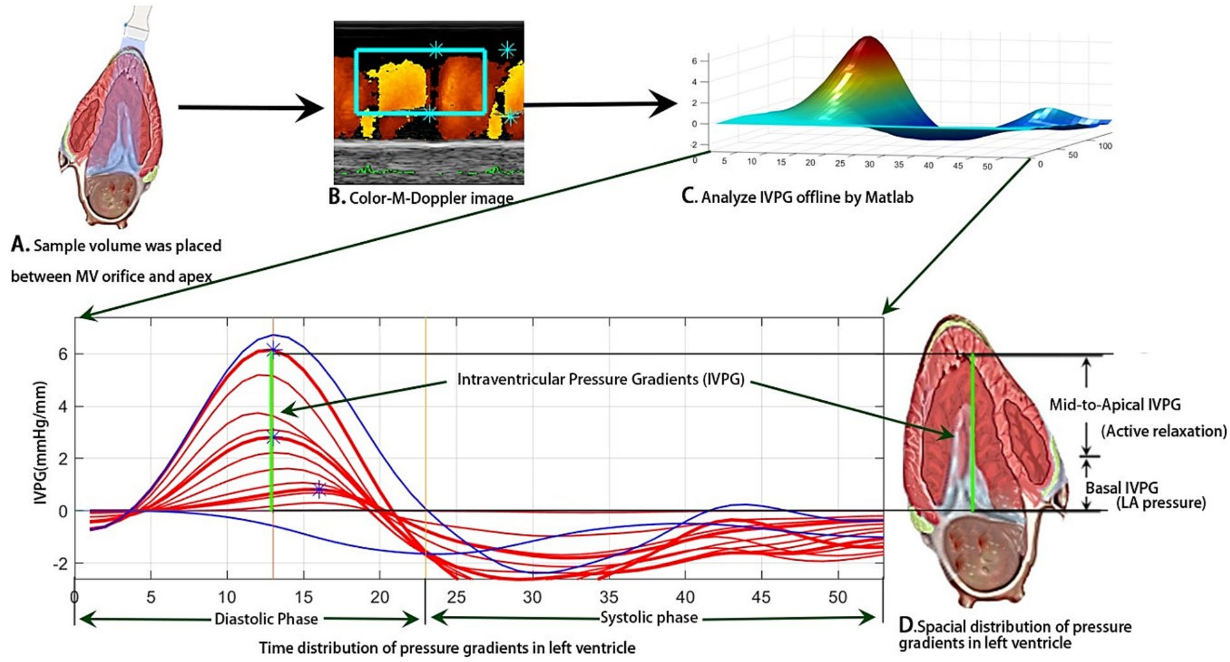


FIGURE 2
Schematic illustration of IVPG measurement through image analysis of photographs obtained from CMME in left apical four-chamber view using MATLAB software.

Prior machine setting was conducted for the proper tracing of the CMME, which includes a sweep speed of 300 mm/s, and a color baseline shift to −64 to increase the Nyquist limit. All images were analyzed with the Euler equation using MATLAB (Figure 2C, The MathWorks, Natick, MA) as previously described (15, 18), and the intraventricular pressure differences (IVPDs) were obtained as follows:

$$(\partial P)/(\partial s) = -\rho\left((\partial v)/(\partial t) + v(\partial v)/(\partial s)\right)$$

where $\partial$ is the change in element followed, P is the pressure, ρ is the constant blood density (1,060 kg/m$^3$), $v$ is the velocity, s is the position along with the color M-mode line, and t is the time. The IVPG values were derived from the IVPDs according to the following formula (16, 19):

$$\text{IVPG}\left(\text{mmHg / cm}\right) = \text{IVPD / LV length.}$$

The total IVPG was divided into two segments based on one-third segments of LV length: The smaller segment near the mitral valve is the basal IVPG, and the mid-to-apical IVPG segment is the other two-thirds near the apical IVPG (Figure 2D). Basal IVPG was proven to be correlated with LA pressure, and mid-to-apical IVPG represents active relaxation of the LV (13).

## Animal classification

Based on the mitral inflow pattern, the Sham-operated and HTN-CM rats were further divided into six groups (three groups in each category) as follows: EA-fusion ($n$ = 7, 15), EA-half-separation ($n$ = 7, 25), and EA-separation ($n$ = 19, 26), respectively, for Sham and HTN-CM (Figures 1A–C).

## Statistical analysis

All data were measured at least five times and are expressed as mean ± SD. The group (Sham vs. HTN-CM) and mitral inflow patterns (EA-fusion, EA-half-separation, and EA-separation) were considered as two variables used for comparison by two-way ANOVA, and Turkey's test was used for the *post-hoc* test. A $p$-value of < 0.05 was considered statistically significant. SPSS (IBM, Armonk, New York) was used to analyze the relationship between cardiac parameters and novel echocardiographic parameters.

## Correlation tests

A prior conversion of the subjective variables, including mitral inflow patterns, into numerical variables was performed before conducting the correlation analysis. For instance, the mitral inflow pattern is coded as 1 = EA-separation, 2 = EA-half-separation, and 3 = EA-fusion. Then, the IVPG, E/E', E, and E' were taken as variables to perform correlation tests with HR and mitral inflow patterns.

# Results

## Conventional echocardiography

Conventional echocardiography parameters are displayed in Table 1 and Supplementary Table S1. The HTN-CM group showed

TABLE 1 Comparison of conventional echocardiographic parameters in the Sham and HTN-CM groups regarding the pattern of the mitral inflow.

| Group | Sham group | | | HTN-CM group | | |
|---|---|---|---|---|---|---|
| Patterns parameters | EA-fusion ($n$ = 7) | EA-half-sep. ($n$ = 7) | EA-sep. ($n$ = 19) | EA-fusion ($n$ = 15) | EA-half-sep. ($n$ = 25) | EA-sep. ($n$ = 26) |
| LVM (g) | 0.62 ± 0.13[c] | 0.62 ± 0.11[c] | 0.65 ± 0.13[c] | 0.83 ± 0.23[ab] | 0.86 ± 0.31[a] | 0.87 ± 0.35[a] |
| EF (%) | 75.13 ± 5.12[a] | 71.93 ± 6.8[a] | 70.37 ± 10.63[a] | 70.21 ± 9.68[a] | 70.9 ± 8.33[a] | 65.33 ± 6.14[a] |
| E (m/S) | 1.01 ± 0.13[abc] | 0.96 ± 0.11[bcd] | 0.90 ± 0.10[d] | 1.06 ± 0.13[a] | 1.02 ± 0.16[ab] | 0.93 ± 0.09[cd] |
| A (m/S) | / | / | 0.63 ± 0.16 | / | / | 0.64 ± 0.11 |
| HR (bpm) | 359.72 ± 42.3[a] | 315.77 ± 54.10[b] | 304.14 ± 43.97[b] | 350.32 ± 40.39[a] | 348.48 ± 36.11[a] | 306.22 ± 39.68[b] |
| E/A ratio | / | / | 1.57 ± 0.09 | / | / | 1.49 ± 0.04 |
| E' (cm/S) | 7.74 ± 0.84[a] | 5.67 ± 0.71[bc] | 5.51 ± 0.81 [c] | 7.59 ± 1.13[a] | 6.22 ± 1.03[b] | 5.40 ± 0.76[c] |
| E/E' | 13.21 ± 2.13[b] | 17.27 ± 2.52[a] | 16.68 ± 2.64 [a] | 14.47 ± 2.93[b] | 16.91 ± 2.78[a] | 17.79 ± 2.85[a] |
| LVEDP (mmHg) | 19.61 ± 0.41[b] | 20.38 ± 0.48[a] | 20.27 ± 0.50 [a] | 19.61 ± 0.41[b] | 20.31 ± 0.53[a] | 20.48 ± 0.54[a] |
| Pre-A LVDP (mmHg) | 10.93 ± 0.64[b] | 12.15 ± 0.76[a] | 11.97 ± 0.79 [a] | 11.31 ± 0.88[b] | 12.04 ± 0.83[a] | 12.31 ± 0.85[a] |
| SAP (mmHg) | 95.05 ± 9.02[c] | 89.28 ± 11.4[c] | 89.79 ± 13.9[c] | 169.26 ± 18.69[ab] | 166.38 ± 13.42[a] | 150.76 ± 19.64[b] |

Echocardiographic measurements in sham and hypertensive cardiomyopathy (HTN-CM) rats after 3 weeks. Each group was classified according to the mitral inflow pattern. The group (Sham vs. HTN-CM) and mitral inflow patterns (EA-fusion, EA-half-separation, and EA-separation) were considered as two variables which were used for comparison by two-way ANOVA. The Turkey test was used for post-hoc comparison. The letters are fitted for comparing means between groups, and different letters in the same raw indicate significant differences ($p < 0.05$). sep., separation; LVM, left ventricle mass; E, the velocity of early mitral inflow; Peak A, the velocity of late mitral inflow; HR, heart rate; E', peak velocity of early diastolic mitral annular motion as determined by pulsed-wave Doppler; E/E', ratio of E to E'; LVEDP, left ventricle end-diastolic pressure; Pre-A LVDP, left ventricle diastolic pressure at the onset of the A-wave; SAP, systolic arterial pressure.

elevated blood pressure (160.79 vs. 90.81, $p < 0.001$) and LVM compared with the Sham group (0.86 vs. 0.64, $p < 0.001$), respectively. The combination of these measurements confirmed the existence of HTN-CM. In addition, no difference was detected in the ejection fraction, which indicates a stable systolic function in HTN-CM rats. As expected, HR and E in EA-fusion rats were significantly higher than in EA-separation rats in both groups.

## Tissue Doppler imaging

In sham and HTN-CM rats, elevated myocardium movement and mitral inflow velocity indicate hyperdynamic states in EA-fusion pattern rats (Table 1). E/E' in the HTN-CM rats was higher than in Sham rats in EA-fusion and EA-separation patterns and higher than 15, although not significant. E/E' was lower in EA-fusion rats compared with EA-half-separation and EA-separation groups, respectively, in sham (13.21 vs. 16.68, $p < 0.001$) and HTN-CM rats (14.47 vs. 17.79, $p < 0.001$). As a result, the LVEDP and pre-A LVDP of EA-fusion groups in the Sham and HTN-CM rats were significantly lower than the LVEDP and pre-A LVDP of the EA-half-separation groups and EA-separation groups in the Sham and HTN-CM rats ($p < 0.001$ and $p < 0.001$).

## IVPG measurements

The IVPG data are summarized in Figure 3. In the sham group, the total IVPG, basal IVPG, and mid-to-apical IVPG were significantly higher in EA-fusion rats than in EA-separation rats (2.61, 1.60, 1.01 vs. 2.26, 1.38, 0.88, $p < 0.001$, $p = 0.008$, 0.015), respectively. Furthermore, EA-fusion rats were significantly higher than EA-half-separation rats in the sham group in terms of the total IVPG and mid-to-apical IVPG (2.61 and 1.01 in EA-fusion vs. 2.27 and 0.86 in EA-half-separation, $p = 0.005$ and 0.024). Meanwhile, in HTN-CM rats (Figures 3D–F), only basal IVPG showed a significant difference between EA-fusion and EA-separation rats (1.68 vs. 1.54, $p = 0.027$).

## Pearson's correlation test of the novel echocardiography

Table 2 shows the correlation results between E/E', IVPG, and other cardiac parameters. HR showed a highly significant positive correlation with total IVPG ($p < 0.001$), basal IVPG ($p < 0.001$), mid-to-apical IVPG ($p = 0.003$), E ($p < 0.001$), and E' ($p < 0.001$) average; meanwhile, HR revealed a highly significant negative correlation with E/E' ($p < 0.001$). Because the mitral inflow pattern is transferred from string variables into numerical variables, the correlation (r) is a relative value rather than an absolute value. In this regard, the mitral inflow patterns showed a significant positive correlation with total IVPG ($p < 0.001$), basal IVPG ($p < 0.001$), E ($p < 0.001$), and E' ($p < 0.001$). Meanwhile, E/E' showed a significant negative correlation with the mitral inflow pattern ($p < 0.001$). In other words, E/E' tends to be lower when the mitral inflow pattern changes from EA-separation to EA-fusion. The HR also correlates with the mitral inflow pattern.

# Discussion

In clinical settings, physicians generally perform echocardiography when the HR is calm and stable to avoid EA wave fusion caused by high HR. Previous studies proved that E and A were related to HR and atrioventricular conduction delay, and E and A were proved influenced by ventricular loading and diastolic property (20, 21). However, the effect of mitral inflow patterns on novel echocardiography techniques such as IVPG has never been explored before. Thus, when the EA-fusion happens, physicians and scientists

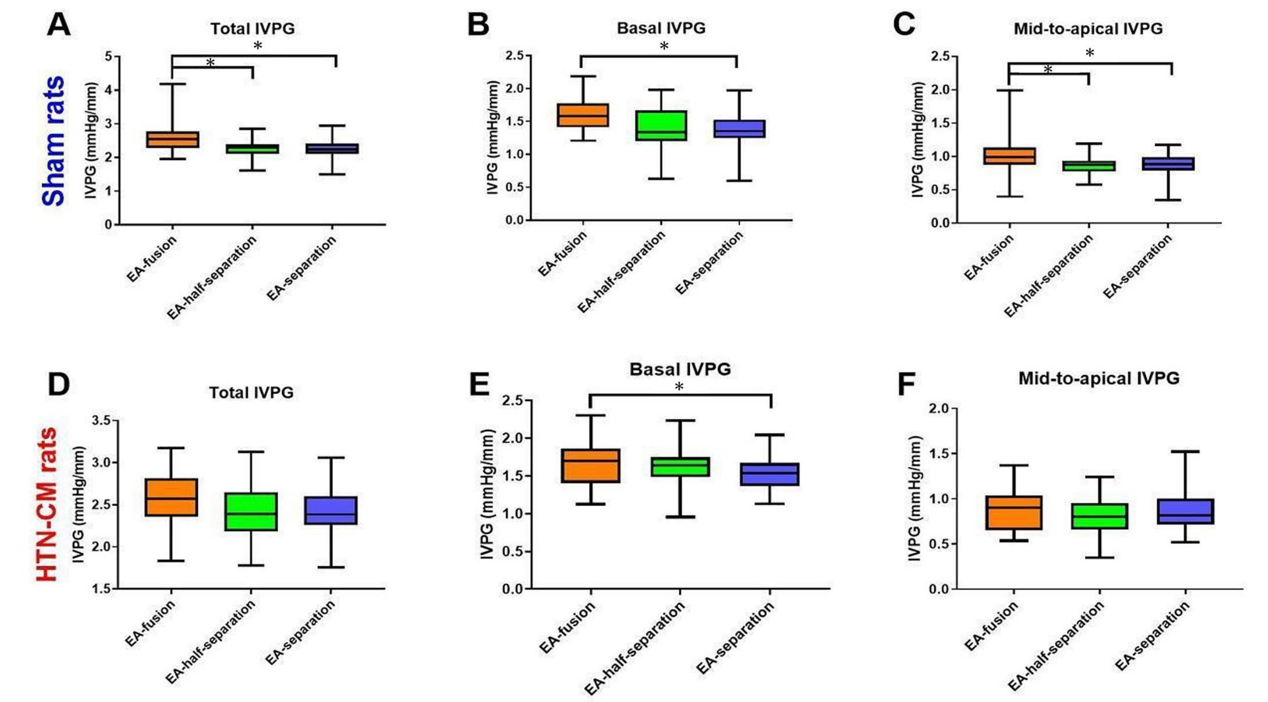


FIGURE 3
Comparison of IVPG data according to the mitral inflow pattern (EA-fusion, EA-half-separation, and EA-separation) in the Sham **(A–C)** and HTN-CM **(D–F)** groups. **p* < 0.05.

TABLE 2 Pearson's correlations test of echocardiography.

| Variables | HR | | Mitral inflow pattern | |
|---|---|---|---|---|
| | *r* | *p* | *r* | *p* |
| Total IVPG | 0.412** | <0.001 | 0.265** | <0.001 |
| Basal IVPG | 0.358** | <0.001 | 0.270** | <0.001 |
| Mid-to-apical IVPG | 0.188** | 0.003 | 0.070 | 0.281 |
| E/E' | −0.291** | <0.001 | −0.381** | <0.001 |
| E | 0.218** | <0.001 | 0.389** | <0.001 |
| E' | 0.443** | <0.001 | 0.665** | <0.001 |
| Mitral inflow pattern | 0.434** | <0.001 | / | / |

The relationship between E/E' and IVPG data and mitral inflow pattern as well as groups. ***p* < 0.05. Total IVPG, the mix of basal and mid-to-apical intraventricular pressure gradients; basal IVPG, the basal intraventricular pressure gradients; mid-to-apical IVPG, the mid-plus apical intraventricular pressure gradients; HR, heart rate; E/é, E to mitral annulus velocity ratio; E, the velocity of early mitral inflow; E' average, average early diastolic mitral annulus velocity.

fail to gain valuable information from novel echocardiography techniques such as IVPG and E/E'. So, we designed this study to reveal whether IVPG and E/E' are affected by mitral inflow patterns or not. We hypothesized that mitral inflow patterns would affect IVPG and E/E' differentially. Our results showed, for the first time, that IVPG was weakly influenced by mitral inflow patterns, while mitral inflow patterns affect E/E'.

In this experiment, elevated blood pressure supports hypertension, and combined with the elevated LVM, HTN-CM is recognized in the HTN-CM group (3). In hypertension patients, the baseline resting HR is higher than 85 bpm, leading to a shrunk value on echocardiography because of the changed mitral inflow pattern (8, 22). In the current study, we chose the surgical hypertension model to mimic early-stage HTN-CM patients in this study (23). The heart rate of awake rats is approximately 300–400 bpm, but the heart rate of rats anesthetized with isoflurane was an average of 326 ± 46 (219–421). Because HTN-CM rats responded differently to anesthesia, instead of intentionally controlling the depth of anesthesia to obtain a stable HR, we performed echocardiography at the same isoflurane dose to confirm that the effect of anesthesia was the same in all rats.

The different mitral inflow patterns had different IVPG values, as shown in Figure 3. In EA-fusion rats, the pressure built up by accumulated pulmonary venous blood in the atrium combined with the left atrial contraction resulted in promoted LV inflow speed, volume, and LV myocardium movement (24). The total and basal IVPG elevation explained the promoted myocardium movement in EA-fusion rats. The basal IVPG is well connected to LA pressure. Similarly, elevated LA pressure and volume in EA-fusion rats led to promoted basal IVPG (13). In the present study, mid-to-apical IVPG was significantly increased in EA-fusion rats in the sham group. The development of compensated hypertrophy leads to non-significantly increased mid-to-apical IVPG in HTN-CM rats. The mitral inflow pattern is not correlated with mid-to-apical IVPG because mid-to-apical IVPG illustrates active relaxation, which stays at the same level when the mitral inflow pattern changes.

E/E' was well correlated with Pre-A LVDP and LVEDP (17). The LVEDP is the same thing as Pre-A LVDP in EA-fusion rats because the E wave is merged with the A wave in EA-fusion patterns. However, based on the theoretical calculation, the LVEDP was approximately twice the Pre-A LVDP in EA-fusion rats, which showed the challenge of using E/E' to speculate LVEDP and Pre-A LVDP in EA-fusion rats.

The result of Pearson's correlation test indicates that the mitral inflow pattern correlates with HR. When HR increases, the mitral inflow changes from EA-separation to EA-fusion, and the total IVPG, basal IVPG, E, and E' average also increases.

However, the E/E' is negatively associated with HR because the E' is elevated more than the E velocity. The EA-fusion pattern owns the lowest preload among the three patterns because it owns only one inflow, while the EA-separation pattern has two mitral inflows. Similarly, preload affects E' velocity more than E velocity (17), and we proved that the mitral inflow patterns correlate more with E' than E ($r = 0.443$ vs. 0.218, Table 2). Because E/E' was calculated by E velocity and E', the changed mitral inflow patterns led to the uncertainty of E/E'. This explains why mitral inflow patterns affected E/E'. This study helps physicians and scientists better understand conventional and novel echocardiography techniques such as E, E/E', and IVPG when mitral inflow is fused into one flow.

### Study limitations

In the present study, only female rats were included in this study. Although both genders develop hypertension, males have a higher incidence and severity of hypertension compared with peer females until they are 60 or over (1, 25). However, the physiological differences, including growing speed, in young rats may interfere with the homogeneous HTN-CM model (26).

## Conclusion

Elevated HR leads to encroached diastasis, which eventually leads to EA-fusion. We proved that HR is associated with the mitral inflow pattern. Both E and E' in EA-fusion are higher than the EA-separation pattern. The preload change has more impact on E' than E, which leads to decreased E/E' in EA-fusion. HR positively correlates with basal IVPG, E, and E', while mid-to-apical IVPG is independent of mitral inflow patterns. It is not necessary to control HR to obtain IVPG because the impact of HR on IVPG is weak.

## Data availability statement

The original contributions presented in the study are included in the article/Supplementary material, further inquiries can be directed to the corresponding author/s.

## Ethics statement

The animal study was approved by the Animal Care and Use Committee of the Tokyo University of Agriculture and Technology. The study was conducted in accordance with the local legislation and institutional requirements.

## Author contributions

MH: Conceptualization, Investigation, Methodology, Writing – original draft. DM: Investigation, Methodology, Visualization, Writing – original draft. KS: Investigation, Software, Writing – review & editing. TY: Investigation, Software, Writing – review & editing. KM: Resources, Validation, Writing – review & editing. PK: Resources, Validation, Writing – review & editing. AH: Methodology, Writing – review & editing. YZ: Formal analysis, Writing – review & editing. KT: Formal analysis, Writing – review & editing. RT: Conceptualization, Supervision, Writing – review & editing. LH: Conceptualization, Data curation, Supervision, Writing – review & editing.

## Funding

The author(s) declare that no financial support was received for the research, authorship, and/or publication of this article.

## Conflict of interest

The authors declare that the research was conducted in the absence of any commercial or financial relationships that could be construed as a potential conflict of interest.

## Generative AI statement

The authors declare that no Gen AI was used in the creation of this manuscript.



## Supplementary material

The Supplementary material for this article can be found online at: https://www.frontiersin.org/articles/10.3389/fvets.2025.1507817/full#supplementary-material

# References


1. Virani SS, Alonso A, Benjamin EJ, Bittencourt MS, Callaway CW, Carson AP, et al. Heart disease and stroke Statistics-2020 update: a report from the American Heart Association. *Circulation*. (2020) 141:e139–596. doi: 10.1161/CIR.0000000000000757

2. Haider AW, Larson MG, Franklin SS, Levy D, Framingham HS. Systolic blood pressure, diastolic blood pressure, and pulse pressure as predictors of risk for congestive heart failure in the Framingham heart study. *Ann Intern Med*. (2003) 138:10–6. doi: 10.7326/0003-4819-138-1-200301070-00006

3. Kishio Kuroda TSK, Amano A. Hypertensive cardiomyopathy: a clinical approach and literature review. World. *J Hypertens*. (2015) 5:41–52. doi: 10.5494/wjh.v5.i2.41

4. Palmiero P, Zito A, Maiello M, Cameli M, Modesti PA, Muiesan ML, et al. Left ventricular diastolic function in hypertension: methodological considerations and clinical implications. *J Clin Med Res*. (2015) 7:137–44. doi: 10.14740/jocmr2050w

5. Mottram PM, Marwick TH. Assessment of diastolic function: what the general cardiologist needs to know. *Heart*. (2005) 91:681–95. doi: 10.1136/hrt.2003.029413

6. Zacchigna S, Paldino A, Falcao-Pires I, Daskalopoulos EP, Dal Ferro M, Vodret S, et al. Towards standardization of echocardiography for the evaluation of left ventricular function in adult rodents: a position paper of the ESC working group on myocardial function. *Cardiovasc Res*. (2021) 117:43–59. doi: 10.1093/cvr/cvaa110

7. Obokata M, Kane GC, Reddy YN, Olson TP, Melenovsky V, Borlaug BAJC. Role of diastolic stress testing in the evaluation for heart failure with preserved ejection fraction: a simultaneous invasive-echocardiographic study. *Circulation*. (2017) 135:825–38. doi: 10.1161/CIRCULATIONAHA.116.024822

8. Palatini P. Role of elevated heart rate in the development of cardiovascular disease in hypertension. *Hypertension*. (2011) 58:745–50. doi: 10.1161/HYPERTENSIONAHA.111.173104

9. Sohn D-W, Kim Y-J, Kim H-C, Chun H-G, Park Y-B, Choi Y-S. Evaluation of left ventricular diastolic function when mitral E and a waves are completely fused: role of assessing mitral annulus velocity. *J Am Soc Echocardiogr*. (1999) 12:203–8. doi: 10.1016/S0894-7317(99)70136-7

10. Schober KE, Chetboul V. Echocardiographic evaluation of left ventricular diastolic function in cats: hemodynamic determinants and pattern recognition. *J Vet Cardiol*. (2015) 17:S102–33. doi: 10.1016/j.jvc.2015.02.002

11. Kadappu KK, Thomas L. Tissue Doppler imaging in echocardiography: value and limitations. *Heart Lung Circ*. (2015) 24:224–33. doi: 10.1016/j.hlc.2014.10.003

12. Ohara T, Niebel CL, Stewart KC, Charonko JJ, Pu M, Vlachos PP, et al. Loss of adrenergic augmentation of diastolic intra-LV pressure difference in patients with diastolic dysfunction evaluation by color M-mode echocardiography. *JACC Cardiovasc Imaging*. (2012) 5:861–70. doi: 10.1016/j.jcmg.2012.05.013

13. Iwano H, Kamimura D, Fox E, Hall M, Vlachos P, Little WC. Altered spatial distribution of the diastolic left ventricular pressure difference in heart failure. *J Am Soc Echocardiogr*. (2015) 28:597–605.e1. doi: 10.1016/j.echo.2015.01.002

14. Pasipoularides A. Right and left ventricular diastolic flow field: why are measured intraventricular pressure gradients small? *Rev Esp Cardiol*. (2013) 66:337–41. doi: 10.1016/j.recesp.2012.07.019

15. Takahashi K, Nii M, Takigiku K, Toyono M, Iwashima S, Inoue N, et al. Development of suction force during early diastole from the left atrium to the left ventricle in infants, children, and adolescents. *Heart Vessel*. (2019) 34:296–306. doi: 10.1007/s00380-018-1239-9

16. Ma D, Mandour AS, Yoshida T, Matsuura K, Shimada K, Kitpipatkun P, et al. Intraventricular pressure gradients change during the development of left ventricular hypertrophy: effect of salvianolic acid B and beta-blocker. *Ultrasound*. (2021) 29:229–40. doi: 10.1177/1742271X20987584

17. Previtali M, Chieffo E, Ferrario M, Klersy C. Is mitral E/E' ratio a reliable predictor of left ventricular diastolic pressures in patients without heart failure? *Eur Heart J Cardiovasc Imaging*. (2012) 13:588–95. doi: 10.1093/ejechocard/jer286

18. Greenberg NL, Vandervoort PM, Firstenberg MS, Garcia MJ, Thomas JD. Estimation of diastolic intraventricular pressure gradients by Doppler M-mode echocardiography. *Am J Physiol Heart Circ Physiol*. (2001) 280:H2507–15. doi: 10.1152/ajpheart.2001.280.6.H2507

19. Popovic ZB, Richards KE, Greenberg NL, Rovner A, Drinko J, Cheng Y, et al. Scaling of diastolic intraventricular pressure gradients is related to filling time duration. *Am J Physiol Heart Circ Physiol*. (2006) 291:H762–9. doi: 10.1152/ajpheart.00081.2006

20. Miyaguchi K, Ogawa S, Iwase M, Yokota M, Hayashi H. Determinants of left ventricular inflow: the relation of the transmitral velocity profile to loading conditions. *J Cardiol*. (1990) 20:737–44.

21. Takeuchi M, Monnaka H, Tsukamoto T, Hayashi T, Tomimoto S, Odake M, et al. Transmitral flow velocity patterns as influenced by preload, afterload and heart rate alterations: pulsed Doppler echocardiographic study. *J Cardiol*. (1991) 21:679–90.

22. Chung CS, Afonso L. Heart rate is an important consideration for cardiac imaging of diastolic function. *JACC Cardiovasc Imaging*. (2016) 9:756–8. doi: 10.1016/j.jcmg.2015.10.021

23. Huang J, Wang D, Zheng J, Huang X, Jin H. Hydrogen sulfide attenuates cardiac hypertrophy and fibrosis induced by abdominal aortic coarctation in rats. *Mol Med Rep*. (2012) 5:923–8. doi: 10.3892/mmr.2012.748

24. Chung CS, Kovacs SJ. Consequences of increasing heart rate on deceleration time, the velocity-time integral, and E/a. *Am J Cardiol*. (2006) 97:130–6. doi: 10.1016/j.amjcard.2005.07.116

25. Yoon SS, Gu Q, Nwankwo T, Wright JD, Hong Y, Burt V. Trends in blood pressure among adults with hypertension: United States, 2003 to 2012. *Hypertension*. (2015) 65:54–61. doi: 10.1161/HYPERTENSIONAHA.114.04012

26. Lillie LE, Temple NJ, Florence LZ. Reference values for young normal Sprague-Dawley rats: weight gain, hematology and clinical chemistry. *Hum Exp Toxicol*. (1996) 15:612–6. doi: 10.1177/096032719601500802

TYPE Review
PUBLISHED 26 February 2025
DOI 10.3389/fvets.2025.1501405



OPEN ACCESS

EDITED BY
Hussein M. El-Husseiny,
Tokyo University of Agriculture and Technology, Japan

REVIEWED BY
Antonio González Cantalapiedra,
University of Santiago de Compostela, Spain
Vaida Vaskeliene,
Kaunas University of Technology, Lithuania

*CORRESPONDENCE
Kyung-Mee Park
✉ parkkm@cbu.ac.kr

RECEIVED 25 September 2024
ACCEPTED 13 February 2025
PUBLISHED 26 February 2025

CITATION
Kim D, Kwon H, Hwang J, Jung JS and Park K-M (2025) An in-depth review on utilizing ultrasound biomicroscopy for assessing the iridocorneal angle and ciliary body in canines. *Front. Vet. Sci.* 12:1501405.
doi: 10.3389/fvets.2025.1501405



# An in-depth review on utilizing ultrasound biomicroscopy for assessing the iridocorneal angle and ciliary body in canines

Donghee Kim, Hyun Kwon, Jiyi Hwang, Ji Seung Jung and Kyung-Mee Park*

Laboratory of Veterinary Surgery and Ophthalmology, College of Veterinary Medicine, Chungbuk National University, Cheongju, Republic of Korea

In this review, we explore the transformative role of Ultrasound Biomicroscopy (UBM) in veterinary ophthalmology, focusing on its utility in evaluating the iridocorneal angle and ciliary body in dogs. We begin by outlining UBM's foundational principles, providing a holistic understanding of its operational mechanics. This is followed by an exploration of the techniques and considerations for optimal UBM imaging, including the use of topical anesthesia, probe positioning, and maintaining a controlled measurement environment. A major section is dedicated to the detailed anatomy of the anterior segment, emphasizing the iridocorneal angle and ciliary body in controlling aqueous humor dynamics within canine and feline eyes. By comparing anatomical structures in humans and animals, we highlight the need for distinct parameters in veterinary medicine. The review also analyzes the parameters obtainable via UBM, emphasizing its potential in monitoring drug-induced ocular changes, gaging post-cataract surgical outcomes, and observing inter-species variations. We conclude by encapsulating the current state of research, addressing existing challenges, and suggesting future research avenues. This synthesis underscores the pivotal role of UBM in advancing veterinary ophthalmic diagnostics and research.

KEYWORDS

**ultrasound biomicroscopy, iridocorneal angle, ciliary body, ciliary cleft, canine**

## 1 Introduction

### 1.1 Introduction to ultrasound biomicroscopy

The development of Ultrasound Biomicroscopy (UBM) began with the work of Pavlin et al. in the early 1990s, introducing high-magnification imaging of anterior segment structures (1, 2). UBM provides detailed visualization of the eye's structures using high-frequency (35–100 MHz) ultrasound technology (2–4). The ultrasound waves, reflected by ocular tissues, are converted into visual representations, allowing for imaging of the anterior chamber, iridocorneal angle (ICA), and ciliary body with axial and lateral resolutions of approximately 0.2 mm and 0.5 mm, respectively (2). UBM is particularly effective in visualizing anterior segments of the eye that are not easily seen with conventional imaging techniques. Its resolution and depth of penetration, achieved with operational frequencies between 35 and 100 MHz, allow for detailed visualization of ocular structures from the corneal endothelium to the posterior lens capsule (2–4).

### 1.2 Comparison of UBM and alternate imaging techniques

Optical Coherence Tomography (OCT) is widely used for imaging the retina and anterior segment, employing infrared ray measurements to produce high-resolution images (5–7). However, OCT encounters limitations when imaging non-transparent or dense structures, such as thick iris tissue and the pigment epithelium (3). In contrast, UBM's ability to penetrate these barriers allows for visualization of deeper anatomical structures and lesions, even in cases where the cornea is opaque or where there is the presence of hyphema (3, 8). This characteristic makes UBM particularly effective in situations where OCT's performance may be limited.

Nevertheless, while UBM is advantageous for visualizing deeper or denser anterior structures, OCT excels in providing high-resolution images of transparent structures and the retina (2, 4, 6). Each modality offers unique strengths and limitations, making them complementary tools rather than direct competitors. The choice of imaging technique should be guided by the specific clinical need, with UBM and OCT often used together to provide a comprehensive view of ocular structures.

In veterinary medicine, Sim et al. utilized spectral domain OCT (SD-OCT) to study the ICA (8). However, many commercial SD-OCT devices have limitations due to their shorter wavelengths (800–880 nm), which restrict tissue penetration and complicate visualization of areas such as the angle recess and ciliary cleft (CC) in dogs (9). Additionally, the light from SD-OCT can be attenuated or absorbed by pigmented tissues, making it challenging to evaluate through pigmented corneas and posterior iris structures. In contrast, UBM is more effective in these situations, offering valuable insights into structures such as the iridociliary complex, zonular abnormalities, and underlying iris masses. Its ability to provide dynamic imaging enhances its utility, especially for evaluating the relationships between ocular structures, such as during angle assessments or post-surgical lens fit evaluations.

High-resolution ultrasound (HRUS), like UBM, is an advanced ultrasound imaging technique used for medical diagnostics (4). HRUS operates at lower frequencies (20–50 MHz) compared to UBM, offering slightly lower resolution but greater depth of penetration (4, 10). For this reason, UBM is primarily used for imaging the anterior segment of the eye. Its ability to provide detailed imaging of structures behind the iris, such as the ciliary body and lens, makes it particularly useful in glaucoma assessment and the diagnosis of anterior segment pathologies (10). Despite UBM offering more detailed imaging, higher resolution does not necessarily correlate with greater clinical utility in every setting. HRUS can provide adequate visualization in many clinical contexts where UBM's higher resolution is not required.

Moreover, while UBM requires a water bath or gel interface and may necessitate more specialized equipment, HRUS is generally easier to perform and more widely available in clinical settings (2, 11). The choice between HRUS and UBM depends on the specific anatomical region and diagnostic requirements. UBM provides superior detailed imaging for anterior eye segments, whereas HRUS offers a balance of high resolution and adaptability for various clinical applications across the body (Table 1).

## 2 Techniques and considerations for UBM imaging

### 2.1 Positioning and technique variations with traditional immersion method and the sterile balloon method

UBM utilizes high-frequency ultrasound to capture detailed images, requiring a water-based coupling medium to reduce reflections between the probe and the eye (12, 13). There are two

TABLE 1 Comparative summary of ocular imaging modalities: UBM, OCT, and HRUS.

| Parameter | UBM (ultrasound biomicroscopy) | OCT (optical coherence tomography) | HRUS (high-resolution ultrasound) |
|---|---|---|---|
| Imaging principle | High-frequency ultrasound | Interferometric imaging using near-infrared light | Moderate-frequency ultrasound |
| Frequency | 35–100 MHz | Not applicable (light-based) (~840 nm or 1,310 nm) | 20–50 MHz |
| Resolution | ~20–50 μm | ~5–10 μm | ~30–100 μm |
| Resolution characteristics | Optimized for detailed anterior segment imaging | Ideal for visualizing transparent tissues (e.g., retina, cornea) | Suitable for various clinical applications |
| Penetration depth | ~4–5 mm | ~2–3 mm | Up to 1–2 cm |
| Advantages | - Excellent for imaging opaque or pigmented anterior structures<br>- Enables dynamic assessments | - Non-contact and rapid acquisition<br>- High resolution for transparent structures | - Widely available and easy to perform<br>- Balances resolution and penetration for various applications |
| Limitations | - Requires a water/gel interface<br>- Optimized mainly for the anterior segment | - Limited penetration in dense tissues<br>- Image quality can be affected by tissue pigmentation | - Lower resolution compared to UBM<br>- May exhibit ultrasound artifacts |
| Clinical applications | Anterior segment evaluation (e.g., iridociliary complex, glaucoma assessments, pre–/post-surgical imaging) | Retinal imaging, assessment of transparent ocular structures, and anatomical studies | Supplemental imaging in ocular diagnostics and broader clinical applications |

primary methods for containing the coupling medium: the immersion method and the sterile balloon (ClearScan®) method (14). The choice of method influences factors such as positioning, sedation, and procedural requirements (Table 2).

In the immersion method, the patient's head is stabilized in dorsal recumbency using a hollow cushion. A tapered cupule is inserted into the palpebral fissure, acting as both a speculum and a watertight chamber for the interface liquid, such as lactated Ringer's solution. This method typically requires the patient to remain still, often necessitating anesthesia to maintain the water-filled state (15, 16). In contrast, the sterile balloon method allows examination with manual restraint in sternal recumbency, with the eyelids manually held open (10, 17–19).

According to the author's experience, the immersion method tends to yield clearer images. However, this technique is challenging in veterinary ophthalmology. Specifically, it requires the patient to be sedated or anesthetized, which is not always ideal in a clinical setting. Moreover, to prevent the water from leaking out of the chamber, continuous pressure must be applied to the eye. This compression can lead to distortion of the iridocorneal angle. In contrast, the balloon method offers the advantage of being performed without sedation, is simpler to execute, and minimizes the distortion associated with compression.

## 2.2 Topical anesthesia and probe positioning

Both methods typically involve the topical application of anesthetics, such as 0.5% proparacaine hydrochloride or 0.4% oxybuprocaine hydrochloride, to facilitate probe positioning (19). This allows for easy examination of the superior and temporal quadrants of the eye (10 to 3 o'clock positions), which are the most accessible areas in dogs (10, 17). The probe is positioned perpendicular to the globe, with the scan plane aligned perpendicular to the limbus. For the sterile balloon method, hydroxymethylcellulose is applied to protect the cornea and sclera from hypoallergenic ultrasound gel (17).

## 2.3 Consistency in measurement environment

Maintaining consistency in lighting conditions, pupil dilation status, and the use of pharmacological agents that affect these parameters is essential for accurate UBM imaging. Rose et al. demonstrated decrease in ICA parameters after pupil dilation in normal eyes without cataracts (20). Additionally, the use of topical agents can induce contraction or relaxation of the ciliary muscle, leading to alterations in the configuration of the ciliary body (15, 21, 22). Therefore, controlling experimental conditions is crucial. To achieve consistency, some studies monitor and maintain the background room illuminance in lux units and regulate the degree of pupil dilation affected by lighting (23). However, stress or excitement in animals visiting the clinic can cause the pupil to assume a midrange or dilated position, which may influence UBM measurement results (24). For this reason, some studies standardize conditions using 1% tropicamide to ensure uniformity in pupil dilation (25, 26).

Nevertheless, this approach also has its drawbacks. There is a possibility that individual responses to the mydriatic agent may distort the results. For example, while 0.5% tropicamide can be used to consistently maintain a dilated state, the response of the ciliary body can vary among subjects. In other words, although tropicamide is known to relax the ciliary body, it does not do so uniformly in all individuals (27). Therefore, the author believes that the best way to prevent distortion is to avoid using pharmacological agents altogether and to capture images under consistent lighting conditions when the patient is calm.

# 3 Role of ultrasound biomicroscopy in anterior segment evaluation

## 3.1 Comprehensive examination of the iridocorneal angle and the ciliary body anatomy

The ICA and ciliary body are key ocular structures involved in the regulation of aqueous humor (AH) flow in dogs. The ICA functions as a crucial site for AH outflow, while the ciliary body is responsible for AH production (28, 29). Together, these structures play essential roles in both the formation and regulation of AH dynamics (Figure 1).

In the conventional outflow pathway, AH exits the eye through the corneoscleral trabecular meshwork (TM). The ICA forms a peripheral portion of the anterior chamber, where the cornea, sclera, and the base of the iris meet (16, 30). The ICA is composed of a reticular network of connective tissue beams, known as trabeculae, which are lined either partially or entirely by a single layer of cells (16, 31, 32).

Using clinical examination techniques such as gonioscopic lenses, the distinctive features of the ICA can be observed, including slender strands of uveal tissue and pectinate ligaments (PLs), which connect parts of the iris to the peripheral cornea (16, 33–36). In ICAs characterized by stout PLs, the anterior chamber communicates freely with the ICA through pores that lead into a network of small channels (29). These channels are surrounded by cords of densely packed

TABLE 2 Comparison of traditional immersion and sterile balloon methods for UBM imaging.

| Parameter | Immersion method | Sterile balloon method |
|---|---|---|
| Patient positioning | Dorsal recumbency with head stabilization | Sternal recumbency with manual restraint |
| Coupling medium | Water-based medium contained in a tapered cupule | Medium enclosed within a sterile balloon |
| Sedation anesthesia | Sedation or anesthesia | Without sedation |
| Pressure compression | Continuous pressure needed; risk of iridocorneal angle distortion | Minimal compression; reduced risk of anatomical distortion |
| Image quality | Typically yields clearer images with stable coupling | Slightly reduced clarity compared to immersion |
| Procedural simplicity | More complex due to sedation and pressure management | Simpler execution with fewer procedural requirements |

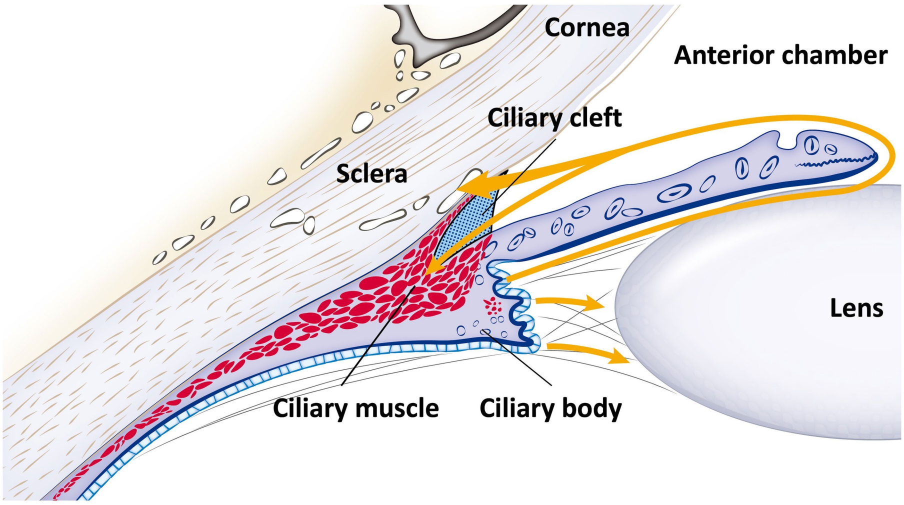


FIGURE 1
Schematic diagram of the iridocorneal angle and ciliary body anatomy, with aqueous humor flow. This schematic representation details the anatomy of the iridocorneal angle and the ciliary body, along with the pathway of aqueous humor flow (indicated by the yellow line with an arrow). Aqueous humor is produced by the ciliary body and flows from the posterior chamber, through the pupil, into the anterior chamber. Subsequently, it exits via the ciliary cleft into the radial collector channels and is then absorbed into the episcleral veins, following the conventional pathway. Additionally, a portion of the aqueous humor diverges into the longitudinal muscle fibers of the ciliary body, illustrating the unconventional pathway.

collagen. Further posteriorly, the PLs interconnect with the anterior beams of the TM, illustrating the complex and finely tuned structure of the outflow pathway (37).

The CC, which is not present in humans but is a characteristic structure in dogs, is a vital triangular space located posterior to the ICA. Functioning as a posterolateral extension of the anterior chamber into the ciliary body, the CC varies in both depth and height. Historically referred to as the cilioscleral sinus, this term has been replaced with CC, as it neither separates the ciliary body from the sclera nor is part of the ciliary venous sinus (30, 38). This virtual space extends beyond the PLs into the posterior ciliary body, forming a triangular shape with an anterior base. Anatomically, the boundaries of the CC include the PLs anteriorly, the iris root and anterior pars plicata of the ciliary body internally, the ciliary body matrix and muscle posteriorly, and the sclera externally (28, 39, 40). The CC is characterized by wide spaces filled with AH and interspersed with cell-lined cords of connective tissue (40). The CC plays a critical role as the container for the uveal trabecular meshwork, a key component in regulating intraocular pressure (IOP) and maintaining overall eye health in dogs.

The ciliary body muscle in a dog's eye is a smooth, nonstriated muscle located primarily in the anterior two-thirds of the ciliary body stroma and is divided into three distinct parts. The outer longitudinal portion, known as Brücke's muscle, is the most external and closest to the sclera (41). It forms a V-shaped structure that constitutes the bi-leaflet of the CC, with carnivorous species exhibiting a similar bi-leaflet configuration but with variations in muscle fiber orientation (38, 42). Contraction of this portion can reduce the space between muscle bundles, decreasing aqueous outflow (43). The middle oblique or reticular portion attaches to collagenous structures near the ciliary processes, while the inner circular part, referred to as Müller's muscle, acts as a sphincter near the major arterial circle of the iris (44). This inner portion influences lens refraction by pulling the ciliary processes and body forward and inward, relaxing the lenticular zonules and altering the lens shape (45–47). The different muscle fibers exhibit ultrastructural and histochemical differences, with the longitudinal portion primarily involved in regulating outflow and the circular portion related to accommodation (48).

## 3.2 Comparative anatomy of iridocorneal angle and ciliary body in humans and dogs

There are anatomical differences in the ICA between humans and dogs (49, 50). In humans, the scleral spur is present as a fibrous ring projecting from the inner aspect of the anterior sclera in a meridional section. The scleral spur is attached anteriorly to the TM and posteriorly to the sclera and the longitudinal portion of the ciliary muscle (51, 52). It serves as an important landmark for determining angle configuration due to its distinctive outline and higher reflectivity compared to the ciliary body, aiding in the identification of the angle during imaging (1, 53). However, this structure is absent in dogs, which can make consistent landmark identification using UBM more challenging. Additionally, in dogs, the TM is located within the recess of the CC, whereas in humans, it is positioned anteriorly relative to the iris root and resides within the scleral sulcus (Figure 2) (28, 40, 48, 54–56). As a result, iris dilation in humans can obstruct access to the TM by causing external and anterior displacement of the iris root (57, 58). In contrast, the location of the TM in dogs makes it less susceptible to such obstructions, ensuring that iris movement has a minimal effect on AH outflow. Therefore, a different approach may be necessary when using UBM in humans compared to dogs.

The ciliary body in humans displays distinct anatomical differences compared to other species. The human ciliary body musculature is highly developed, comprising three distinct components: radial, meridional, and circular fibers. These fibers form a prominent anterior pyramidal structure, which provides a stable and robust base for iris attachment (59). The development of the circular fibers within this muscle facilitates the anterior inward movement of the ciliary body (60). In humans, the anterior segment of the ciliary body muscle has largely taken over the functions of the CC, which is nearly absent, and the PLs, which persist only as sparse iridal processes (40). In contrast, canine anatomy is characterized by a predominance of meridional (or longitudinal) fibers in the ciliary body muscle, with fewer circular fibers compared to humans (61, 62). Therefore, in dogs, it is believed that the anterior inward movement of the ciliary body is primarily regulated by meridional fibers rather than circular fibers (Table 3).

## 3.3 Comparison of histological and UBM images

To validate the accuracy of UBM in visualizing anterior segment structures, histological sections of the ICA were compared with corresponding UBM images obtained from the same subjects. Figure 3 illustrates these comparisons, highlighting key anatomical landmarks observed in both imaging modalities (16).

Histological sections stained with hematoxylin/eosin (Figure 3A) provided a detailed view of ICA structures, including the PLs, TM, and CC. These features were also visualized in UBM images (Figure 3B), demonstrating the capacity of UBM to delineate ICA structures *in vivo*. The PLs were clearly identified in both histological and UBM images, marking the anterior boundary of the CC. The TM, occupying the CC, was similarly observed in both modalities, although the histological sections revealed finer details of its cellular organization, which could not be resolved with UBM.

# 4 Interpreting parameters evaluated via UBM in the assessment of the iridocorneal angle and ciliary body

## 4.1 Iridocorneal angle parameters: ICA, AOD

The ICA and angle-opening distance (AOD) are commonly used parameters in both human ophthalmology and veterinary practices

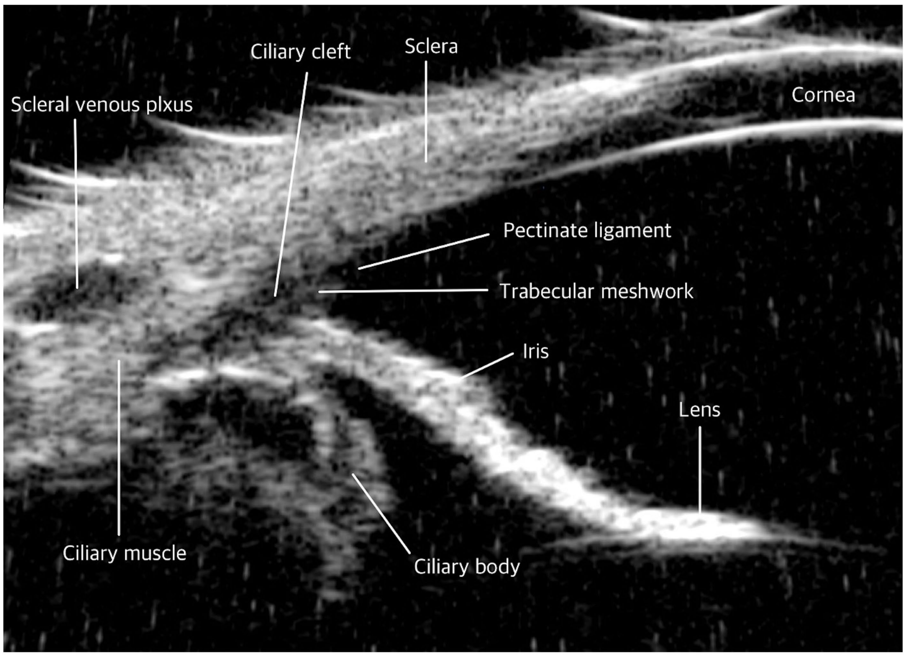


FIGURE 2
Comparative ultrasound biomicroscopy (UBM) images of the iridocorneal angle in dog. Iridocorneal angle: In contrast to humans, dogs do not possess a scleral spur. The trabecular meshwork in dogs is uniquely structured; it is exposed beyond the sclera and situated within the recess of the ciliary cleft.

TABLE 3 Comparative anatomy of the iridocorneal angle and ciliary body in humans and animals.

| Anatomical region | Parameter | Humans | Dogs |
|---|---|---|---|
| Iridocorneal angle | Scleral spur | Present as a fibrous ring; serves as a key landmark | Absent |
| | Trabecular meshwork | Located anterior to the iris root in the scleral sulcus | Located within the recess of the ciliary cleft |
| | Iris dilation effect | Iris dilation can obstruct TM access | Minimal impact due to the recessed TM position |
| Ciliary body | Muscle composition | Radial, meridional, circular fibers | Predominantly meridional fibers |
| | Structural features | Prominent pyramidal structure; ciliary cleft nearly absent | Less developed CC; anterior movement mainly via meridional fibers |

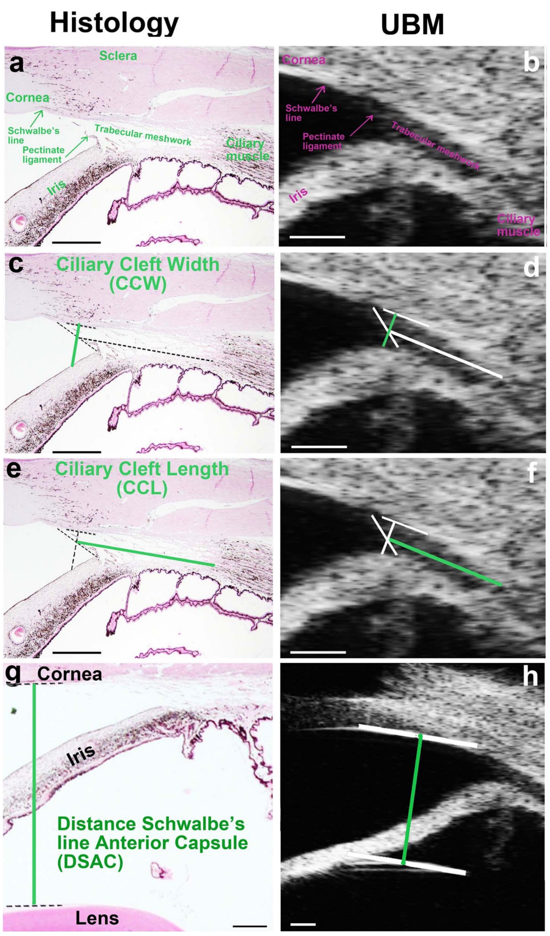


FIGURE 3
Comparison of histological and UBM images of the iridocorneal angle (ICA) in dogs. **(a, c, e, g)** Histological section of the ICA stained with hematoxylin/eosin, highlighting key anatomical structures including the pectinate ligaments (PLs), trabecular meshwork (TM), and ciliary cleft (CC). **(b, d, f, h)** Corresponding UBM image of the same ICA region, demonstrating the ability of UBM to delineate these structures *in vivo*. The PLs are distinctly visible in both imaging modalities, forming the anterior boundary of the CC. The TM, occupying the CC, is observed in both images, though finer cellular details are more clearly defined in histological sections. Reproduced from Boillot et al. (16), CC BY 4.0.

for animals such as dogs (53, 63). The ICA is typically measured by locating the apex of the angle at the junction of the iris, TM, and sclera. From this apex, lines are extended along the inner surface of the sclera and iris to the level of the limbus, allowing for precise measurement (15, 20, 33).

For AOD, several distinct methodologies are employed. One method defines the AOD as the distance, measured in micrometers, from the end of Descemet's membrane to the surface of the iris (Figures 4A,B) (8). Another method involves drawing a 500-µm line from the apex of the ICA to a point on the inner corneoscleral surface, from which a perpendicular line is drawn to the iris, and the length of this line is measured (15). A third method estimates the AOD by using the distance between the limbus and the ciliary process (DLCP). A line perpendicular to the DLCP is drawn from a point located under the midline (0.45 × DLCP, measured from the ciliary process) from the sclera to the iris; this line represents the AOD (Figures 4C,D) (50)

These parameters have been adapted from human ophthalmology to account for the distinct anatomical structures of dogs. In human studies, AOD is frequently measured using the scleral spur as a consistent anatomical landmark, particularly when assessing AOD at 500 µm (AOD500) (64). However, in animals such as dogs and cats, the absence of a consistent landmark like the scleral spur has necessitated the use of alternative reference points, such as the angle recess and Descemet's membrane (8, 15).

The importance of these parameters is evident in their application for evaluating angle-closure glaucoma (ACG) in humans (64, 65). ACG refers to a group of diseases in which there is either reversible or adhesional closure of the anterior chamber angle, obstructing AH flow through the canal of Schlemm (66). The ICA and AOD parameters are used to assess the proximity of the iris to the scleral spur, which serves as a landmark for the canal of Schlemm (67). However, there is skepticism regarding the relevance of these parameters in dogs, given their anatomical differences from humans (26). The use of the angle recess and Descemet's membrane as alternative landmarks may not have the same significance in these species, raising debate about the appropriateness and interpretation of these measurements in veterinary ophthalmology (26).

## 4.2 Quantitative analysis of iris configuration using UBM parameters

The morphological characteristics of the iris play a crucial role in anterior segment dynamics and AH outflow regulation. To quantitatively assess these structural variations, two key parameters, iris-lens contact (ILC) and iris deviation (ID), were evaluated using UBM. These parameters provide insight into anatomical factors that may contribute to primary angle-closure glaucoma (PACG) (Figure 5) (49, 68).

ILC represents the extent of contact between the posterior iris and the anterior lens capsule. An increased ILC value indicates greater contact, which can lead to pupillary block, where aqueous humor accumulation in the posterior chamber causes anterior displacement of the peripheral iris, narrowing the iridocorneal angle. In human ophthalmology, elevated ILC is a well-established risk factor for PACG (69, 70). While a direct correlation in veterinary medicine has yet to be confirmed, comparative studies suggest that breeds predisposed to PACG, such as American Cocker Spaniels, exhibit higher ILC values than breeds with lower glaucoma incidence, such as Beagles (49).

ID quantifies the curvature of the iris by measuring its deviation from a reference baseline. A higher ID value indicates greater anterior bowing of the iris, which can contribute to angle crowding and increased AH outflow resistance. Conversely, a lower ID value suggests a flatter iris profile, typically associated with an open iridocorneal angle and lower risk of AH obstruction (24). Given the role of anterior iris displacement in PACG, ID may serve as a useful supplementary parameter alongside ICA and ciliary cleft width (CCW) for evaluating anatomical predisposition to glaucoma.

While ILC and ID have been extensively studied in human glaucoma research, their clinical relevance in veterinary ophthalmology requires further investigation (71, 72). Establishing normative values for these parameters in different breeds and assessing their changes over time may help clarify their role in PACG pathogenesis. Future research should also explore their potential as early indicators of disease progression and treatment response.

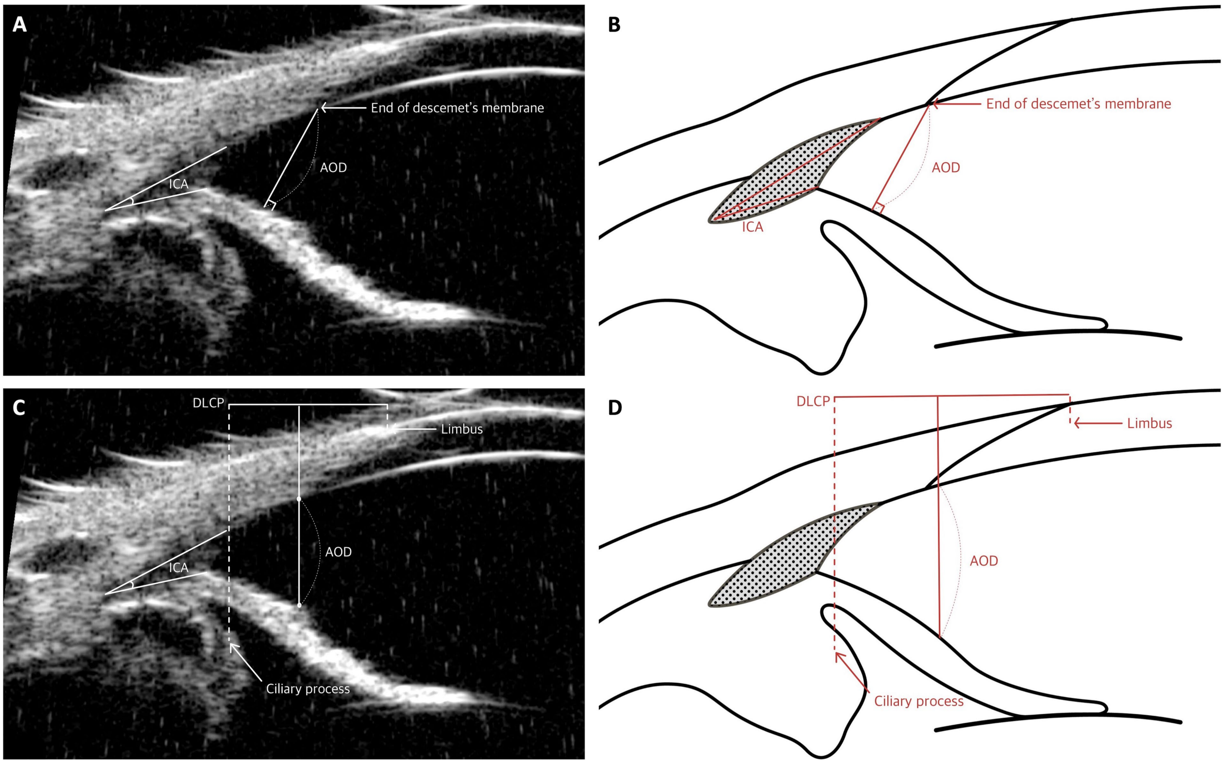


FIGURE 4
Measurement techniques of the iridocorneal angle (ICA) and angle-opening distance (AOD) utilizing UBM images in dog. **(A,B)** Measurement of ICA and AOD: These panels demonstrate the method for measuring both the iridocorneal angle and the AOD. The apex of the ICA is positioned at the junction where the iris, trabecular meshwork, and sclera meet, with measurement lines extending from this apex along the inner surface of the sclera and iris up to the level of the limbus to determine the angle. Additionally, the AOD is quantified as the distance from the end of Descemet's membrane to the iris. **(C,D)** Measurement of AOD: These images depict the technique for approximating AOD using the distance from the limbus to the ciliary process (DLCP). A perpendicular line to the DLCP is drawn from a point slightly below the midline, specifically at 0.45 times the DLCP, extending from the sclera to the iris.

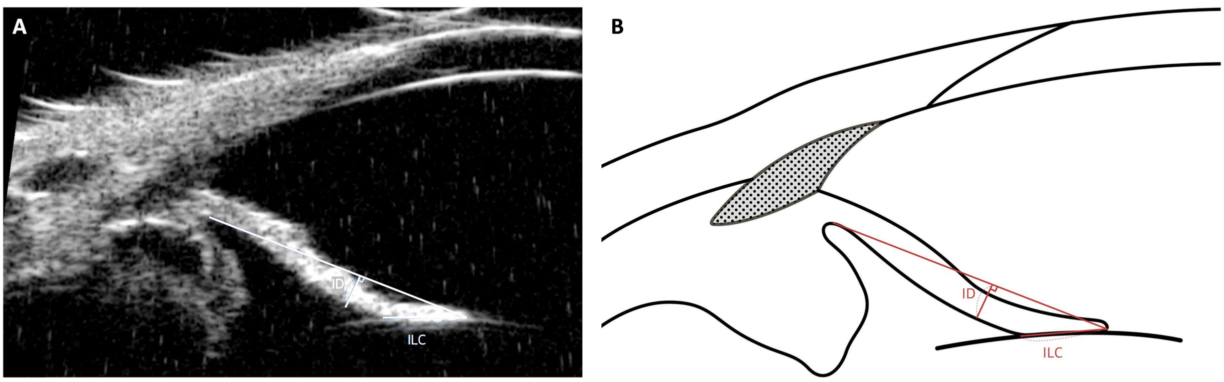


FIGURE 5
Measurement techniques of iris-lens contact (ILC) and iris deviation (ID) using UBM images in dog. This figure demonstrates the methods used to measure ILC and Iris Deviation (ID). The ILC is assessed by measuring the distance between the innermost and outermost contact points of the iris's posterior pigmented epithelium with the anterior capsule of the lens. The ID provides insights into the curvature of the iris, measured from the point of iris-lens contact to the furthest edge at the iris root.

## 4.3 Ciliary cleft parameters: CCW, mid-CCW, CCL, CCA

The CC serves as a common pathway for the outflow of AH, regulating its flow (28). It plays a significant role in various research and clinical applications, such as the analysis of breeds with glaucoma predisposition, the examination of drug responses to glaucoma medications, and studies to identify the causes of post-operative hypertension (POH) or glaucoma before and after cataract surgery, utilizing parameters associated with the CC (15, 16, 18, 19, 23, 73).

The parameters used to assess the CC include:

1. Ciliary Cleft Width (CCW): This is measured as the distance from the point where the PLs contact the sclera to the point where they meet the iris (Figures 6A,B).
2. Mid-Ciliary Cleft Width (Mid-CCW): This represents the distance between the inner sclera and the ciliary process in the central portion of the CC (Figures 6A,B).
3. Ciliary Cleft Length (CCL): This measurement extends from the angle recess to the midpoint of the PLs (Figures 6A,B).
4. Ciliary Cleft Area (CCA): The CCA is calculated as the area enclosed by the CCW, the lines tracing the inner scleral side of the CC from the inner surface of the sclera to the angle recess, and the line tracing the superior surface of the iris root from the angle recess to the superior surface of the iris root (Figures 6C,D).

Comparing CCW and CCA measured by UBM across dogs can be challenging, as these values may vary due to differences in ocular size, which are often influenced by body size or weight (74). In a study by Kawata et al., dogs were classified into four groups based on body weight, and differences in CCW and CCA were observed between the groups (17). To enable valid comparisons between animals of varying sizes and weights, the CCW and CCA values obtained from UBM images must be adjusted or rectified. In this study, rectification was achieved using the distance from Schwalbe's line (the boundary between the cornea and sclera) to the anterior lens capsule (SLD) (Figures 6C,D) (17, 23, 75). The researchers employed an optional fixed SLD (OFS), such as the mean SLD of the examined dogs. The formulas for rectified CCW (r-CCW) and rectified CCA (r-CCA) were as follows:

$$r-CCW = CCW \times \left(OFS / SLD\right)$$

$$r-CCA = CCA \times \left(OFS / SLD\right)^2.$$

After rectification, no differences were found in r-CCW and r-CCA across the groups (17). These findings highlight the importance of accounting for body size and weight when evaluating CC parameters using UBM in veterinary ophthalmology.

However, there are limitations when comparing different sexes using this rectification method. The underlying assumption in this approach is that there is no sex difference in the SLD. In contrast, our previous study reported that the peripheral-anterior chamber depth corresponding to the SLD is smaller in female dogs (76). Consequently,

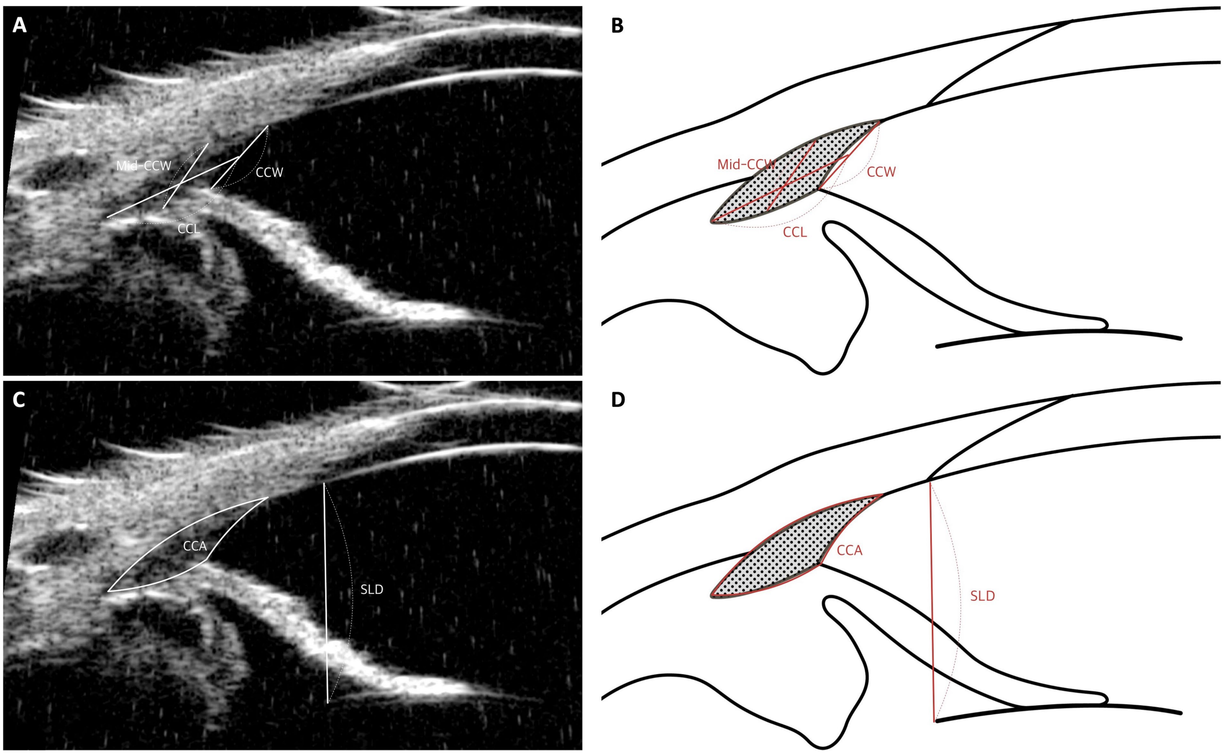


FIGURE 6
Measurement techniques of ciliary cleft parameters using UBM images in dog. **(A,B)** Measurement of ciliary cleft parameters: The width at the ciliary cleft (CCW) is quantified by the distance from the corneoscleral limbus to the iris root. The width at the mid-point of the cleft (Mid-CCW) is calculated between the inner wall of the sclera and the nearest ciliary process. The length of the ciliary cleft (CCL) spans from the pectinate ligament or the most forward part of the uveal trabecular meshwork to the front of the ciliary body. **(C,D)** Measurement of ciliary cleft area and Schwalbe's line to lens distance (SLD): The ciliary cleft area (CCA) is determined by outlining the area formed by the CCW and lines delineating the inner scleral boundary from the inner sclera to the angle recess, along with a line marking the upper edge of the iris root from the angle recess to the top of the iris root. Additionally, the distance from Schwalbe's line, which marks the transition from cornea to sclera, to the anterior lens capsule (SLD) is meticulously measured.

when applying the rectification method, the rectified values (r-CCW and r-CCA) may be measured as smaller in female dogs compared to male dogs. Therefore, caution is warranted when utilizing this method for inter-sex comparisons.

## 4.4 Ciliary body movement parameters: CPSA, CBAXL

In human medicine, ciliary body movement plays a crucial role in controlling accommodation, and UBM studies have been conducted to investigate this aspect (77–79). Accommodation refers to the eye's ability to adjust its refractive power, allowing for clear vision of objects at different distances (80). During accommodation, the ciliary muscle contracts, causing the ciliary body to move both forward and inward. This movement reduces tension on the zonule, enabling the lens equator to shift further from the sclera (45, 81).

While the significance of ciliary body movement is generally considered low in dogs, recent studies have linked it to the expansion and contraction of the CC (25, 26). This connection is based on the fact that the CC is enclosed by the inner and outer leaflets of the longitudinal ciliary muscle (38, 42). For example, ciliary body contraction causes the ciliary muscle to move inward and anteriorly, leading to the compression and subsequent contraction of the CC (25).

The specific parameters used to evaluate ciliary body movement are as follows (Figure 7):

1. Ciliary Body Axial Length (CBAXL): This is determined by drawing a line from the apex of the dome-shaped ciliary body through its center to measure the CBAXL.
2. Ciliary Process-Scleral Angle (CPSA): This angle is measured by calculating the angle formed between the longitudinal axis of the ciliary body and the sclera.

An increase in CBAXL serves as an indirect indicator of centripetal ciliary body movement, while the posterior movement of the ciliary body process is reflected by an increase in CPSA measurements. Simply put, contraction of the ciliary body leads to an increase in CBAXL and a reduction in CPSA values (77, 78). Understanding these dynamics in ciliary body movement enhances insight into the eye's accommodative function and related physiological processes in both human and veterinary contexts.

In the author's opinion, these parameters are well-suited for observing changes in the ciliary body before and after surgery or following the application of topical medications. However, changes in the ciliary body associated with glaucoma cannot be explained solely by simple contraction and relaxation. Studies in humans have shown that in glaucoma, the ciliary body may undergo atrophy (82). Therefore, when comparing the ciliary bodies of glaucomatous eyes with those of normal dogs, alternative methods beyond these parameters should be considered.

## 4.5 Ciliary body muscle parameters: CBT, Lf-CMT, LRf-CMT

The ciliary body, in addition to its role in producing AH via the ciliary process, plays a key role in the uveoscleral outflow pathway (83, 84). Since this pathway passes through the interstitium of the ciliary muscle and is thought to be influenced by the contraction and relaxation of the ciliary muscle, monitoring structural changes in the ciliary musculature may be the most effective way to confirm the involvement of uveoscleral outflow (21, 22, 43, 48).

In research conducted by Park et al., ciliary body thickness (CBT) was defined with the understanding that the attached outer portion of the ciliary body is negligible compared to the inner portion. Thus, CBT was measured as the distance between the posterior end of the CC and the edge of the ciliary pigmented epithelium, which appears as hyperechoic on UBM images (Figures 8C,D) (19). These parameters reflect changes in ciliary body thickness resulting from the relaxation and contraction of the ciliary muscle.

Building on this, our previous study identified changes in ciliary muscle fiber thickness following phacoemulsification and hypothesized that these changes may be related to the uveoscleral pathway. This led to the definition of parameters such as longitudinal fiber of ciliary muscle thickness (Lf-CMT) and longitudinal and radial

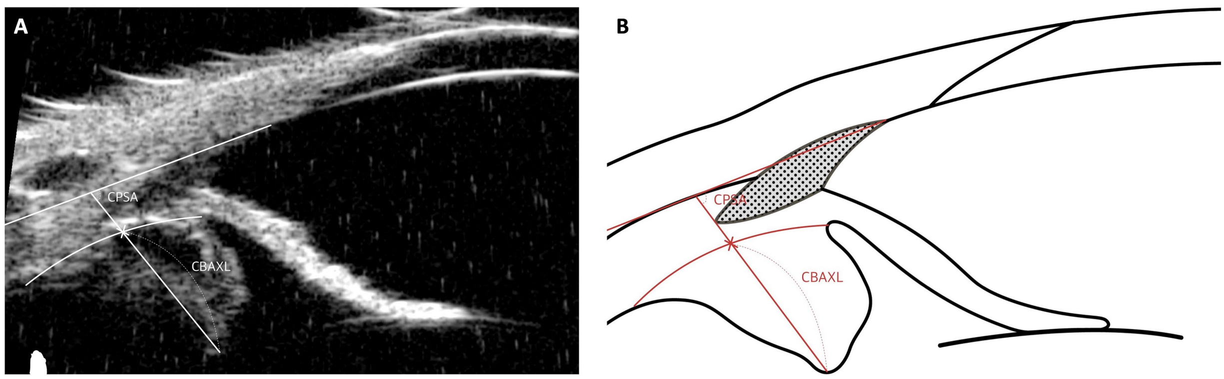


FIGURE 7
Measurement techniques of ciliary body movement parameters using UBM images in dog. This figure illustrates the methodologies used to evaluate ciliary body movement parameters. The Ciliary Body Axial Length (CBAXL) is measured by tracing a central line from the dome-shaped apex to the base of the ciliary body, accurately depicting its axial length. The Ciliary Process-Scleral Angle (CPSA), measuring the angle formed between the longitudinal axis of the ciliary body and the sclera, is essential for assessing the anatomical relationship between the ciliary body and the sclera.

fiber of ciliary muscle-choroid thickness (LRf-CMT). The measurement of Lf-CMT involves drawing a line through the inner layer of the sclera and the angle recess, with another line parallel to the inner scleral layer starting from where the inner layer of the iris root meets the PLs. The measurement of LRf-CMT requires drawing a line through the inner layer of the sclera and the angle recess, along with a parallel line starting from the point where the outer layer of the iris root meets the dome-shaped ciliary body (Figures 8A,B) (25).

The ciliary body is known to contract into a dome-shaped structure, moving in a centripetal or anterior inward direction, as observed in human studies (85). Therefore, depending on the location of the measurement, CBT may either increase or decrease even when the ciliary body contracts. Unlike in humans, dogs lack a clearly defined scleral spur, which limits the usefulness of CBT measurements in these cases. To overcome the limitations of CBT, alternative methods—such as measuring the thickness of the ciliary muscle using Lf-CMT and LRf-CMT—have been developed (25). The ciliary muscle is irregularly arranged when relaxed and becomes regularly packed upon contraction (85). From the perspective of the muscle bundle, the ciliary muscle tends to be thicker when relaxed and thinner when contracted, yielding consistent results. However, despite the advantage of providing more consistent outcomes than CBT, these methods are challenging to measure. Depending on the equipment used, the sclera might not be clearly visualized, making it difficult to establish precise measurement criteria and complicating the measurement process in dogs.

# 5 Drug-induced modifications in the iridocorneal angle and ciliary body

## 5.1 Understanding how drugs alter the structure and function of the iridocorneal angle and ciliary body

To date, research in veterinary ophthalmology has primarily focused on the CC. It is well known that changes in the width and size (expansion or contraction) of the ciliary cleft affect IOP (86). Therefore, drug responses are ultimately centered on how the CC is altered.

In the opinion of the author of this review paper, there are two main factors that affect the CC. The first is the miosis and mydriasis of the iris. It is thought that mydriasis exerts an effect by compressing the CC, thereby reducing its size, whereas miosis tends to enlarge the CC (15, 18). The second factor is the contraction and relaxation of the ciliary body. Relaxation of the ciliary body moves it in a posterior outward direction, reducing pressure on the CC; conversely, contraction moves the ciliary body in an anterior inward direction, increasing pressure on the CC (25).

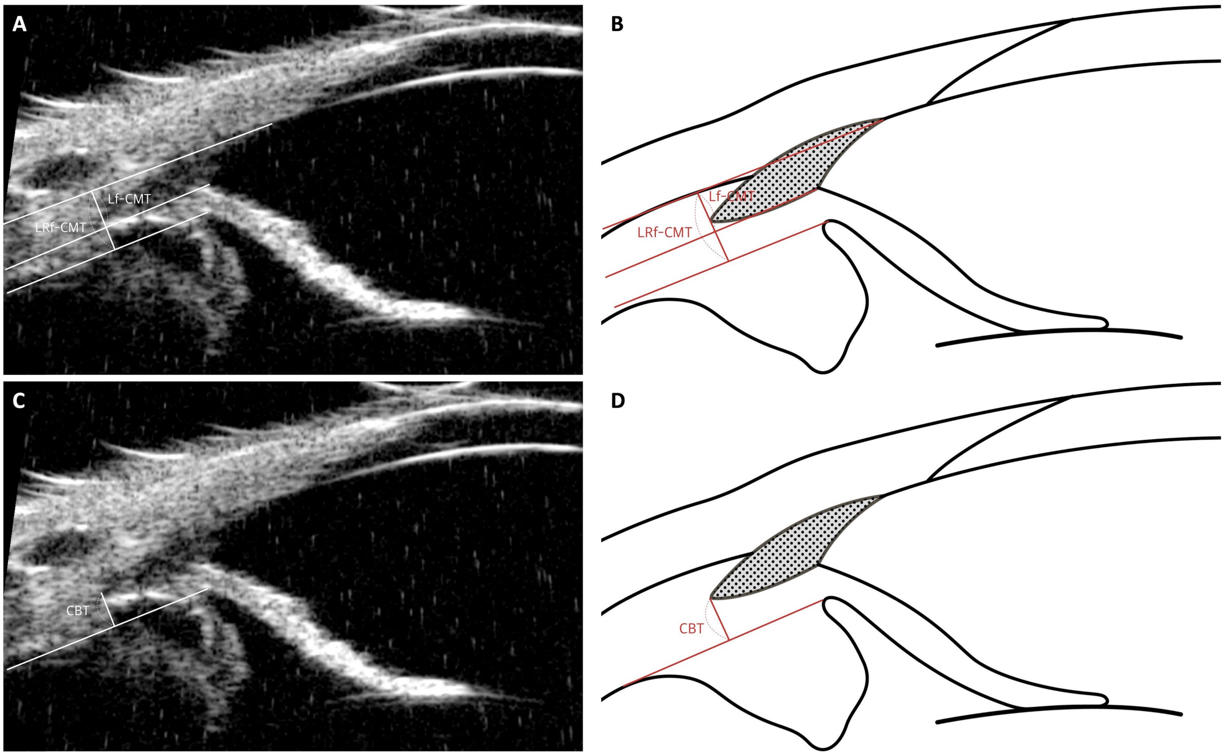


FIGURE 8
Measurement techniques of ciliary body muscle parameters using UBM images in dog. This figure presents the methods for assessing ciliary muscle parameters through UBM imaging. **(A, B)** The Lf-CMT (Longitudinal Fiber Ciliary Muscle Thickness) is determined by drawing a line through the inner scleral layer and the angle recess, with another line parallel to the inner scleral layer originating from the point where the iris root's inner layer meets the pectinate ligament. The LRf-CMT (Lateral Root Fiber Ciliary Muscle Thickness) measurement involves tracing a line through the inner scleral layer and the angle recess, and a parallel line from the point where the outer layer of the iris root connects to the dome-shaped ciliary body. **(C, D)** The CBT (Ciliary Body Thickness) is measured as the distance from the posterior end of the ciliary cleft (CC) to the edge of the ciliary pigmented epithelium, identified by its hyperechoic appearance on UBM images.

For these reasons, it is necessary for studies to pay attention to pharmacological agents that act on the iris and ciliary body in relation to the CC. The iris is influenced by receptors in the iris sphincter muscle, which contains muscarinic receptors, and in the iris dilator muscle, which contains $\alpha_1$-adrenergic receptors (87). In addition, the canine iris is highly populated with prostaglandin F (FP) receptors, resulting in miosis in response to drugs such as latanoprost (18).

The ciliary muscle is primarily controlled by parasympathetic innervation, which is mediated through the action of acetylcholine on muscarinic receptors. In the absence of parasympathetic stimulation, the ciliary muscle remains in a relaxed position. Upon parasympathetic stimulation, the ciliary muscle contracts (88, 89). Additionally, the ciliary muscle has well-developed prostaglandin receptors, particularly in dogs, where the prostaglandin F (FP) receptor is highly developed. This results in a strong responsiveness to drugs such as latanoprost, bimatoprost, and travoprost (90).

## 5.2 Influence of cholinergic antagonist drugs: tropicamide

Tropicamide is commonly used as a diagnostic agent to induce mydriasis due to its ability to rapidly dilate the pupil for a short duration. Research has investigated the effects of pharmaceutically induced mydriasis on intraocular pressure (IOP) in both dogs (15, 91).

A study by Thomas Dulaurent et al. evaluated structural changes associated with pupillary dilation, finding that the geometric angle formed by the plane of the iris root and the corneoscleral limbus (ICA) was larger in eyes with a dilated pupil compared to control eyes (15). This finding is consistent with earlier human studies, where mydriasis induced by three different mydriatics led to an enlargement of the geometric ICA. However, these results contradict a study by Rose et al., which reported that in noncataractous eyes, the ICA after pupillary dilation was smaller than before dilation (20). This discrepancy may be attributed to differences in measurement methodologies. In Rose et al.'s study, the ICA measurements included the most posterior portion of the CC, whereas Thomas Dulaurent et al. measured the geometric ICA formed by the iris root and the inner corneal surface (15, 20).

Moreover, the research by Thomas Dulaurent et al. demonstrated that the entry of the CC was narrower in eyes with dilated iris compared to control eyes. However, the mid-CC width and CC length did not differ between the two groups (15). These findings suggest that the CC width and functionality may be independent of the geometric angle formed by the iris and cornea. Their data indicated that mydriasis induced by topical tropicamide is associated with a constriction of the CC's entry, while its central width and length remain unchanged. This phenomenon may be explained by the anterior displacement of the iris root during mydriasis, with the folds on the anterior surface of the iris root potentially contributing to the narrowing of the CC by contraction. However, the lack of change in the mid-CC width and CC length could be explained by the relaxation of the ciliary body. Previous studies in humans have shown that 0.5% tropicamide induces relaxation of the ciliary body (92). Based on these findings, it appears that although iris movement due to mydriasis may compress the CC, the relaxation of the ciliary body may mitigate this effect.

## 5.3 Influence of cholinergic drugs: pilocarpine

Pilocarpine, a direct-acting parasympathomimetic, is known for inducing contractions in the ciliary muscle (21). In human studies, pilocarpine has been shown to cause the ciliary muscle bundles to pull on the scleral spur, which leads to the opening of fluid pathways in the TM, thereby increasing trabecular outflow (93).

In a canine study conducted by Park et al., parameters such as AOD, CCW, and CCA were elevated in eyes administered pilocarpine (18). Although the aqueous humor pathway was enhanced in this canine study as it was in human studies, the underlying mechanism appears to differ between the two species. Pilocarpine administration induces miosis of the iris and contraction of the ciliary body. From the perspective of the CC, these actions are opposing; however, it is presumed that the iris constriction predominated, ultimately resulting in an expansion of the CC.

While the ciliary body's response to pilocarpine—contraction—is similar in both humans and dogs, its effects on the TM and the CC appear to be contradictory. In humans, the ciliary muscle bundle attached to the scleral spur facilitates opening of the TM, whereas in dogs, the anteriorly inward movement of the ciliary body seems to narrow CC corresponding to the TM (94). In the author's opinion, these opposing outcomes are likely due to the anatomical differences between humans and dogs.

## 5.4 Influence of prostaglandin analogs: latanoprost, tafluprost

Prostaglandin analogs are potent agents for reducing IOP, known for their effectiveness in both canine and human subjects. In humans, prostaglandin analogs have been shown to lower IOP through a dual mechanism: an immediate relaxation of the ciliary muscle, followed by a gradual restructuring of the extracellular matrix between muscle bundles, which enhances uveoscleral outflow (22).

In a canine study led by Park et al., after administering 0.005% latanoprost, the AOD and CCA values were higher in treated eyes compared to control eyes (18). In a parallel study led by Kwak et al., tafluprost, a prostaglandin FP receptor agonist, resulted in an increase in CCW (95). In both of these studies, however, although a direct relationship between the configuration of the CC and the reduction in IOP was proposed, the supporting evidence was less robust than anticipated.

The likely reason for the inability to correlate IOP with the CC in these studies is the insufficient consideration of uveoscleral outflow. In the case of prostaglandin analogs, relaxation of the ciliary body decreases the pressure exerted on the CC, thereby leading to an increase in its size. Furthermore, the relaxation of the ciliary muscle increases the interstitial space between muscle bundles, which in turn enhances the outflow of aqueous humor (96). Consequently, simply correlating the CC with IOP may not adequately capture the underlying relationship. By utilizing UBM, it is possible to evaluate the first aspect of the prostaglandin analog's dual mechanism—that is, the changes in muscle thickness. Therefore, future studies employing parameters based on the ciliary muscle may help elucidate the relationship between these drugs and IOP more effectively.

## 6 Alterations in the iridocorneal angle and ciliary body post-cataract surgery

Following cataract surgery, particularly phacoemulsification, one concerning complication is glaucoma, which can lead to permanent vision loss and severe pain in dogs (97, 98). Another potential issue is POH, which occurs in 20–49% of dogs after phacoemulsification and IOL implantation (99). To better understand these complications, several studies have been conducted to investigate structural changes in the ICA of dogs, comparing its condition before and immediately after cataract surgery and IOL placement.

### 6.1 Parameter differences according to cataract progression stages

In our previous study., differences in CC parameters based on cataract stages were highlighted. As cataract progression advanced, metrics such as CCW, CCL, and CCA tended to increase. Specifically, CCW showed a rise in eyes with immature cataracts compared to normal eyes. CCL also exhibited a notable increase in both immature and mature cataracts relative to normal eyes, with this increase being more pronounced in mature cataracts compared to incipient ones. While CCA values were elevated in both immature and mature cataracts compared to normal and incipient cataract eyes, no differences were observed in ICA and AOD across the various stages of cataract progression (26).

In another study by the same author, it was observed that as cataract stages progressed, there was a consistent decrease in CBAXL. Significant differences were particularly noticeable between normal eyes and those with both immature and mature cataracts. This trend suggests a gradual relaxation of the ciliary body as cataracts advance. Although CPSA exhibited an increasing trend with cataract progression, this rise was not statistically significant across the various stages. Lf-CMT, however, showed a notable increase as cataracts developed, indicating a thickening of the longitudinal fibers of the ciliary muscle. These findings highlight that the axial length and muscle thickness of the ciliary body undergo measurable changes as cataracts progress (25).

The underlying rationale for these observations is as follows: as cataracts mature, there is a tendency for the ciliary muscle to enter a more relaxed state, leading to outward and backward shifts of the ciliary body (77, 78). These human findings are consistent with the our previous two studies in dogs. In dogs, as cataracts progress, the lens thickens, increasing tension on the zonular fibers, which promotes relaxation of the ciliary body. Given these movements of the ciliary body, it appears that the CC also undergoes expansion as cataracts advance (25, 26).

Pathological changes in the lens and the resulting alterations in the ciliary body are also well-documented in human studies. Research by Park et al. indicates that in cataract patients, the contractility of the ciliary body decreases but improves following cataract surgery. This was demonstrated through CBAXL measurements, where no difference was observed after pilocarpine instillation in cataract patients, but a increase was noted post-surgery. These findings are consistent with the results of the study by Park et al. (77)

### 6.2 Parameter modifications pre-and post-cataract surgery

In a study by Crumley et al., UBM was used to investigate the relationship between the pre-operative morphology of the ICA in dogs scheduled for cataract surgery and their post-operative IOPs. The researchers identified a weak correlation between pre-operative AOD and IOP measured one day after phacoemulsification (100).

Rose et al. suggested that POH is more likely to occur when the preoperative ICA exceeds 13 degrees, indicating that certain predisposing factors prior to phacoemulsification may trigger POH. However, the AOD and ICA did not show consistent changes before and after surgery, likely due to significant individual variations (20).

Our previous research revealed notable differences between the cataract group and the post-phaco group. The post-phaco group displayed smaller values for CCW, CCL, and CCA, suggesting a contraction of the CC following phacoemulsification. However, when assessing AOD and ICA, no differences were observed between the two groups, indicating that neither cataract progression nor phacoemulsification had a substantial impact on these parameters in canines (26).

In another our previous study, clear differences were observed between the cataract and post-surgery groups. The cataract group had a lower CBAXL value compared to the post-surgery group. Additionally, the CPSA value was lower in the post-surgery group than in the cataract group. The Lf-CMT value was higher in the cataract group but decreased following surgery. These findings indicate significant changes in these parameters before and after cataract surgery (25).

The rationale behind our previous findings is based on the behavior of the ciliary muscle. After phacoemulsification, the ciliary muscle contracts, causing the ciliary body to move inward and anteriorly (25, 26). These observations align with previous human studies, where cataract extraction led to reduced lens thickness, which may relieve zonular tension and allow for smoother movement of the ciliary body (77, 78).

## 7 Inter-breed differences in the canine anterior segment

In veterinary clinical practice, PACG is more common than primary open-angle glaucoma (POAG) in dogs, leading to a greater focus on the former (24). Canine PACG is characterized by the progressive narrowing and eventual collapse of the CC and ICA (101, 102). Breeds such as the American Cocker Spaniel (ACS), Basset Hound, Chow Chow, and Siberian Husky are known to be particularly predisposed to developing PACG, with the ACS showing the highest susceptibility, especially in North America (103). This increased predisposition in specific breeds has driven substantial research interest in the unique characteristics of the anterior segment in these dogs, resulting in various studies focused on this area. This breed predisposition has led to increased interest in the anatomical characteristics of the anterior segment, prompting comparative studies among breeds.

While POAG is rarely observed in clinical practice, it is most commonly reported in Beagles, whereas ACSs demonstrate a significantly higher susceptibility to PACG (49). A study led by Park et al. compared the anterior segment morphology of ACSs and Beagles, highlighting key differences in ocular dimensions (49). Despite similar overall globe sizes, the ACS exhibited a more compact anterior segment, characterized by a notably shallower anterior chamber depth and a thinner yet more anteriorly positioned lens compared to the Beagle (49). In human ophthalmology, the anterior position of the lens is considered a more critical factor than its thickness in determining the risk of angle closure. A more anteriorly positioned or protruding lens is associated with an increased likelihood of pupillary block, leading to greater iridolenticular contact and subsequent angle narrowing (104, 105). The findings from a Park's study support this concept, demonstrating greater contact between the ACS's posterior iris surface and the anterior lens capsule (49). This heightened iridolenticular contact exacerbates fluid entrapment at the pupillary margin, increasing resistance to aqueous humor outflow and resulting in a distinctive concave, sigmoidal-shaped iris configuration, which was more pronounced in ACSs compared to Beagles. These breed-specific anatomical differences may contribute to the higher prevalence of PACG in ACSs and warrant further investigation into their role in disease pathogenesis (49).

## 8 Discussion and future prospects

In veterinary science, UBM has emerged as an invaluable tool for the detailed examination of anterior eye segments, enabling precise study of the anatomical structures of anterior segment (10) UBM's ability to accurately assess key components, such as the ICA and ciliary body, is particularly noteworthy (3). Despite its potential, research in the veterinary field remains in its early stages, with much of the initial work adopting parameters from human medical studies. However, there is a growing focus on understanding the differences in ICA anatomy between humans and animals, with increasing emphasis on the role of the CC in regulating AH outflow.

Several gaps in our understanding remain. A primary concern is the limited literature addressing the underlying causes of changes in the CC. Many existing studies simply report the expansion or contraction of the CC without providing substantive explanations. However, recent efforts appear to be more focused on elucidating these changes. While current knowledge acknowledges the role of ciliary muscle actions (both relaxation and contraction) and the oscillatory movements of the iris, in-depth investigations into the root causes are still lacking (15, 25). It is anticipated that future research will explore the effects of drug-induced modifications on the ciliary muscle and iris and how these changes influence the transformation of the CC.

Another significant gap is the limited focus on the unconventional outflow pathway of AH. Given UBM's precision in measuring the ciliary body and studies suggesting a relationship between ciliary body dynamics and unconventional outflow, it is noteworthy that this crucial area remains under-researched (85, 96). Additionally, it is ironic that the ciliary body receives minimal attention in studies involving prostaglandin analogs, despite their well-documented effect on relaxing the ciliary muscle and subsequently reducing IOP.

Furthermore, research linking UBM-measurable parameters to IOP remains insufficient. Although existing studies do not show a clear correlation between parameters such as ICA or CC and IOP, this may be due to the compensatory mechanisms of IOP regulation. The eye adjusts both the production and outflow of AH in response to IOP fluctuations, often causing IOP to return to near baseline values (106). Nonetheless, a more in-depth exploration of the relationship between UBM parameters and IOP seems essential.

There is a notable lack of research utilizing UBM in feline studies. While PACG accounts for approximately 87% of all glaucoma cases in dogs, it represents only 2% of cases in cats (107–109). Additionally, unlike dogs, cats have anatomical differences that pose challenges for UBM imaging, particularly due to the difficulty in exposing the sclera beneath the eyelid. These factors likely contribute to the limited research on aqueous humor dynamics in felines using UBM. However, comparative anatomical studies in cats may provide valuable insights that could aid in the development of improved glaucoma treatment strategies for both dogs and humans.

Several areas for further research remain in the field of veterinary ophthalmology. In canine glaucoma, mydriasis is known to induce ICA crowding, leading to increased IOP (24, 49, 110). However, the precise underlying mechanism remains unclear. The authors hypothesize that pupillary dilation may cause anterior displacement of the iris, exerting pressure on the CC. To alleviate this effect, promoting ciliary body relaxation may help mitigate ICA crowding. Further investigation is required to elucidate these interactions and their implications for glaucoma management.

Beyond glaucoma research, UBM has also been widely utilized in human ophthalmology for diagnosing lens subluxation (111). In canine patients, lens subluxation may be detected during the preoperative evaluation for phacoemulsification, necessitating surgical interventions such as capsular tension ring placement or scleral fixation to ensure stable intraocular lens implantation (112). The ability of UBM to assess the positional dynamics and orientation of the lens may provide a valuable tool for diagnosing and managing lens subluxation in dogs, similar to its application in human medicine.

This study explores the application of UBM in canine ophthalmology, summarizing existing research, the authors' perspectives, and directions for future investigations. It is hoped that this paper will serve as a valuable resource for researchers initiating studies using UBM as well as clinicians utilizing it in practice.

## Author contributions

DK: Conceptualization, Software, Validation, Visualization, Writing – original draft, Writing – review & editing. HK: Validation, Writing – review & editing. JH: Visualization, Writing – review & editing. JJ: Validation, Writing – review & editing. K-MP: Funding acquisition, Resources, Supervision, Writing – review & editing.

## Funding

The author(s) declare that financial support was received for the research, authorship, and/or publication of this article. This work was supported by a grant from the National Research Foundation of Korea (NRF), funded by the Korean government (MSIT) (RS-2024-00344226). Additionally, this study was funded by the Ministry of Science and ICT and the Korean Fund for Regenerative Medicine (KFRM) grant, supported by the Ministry of Science and ICT and the Ministry of Health & Welfare (No. 22A0101L1-11).

## Conflict of interest

The authors declare that the research was conducted in the absence of any commercial or financial relationships that could be construed as a potential conflict of interest.

## Publisher's note

All claims expressed in this article are solely those of the authors and do not necessarily represent those of their affiliated organizations, or those of the publisher, the editors and the reviewers. Any product that may be evaluated in this article, or claim that may be made by its manufacturer, is not guaranteed or endorsed by the publisher.

## References

1. Pavlin CJ, Harasiewicz K, Sherar MD, Foster FS. Clinical use of ultrasound biomicroscopy. *Ophthalmology*. (1991) 98:287–95. doi: 10.1016/S0161-6420(91)32298-X

2. Pavlin CJ, Foster FS. Ultrasound biomicroscopy. High-frequency ultrasound imaging of the eye at microscopic resolution. *Radiol Clin North Am*. (1998) 36:1047–58. doi: 10.1016/S0033-8389(05)70230-X

3. Nolan W. Anterior segment imaging: ultrasound biomicroscopy and anterior segment optical coherence tomography. *Curr Opin Ophthalmol*. (2008) 19:115–21. doi: 10.1097/ICU.0b013e3282f40bba

4. Silverman RH. High-resolution ultrasound imaging of the eye - a review. *Clin Experiment Ophthalmol*. (2009) 37:54–67. doi: 10.1111/j.1442-9071.2008.01892.x

5. Ang M, Baskaran M, Werkmeister RM, Chua J, Schmidl D, Aranha dos Santos V, et al. Anterior segment optical coherence tomography. *Prog Retin Eye Res*. (2018) 66:132–56. doi: 10.1016/j.preteyeres.2018.04.002

6. Sakata LM, Deleon-Ortega J, Sakata V, Girkin CA. Optical coherence tomography of the retina and optic nerve - a review. *Clin Experiment Ophthalmol*. (2009) 37:90–9. doi: 10.1111/j.1442-9071.2009.02015.x

7. Israelsen NM, Petersen CR, Barh A, Jain D, Jensen M, Hannesschläger G, et al. Real-time high-resolution mid-infrared optical coherence tomography. *Light Sci Appl*. (2019) 8:11. doi: 10.1038/s41377-019-0122-5

8. Shim J, Kang S, Jeong Y, Lee E, Jeong D, Seo K. Comparison of iridocorneal angle parameters measured by spectral domain optical coherence tomography and ultrasound biomicroscopy in dogs. *Vet Ophthalmol*. (2022) 25:103–10. doi: 10.1111/vop.12950

9. Adhi M, Duker JS. Optical coherence tomography--current and future applications. *Curr Opin Ophthalmol*. (2013) 24:213–21. doi: 10.1097/ICU.0b013e32835f8bf8

10. Bentley E, Miller PE, Diehl KA. Use of high-resolution ultrasound as a diagnostic tool in veterinary ophthalmology. *J Am Vet Med Assoc*. (2003) 223:1617–22. doi: 10.2460/javma.2003.223.1617

11. Parvathy G, Nazir A, Morani Z, Nazir A. Unveiling the power of imaging techniques: comparing high-resolution ultrasound and functional MR neurography in peripheral nervous system pathology: a short communication. *Ann Med Surg (Lond)*. (2023) 85:5834–7. doi: 10.1097/MS9.0000000000001368

12. Kim MG, Yoon S, Kim HH, Shung K. Impedance matching network for high frequency ultrasonic transducer for cellular applications. *Ultrasonics*. (2015) 65:258–67. doi: 10.1016/j.ultras.2015.09.016

13. Kapetansky F. An improved water Bath for Ultrasound biomicroscopy. *Ophthalmic Surg Lasers Imaging*. (2005) 36:523–5. doi: 10.3928/1542-8877-20051101-17

14. Snehi S, Singh AK, Kaushik S. Ultrasound biomicroscopy: an invaluable asset in glaucoma. Kerala. *J Ophthalmol*. (2023) 35:8–16. doi: 10.4103/kjo.kjo_116_22

15. Dulaurent T, Goulle F, Dulaurent A, Mentek M, Peiffer RL, Isard P-F. Effect of mydriasis induced by topical instillations of 0.5% tropicamide on the anterior segment in normotensive dogs using ultrasound biomicroscopy. *Vet Ophthalmol*. (2012) 15:8–13. doi: 10.1111/j.1463-5224.2011.00898.x

16. Boillot T, Rosolen SG, Dulaurent T, Goulle F, Thomas P, Isard PF, et al. Determination of morphological, biometric and biochemical susceptibilities in healthy Eurasier dogs with suspected inherited glaucoma. *PLoS One*. (2014) 9:e111873. doi: 10.1371/journal.pone.0111873

17. Kawata M, Tsukizawa H, Nakayama M, Hasegawa T. Rectification of width and area of the ciliary cleft in dogs. *J Vet Med Sci*. (2010) 72:533–7. doi: 10.1292/jvms.09-0507

18. Park S, Kang S, Lim J, Park E, Nam T, Jeong S, et al. Effects of prostaglandin-mediated and cholinergic-mediated miosis on morphology of the ciliary cleft region in dogs. *Am J Vet Res*. (2018) 79:980–5. doi: 10.2460/ajvr.79.9.980

19. Park S, Kang S, Lee E, Kwak J, Park E, Lim J, et al. Ultrasound biomicroscopic study of the effects of topical latanoprost on the anterior segment and ciliary body thickness in dogs. *Vet Ophthalmol*. (2016) 19:498–503. doi: 10.1111/vop.12339

20. Rose MD, Mattoon JS, Gemensky-Metzler AJ, Wilkie DA, Rajala-Schultz PJ. Ultrasound biomicroscopy of the iridocorneal angle of the eye before and after phacoemulsification and intraocular lens implantation in dogs. *Am J Vet Res*. (2008) 69:279–88. doi: 10.2460/ajvr.69.2.279

21. Crawford K, Kaufman PL. Pilocarpine antagonizes prostaglandin F2α-induced ocular hypotension in monkeys: evidence for enhancement of Uveoscleral outflow by prostaglandin F2α. *Arch Ophthalmol*. (1987) 105:1112–6. doi: 10.1001/archopht.1987.01060080114039

22. Lütjen-Drecoll E, Tamm E. Morphological study of the anterior segment of cynomolgus monkey eyes following treatment with prostaglandin F2 alpha. *Exp Eye Res*. (1988) 47:761–9. doi: 10.1016/0014-4835(88)90043-7

23. Hasegawa T, Kawata M, Ota M. Ultrasound biomicroscopic findings of the iridocorneal angle in live healthy and glaucomatous dogs. *J Vet Med Sci*. (2016) 77:1625–31. doi: 10.1292/jvms.15-0311

24. Miller PE, Bentley E. Clinical signs and diagnosis of the canine primary Glaucomas. *Vet Clin North Am Small Anim Pract*. (2015) 45:1183–1212, vi. doi: 10.1016/j.cvsm.2015.06.006

25. Kim D, Park S-E, Hwang J, Kang N, Jung JS, Park K-M. Ultrasound biomicroscopy analysis of ciliary muscle dynamics and its relation to intra-ocular pressure after phacoemulsification in dogs. Frontiers in veterinary. *Science*. (2024) 11:11. doi: 10.3389/fvets.2024.1366997

26. Kim D, Goh Y-S, Kim H, Park S-E, Hwang J, Kang N, et al. Evaluation of ciliary cleft changes after phacoemulsification using ultrasound biomicroscopy in dogs with cataracts. Frontiers in veterinary. *Science*. (2023) 10:10. doi: 10.3389/fvets.2023.1247127

27. Siam GA, de Barros DS, Gheith ME, Da Silva RS, Lankaranian D, Tittler EH, et al. The amount of intraocular pressure rise during pharmacological pupillary dilatation is an indicator of the likelihood of future progression of glaucoma. *Br J Ophthalmol*. (2007) 91:1170–2. doi: 10.1136/bjo.2007.116855

28. Pizzirani S, Gong H. Functional anatomy of the outflow facilities. *Vet Clin North Am Small Anim Pract*. (2015) 45:1101–26, v. doi: 10.1016/j.cvsm.2015.06.005

29. Johnson M, Erickson K. Mechanisms and routes of aqueous humor drainage. In: DM Albert and FA Jakobiec editors. *Principles and Practice of Ophthalmology*. (Philadelphia: WB Saunders Co), (2000).

30. Tripathi RC. Ultrastructure of the exit pathway of the aqueous in lower mammals. (a preliminary report on the "angular aqueous plexus"). *Exp Eye Res*. (1971) 12:311–4. doi: 10.1016/0014-4835(71)90155-2

31. Abu-Hassan DW, Acott TS, Kelley MJ. The trabecular meshwork: a basic review of form and function. *J Ocul Biol*. (2014) 2:9. doi: 10.13188/2334-2838.1000017

32. Buffault J, Labbé A, Hamard P, Brignole-Baudouin F, Baudouin C. The trabecular meshwork: structure, function and clinical implications. A review of the literature. *J Fr Ophtalmol*. (2020) 43:e217–30. doi: 10.1016/j.jfo.2020.05.002

33. Gibson TE, Roberts SM, Severin GA, Steyn PF, Wrigley RH. Comparison of gonioscopy and ultrasound biomicroscopy for evaluating the iridocorneal angle in dogs. *J Am Vet Med Assoc*. (1998) 213:635–8. doi: 10.2460/javma.1998.213.05.635

34. Bedford PG. A gonioscopic study of the iridocorneal angle in the English and American breeds of cocker spaniel and the basset hound. *J Small Anim Pract*. (1977) 18:631–42. doi: 10.1111/j.1748-5827.1977.tb05831.x

35. Simones P, De Geest JP, Lauwers H. Comparative morphology of the pectinate ligaments of domestic mammals, as observed under the dissecting microscope and the scanning electron microscope. *J Vet Med Sci*. (1996) 58:977–82. doi: 10.1292/jvms.58.10_977

36. Leeson TS, Speakman JS. The fine structure of extracellular material in the pectinate ligament (trabecular meshwork) of the human iris. *Acta Anat (Basel)*. (1961) 46:363–79. doi: 10.1159/000141795

37. Bedford PGC, Grierson I. Aqueous drainage in the dog. *Res Vet Sci*. (1986) 41:172–86. doi: 10.1016/S0034-5288(18)30595-2

38. Duke-Elder ES, Duke-Elder S, Wybar KC. System of Ophthalmology: The eye in evolution. *Anatomy and histology of the eye and orbit in domestic animals*. London, UK: Kimpton (1958).

39. Bill A, Hellsing K. Production and drainage of aqueous humor in the cynomolgus monkey (*Macaca irus*). *Investig Ophthalmol*. (1965) 4:920–6.

40. Samuelson D. A reevaluation of the comparative anatomy of the eutherian iridocorneal angle and associated ciliary body musculature In: Veterinary and comparative ophthalmology (USA) (1996)

41. Yanoff M, Sassani JW. 9 - Uvea In: M Yanoff and JW Sassani, editors. Ocular pathology. *8th* ed. London: Elsevier (2020). 357–79.e5.

42. Miller PE. Chapter 11 - Uvea In: DJ Maggs, PE Miller and R Ofri, editors. Slatter's fundamentals of veterinary ophthalmology. *4th* ed. Saint Louis: W.B. Saunders (2008). 203–29.

43. Tamm S, Tamm E, Rohen JW. Age-related changes of the human ciliary muscle. A quantitative morphometric study. *Mech Ageing Dev*. (1992) 62:209–21. doi: 10.1016/0047-6374(92)90057-K

44. Remington LA. Chapter 3 - Uvea In: LA Remington, editor. Clinical anatomy and physiology of the visual system. *3rd* ed. Saint Louis: Butterworth-Heinemann (2012). 40–60.

45. Glasser A, Kaufman PL. The mechanism of accommodation in primates. *Ophthalmology*. (1999) 106:863–72. doi: 10.1016/S0161-6420(99)00502-3

46. Croft MA, Glasser A, Heatley G, McDonald J, Ebbert T, Dahl DB, et al. Accommodative ciliary body and lens function in rhesus monkeys, I: normal lens, zonule and ciliary process configuration in the iridectomized eye. *Invest Ophthalmol Vis Sci*. (2006) 47:1076–86. doi: 10.1167/iovs.04-1523

47. Ott M. Visual accommodation in vertebrates: mechanisms, physiological response and stimuli. *J Comp Physiol A Neuroethol Sens Neural Behav Physiol*. (2006) 192:97–111. doi: 10.1007/s00359-005-0049-6

48. Goel M, Picciani RG, Lee RK, Bhattacharya SK. Aqueous humor dynamics: a review. *Open Ophthalmol J*. (2010) 4:52–9. doi: 10.2174/1874364101004010052

49. Park S, Casanova MI, Bannasch DL, Daley NL, Kim S, Kuchtey J, et al. Ocular morphologic traits in the American cocker spaniel may confer primary angle closure glaucoma susceptibility. *Sci Rep*. (2022) 12:18980. doi: 10.1038/s41598-022-23238-1

50. Aubin ML, Powell CC, Gionfriddo JR, Fails AD. Ultrasound biomicroscopy of the feline anterior segment. *Vet Ophthalmol*. (2003) 6:15–7. doi: 10.1046/j.1463-5224.2003.00255.x

51. Johnstone MA. CHAPTER 3 - aqueous humor outflow system overview In: RL Stamper, MF Lieberman and MV Drake, editors. Becker-Shaffer's diagnosis and therapy of the Glaucomas. *8th* ed. Edinburgh: Mosby (2009). 25–46.

52. Remington LA. Chapter 2 - cornea and sclera In: LA Remington, editor. Clinical anatomy and physiology of the visual system. *Third* ed. Saint Louis: Butterworth-Heinemann (2012). 10–39.

53. Kurimoto Y, Park M, Sakaue H, Kondo T. Changes in the anterior chamber configuration after small-incision cataract surgery with posterior chamber intraocular lens implantation. *Am J Ophthalmol*. (1997) 124:775–80. doi: 10.1016/S0002-9394(14)71694-0

54. Fernández-Vigo JI, Fernández-Vigo C, de la Casa JM M, Sáenz-Francés F, Santos-Bueso E, García Feijóo J, et al. Identification of iridocorneal angle structures assessed by Fourier domain optical coherence tomography. *Arch Soc Esp Oftalmol*. (2016) 91:74–80. doi: 10.1016/j.oftal.2015.10.007

55. Crowell EL, Baker L, Chuang AZ, Feldman RM, Bell NP, Chévez-Barrios P, et al. Characterizing anterior segment OCT angle landmarks of the trabecular meshwork complex. *Ophthalmology*. (2018) 125:994–1002. doi: 10.1016/j.ophtha.2018.01.018

56. King B, Burns S, Sapoznik K, Luo T, Gast T. High-resolution, adaptive optics imaging of the human trabecular meshwork in vivo. *Transl Vis Sci Technol*. (2019) 8:5. doi: 10.1167/tvst.8.5.5

57. Jiang Y, He M, Huang W, Huang Q, Zhang J, Foster PJ. Qualitative assessment of ultrasound biomicroscopic images using standard photographs: the liwan eye study. *Invest Ophthalmol Vis Sci*. (2010) 51:2035–42. doi: 10.1167/iovs.09-4145

58. Chen D, Gong XH, Xie H, Zhu XN, Li J, Zhao YE. The long-term anterior segment configuration after pediatric cataract surgery and the association with secondary glaucoma. *Sci Rep*. (2017) 7:43015. doi: 10.1038/srep43015

59. Adriana Silva Borges G, Jair GJ. Anatomy of ciliary body, ciliary processes, anterior chamber angle and collector vessels In: R Shimon, editor. Glaucoma. Rijeka: IntechOpen (2013). Ch. 1.

60. Accommodation GA In: DA Dartt, editor. Encyclopedia of the eye. Oxford: Academic Press (2010). 8–17.

61. Ebersberger A, Flügel C, Lütjen-Drecoll E. Ultrastructural and enzyme histochemical studies of regional structural differences within the ciliary muscle in various species. *Klin Monatsbl Augenheilkd*. (1993) 203:53–8. doi: 10.1055/s-2008-1045648

62. Prince JH, Diesem CD, Eglitis I, Ruskell G. Anatomy and histology of the eye and orbit in domestic animals. ed. CC Thomas USA: Springfield, IL, (1960).

63. Wang YE, Li Y, Wang D, He M, Wu L, Lin SC. Comparison of iris insertion classification among american caucasian and ethnic Chinese using ultrasound biomicroscopy. *Invest Ophthalmol Vis Sci*. (2013) 54:3837–43. doi: 10.1167/iovs.12-11585

64. Dada T, Mohan S, Sihota R, Gupta R, Gupta V, Pandey RM. Comparison of ultrasound biomicroscopic parameters after laser iridotomy in eyes with primary angle closure and primary angle closure glaucoma. *Eye*. (2007) 21:956–61. doi: 10.1038/sj.eye.6702360

65. Kaushik S, Kumar S, Jain R, Bansal R, Pandav SS, Gupta A. Ultrasound biomicroscopic quantification of the change in anterior chamber angle following laser peripheral iridotomy in early chronic primary angle closure glaucoma. *Eye*. (2007) 21:735–41. doi: 10.1038/sj.eye.6702317

66. Gupta D, Chen PP. Glaucoma. *Am Fam Physician*. (2016) 93:668.

67. Stamper RL, Lieberman MF, Drake MV. CHAPTER 5 - Gonioscopic anatomy In: RL Stamper, MF Lieberman and MV Drake, editors. Becker-Shaffer's diagnosis and therapy of the Glaucomas. *8th* ed. Edinburgh: Mosby (2009). 68–72.

68. Carassa RG, Bettin P, Fiori M, Brancato R. Nd:YAG laser iridotomy in pigment dispersion syndrome: an ultrasound biomicroscopic study. *Br J Ophthalmol*. (1998) 82:150–3. doi: 10.1136/bjo.82.2.150

69. Zhang Y, Li SZ, Li L, He MG, Thomas R, Wang NL. Dynamic Iris changes as a risk factor in primary angle closure disease. *Invest Ophthalmol Vis Sci*. (2016) 57:218–26. doi: 10.1167/iovs.15-17651

70. Tarongoy P, Ho CL, Walton DS. Angle-closure glaucoma: the role of the lens in the pathogenesis, prevention, and treatment. *Surv Ophthalmol*. (2009) 54:211–25. doi: 10.1016/j.survophthal.2008.12.002

71. Caronia RM, Liebmann JM, Stegman Z, Sokol J, Ritch R. Increase in iris-lens contact after laser iridotomy for pupillary block angle closure. *Am J Ophthalmol*. (1996) 122:53–7. doi: 10.1016/S0002-9394(14)71963-4

72. Boese EA, Critser DB, Fingert JH. High Iris insertion in Axenfeld-Rieger syndrome. *Ophthalmology*. (2020) 127:768. doi: 10.1016/j.ophtha.2020.02.012

73. Choi K-H, Choo SW, Jeong S-w, Kim JY. Ultrasound biomicroscopy studies to evaluate ciliary cleft parameters in healthy eyes of American cocker spaniels. *Pak Vet J*. (2019) 39:66–70. doi: 10.29261/pakvetj/2019.002

74. Cottrill NB, Banks WJ, Pechman RD. Ultrasonographic and biometric evaluation of the eye and orbit of dogs. *Am J Vet Res*. (1989) 50:898–903. doi: 10.2460/ajvr.1989.50.06.898

75. Kawata M, Hasegawa T. Evaluation of the distance between Schwalbe's line and the anterior lens capsule as a parameter for the correction of ultrasound biomicroscopic values of the canine iridocorneal angle. *Vet Ophthalmol*. (2013) 16:169–74. doi: 10.1111/j.1463-5224.2012.01043.x

76. Kim D, Kwon H, Hwang J, Jung JS, Kwon M, Yong J, et al. Sex differences in canine anterior chamber dimensions: potential implications for primary angle-closure glaucoma. *Vet Ophthalmol*. (2024). doi: 10.1111/vop.13303

77. Park KA, Yun JH, Kee C. The effect of cataract extraction on the contractility of ciliary muscle. *Am J Ophthalmol*. (2008) 146:8–14.e2. doi: 10.1016/j.ajo.2008.02.026

78. Fayed AAE. Ultrasound biomicroscopy value in evaluation of restoration of ciliary muscles contractility after cataract extraction. *Clin Ophthalmol*. (2017) 11:855–9. doi: 10.2147/OPTH.S131399

79. Ramasubramanian V, Glasser A. Can ultrasound biomicroscopy be used to predict accommodation accurately? *J Refract Surg*. (2015) 31:266–73. doi: 10.3928/1081597X-20150319-06

80. Motlagh M, Geetha R. Physiology, Accommodation. StatPearls. Treasure Island, FL: StatPearls Publishing Copyright © 2023: StatPearls Publishing LLC (2023).

81. Peddie W. Helmholtz's treatise on physiological optics. *Nature*. (1926) 118:74–6. doi: 10.1038/118074a0

82. Jonas JB, Jonas RA, Jonas SB, Panda-Jonas S. Ciliary body size in chronic angle-closure glaucoma. *Sci Rep*. (2023) 13:16914. doi: 10.1038/s41598-023-44085-8

83. Alm A, Nilsson SFE. Uveoscleral outflow – a review. *Exp Eye Res*. (2009) 88:760–8. doi: 10.1016/j.exer.2008.12.012

84. Bill A, Phillips CI. Uveoscleral drainage of aqueous humour in human eyes. *Exp Eye Res*. (1971) 12:275–81. doi: 10.1016/0014-4835(71)90149-7

85. Lütjen-Drecoll E, Tamm E, Kaufman PL. Age-related loss of morphologic responses to pilocarpine in rhesus monkey ciliary muscle. *Arch Ophthalmol*. (1988) 106:1591–8. doi: 10.1001/archopht.1988.01060140759051

86. Dubin AJ, Bentley E, Buhr KA, Miller PE. Evaluation of potential risk factors for development of primary angle-closure glaucoma in Bouviers des Flandres. *J Am Vet Med Assoc*. (2017) 250:60–7. doi: 10.2460/javma.250.1.60

87. Beau SL, Hand DE, Schuessler RB, Bromberg BI, Kwon B, Boineau JP, et al. Relative densities of muscarinic cholinergic and beta-adrenergic receptors in the canine sinoatrial node and their relation to sites of pacemaker activity. *Circ Res*. (1995) 77:957–63. doi: 10.1161/01.RES.77.5.957

88. Waller DG, Sampson AP. 50 - the eye In: DG Waller and AP Sampson, editors. Medical pharmacology and therapeutics. *5th* ed. Elsevier, Amsterdam, Netherlands: Elsevier (2018). 569–78.

89. Benarroch EE. Parasympathetic system; overview In: MJ Aminoff and RB Daroff, editors. Encyclopedia of the neurological sciences. *2nd* ed. Oxford: Academic Press (2014). 805–8.

90. Yousufzai SYK, Ye ZHI, Abdel-Latif AA. Prostaglandin F2αand its analogs induce release of endogenous prostaglandins in Iris and ciliary muscles isolated from cat and other mammalian species. *Exp Eye Res*. (1996) 63:305–10. doi: 10.1006/exer.1996.0119

91. Kovalcuka L, Ilgazs A, Bandere D, Williams DL. Changes in intraocular pressure and horizontal pupil diameter during use of topical mydriatics in the canine eye. *Open Vet J*. (2017) 7:16–22. doi: 10.4314/ovj.v7i1.3

92. Chen Y, Gao J, Li L, Sellitto C, Mathias RT, Donaldson PJ, et al. The ciliary muscle and Zonules of Zinn modulate Lens intracellular hydrostatic pressure through transient receptor potential Vanilloid channels. *Invest Ophthalmol Vis Sci*. (2019) 60:4416–24. doi: 10.1167/iovs.19-27794

93. Grierson I, Lee WR, Abraham S. Effects of pilocarpine on the morphology of the human outflow apparatus. *Br J Ophthalmol*. (1978) 62:302–13. doi: 10.1136/bjo.62.5.302

94. Carreras FJ, Porcel D, González-Caballero F. Expanding forces in aqueous outflow pathways of a nonaccommodating mammal: an approach via comparative dynamic morphology. *Comp Biochem Physiol A Physiol*. (1997) 117:197–209. doi: 10.1016/S0300-9629(96)00280-0

95. Kwak J, Kang S, Lee ER, Park S, Park S, Park E, et al. Effect of preservative-free tafluprost on intraocular pressure, pupil diameter, and anterior segment structures in normal canine eyes. *Vet Ophthalmol*. (2017) 20:34–9. doi: 10.1111/vop.12341

96. Johnson M, McLaren JW, Overby DR. Unconventional aqueous humor outflow: a review. *Exp Eye Res*. (2017) 158:94–111. doi: 10.1016/j.exer.2016.01.017

97. Klein HE, Krohne SG, Moore GE, Stiles J. Postoperative complications and visual outcomes of phacoemulsification in 103 dogs (179 eyes): 2006–2008. *Vet Ophthalmol*. (2011) 14:114–20. doi: 10.1111/j.1463-5224.2010.00853.x

98. Lannek EB, Miller PE. Development of glaucoma after phacoemulsification for removal of cataracts in dogs: 22 cases (1987-1997). *J Am Vet Med Assoc*. (2001) 218:70–6. doi: 10.2460/javma.2001.218.70

99. Smith PJ, Brooks DE, Lazarus JA, Kubilis PS, Gelatt KN. Ocular hypertension following cataract surgery in dogs: 139 cases (1992-1993). *J Am Vet Med Assoc*. (1996) 209:105–11. doi: 10.2460/javma.1996.209.01.105

100. Crumley W, Gionfriddo JR, Radecki SV. Relationship of the iridocorneal angle, as measured using ultrasound biomicroscopy, with post-operative increases in intraocular pressure post-phacoemulsification in dogs. *Vet Ophthalmol*. (2009) 12:22–7. doi: 10.1111/j.1463-5224.2009.00669.x

101. Pearl R, Gould D, Spiess B. Progression of pectinate ligament dysplasia over time in two populations of flat-coated retrievers. *Vet Ophthalmol*. (2015) 18:6–12. doi: 10.1111/vop.12098

102. Uvea MP. Slatter's fundamentals of veterinary ophthalmology. Philadelphia: Saunders Elsevier (2008).

103. Gelatt KN, MacKay EO. Prevalence of the breed-related glaucomas in pure-bred dogs in North America. *Vet Ophthalmol*. (2004) 7:97–111. doi: 10.1111/j.1463-5224.2004.04006.x

104. Nongpiur ME, He M, Amerasinghe N, Friedman DS, Tay WT, Baskaran M, et al. Lens vault, thickness, and position in Chinese subjects with angle closure. *Ophthalmology*. (2011) 118:474–9. doi: 10.1016/j.ophtha.2010.07.025

105. Tan GS, He M, Zhao W, Sakata LM, Li J, Nongpiur ME, et al. Determinants of lens vault and association with narrow angles in patients from Singapore. *Am J Ophthalmol*. (2012) 154:39–46. doi: 10.1016/j.ajo.2012.01.015

106. Kupfer C. Pseudofacility in the human eye. *Trans Am Ophthalmol Soc*. (1971) 69:383–96.

107. Yun S, Kang S, Kim Y, Seo K. A retrospective study of canine primary Glaucoma (2011-2020). *J Vet Clin*. (2022) 39:162–7. doi: 10.17555/jvc.2022.39.4.162

108. McLellan GJ, Miller PE. Feline glaucoma--a comprehensive review. *Vet Ophthalmol*. (2011) 14:15–29. doi: 10.1111/j.1463-5224.2011.00912.x

109. Blocker T, Van Der Woerdt A. The feline glaucomas: 82 cases (1995-1999). *Vet Ophthalmol*. (2001) 4:81–5. doi: 10.1046/j.1463-5224.2001.00169.x

110. Prabhakar SK, Hiremath M. A study of mydriatic effect on intraocular pressure and anterior chamber angle morphology by anterior segment optical coherence tomography. Journal of the Egyptian ophthalmological. *Society*. (2024) 117:93–9. doi: 10.4103/ejos.ejos_67_23

111. Wang A, Mou D, Wang N, Wang H. The imaging characteristics of Lens subluxation on the Ultrasound biomicroscopy. *Contrast Media Mol Imaging*. (2022) 2022:7030866. doi: 10.1155/2022/7030866

112. Fukumoto S, Minamoto T. Traction suture fixation technique using a capsular tension ring fragment for severe lens displacement during cataract surgery in dogs. *Vet Ophthalmol*. (2023). doi: 10.1111/vop.13167

frontiers | Frontiers in Veterinary Science

TYPE Review
PUBLISHED 17 March 2025
DOI 10.3389/fvets.2025.1562097

Check for updates

OPEN ACCESS

EDITED BY
Hussein M. El-Husseiny,
Tokyo University of Agriculture and Technology, Japan

REVIEWED BY
Abdelmonem Mohamed,
University of Prince Edward Island, Canada
Hakim Athar,
Sher-e-Kashmir University of Agricultural Sciences and Technology, India

*CORRESPONDENCE
Mohamed Marzok
mmarzok@kfu.edu.sa
Mohamed Tharwat
atieh@qu.edu.sa

RECEIVED 16 January 2025
ACCEPTED 03 March 2025
PUBLISHED 17 March 2025

CITATION
Marzok M and Tharwat M (2025) Fundamentals of diagnostic ultrasonography in sheep and goat medicine: a comprehensive illustrated overview.
*Front. Vet. Sci.* 12:1562097.
doi: 10.3389/fvets.2025.1562097



# Fundamentals of diagnostic ultrasonography in sheep and goat medicine: a comprehensive illustrated overview

Mohamed Marzok[1]* and Mohamed Tharwat[2]*

[1]Department of Clinical Sciences, College of Veterinary Medicine, King Faisal University, Al-Ahsa, Saudi Arabia, [2]Department of Clinical Sciences, College of Veterinary Medicine, Qassim University, Buraidah, Saudi Arabia

This illustrated review emphasizes the fundamentals of diagnostic ultrasonography in sheep and goat medicine. The procedure can effectively assess the thoracic and abdominal organs in both healthy and diseased states. The review discusses five main sections. The first one clarifies the principles of pulmonary sonography in sheep and goats followed by image finding in animals with respiratory disorders including pneumonia, pleuropneumonia, lung abscessation and pleuritis. Second section shows the fundamentals of echography in sheep and goats followed by scanning of animals with cardiovascular disorders including heart failure, fibrinous pericarditis, endocarditis and nutritional muscular dystrophy. Third section of this review discusses the principles of gastrointestinal sonography in sheep and goats followed by picture in some digestive disorders including peritonitis, enteritis and retroperitoneal abscessation. Fourth part shows the basics in hepatic and biliary tissue followed by sonography of sheep and goats with hepatic and biliary disorders including fatty liver, hepatitis cysticercosis, cholangitis, cholecystitis, cholestasis and choledocholithiasis. Last section of this review discusses the fundamentals of urinary system ultrasonography followed by imaging of the urinary disorders including renal failure, hydronephrosis, pyelonephritis, obstructive urolithiasis, cystitis and paralysis of the urinary bladder. In conclusion, ultrasonography of either healthy or diseased sheep or goats is very useful for assessing the normal structure and function of both healthy and dysfunctional organs. It is highly recommended to adopt this procedure as a standard preliminary method for examining sheep and goats with any medical condition.

KEYWORDS

**animals, goat, sheep, small ruminants, ultrasonography**

## 1 Introduction

Sheep and goats are vital sources of food, fiber, and income for rural populations, but they are often managed under low-input systems, making them susceptible to health issues (1). Ultrasonography has become an essential tool in veterinary practice, particularly for small ruminants as it is non-invasive and real-time imaging tool that allows for detailed internal assessments without the need for surgery (2). Given the small size of ruminants like sheep and goats, ultrasonography provides an efficient way to detect abnormalities, monitor pregnancies, and diagnose various medical conditions with minimal stress to the animals (2). This non-invasive imaging technique uses the transmission and reception of sound waves to create two-dimensional grey-scale images of the internal structural anatomy. From its early use as an experimental technique in the late 1950s and early 1960s, basic ultrasonography has now become standard for most domestic species in veterinary practice, with various individual applications.

Ultrasonography is a safe and effective method providing excellent and detailed images of organ morphology and pathology. It is a non-invasive technique that can be used to evaluate the health of internal organs without the stress of an invasive surgical approach. Ultrasonography is now the only practical method of non-invasive imaging for many of the most important pathological processes in small ruminants. It has the potential to significantly improve productivity and welfare by enabling early detection of pathologies that often go undiagnosed, thereby minimizing adverse events following treatment (3).

In our clinic, we have used ultrasonography for diagnosing sheep and goats with respiratory (4), digestive (5), hepatic (6–8) and urinary (3, 9, 10) disorders. This review article was designed to investigate the principles of diagnostic ultrasonography in sheep and goat with thoracic and abdominal disorders. The procedure can also be used to evaluate the thoracic and abdominal organs in healthy sheep and goats.

## 2 Diseases and disorders of the lungs and pleurae

In sheep and goats, the lungs are anatomically divided into bilateral cranial lobes, each containing a cranial and caudal segment. The right lung also features a middle (cardiac) lobe and an accessory lobe that extends ventrally along the midline. Both lungs have bilateral caudal (diaphragmatic) lobes (11). Because of their grazing habits and the requirement for effective oxygen exchange in open pastures, sheep's lungs are comparatively larger and have a more lobulated structure with finer divisions than goats'. The lungs of both animals look like spongy soft organ, surrounded the heart which was located in the mediastinum and enveloped by visceral and parietal pleura. Both animals' lungs have an anterior apex and a posterior base. The lungs' right and left lobes are separated into cranial and caudal parts, whereas the goat's lung is undivided. The left lung of both animals is made up of apical and caudal lobes, with the apical being divided into cranial and caudal parts part (12).

From a histological perspective, the alveoli are approximately spherical structures that connect to alveolar ducts, alveolar sacs, or respiratory bronchioles. They consist of two primary cell types: Type-I and Type-II pneumocytes. Type-I pneumocytes form the main epithelial lining of the alveoli, characterized by their squamous shape, prominent perinuclear region, and centrally positioned nucleus. In contrast, Type-II pneumocytes are cuboidal with a central nucleus and are occasionally interspersed among the Type-I cells within the alveolar epithelium (13).

### 2.1 Ultrasonographic examination of the lungs

As reported, ultrasonographic assessment of the dorsal lung field is preferred to start at the 9th or 10th intercostal space (14, 15). This technique is effective for identifying pleural fluid accumulation, pleural abscesses, tumors, and lung consolidation resulting from bacterial or interstitial viral pneumonia. In healthy, aerated lungs, the ultrasound beam cannot penetrate the lung tissue, producing only a bright linear echo and reverberation artifacts during the examination (Figure 1) (15–18). To best localize pulmonary lesions, each lung area may be divided in four quadrants by two lines: one horizontal parallel to the floor, passing through the shoulder joint, and one vertical passing through the 5th intercostal space. So, eight quadrants per animal are obtained and labeled alphabetically on the right side from A to D, on the left from E to H. So, each side had craniodorsal (A-E), caudodorsal (B-F), cranioventral (C-G), caudoventral (D-H) quadrant (19).

### 2.2 Respiratory disorders

#### 2.2.1 Pneumonia

Pulmonary parenchyma inflammation, primarily affecting the alveoli, is often accompanied by bronchiolar inflammation and sometimes pleuritis (20). Clinically, pneumonia is characterized by symptoms such as coughing, abnormal respiratory sounds, rapid shallow breathing, and changes in respiratory depth and pattern (20). While chest auscultation is an integral part of veterinary clinical examination, its ability to detect, localize, and specify lung pathology is limited. Although clinical examination and auscultation are valuable, they are insufficient for diagnosing many specific conditions. Therefore, supplementary diagnostic methods are necessary to confirm provisional diagnoses made during clinical evaluations (11). Ultrasonography, for instance, can reveal consolidated lung parenchyma.

#### 2.2.2 Pleuropneumonia

Pleuropneumonia, particularly contagious caprine pleuropneumonia (CCPP), is a severe respiratory disease affecting goats in various countries across Africa and Asia. It is caused by *Mycoplasma capricolum* subsp. *capripneumoniae* (*Mccp*). The acute form of CCPP is characterized by unilateral sero-fibrinous pleuropneumonia accompanied by significant pleural effusion (4, 21–24). During CCPP outbreaks in mixed herds of goats and sheep, sheep

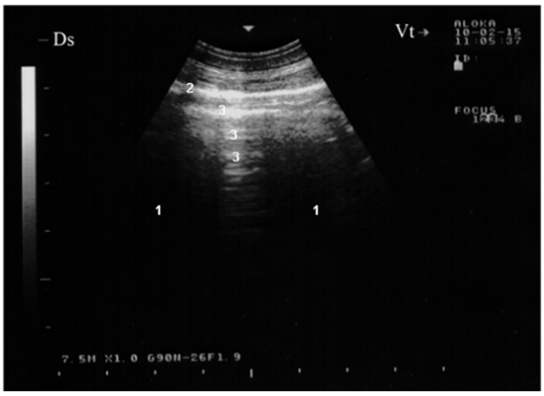


FIGURE 1
Ultrasonogram of the surface of a normal lung (7.5 MHz) in a healthy goat. Normally aerated lung parenchyma (1) does not permit penetration of the ultrasound beam, so a bright linear echo (2) and reverberation artifacts (3) are all that are seen during examination of a normal animal. Ds, dorsal; Vt, ventral (16).

can also become infected, as evidenced by the isolation of Mccp or the presence of antibodies in clinically affected individuals. Additionally, *Mccp* has been isolated from healthy sheep, suggesting their potential role as a reservoir for the disease. Recent reports confirm CCPP in wild ruminants housed in a wildlife preservation reserve in Qatar, and it has also been identified in gazelles in the United Arab Emirates (25).

In goats, contagious caprine pleuropneumonia (CCPP) presents with symptoms such as anorexia, fever, and respiratory distress, including dyspnea, rapid shallow breathing, coughing, and nasal discharge. CCPP cause major economic losses in Africa, Asia and in the Middle East (4). Affected goats often hold their heads low, exhibit frothy nasal discharge and salivation, and show reluctance to move. Death typically occurs within 2 to 10 days following the onset of clinical signs (26). The acute and subacute forms of CCPP are marked by unilateral sero-fibrinous pleuropneumonia accompanied by significant pleural effusion. Diagnosis is based on clinical and necropsy findings, which should be confirmed through laboratory testing. Due to the challenges in isolating *Mycoplasma capricolum* subsp. *capripneumoniae* (Mccp), molecular diagnostic techniques are recommended for confirmation (4, 27).

The presence of gas echoes within pleural or abscess fluid is a highly sensitive and specific indicator of anaerobic infection, similar to the detection of putrid breath or foul-smelling pleural fluid. Ultrasonographic evaluation of both sides of the thorax often reveals accumulations of anechoic or hypoechoic fluid in the ventral pleural space. In such cases, pleural effusion associated with pleuritis is typically unilateral due to the lack of communication between the pleural sacs. However, bilateral pleural effusion may suggest either bilateral pulmonary disease or non-inflammatory conditions such as right-sided congestive heart failure or hypoproteinemia. Pleural fluid readily transmits sound waves, appearing as an anechoic region on ultrasound. Gas pockets within pleural fluid or abscesses are visualized as bright hyperechoic spots within the anechoic area, creating a "snowstorm appearance." The pleural fluid may be clear yellow, turbid and yellowish, reddish or dark red (4) (Figure 2).

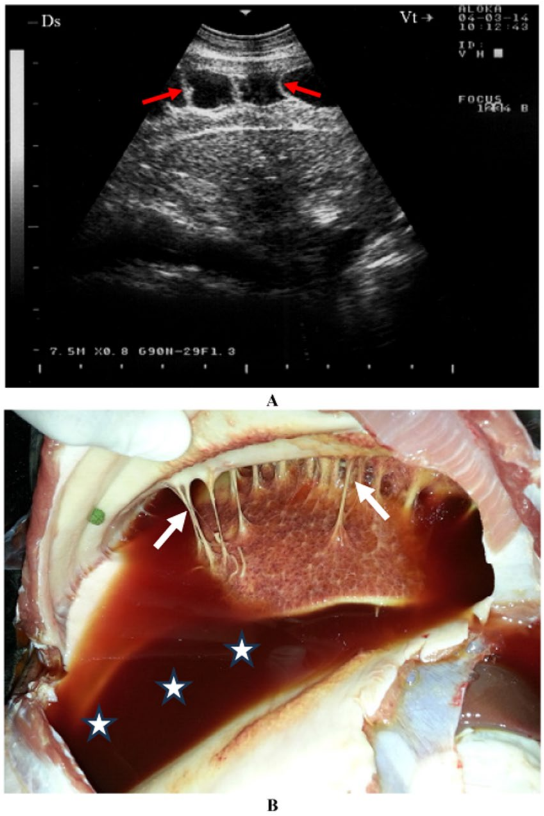


FIGURE 2
A goat with contagious caprine pleuropneumonia caused by *Mycoplasma capricolum* subsp. *Capripneumoniae*. Image **(A)** shows sonographic finding of a marked fibrinous pleurisy (red arrow). Necropsy reveals dark red pleural fluid **(B)** (stars) and fibrinous adhesions (white arrows) (4).

### 2.2.3 Chronic suppurative pneumonia (lung abscesses)

Chronic suppurative pneumonia is a common condition in sheep and goats. It can result from bacterial infections in lung tissue compromised by viral infections, inhalation of infectious agents from the oropharynx—commonly associated with *Fusobacterium necrophorum* in young lambs and kids—or hematogenous spread from septic foci in other parts of the body, such as the udder, uterus, or cellulitis lesions (28, 29).

Clinically, affected animals present with chronic weight loss, lethargy, depression, rapid breathing, occasional coughing, and mucopurulent nasal discharge. On ultrasonographic examination, the abscess capsule is often visible in well-encapsulated lesions, which may extend to occupy an entire side of the chest. For chronic respiratory diseases, penicillin administered for 20–30 days is the treatment of choice, as *Fusobacterium necrophorum* is frequently isolated (28). Regular aspiration of pulmonary abscesses combined with penicillin treatment yields promising results.

### 2.2.4 Pleurisy (pleuritis)

Inflammation of the parietal and visceral pleura leads to fluid accumulation in the pleural cavity, characterized by varying levels of toxemia, painful shallow breathing, pleural friction sounds, and dullness on thoracic percussion due to pleural effusion (28). On ultrasonographic examination, pleural fluid is visible as hypoechoic to anechoic fluid located between the parietal pleura, diaphragm, and lung. Transudative fluid appears uniformly anechoic to hypoechoic, while fibrin appears as thin, filamentous strands floating within the effusion, loosely attached to pleural surfaces. Serosanguineous, hemorrhagic, or purulent fluid exhibits higher echogenicity compared to transudates. In fibrinous pleuritis, ultrasonography reveals separation of the pleurae and lung lobes by a hypoechoic region with acoustic enhancement of the visceral pleura. In severe cases, fibrin deposits display a hyperechoic lattice-like appearance interspersed with hypoechoic areas. Pleural abscesses present as uniform hypoechoic areas containing numerous hyperechoic spots, extending up to 16 cm in depth and often confined to one side of the thorax, with volumes of purulent material (pyothorax) reaching 2–3 liters (4, 20).

## 3 Diseases and disorders of the cardiovascular system

### 3.1 Anatomical background

In sheep and goats, the heart extends from the 3rd to the 6th rib and may make contact with the diaphragm along its caudal edge. Its position and orientation within the thorax are similar to those of other ruminants (11, 20, 28, 29). Histologically, cardiac muscle fibers appear in longitudinal sections, with visible striations along the length of the muscle fibers. The nuclei of the cardiac muscle cells are centrally located within the cells. In a well-prepared section, the nucleolus is prominently stained, and the surrounding nucleus displays a delicate pattern. The myofibrils often bypass the nucleus, and a perinuclear region, devoid of striations, can be seen. This region contains cytoplasmic organelles that are not directly involved in muscle contraction. Each muscle fiber is encased in an endomysium of delicate connective tissue, which includes a dense network of capillaries. Although the reticular fibers of the endomysium are typically not visible, the nuclei of fibroblasts, which lie between the muscle fibers and the numerous capillaries alongside the fibers, are easily seen. The fibroblast nuclei are typically more flattened and darker-stained compared to the cardiac muscle cell nuclei, and they are located peripherally (13).

## 3.2 Echocardiography

Echocardiography has become a standard non-invasive method for diagnosing cardiac conditions in various species. In sheep and goats, two-dimensional (B-mode) echocardiography is increasingly utilized to diagnose suspected heart disease (30–41).

### 3.2.1 Right parasternal ultrasonogram

When the probe is positioned longitudinally in the right 4th intercostal space, the caudal long-axis four-chamber view of the ventricles, atria, and interventricular septum is imaged (Figure 3A) (16). This view provides images of the right and left ventricles, the right and left atria, the mitral and tricuspid valves, and the interventricular septum. Additionally, the ossa chordis appears as a hyperechoic area in this position (30–34, 37, 39).

### 3.2.2 Left parasternal ultrasonogram

When the probe is positioned longitudinally in the left 4th intercostal space, it provides a view of the ventricles, atria, and atrioventricular valves. This view includes images of the left and right ventricles, the right and left atria, the mitral and tricuspid valves, and the interventricular septum (Figure 3B) (16). The ossa chordis also appears as a hyperechoic area in this position (30–34, 37, 39). The right ventricular outflow tract is visible from the 3rd intercostal space on the left side (Figure 3C) (16). In this view, the right ventricle, tricuspid valve, and right atrium are imaged, along with the pulmonary artery, pulmonary valve, aorta, and aortic valve (30–34, 37, 39, 42).

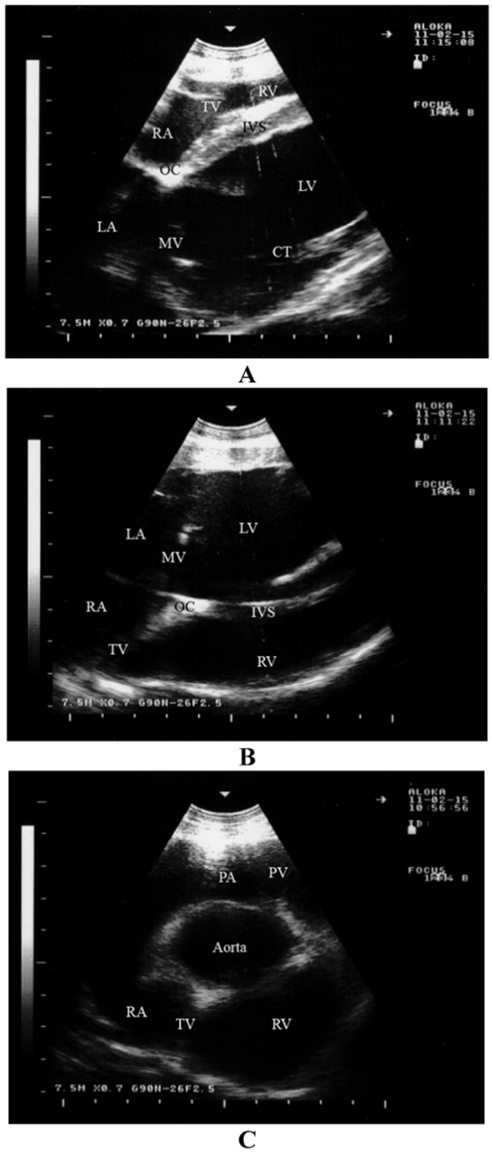


FIGURE 3
Echocardiography in a healthy sheep. Image **(A)** shows a right parasternal caudal long-axis view of the right and left ventricles (four-chamber view) obtained from the right 4th intercostal space. The chordae tendinae of the mitral valve are seen as echoic lines. Image **(B)** shows a left parasternal caudal long-axis, where the four cardiac chambers are observed as well as the atrioventricular valves. Image **(C)** shows a left parasternal cranial long-axis view of the right ventricular outflow tract where the pulmonary artery and aorta are imaged. IVS, interventricular septum; LA, left atrium; LV, left ventricle; MV, mitral valve; RA, right atrium; RV, right ventricle; TV, tricuspid valve; CT, chordae tendinae; OC, ossa chordis (16).

## 3.3 Cardiovascular disorders

### 3.3.1 Heart failure

Heart failure occurs when the heart cannot pump effectively enough to meet the body's blood flow requirements. Several condition can cause heart failure in sheep and goats such as valvular diseases, endocarditis, myocardial diseases, cardiomyopathy, core pulmonale, cardiac toxicosis and pericarditis (20, 68, 70). It can manifest as either right-sided or left-sided failure and may result from conditions affecting the heart valves (e.g., endocarditis) or the myocardium (e.g., myocarditis). Congenital heart defects, including ventricular or atrial septal defects, tetralogy of Fallot, and patent ductus arteriosus, can also lead to heart failure (11, 28, 29, 36). It is important to note that while hypoproteinemia can cause ventral and submandibular edema, it does not lead to jugular or mammary vein distention and pulsation. Therefore, key indicators of heart failure in livestock include venous distention and pulsation combined with abnormal heart sounds or rhythms (20). Ultrasonographic evaluations may reveal subcutaneous fluid accumulation (anasarca), as well as pericardial, pleural, and peritoneal effusions, and intestinal edema. Treatment options for sheep and goats are limited to stall rest and the use of diuretics administered parenterally, in addition to addressing the underlying cause, if identifiable (11, 28, 29).

### 3.3.2 Fibrinous pericarditis

Pericarditis is an uncommon condition in sheep and goats. A female Nagde sheep was brought to the Veterinary Teaching Hospital at Qassim University with a seven-day history of reduced appetite, along with symptoms including lethargy, dyspnea, coughing, nasal discharge, and an elevated respiratory rate. Mycoplasma species, particularly *Mycoplasma capricolum subsp. capripneumoniae* and *Mycoplasma mycoides subsp. mycoides*, are often incriminated. Ultrasonographic evaluation of both sides of the thorax revealed significant pleural and pericardial effusions containing anechoic to echogenic fluid, lung parenchyma consolidation, and fibrinous pleuritis. Fibrin strands were also observed extending from the epicardium and floating in the fluid. Postmortem findings included extensive mucopurulent pleuropneumonia, serosanguineous pleural and pericardial effusions, and fibrinous pericarditis (Figure 4). Histopathological analysis showed substantial thickening of the pericardium due to fibrin deposition and edema, along with moderate infiltration of loosely arranged lymphocytes. Some regions exhibited scattered neutrophils, fragmented necrotic nuclear debris, and multiple localized areas of necrosis within the pericardium.

### 3.3.3 Endocarditis

Compared to cattle, detailed clinical reports on ovine and caprine vegetative endocarditis are relatively scarce, primarily because the condition often occurs without an audible murmur. Bacteremia plays a crucial role in the development of bacterial endocarditis. In cattle, *Corynebacterium pyogenes* is the most frequently isolated pathogen from blood and endocardial lesions, although *Streptococcus* species, *Staphylococcus* species, and Gram-negative bacteria can also cause the disease. The tentative diagnosis of vegetative endocarditis relies on clinical signs such as depression, chronic weight loss, recumbency, pain, fever, polyarthritis, shifting weight due to discomfort, and dyspnea. Ultrasonographic examination is typically used for clinical diagnosis, which is later confirmed through postmortem examination. Attempts to treat ovine vegetative endocarditis with procaine penicillin (44,000 IU/kg daily for at least 10 days) have generally been unsuccessful (20).

### 3.3.4 Nutritional muscular dystrophy

Nutritional muscular dystrophy, also known as white muscle disease, can be either congenital or acquired and may affect both cardiac and skeletal muscles. This condition is a leading cause of sudden death in young kids due to cardiac failure. It is the most prevalent disorder linked to selenium and/or vitamin E deficiency in sheep and goats. Inadequate levels of these nutrients hinder the body's ability to regulate oxidative processes within cells, potentially leading to significant muscle necrosis. The cardiac muscle, diaphragm, and other skeletal muscles may be involved, resulting in diverse clinical signs that complicate accurate diagnosis (11, 28, 29). Ultrasonographic imaging of the heart typically reveals increased echogenicity in the myocardium and skeletal muscles.

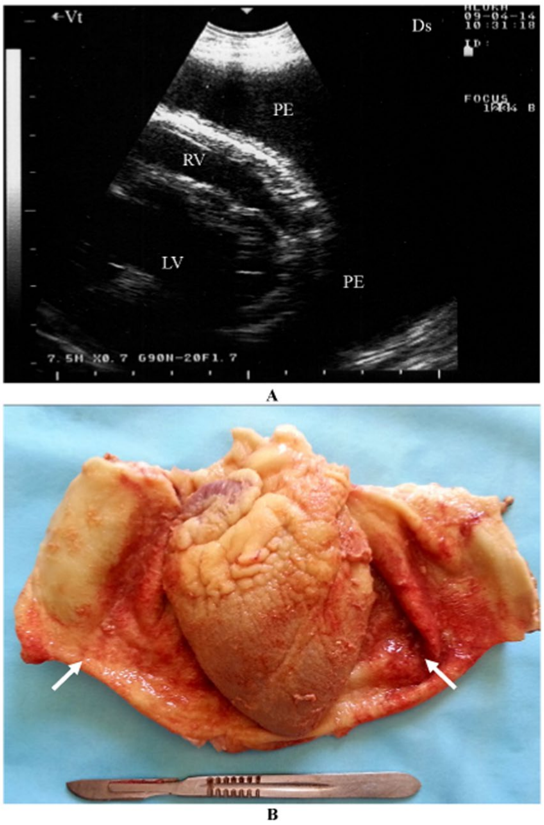


FIGURE 4
Pericardial effusions and echogenic tags of epicardium in CCPP goat **(A)**. Necropsy showed thickened and roughened surfaces of the pericardium (arrows) **(B)** (4). PE, pericardial effusion; RV, right ventricle; LV, left ventricle.

## 4 Diseases and disorders of the digestive system

The caprine digestive system shares the fundamental ruminant structure and function observed in sheep, with only minor differences. However, goats possess unique anatomical and physiological traits that set them apart from sheep, reflecting their specialized feeding habits and remarkable adaptability to challenging environments unsuitable for other domesticated ruminants (11, 28, 29). The range of diseases affecting the goat digestive system is comparable to those found in sheep and cattle, with infectious and metabolic disorders being most prevalent. Although many of these diseases occur in both species, their incidence may vary. For instance, while abomasal displacement and traumatic reticulitis are common in dairy cattle, these conditions are rarely observed in goats (11, 20, 28, 29).

### 4.1 Ultrasonographic examination of the digestive system

### 4.1.1 Rumen

The rumen is visible from the 9th to the 12th intercostal spaces and from the flank on the left side. Its dorsal margin runs parallel to the lung margin, extending cranioventrally to caudodorsally, while its ventral margin extends cranioventrally. The longitudinal groove of the rumen is identifiable in all goats and is located farthest from the midline of the back at the 8th intercostal space (43, 44). Positioned largely adjacent to the left abdominal wall, the rumen extends medially and appears as a thick echogenic line on imaging. Due to its gaseous contents, the internal structure of the rumen, similar to cattle, is challenging to image (Figure 5A) (16). Between the 8th and 12th intercostal spaces, the spleen is observed dorsolateral to the rumen (43, 44).

### 4.1.2 Reticulum

The reticulum can be visualized from the *linea alba*, the left and right paramedian regions, and between the 5th and 9th intercostal spaces on both sides (44, 45). It appears as a crescent-shaped structure with a smooth contour and is located immediately adjacent to the diaphragm (Figure 5B) (16). Biphasic reticular contractions are evident, beginning with an incomplete contraction followed by partial relaxation. This is succeeded by a full contraction and subsequent complete relaxation of the organ (44, 45).

### 4.1.3 Omasum

The omasum is visible between the 6th and 11th intercostal spaces, typically spanning 3 to 5 consecutive spaces (44, 46). Unlike in cattle, the omasum in goats is not directly adjacent to the abdominal wall but is instead separated by the liver. The organ appears as a curved echogenic line medial to the liver (Figure 5C) (16). On imaging, the omasum appears as a curved echogenic line, representing the omasal wall nearest to the transducer (44, 46).

### 4.1.4 Abomasum

The abomasum is visualized as a heterogeneous, moderately echogenic structure with echogenic stippling, similar to its appearance in cattle. It is consistently visible from the ventral midline, as it lies directly adjacent to the abdominal wall in this region (44, 47). The abomasal folds are seen as distinct echogenic bands. The abomasum occupies a similar amount of space on both the left and right sides, extending further cranially on the left and further caudally on the right. The abomasum is seen caudal to the reticulum and appears as a heterogeneous, moderately echogenic structure with multifocal echogenic foci (Figure 5D) (16). It is important to note that the ultrasonographic length of the abomasum appears shorter than its actual length due to overlapping structures such as the reticulum and rumen (44, 47).

### 4.1.5 Small intestine

The cranial part of the duodenum is typically indistinguishable from the rest of the intestinal tract, but the descending duodenum can be clearly differentiated from other segments of the small and large

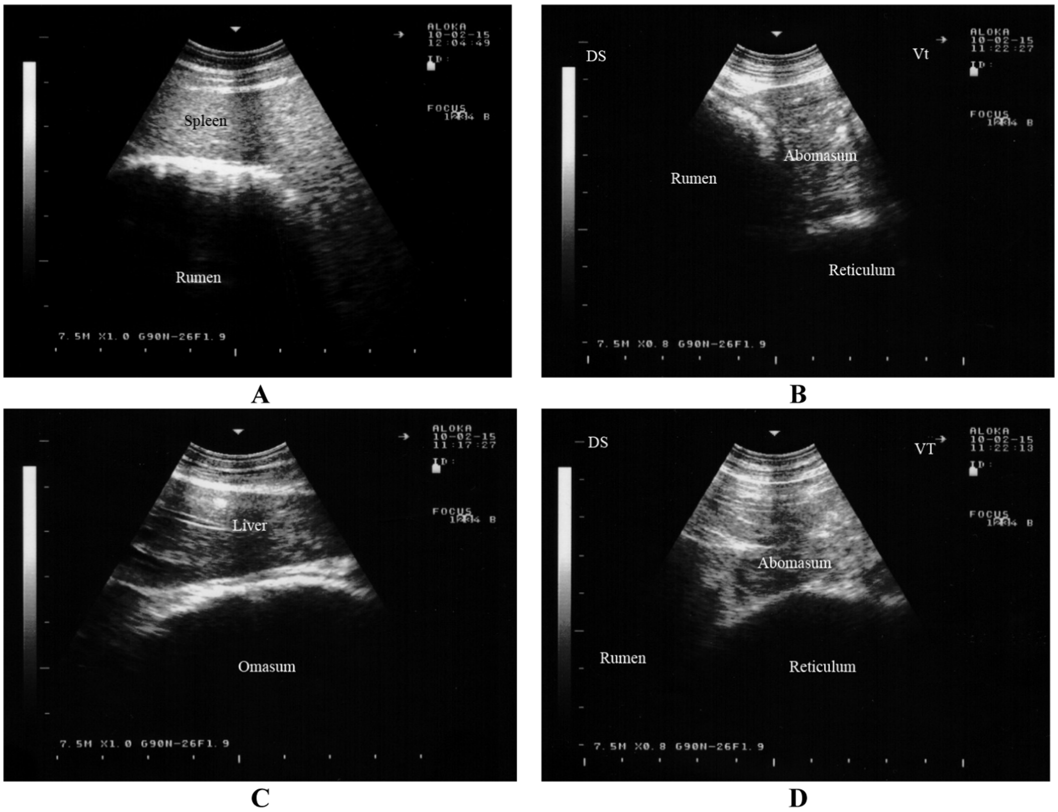


FIGURE 5
Ultrasonography of the rumen, reticulum, omasum and abomasum in a healthy goat. Image **(A)** shows an ultrasonogram of the rumen and spleen at the 11th intercostal space to the left side. Image **(B)** shows an ultrasonogram of the reticulum at the left paramedian of the sternal region. Image **(C)** shows an ultrasonogram of the omasum and liver where the omasum appears as a curved echogenic line medial to the liver. Image **(D)** shows an ultrasonogram of the abomasum caudal to the reticulum and it appears as a heterogeneous, moderately echogenic structure with multifocal echogenic foci (16).

intestines. While the jejunum and ileum are visible, they cannot be distinguished from one another. These portions of the small intestine are most commonly observed in the ventral right flank, less often in the ventral regions of the last intercostal spaces, and occasionally in the dorsal flank. Jejunal and ileal loops are usually seen in cross-section but can also be visualized longitudinally and exhibit strong motility (Figure 6A) (16). The frequency of contractions cannot be accurately measured due to their constant motion. The intestinal contents are generally homogeneous and echogenic (44, 48).

### 4.1.6 Large intestine

The large intestine is most frequently visible dorsally in the right flank, with occasional visibility in the ventral area. The spiral colon is easily recognized by the distinctive garland-like appearance of its centripetal and centrifugal coils. It is often positioned medially to the small intestine, not directly next to the abdominal wall. In the cecum, only the wall nearest to the transducer can be visualized (Figure 6B) (16). This wall appears as a thick, echogenic line with slight undulations (44, 48).

### 4.1.7 Spleen

The dorsal margin of the spleen is visible running from cranioventral to caudodorsal, due to the superimposition of the lungs, similar to the liver. As a result, the distance between the dorsal visible margin of the spleen and the dorsal midline is greatest at the 8th intercostal space (ICS) and smallest just caudal to the last rib. The ventral margin follows a similar course (49). The spleen can be seen between the 8th and 12th intercostal spaces. It is located between the rumen and the abdominal wall, and in the 8th intercostal space, it is adjacent to the cranial blind sac of the rumen. The spleen is surrounded by an echogenic capsule, and its parenchyma shows a pattern of numerous weak echoes evenly distributed throughout the organ. The splenic vessels, embedded within the parenchyma, can be seen either in longitudinal or cross-section (Figure 7) (16).

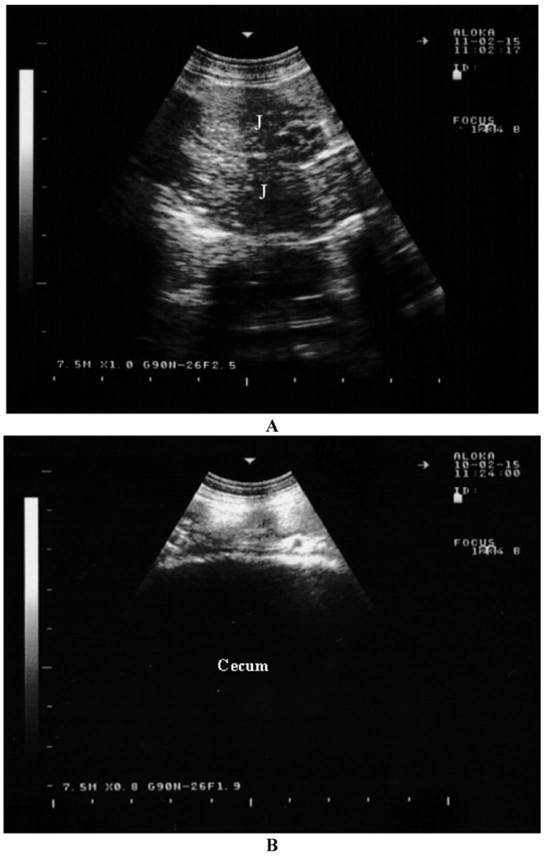


FIGURE 6
Sonographic appearance of the intestines in a healthy goat. Image **(A)** shows an ultrasonogram of the jejunum (J) in a longitudinal view in the cranioventral flank. Image **(B)** shows an ultrasonogram of the cecum located at the caudodorsal left flank (16).

## 4.2 Digestive disorders

### 4.2.1 Peritonitis

Peritonitis is an inflammation of the peritoneum, the thin membrane that lines the inner abdominal wall and covers most of the abdominal organs. It can be localized or widespread, acute or chronic, and may result from either an infectious or non-infectious cause (67). In sheep and goats, common triggers include abdominal surgery, ruptured ulcers in the abomasum or intestines, penetration of the intestinal tract by foreign bodies, rupture of the urinary tract, rectum, uterus, or large intestine, and liver abscesses. Peritonitis may also occasionally follow conditions such as metritis, dystocia, retained fetal membranes, or pyometra. Clinically, peritonitis can be challenging to diagnose (11, 20, 50). In affected animals, ultrasonography typically shows the presence of large amounts of echogenic fluid, sometimes accompanied by fibrin tags. Postmortem examination reveals exudation and fibrin deposits within the peritoneal cavity, along with fresh adhesions that are easily broken.

### 4.2.2 Enteritis

Enteritis is an inflammation of the intestinal mucosa, commonly caused by factors such as abrupt dietary changes, toxicity, viral infections, parasitic infestations, and bacterial infections like salmonellosis, colibacillosis, paratuberculosis, tuberculosis, and clostridial enterotoxemia (20). Clinically, enteritis is characterized by diarrhea that may be foul-smelling, watery, and contain excessive mucus, blood, undigested food particles, and sloughed mucosal tissue. Other symptoms include dehydration, tenesmus, anorexia, colic, depression, and weight loss (11). Diagnosis is typically based on the animal's history and clinical signs. To identify the underlying cause, cultures, fecal examination for cytology, and checking for parasitic ova are necessary. In cases of chronic enteritis in sheep and goats, ultrasonography can help assess the severity of the lesions. It can detect mild, moderate, and severe thickening of the intestinal wall, as well as the corrugation of the intestinal mucosa, both in longitudinal and cross-sectional views. Enlarged mesenteric lymph nodes are also commonly observed (51). Necropsy reveals thickened intestinal walls, corrugated mucosa in the small intestine, and enlarged mesenteric lymph nodes (Figure 8) (5).

### 4.2.3 Retroperitoneal abscesses

A well-known form of chronic or, less frequently, intermittent colic is linked to an abscess within the abdominal cavity. These abscesses are typically retroperitoneal, and chronic leakage from them into the peritoneal cavity leads to persistent or recurrent

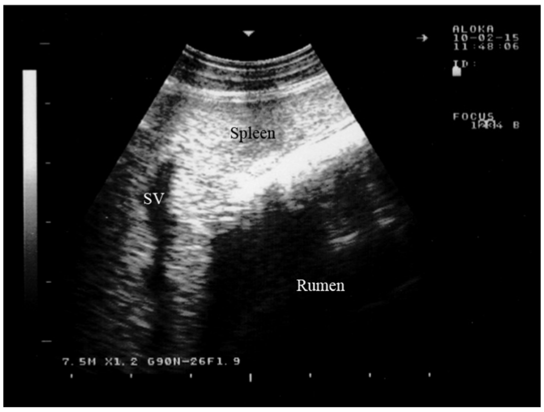


FIGURE 7
Ultrasonogram of the splenic parenchyma in a goat viewed from the 11th intercostal space to the left side. SV, splenic vein (16).

peritonitis. Achieving full recovery is challenging, and treatment often has a high failure rate. Clinical signs indicative of this condition includes persistent or intermittent chronic colic, weight loss, and fever, along with varying levels of anorexia. In cases involving concurrent chronic peritonitis, the inflammatory exudate may accumulate enough to cause abdominal distension. Ultrasonography may help detect the abscess. Ultrasound has been reported as an effective, straightforward, and rapid diagnostic method for identifying, confirming, and planning invasive treatments for deeply located surgical lesions in sheep and goats (52).

## 5 Diseases and disorders of the liver and biliary system

In sheep and goats, the liver is made up of four distinct lobes: the right, left, quadrate, and caudate. It is located in the dorsal two-thirds of the right anterior abdomen, in contact with both the diaphragm and the abdominal wall from the seventh rib to the last rib. The liver is covered dorsally by the lung up to the ninth rib space, but biopsy access can be obtained between the ventral lung border and the costochondral junctions in the seventh to ninth rib spaces. The gallbladder extends beneath the liver's ventral border (11).

Histologically, the central vein is positioned at the center of the hepatic lobule, and its edges are collapsed. The endothelium is visible, and the fenestrations at the margins are more pronounced near the sinusoids. The hepatic lobule is roughly hexagonal, and the hepatocytes are polygonal, with small nuclei. Hepatic sinusoids are present among the radiating cords of liver cells. In goats, a connective tissue septum exists between the portal triads but merges with the hepatic lobule. The connective tissue also contains branches of the portal vein, hepatic artery, and bile duct (13).

The gallbladder consists of several layers: the mucosa (including the epithelium and lamina propria), the muscularis, the perimuscular layer, and the serosa. The lining epithelium is tall and columnar, with a striated border. The glands are both mucous and serous, and their secretions, along with those of the surface cells, form a polysaccharide-protein complex (13).

### 5.1 Ultrasonographic examination of the hepatic parenchyma

Ultrasonographic assessment of the hepatic parenchyma is a valuable tool in clinical evaluations and plays a crucial role in diagnosing various conditions. This imaging technique offers a non-invasive, bedside approach for examining the liver parenchyma, blood vessels, as well as the renal cortex, medulla, and sinus. In sheep and goats, the dorsal margin of the liver extends in a cranioventral to caudodorsal direction, parallel to the caudal margin of the lungs. The liver's greatest visible extent is typically seen at the seventh and eighth intercostal spaces (mean value, 15.9 cm), while its width is most noticeable at the 10th intercostal space (mean value, 5.2 cm) (11, 44). The caudal vena cava appears triangular in cross section, with its maximum width, circumference, and surface area ranging from 1.2 to 1.8 cm, 4.8 to 5.2 cm, and 0.8 to 1.1 $cm^2$, respectively. The portal vein is round in cross section, with a diameter between 0.8 and 1.7 cm, and it exhibits stellate branches extending into the liver parenchyma. The gallbladder is pear-shaped and its size varies; it typically extends beyond the ventral border of the liver depending on the amount of bile present (Figure 9) (16).

Sheep and goats are often presented with nonspecific symptoms, and without hepatic ultrasonography, it can be challenging to make an antemortem diagnosis in these cases. Ultrasonographic findings almost always correlate with postmortem results, so it is recommended to routinely scan the thorax and abdomen of sheep and goats that are referred for general symptoms (6).

### 5.2 Ultrasonographic findings

Ultrasonographic examination of the liver can be performed at three or more intercostal spaces, with the liver being visible in all sheep and goats from the seventh to the ninth intercostal spaces. The dorsal margin of the liver runs parallel to the lung border, extending from cranioventral to caudodorsal (11, 44). The normal liver parenchyma exhibits a pattern of fine echoes distributed evenly throughout the organ. The caudal vena cava appears triangular in cross section, as it is located within the sulcus of the vena cava in the liver. The portal vein is round to oval in shape on cross section, and its wall is more distinct than that of the caudal vena cava. Additionally, the wall of the intrahepatic portal vein appears more echogenic compared to the hepatic vein.

The gallbladder has a pear shape and may extend beyond the liver's ventral margin, depending on the bile volume. It can be observed at the 7th to 9th intercostal spaces, and its size varies based on the amount of bile present. The contents of the gallbladder appear anechoic to hypoechoic. Visualizing the intrahepatic bile ducts, the common hepatic duct, and the common bile duct is typically difficult. However, the junction of the cystic duct and the gallbladder neck can be imaged (11, 44).

### 5.3 Hepatic disorders

#### 5.3.1 Fatty liver

Fatty liver syndrome, also known as hepatic lipidosis, is a significant metabolic disorder with multiple contributing factors that

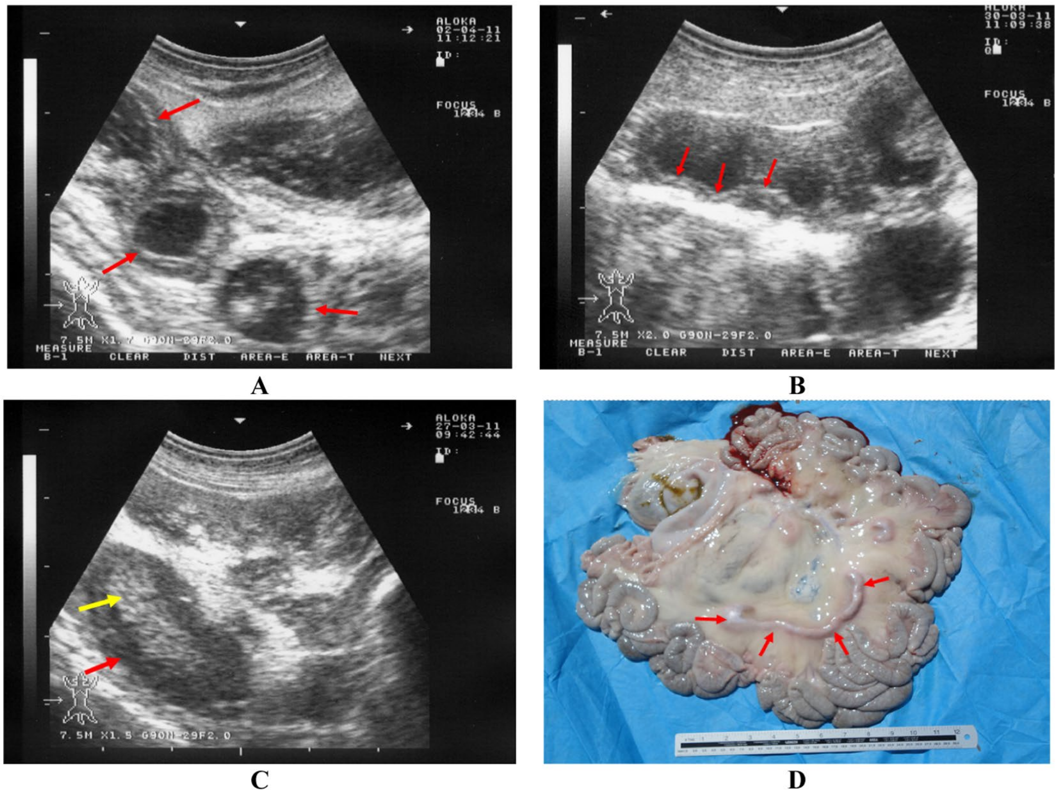


FIGURE 8
Ultrasonography and postmortem findings in a goat with paratuberculosis. Thickened intestinal walls were apparent cross sectionally **(A)** and longitudinally **(B)** (red arrows). Image **(C)** shows enlarged mesenteric lymph node with a hypoechoic cortex (red arrow) and a hyperechoic medulla (yellow arrow). Image **(D)** shows enlargement of the mesenteric lymph nodes (red arrows) (5).

negatively affect the health and reproductive performance of farm animals. This condition occurs when excess fat is mobilized from body fat stores to the liver, where it is deposited as triglycerides, leading to impaired liver function (40, 53, 69). Fatty liver commonly affects pregnant sheep and goats carrying multiple fetuses (pregnancy toxemia) and can also develop in the days following parturition. It is often triggered by factors that temporarily reduce the animal's appetite, such as milk fever, indigestion, retained fetal membranes, mastitis, dystocia, or prolonged recumbency. On ultrasonography, the hepatic parenchyma appears more echogenic than usual, with the degree of echogenicity corresponding to the volume of fat vacuoles and triglyceride accumulation in the liver (53, 54). In sheep and goats and similar to dairy cows, the liver appears bright and more echogenic than healthy animals (7).

### 5.3.2 Hepatitis cysticercosis

The disease is caused by the migration of *Cysticercus tenuicollis*, the intermediate stage of *Taenia hydatigena* (found in the intestines of dogs, coyotes, wolves, and other carnivores), into the liver and lung tissues of intermediate hosts such as sheep, goats, cattle, pigs, and squirrels (8, 55). The eggs of the parasite are excreted in feces and ingested by various domestic and wild ruminants, including goats and sheep. After hatching in the small intestine of the intermediate host, the larvae enter the bloodstream. Upon reaching the liver, they leave the portal circulation and migrate through the hepatic tissue into the peritoneal cavity, creating distinct hemorrhagic tracks within the liver.

The metacestode, which is the stage that develops in ruminants, is known as *Cysticercus tenuicollis*. It matures over 5 to 8 weeks and attaches to the mesentery, omentum, and serosal surfaces of abdominal organs (56). In some cases, the cysticercus may remain within the liver instead of migrating, and aberrant migrations may lead to cysts being found in other organs such as the lungs (11, 20, 28, 29, 57). Peritonitis can cause fever, though chronic cysticercosis is typically asymptomatic. Ultrasonographic examination of the liver in sheep with cysticercosis reveals coarse hyperechogenic pattern (Figure 10) (8, 11, 58). At postmortem, serofibrinous or serosanguineous fluid may be present in the peritoneal cavity. Acute cysticercosis is identified by red, blood-filled tubular tracts, 2 to 4 mm in diameter, within the liver. *Cysticercus tenuicollis* cysts are commonly found in the mesentery, omentum, and serosal surface of abdominal organs, although they can also occur in the liver parenchyma. The mature cysticerci have a smooth inner surface and contain a single invaginated scolex, unlike hydatid cysts. Other postmortem findings may include migrating cysticerci in the lungs and jaundiced organs. Histopathological examination of liver tissue reveals preserved architecture with hepatitis and congestion in the large vascular spaces (8, 28).

### 5.3.3 Cholangitis, cholecystitis, cholestasis, and choledocholithiasis

Cholangitis refers to an infection of the common bile duct, which transports bile from the liver to the gallbladder and intestines, while

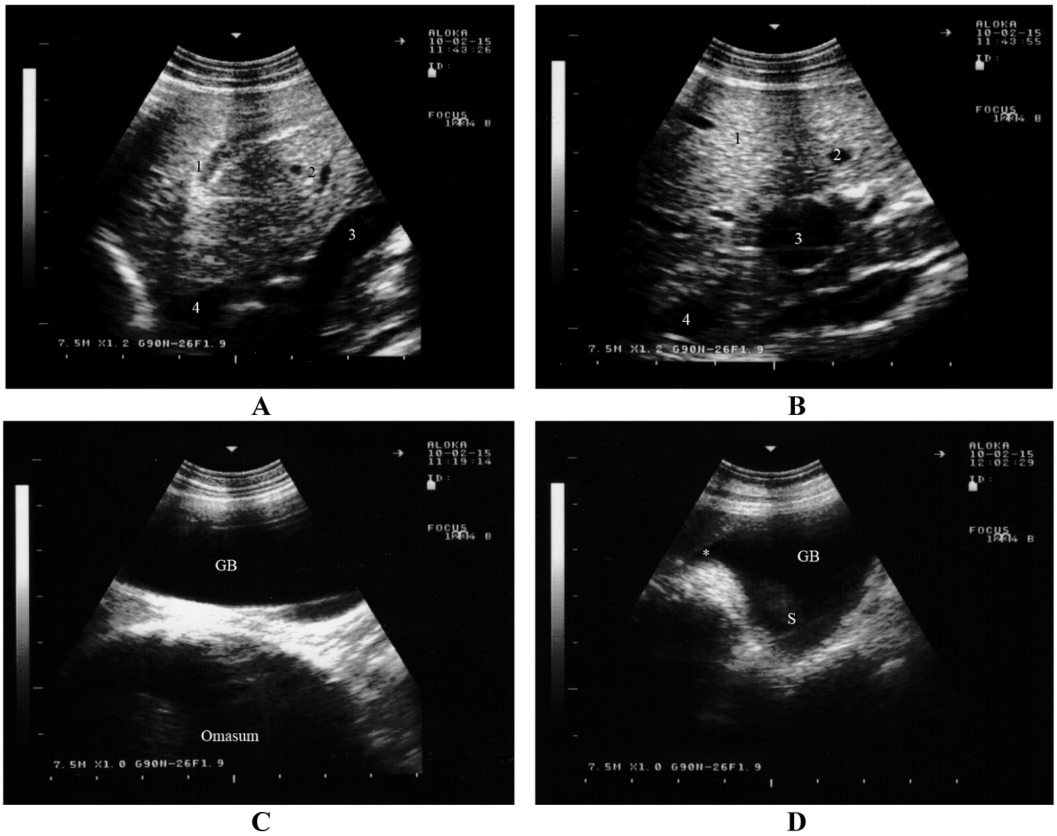


FIGURE 9
Ultrasonogram of the hepatic parenchyma in a goat. The parenchymal pattern of the normal liver consists of numerous fine echoes homogeneously distributed over the entire area of the liver. The caudal vena cava has a triangular shape on cross section because it is embedded in the sulcus of the vena cava in the liver **(A)**. The portal vein is circular to oval on cross section. The wall of the portal vein is more distinct than that of the caudal vena cava. The wall of the intrahepatic portal vein is more echoic than that of the hepatic vein **(B)**. The gallbladder is a pear-shaped and sometimes extended beyond the ventral margin of the liver depending on the amount of bile. The content of the gallbladder is anechoic to hypoechoic **(C)**. The junction of the cystic duct and the neck of the gallbladder can be imaged **(D)** (16). 1, hepatic parenchyma; 2, hepatic vein; 3, portal vein; 4, caudal vena cava. S, gallbladder sediment; *, junction of the cystic duct and the neck of the gallbladder (16).

cholecystitis involves inflammation of the gallbladder (59). Cholestasis, on the other hand, is the cessation of bile flow. The diagnosis of obstructive cholestasis is often confirmed through the observation of a dilated bile duct and a distended gallbladder. However, it's important to note that a distended gallbladder may also be observed at necropsy in cases of diseases that result in inappetence or anorexia (20).

In sheep and goats, common causes of cholangitis, cholecystitis, and cholestasis include fascioliasis, gallstones, and bacterial infections. Other causes of biliary tract disease include gallbladder empyema and a bile duct carcinoma (20). Ultrasonographically, thickening of the gallbladder wall is typically seen. In the differential diagnosis, it's crucial to differentiate between gallbladder wall thickening due to right-sided heart failure, which leads to edema, and inflammatory changes confirmed at necropsy (11, 60). Choledocholithiasis, or the presence of gallstones in the common bile duct, is characterized by microliths within the duct. These stones appear on ultrasound with acoustic enhancement and an area of acoustic shadowing beneath, which can also be confirmed at necropsy (60).

Ultrasonographic findings in such cases include a dilated gallbladder with the presence of a calculus, along with dilation of the common bile duct and multiple bile ducts within the hepatic parenchyma. At postmortem, findings typically include an icteric carcass, a firm liver, and a distended gallbladder. Other necropsy results may reveal a thickened gallbladder wall, a dilated common bile duct, and a white friable mass obstructing the bile duct lumen, along with distended intrahepatic bile ducts and icteric kidneys and heart (60).

### 5.3.4 Hydatic cyst

Cystic echinococcosis is a parasitic infection that affects various mammalian species, resulting from the larvae of *Echinococcus granulosus*, typically located in the small intestines of dogs and other carnivorous animals. Sheep, cattle, and camels serve as intermediate hosts. Liver and lung cysts caused by *E. granulosus* represent a global parasitic disease, particularly prevalent in regions where sheep are grazed with the assistance of dogs (61). The disease holds significant implications for public health at large. Humans serve as unintentional intermediate hosts (62). Sheep and goats seem to serve as the primary reservoir for human hydatiosis due to common practices such as home slaughtering, the feeding of infected offal to the definitive host and the significant prevalence of fertile cysts identified in small ruminants (63). In sonographic examinations, the intrahepatic hydatid cyst in sheep presents with indistinct borders and anechoic

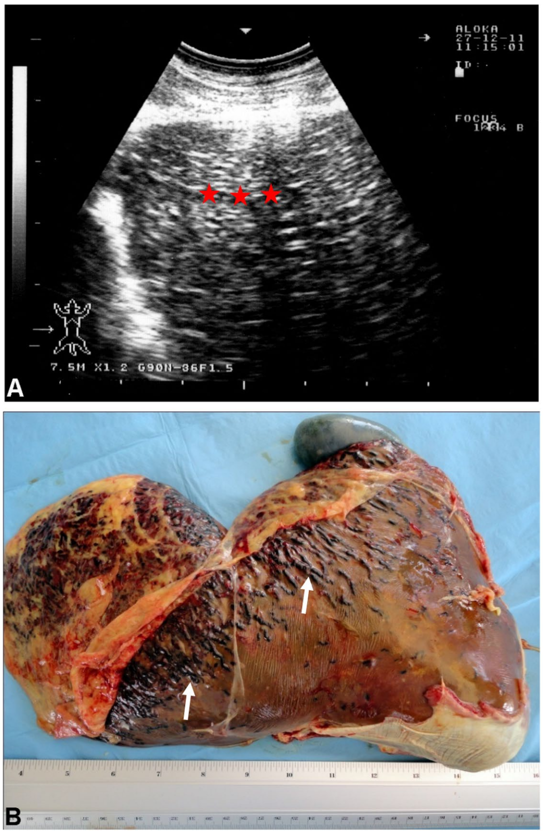


FIGURE 10
Ultrasonogram **(A)** and macroscopic view **(B)** of cysticercosis in the liver of an ovine case. **(A)** The liver parenchyma is demonstrated as heterogeneously hyperechoic (stars). **(B)** Blood-filled tracts (arrows) are seen within the swollen liver due to the migration of *Cysticercus tenuicollis* (the embryos of *Taenia hydatigena*) (58).

content that includes echogenic septa (64). The lesions can be visualized as (1) multivesicular, multiseptated cysts, indicating activity; (2) a unilocular cyst, characterized by the detachment of a laminated membrane from the cyst wall, which may harbor daughter cysts, suggesting a transitional state; and (3) a thick calcified wall that is arch-shaped, resulting in a cone-shaped shadow, indicating inactivity (19).

## 6 Diseases and disorders of the urinary system

The kidneys of sheep and goats are smooth, oval-shaped organs, with the left kidney being surrounded by more perirenal fat than the right. The right kidney is positioned in the dorsal abdomen, at the level of the T13 to L3 vertebrae, while the left kidney is situated more caudally at L4 to L5, with its lateral side in contact with the dorsal sac of the rumen. A full rumen can push the left kidney toward the right side of the abdominal midline (11). The right ureter runs alongside the vena cava, dorsal to the left kidney. The left ureter starts to the right of the midline, moves ventral to the right ureter, and then crosses back to the left to enter the bladder. The ureters pass obliquely through the bladder wall, entering the dorsal part of the bladder (28). The urinary bladder is ovoid and extends into the abdominal cavity when full, lying ventral to the uterus in females. The penis of ruminants is fibroelastic and has a sigmoid flexure. The penile urethra's spongy part extends beyond the glans penis, forming a 2.5 cm vermiform appendage called the urethral process. In sheep, this process is attached to the left side of the glans, while in goats, it is centrally located. When the penis is flaccid, the process is folded inside the prepuce but becomes rigid and extended when erect. During ejaculation, the process rotates spirally and is thought to spray semen on the external uterine orifice or potentially enter the cervix's external os (20).

Urinary calculi can often become trapped in the urethral process, obstructing urine flow, especially in castrated males. This is due to a reduced urethral diameter and the adhesion of the urethral process to the preputial mucosa, resulting from the loss of testosterone's developmental effects. The urethral process is often removed during the treatment of obstructive urolithiasis to restore urine flow, and there is no evidence suggesting that this removal affects fertility in sheep and goats (29).

Histologically, the renal cortex contains renal corpuscles, tubules (including convoluted and straight parts of the nephron), collecting tubules, and an extensive vascular network. The renal corpuscle consists of a glomerular capillary bed surrounded by Bowman's capsule. The renal medulla contains only straight tubules, ascending and descending limbs of the loop of Henle, and collecting tubules (13). The urinary bladder has three layers of smooth muscle and a multilayered transitional epithelium (urothelium). The mucosa is heavily folded to accommodate large volume changes, and the transitional epithelium can stretch to resemble stratified squamous epithelium. The submucosa consists of connective tissue, including collagen, elastin, and other extracellular matrix proteins. The bladder's tunica muscularis is made up of the detrusor muscle, whose fibers run in all directions (13).

### 6.1 Ultrasonographic examination of the urinary system

Examination of the urinary tract is typically performed from several locations, with the most important being the flank and the last two intercostal spaces on the right side. These sites allow visualization of the right kidney and, in most goats, the left kidney as well. The urinary bladder and urethra can be assessed transrectally, but can also be seen from either the left or right inguinal region. The same equipment used for examining other organs is employed for transcutaneous ultrasound, while transrectal exams are best conducted with a 5.0 to 7.5-MHz probe (44, 65).

The right kidney is generally visible from the right, with the optimal viewing site being the dorsal region of the 11th or 12th intercostal space and from the craniodorsal flank. The right kidney is almost always oriented with its long axis parallel to the ribs, and only rarely does it appear perpendicular to them. The left kidney can typically be seen in most sheep and goats from the right, and less often from the left, though in some cases, it may not be visible from either side. When seen from the right, the left kidney is most commonly viewed from the dorsal flank or occasionally from the last intercostal space. On the left side, the left kidney may be observed, though rarely, from the dorsal flank. The long axis of the left kidney is usually parallel to the vertebral column (3, 11, 44).

The renal capsule may appear as a faint echoic line, though it is not always clearly visible. The kidneys' ultrasonographic appearance changes depending on the sectional plane. In a sagittal plane through the hilus, the kidney has an oval shape, and its parenchyma appears homogeneous with fine, evenly distributed echoes. The medullary pyramids near the sinus appear as oval to circular hypoechoic structures, and the sinus itself appears hyperechoic. In a longitudinal section through the medullary pyramids, the kidney remains oval, with the renal cortex being distinct and easily differentiated from the renal medulla and pyramids. The interlobar veins and arteries appear as elongated hypoechoic structures between the pyramids, and the renal sinus is visible as a hyperechoic band. Oblong hypoechoic structures within the renal sinus correspond to the renal artery, vein, and ureter (Figures 11A,B) (16). Non-dilated ureters are typically not visible through either the flank or transrectally (65). The urinary bladder is most clearly visible during a transrectal examination, although it can also be seen from either inguinal region. The bladder wall appears as an echoic line with smooth borders, and its contents are normally anechoic. In most sheep and goats, the urethra is seen transrectally as two parallel echoic lines, but the lumen is usually not visible (Figure 11C) (16).

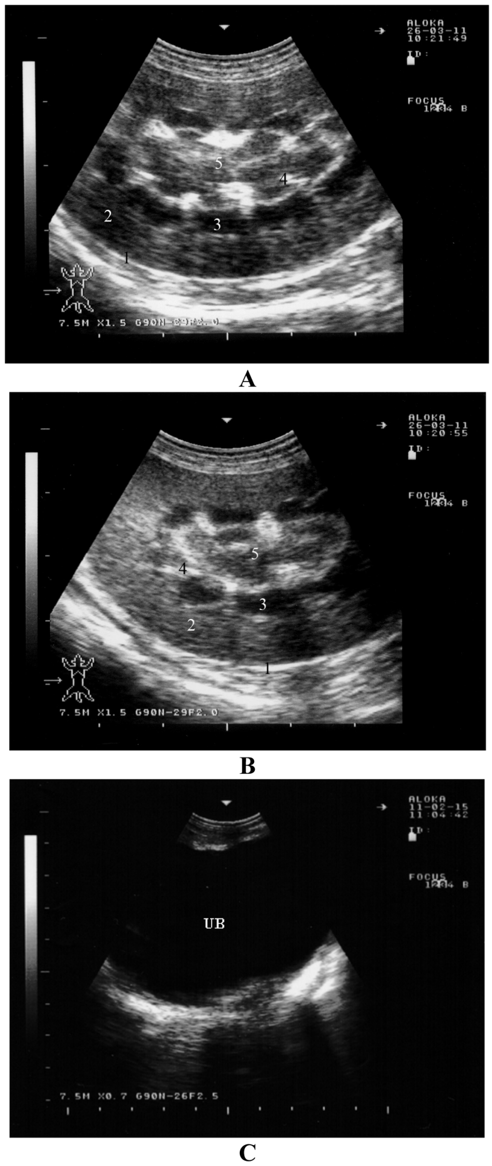


FIGURE 11
Ultrasonography of the kidneys and urinary bladder in a healthy goat. Image **(A,B)** show ultrasonograms of the right **(A)** and left **(B)** kidneys in longitudinal section through the region of the medullary pyramides viewed from the right flank. Image **(C)** shows transrectal imaging of the urinary bladder (UB) with anechoic urine 1, renal capsule; 2, renal cortex; 3, medullary pyramids; 4, interlobar vessels; 5, renal sinus (16).

## 6.2 Urinary disorders

### 6.2.1 Renal failure

Renal function is influenced by the number and proper functioning of the nephrons. Renal failure can be categorized into pre-renal, renal, and post-renal causes (20, 66). Common clinical signs of renal failure include depression, loss of appetite, weight loss, oral mucosal lesions, and diarrhea. A male goat presented to our clinic exhibited the typical clinical signs of renal failure. The animal showed signs of depression, lethargy, and loss of appetite, with abdominal distension being the first noticeable symptom. Abdominocentesis revealed a significant amount of watery abdominal fluid. Ultrasonography showed increased echogenicity of the renal cortex, the presence of a kidney calculus in the right kidney, and an effusion of anechoic fluid in the abdomen. Blood tests indicated elevated serum levels of blood urea nitrogen (64.3 mmol/L, with a normal range of 3–10 mmol/L) and creatinine (1,637 µmol/L, with a normal range of 70–105 µmol/L).

### 6.2.2 Hydronephrosis

Hydronephrosis is the enlargement of the renal pelvis accompanied by progressive atrophy of the renal parenchyma. It can be either congenital or acquired due to urinary tract obstruction. Any blockage in the urinary tract may lead to hydronephrosis, with the severity of the renal damage depending on the extent and duration of the obstruction (66). Chronic, unilateral, and partial urinary tract obstructions are more likely to cause hydronephrosis. In cases of acute and complete obstruction, symptoms typically include anuria, dysuria, or stranguria. Chronic or partial obstructions result in gradual dilation of the renal pelvis and pressure-induced atrophy of the renal tissue (29). When the obstruction is unilateral, the unaffected kidney may compensate for the loss of function, potentially preventing kidney failure. Ultrasonography can help in diagnosing hydronephrosis, revealing a dilated renal pelvis and signs of pressure atrophy in the renal parenchyma (Figure 12). Postmortem examination can confirm whether the condition is unilateral or bilateral.

### 6.2.3 Pyelonephritis

Pyelonephritis is an uncommon condition in sheep and goats, and it can be caused by organisms other than *Corynebacterium renale*, such as *Trueperella pyogenes* (previously *Arcanobacterium pyogenes*). The relatively low rate of post-partum uterine infections in sheep and goats, compared to cattle, may partly explain why this ascending kidney infection is less frequent in these animals. The disease generally progresses slowly and is characterized by symptoms such as fever, colic, pyuria, hematuria, cystitis, ureteritis, and suppurative nephritis.

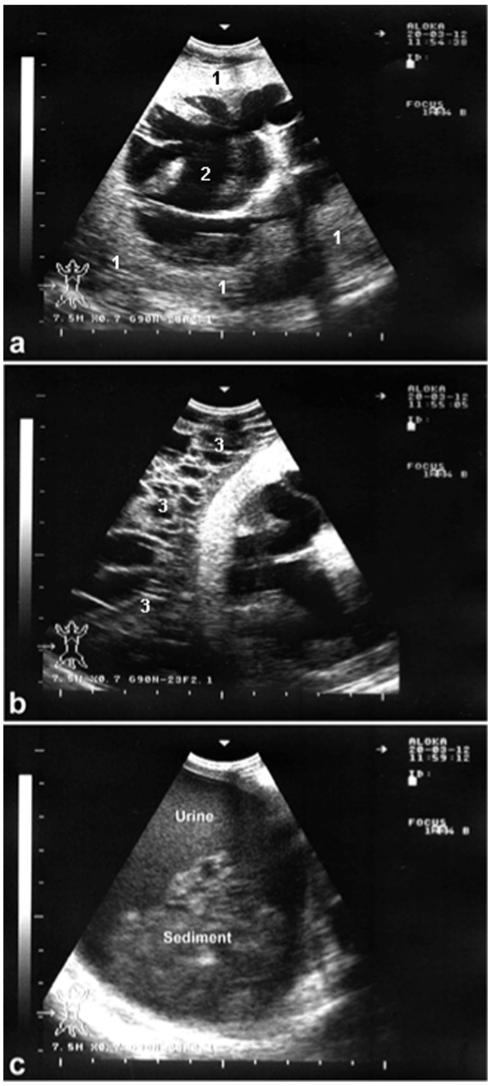


FIGURE 12
Ultrasonographic findings in a ram with hydronephrosis using a 7.5 MHz convex transducer: **(A)** Severely enlarged kidney (1) with dilated renal pelvis (2) and pressure atrophy of the renal parenchyma; **(B)** perirenal edema (3); **(C)** ventral sludge in the urinary bladder (3).

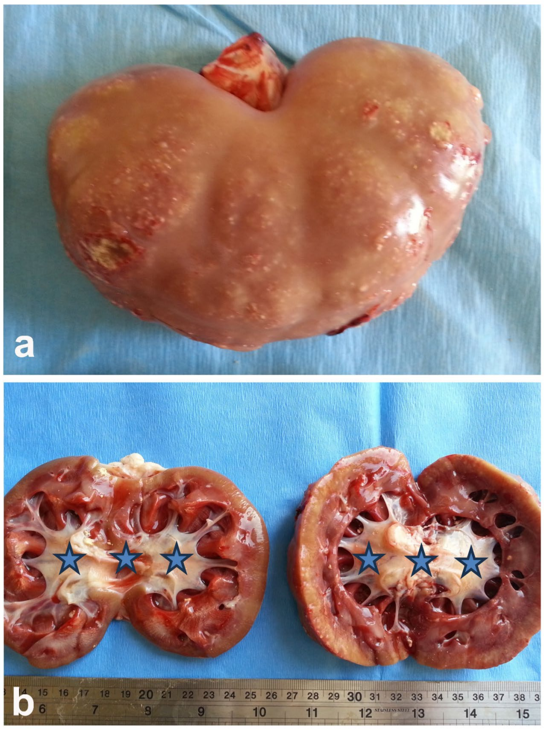


FIGURE 13
Postmortem finding of a buck with pyelonephritis. **(A)** Sub-capsular pinpoint micro-abscesses. **(B)** Bilateral dilatation of the renal pelvises (stars) (3).

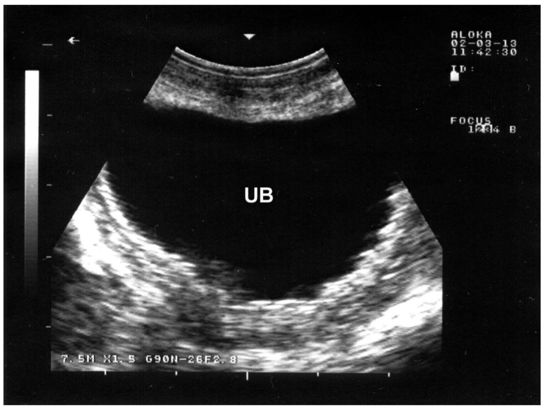


FIGURE 14
Ultrasonographic findings in a goat with cystitis showing the thickened and corrugated mucosa of the urinary bladder (UB). Image was taking using a 7.5 MHz convex transducer (3).

Ultrasonography can assist in diagnosing pyelonephritis by showing irregularly shaped kidneys with a loss of the corticomedullary boundary, as well as hypo- or hyperechoic changes in the renal cortex and increased echogenicity. Additionally, hyperechogenic urine and bladder sediment containing cellular debris, red blood cells, and pus cells may be detected (9). Upon postmortem examination, the affected kidney is often enlarged, with lesions in various stages of development within the parenchyma with dilated renal pelvis (Figure 13). Necrotic gray streaks may extend from the medulla to the cortex, and the kidney may show multicystic changes. Histological examination reveals widespread suppurative pyelonephritis in both the renal cortex and medulla (11, 28).

### 6.2.4 Obstructive urolithiasis

Obstructive urolithiasis refers to the inability to pass urine due to blockage in the urinary outflow tract caused by calculi. In sheep and goats, this condition is most commonly seen in young, castrated males, with the calculi typically composed of phosphate salts, such as calcium phosphate (apatite) and magnesium ammonium phosphate (struvite). The formation of these urinary stones is influenced by various physiological, nutritional, and management factors. The likelihood of urinary calculi getting stuck in the urethra is linked to anatomical features and the practice of castrating male ruminants (10, 66). Ultrasonography of the urinary system may reveal the presence of calculi, a collapsed bladder, and uroperitoneum. Ruptured urethra should be distinguished from abdominal herniation. In an adult goat buck that was admitted with a ruptured urinary bladder, abdominocentesis showed reddish urine, with red blood cell sediment found after centrifugation. The urethral process and glans penis were congested and blackish. Ultrasonography indicated a distended bladder with uroperitoneum. At necropsy, dissection of the urinary tract revealed calculi, urethral trauma, and rupture of the bladder or urethra. Calculi were found in the renal cortex, renal pelvis, or within the urethral process. Other postmortem findings included a collapsed and perforated bladder, bilateral hydronephrosis, and uroperitoneum (11, 20, 28, 29).

### 6.2.5 Cystitis

Inflammation of the urinary bladder typically occurs as a result of bladder paralysis, which leads to urine retention, dystocia, ascending infection from the urethra, or chronic irritation caused by cystic calculi (28). Clinically, the condition is marked by frequent, painful urination (pollakiuria and dysuria), as well as the presence of blood (hematuria), inflammatory cells, and bacteria in the urine. The urine may visibly contain blood or pus. A microscopic urinalysis may show pyuria and the presence of bacteria. Ultrasonographic imaging of the inflamed bladder typically reveals a thickened, corrugated mucosal lining (Figure 14) (66).

### 6.2.6 Paralysis of the urinary bladder

Bladder paralysis is rare in large animals and typically results from neurological conditions that affect the lumbosacral spinal cord. In lambs, ascending spinal meningitis is a significant cause, especially following tail docking. In all species, bladder paralysis can also occur due to compression of the lumbar spinal cord by tumors (such as lymphosarcoma or melanoma) or infected tissue (such as vertebral osteomyelitis) (20). Incontinence, with constant or intermittent urine dribbling, often worsens during physical activity. Abdominal examination reveals an enlarged bladder, and urine can be easily expelled through manual compression. The retention of urine creates favorable conditions for bacterial growth, often leading to cystitis. Ultrasonography shows a dilated bladder with a thickened wall,

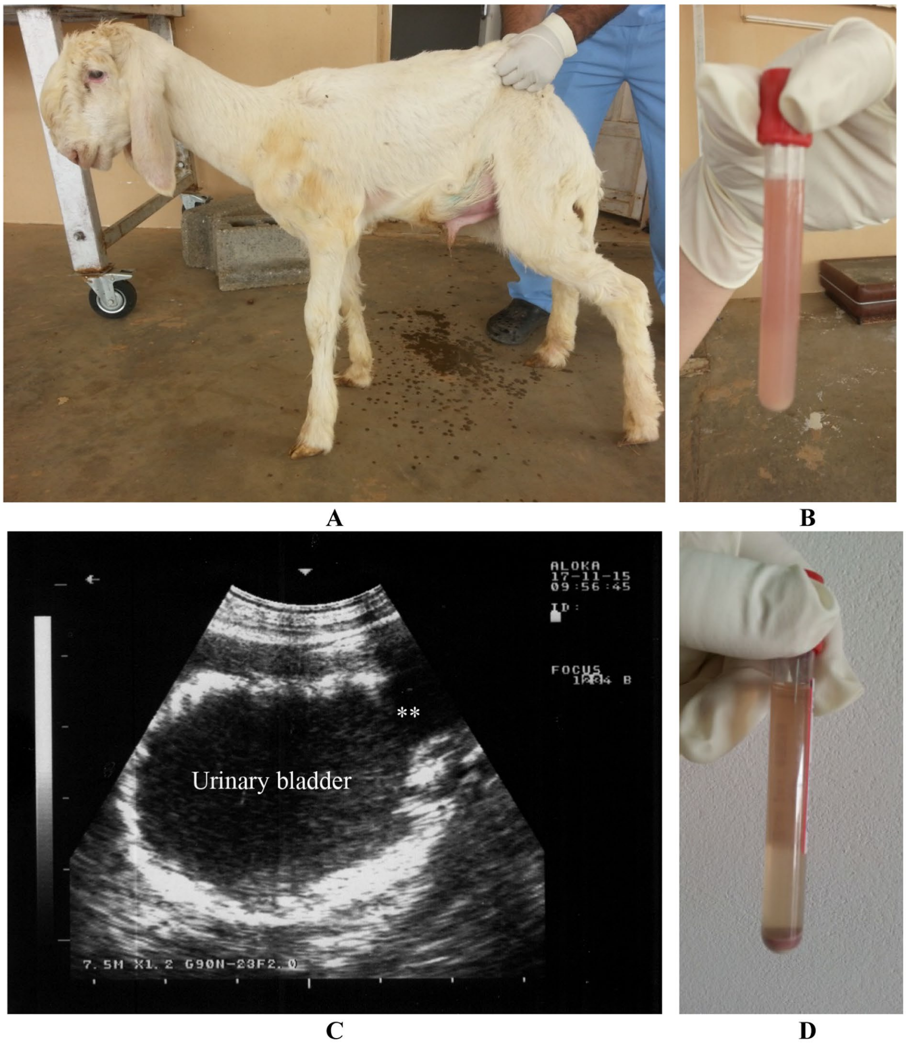


FIGURE 15
Paralysis of the urinary bladder in a lamb. Incontinence with dribbling of urine was the owner's complaint **(A)**. Urine sample was cloudy **(B)**. Ultrasonographic examination reveals dilated bladder, thickened wall, echogenic content and dilated bladder neck (stars) **(C)**. Urine sediment is clear upon centrifugation **(D)** (3).

echogenic contents, and a dilated bladder neck. Urine sediment remains clear after centrifugation of a sample (11) (Figure 15).

## 7 Conclusion

This review article highlights the effectiveness of sonography in both healthy and diseased sheep and goats. The technique can be employed to assess the normal structure and function of healthy thoracic and abdominal organs. Additionally, it serves as a valuable tool for diagnosing and predicting respiratory, cardiovascular, gastrointestinal, hepatic, and urinary conditions. It is strongly recommended to use ultrasonography as an initial diagnostic tool when evaluating sheep and goats with thoracic and abdominal medical issues. While ultrasonography is a valuable tool for examining sheep and goats, there are few limitations to its use such as operator skill, technical equipment limitations, animal stress and limited depth penetration especially in well-fattened animals. These limitations highlight the need for careful consideration when choosing ultrasonography as a diagnostic tool for sheep and goats.

## Author contributions

MM: Data curation, Funding acquisition, Writing – review & editing. MT: Conceptualization, Data curation, Writing – original draft.

## Funding

The author(s) declare that financial support was received for the research and/or publication of this article. This work was supported by the Deanship of Scientific Research, Vice Presidency for Graduate Studies and Scientific Research, King Faisal University, Saudi Arabia (grant no. KFU250106).

## Acknowledgments

The authors would like to acknowledge the Deanship of Scientific Research, Vice Presidency for Graduate Studies and Scientific Research, King Faisal University, Saudi Arabia for the financial support.

## Conflict of interest

The authors declare that the research was conducted in the absence of any commercial or financial relationships that could be construed as a potential conflict of interest.

## Generative AI statement

The authors declare that no Gen AI was used in the creation of this manuscript.

## Publisher's note



## References

1. Banda LJ, Tanganyika J. Livestock provide more than food in smallholder production systems of developing countries. *Anim Front*. (2021) 11:7–14. doi: 10.1093/af/vfab001

2. Crilly JP, Politis AP, Hamer K. Use of ultrasonographic examination in sheep veterinary practice. *Small Rumin Res*. (2017) 152:166–73. doi: 10.1016/j.smallrumres.2016.12.021

3. Tharwat M. Clinical, ultrasonographic, and postmortem findings in sheep and goats with urinary tract disorders. *Vet World*. (2021) 14:1879–87. doi: 10.14202/vetworld.2021.1879-1887

4. Tharwat M, Al-Sobayil F. Diagnostic ultrasonography in goats with contagious caprine pleuropneumonia caused by *Mycoplasma capricolum* subsp. *capripneumoniae*. *BMC Vet Res*. (2017) 13:263. doi: 10.1186/s12917-017-1167-4

5. Tharwat M, Ali H, Alkheraif AA. Paratuberculosis in sheep and goats: pathogenesis, diagnostic findings, and control strategies. *Open Vet J*. (2025) 15:1–7. doi: 10.5455/OVJ.2025.v15.i1.1

6. Tharwat M, Al-Hawas A. Liver diseases in sheep and goats: parallel sonographic and pathologic findings. *Int J Vet Sci*. (2024) 13:284–90. doi: 10.47278/journal.ijvs/2023.094

7. Tharwat M, Alkheraif AA, Marzok M. Pregnancy toxemia in small ruminants: clinical, sonographic, hematobiochemical and pathologic findings. *Int J Vet Sci*. (2025) 14:204–11. doi: 10.47278/journal.ijvs/2024.222

8. Tharwat M, Omar HM, Safaa H, Aboollo B, El-Manakhly EM. Acute hepatic cysticercosis in Naemi sheep: ultrasonography and pathology. *J Agricul Vet Sci*. (2017) 10:101–12.

9. Tharwat M, Al-Hawas A. Suppurative pyelonephritis in a caprine buck: clinical, laboratory, ultrasonographic and pathologic findings. *Int J Vet Sci*. (2024) 13:479–83.

10. Tharwat M, Hegazy Y, Alkheraif AA. Discolored urine in sheep and goats: clinical, etiological, hematobiochemical, sonographic and postmortem findings. *Open Vet J*. (2024) 14:1059–71. doi: 10.5455/OVJ.2024.v14.i4.13

11. Pugh DG, Baird AN. Sheep and goat medicine. *2nd Edn*. Riverport Lane Maryland Heights, Missouri, USA: Elsevier (Saunders) (2012).

12. Yousif NH, Dawood MS. Morphometric comparative anatomical study of lower respiratory tract between sheep (Ovis aris) and goat (*Caprus hircus*) in Baghdad province. *Kufa J Vet Med Sci*. (2019) 10:26–36. doi: 10.36326/kjvs/2019/v10i23311

13. Banks WJ. Applied veterinary histology. *3rd* ed. St. Louis: Mosby (1993).

14. Reissig A, Kroegel C. Ultrasound of the lung and pleura In: GJ Gibson, DM Geddes and U Coastabel, editors. Respiratory medicine. *3rd* ed. London: Elsevier Science (2002). 370–7.

15. Scott P, Collie D, McGorum B, Sargison N. Relationship between thoracic auscultation and lung pathology detected by ultrasonography in sheep. *Vet J*. (2010) 186:53–7. doi: 10.1016/j.tvjl.2009.07.020

16. Tharwat M, Al-Sobayil F. Thoracoabdominal diseases and disorders in sheep and goats. Buraydah, Saudi Arabia: Qassim University (2020).

17. Mohamed T, Oikawa S. Ultrasonographic characteristics of abdominal and thoracic abscesses in cattle and buffaloes. *J Vet Med A*. (2007) 54:512–7. doi: 10.1111/j.1439-0442.2007.00989.x

18. Tharwat M, Oikawa S. Ultrasonographic evaluation of cattle and buffaloes with respiratory disorders. *Trop Anim Health Prod*. (2011) 43:803–10. doi: 10.1007/s11250-010-9766-0

19. Borriello G, Valentini F, Cagnotti G, Capucchio MT, Ferrini S, Zoppi S, et al. Assessing lung consolidation in goats using different ultrasonographic techniques. *Vet Res Commun*. (2024) 48:3307–13. doi: 10.1007/s11259-024-10458-1

20. Constable PD, Hinchcliff KW, Done SH, Gruenberg W. Veterinary medicine: A textbook of the diseases of cattle, horses, sheep, pigs and goats. *11th* ed Saunders Ltd. (2017).

21. Amirbekov M, Murvatulloev S, Ferrari G. Contagious caprine pleuropneumonia detected for the first time in Tajikistan. *EMPRES Transboundary Animal Diseases Bulletin*. (2010) 35:20–2.

22. Chu Y, Gao P, Zhao P, He Y, Liao N, Jackman S, et al. Genome sequence of *Mycoplasma capricolum* subsp. capripneumoniae strain M1601. *J Bacteriol*. (2011) 193:6098–9. doi: 10.1128/JB.05980-11

23. Lorenzon S, Manso-Silván L, Thiaucourt F. Specific real-time PCR assays for the detection and quantification of *Mycoplasma mycoides* subsp. mycoides SC and *Mycoplasma capricolum* subsp. capripneumoniae. *Mol Cell Probes*. (2008) 22:324–8. doi: 10.1016/j.mcp.2008.07.003

24. March JB, Harrison JC, Borich SM. Humoral immune responses following experimental infection of goats with *Mycoplasma capricolum* subsp. capripneumoniae. *Vet Microbiol*. (2002) 84:29–45. doi: 10.1016/S0378-1135(01)00434-5

25. Arif A, Schulz J, Thiaucourt F, Taha A, Hammer S. An outbreak of contagious caprine pleuropneumonia at Al Wabra wildlife preservation, State of Qatar. *J Zoo Wildl Med*. (2005) 38:93–6.

26. Nicholas R, Churchward C. Contagious caprine pleuropneumonia: new aspects of an old disease. *Transbound Emerg Dis*. (2011) 59:189–96. doi: 10.1111/j.1865-1682.2011.01262.x

27. Ozdemir UI, Ozdemir E, March JB, Churchward C, Nicholas RA. Contagious caprine pleuropneumonia in the Thrace region of Turkey. *Vet Rec*. (2005) 156:286–7. doi: 10.1136/vr.156.9.286

28. Scott R. Sheep medicine. *2nd* ed. Thames, Oxfordshire, UK: CRC Press, Taylor & Francis Group (2020).

29. Smith MC, Sherman DM. Goat Medicine. *2nd* ed. State Avenue, Ames, Iowa, USA: Wiley-Blackwell (2009).

30. Belanger MC. Echocardiography In: SJ Ettinger and EC Feldman, editors. Textbook of veterinary internal medicine. *7th* ed. St. Louis, Missouri: Saunders Elsevier (2010). 415–31.

31. Braun U, Schweizer T, Pusterla N. Echocardiography of the normal bovine heart: technique and ultrasonographic appearance. *Vet Rec*. (2001) 148:47–51. doi: 10.1136/vr.148.2.47

32. Buczinski S, Tsuka T, Tharwat M. The diagnostic criteria used in bovine bacterial endocarditis: a meta-analysis of 460 published cases from 1973 to 2011. *Ann Cong Am College Vet Int Med New*. (2012) 193:349–57. doi: 10.1016/j.tvjl.2012.02.012

33. Buczinski S, Tolouei M, Rezakhani A, Tharwat M. Echocardiographic measurement of cardiac valvular thickness in healthy cows, cows with bacterial endocarditis, and cows with cardiorespiratory diseases. *J Vet Cardiol*. (2013) 15:253–61. doi: 10.1016/j.jvc.2013.08.001

34. Buczinski S, Pinard J, Ferrouillet C, Veillette M. Echocardiographic findings in a goat with cor pulmonale secondary to chronic parasitic pneumonia. *Schweiz Arch Tierheilkd*. (2010) 152:81–5. doi: 10.1024/0036-7281.a000018

35. Buczinski S. Cardiovascular ultrasonography in cattle. *Vet Clin North Am Food Anim Pract*. (2009) 25:611–32. doi: 10.1016/j.cvfa.2009.07.010

36. Hallowell GD, Potter TJ, Bowen IM. Reliability of quantitative echocardiography in adult sheep and goats. *BMC Vet Res*. (2012) 27:181. doi: 10.1186/1746-6148-8-181

37. Leroux AA, Moonen ML, Farnir F, Sandersen CF, Deleuze S, Salciccia A, et al. Two-dimensional and M-mode echocardiographic reference values in healthy adult Saanen goats. *Vet Rec*. (2012) 170:154. doi: 10.1136/vr.100192

38. Mohamed T, Buczinski S. Clinicopathological findings and echocardiographic prediction of the localisation of bovine endocarditis: 36 cases. *Vet Rec*. (2011) 169:180. doi: 10.1136/vr.d4346

39. Steininger K, Berli AS, Jud R, Schwarzwald CC. Echocardiography in Saanen-goats: Normal findings, reference intervals in awake goats, and the effect of general anesthesia. *Schweiz Arch Tierheilkd*. (2011) 153:553–64. doi: 10.1024/0036-7281/a000273

40. Tharwat M, Oikawa S, Kurosawa T, Takehana K, Hosaka Y, Okada H, et al. Focal fatty liver in a heifer: utility of ultrasonography in diagnosis. *J Vet Med Sci*. (2004) 66:341–4. doi: 10.1292/jvms.66.341

41. Tharwat M. Clinicopathological and ultrasonographic findings in 40 water buffaloes (*Bubalus bubalis*) with traumatic pericarditis. *Vet Rec*. (2010) 167:819–24. doi: 10.1136/vr.c3113

42. Poser H, Semplicini L, De Benedictis GM, Gerardi G, Contiero B, Maschietto N, et al. Two-dimensional, M-mode and Doppler-derived echocardiographic parameters in sedated healthy growing female sheep. *Lab Anim*. (2013) 47:194–202. doi: 10.1177/0023677213486895

43. Braun U, Jacquat D, Hässig M. Ultrasonography of the rumen in 30 Saanen goats. *Schweiz Arch Tierheilkd*. (2011) 153:393–9. doi: 10.1024/0036-7281/a000231

44. Braun U, Jacquat D, Steininger K. Ultrasonographic examination of the abdomen of the goat. II. Liver, spleen, urinary tract and greater omentum. *Schweiz Arch Tierheilkd*. (2013) 155:185–95. doi: 10.1024/0036-7281/a000442

45. Braun U, Jacquat D. Ultrasonography of the reticulum in 30 healthy Saanen goats. *Acta Vet Scand*. (2011) 53:19. doi: 10.1186/1751-0147-53-19

46. Braun U, Jacquat D. Ultrasonography of the omasum in 30 Saanen goats. *BMC Vet Res*. (2011) 7:11. doi: 10.1186/1746-6148-7-11

47. Braun U, Jacquat D. Ultrasonography of the abomasum in 30 Saanen goats. *Res Vet Sci*. (2012) 92:295–8. doi: 10.1016/j.rvsc.2011.03.013

48. Braun U, Schwarzwald CC, Forster E, Becker-Birck M, Borel N, Ohlerth S. Extraskeletal osteosarcoma of the thorax in a goat: case report. *BMC Vet Res*. (2011) 7:55. doi: 10.1186/1746-6148-7-55

49. Braun U, Steininger K. Ultrasonographic examination of the spleen in 30 goats. *Schweiz Arch Tierheilkd*. (2010) 152:477–81. doi: 10.1024/0036-7281/a000108

50. Tharwat M, Ahmed AF, El-Tookhy O. Chronic peritonitis in buffaloes and cattle: clinical, hematological, ultrasonographic findings and treatment. *J Anim Vet Adv*. (2012) 15:2775–81.

51. Tharwat M, Al-Sobayil F, Hashad M, Buczinski S. Transabdominal ultrasonographic findings in goats with paratuberculosis. *Can Vet J*. (2012) 53:1063–70.

52. Sadan M, Tharwat M, El-Deeb W. Deep swellings in sheep and goats: clinical, ultrasonographic and post-mortem findings. *Int J Vet Sci*. (2023) 12:793–801. doi: 10.47278/journal.ijvs/2023.050

53. Tharwat M. Ultrasonography as a diagnostic and prognostic approach in cattle and buffaloes with fatty infiltration of the liver. *Pol J Vet Sci*. (2011) 15:83–93. doi: 10.2478/v10181-011-0118-4

54. Bobe G, Amin VR, Hippen AR, She P, Young JW, Beitz DC. Non-invasive detection of fatty liver in dairy cows by digital analyses of hepatic ultrasonograms. *J Dairy Res*. (2008) 75:84–9. doi: 10.1017/S002202990700297X

55. Samuel W, Zewde GG. Prevalence, risk factors, and distribution of Cysticercus tenuicollis in visceral organs of slaughtered sheep and goats in Central Ethiopia. *Trop Anim Health Prod*. (2010) 42:1049–51. doi: 10.1007/s11250-010-9537-y

56. Sissay MM, Uggla A, Waller PJ. Prevalence and seasonal incidence of larval and adult cestode infections of sheep and goats in eastern Ethiopia. *Trop Anim Health Prod*. (2008) 40:387–94. doi: 10.1007/s11250-007-9096-z

57. Radfar MH, Tajalli S, Jalalzadeh M. Prevalence and morphological characterization of Cysticercus tenuicollis (Taenia hydatigena cysticerci) from sheep and goats in Iran. *Veterinarski Arhiv*. (2005) 75:469–76.

58. Tharwat M, Tsuka T. Diagnostic utility of ultrasonography for thoracic and abdominal bacterial and parasitic diseases in ruminants: a comprehensive overview. *Front Vet Sci*. (2024) 11:1435395. doi: 10.3389/fvets.2024.1435395

59. Woods LW, Walters NG, Johnson B. Cholangiohepatitis associated with adenovirus-like particles in a pygmy goat kid. *J Vet Diagn Invest*. (1991) 3:89–92. doi: 10.1177/104063879100300124

60. Cruz C, Driemeier D, Pires VS, Schenkel EP. Experimentally induced cholangiohepatopathy by dosing sheep with fractionated extracts from *Brachiaria decumbens*. *J Vet Diagn Invest*. (2001) 13:170–2. doi: 10.1177/104063870101300215

61. Tharwat M, El Moghazy HM, Oikawa S. Ultrasonographic verification of hepatic hydatidosis in a female dromedary camel: a case report. *J Vet Med Sci*. (2023) 85:1286–90. doi: 10.1292/jvms.23-0325

62. Eckert J, Deplazes P, Craig PS, Gemmell MS, Gottstein B, Heath D, et al. Echinococcosis in animals: clinical aspects, diagnosis and treatment. In: J Eckert In: MA Gemmell, F-X Meslin and ZS Pawlowski, editors. WHO/OIE manual on echinococcosis in humans and animals: A public health problem of global concern. Paris: World Organisation for Animal Health (2001). 72–99.

63. Khuroo MS, Zargar SA, Mahajan R. Echinococcus granulosus cysts in the liver: management with percutaneous drainage. *Radiology*. (1991) 180:141–5. doi: 10.1148/radiology.180.1.2052682

64. Hussein HA, Elrashidy M. Ultrasonographic features of the liver with cystic echinococcosis in sheep. *Vet Rec Open*. (2014) 1:e000004. doi: 10.1136/vropen-2013-000004

65. Steininger K, Braun U. Ultrasonography of the urinary tract in 29 female Saanen goats. *Schweiz Arch Tierheilk*. (2012) 154:67–74. doi: 10.1024/0036-7281/a000298

66. Scott P. Transabdominal Ultrasonographic examination of 26 sheep with suspected urinary tract disease (2010-2012). *J Vet Sci Med Diagn*. (2013) 2:1. doi: 10.4172/2325-9590.1000107

67. Tharwat M, Ahmed AF. Abomasal ulceration in buffaloes and cattle: clinico-biochemical and pathological findings. *J Anim Vet Adv*. (2012) 9:1327–31.

68. Tharwat M, Al-Sobayil F, El-Sayed M. Cardiac troponin I in healthy newborn goat kids and in goat kids with cardiac nutritional muscular dystrophy. *Acta Vet Hung*. (2013) 61:442–53. doi: 10.1556/avet.2013.041

69. Tharwat M, Mizunuma Y, Iwasaki Y, Oikawa S. Changes of very low-density lipoprotein concentration in hepatic blood from cows with fasting-induced hepatic lipidosis. *Can J Vet Res*. (2011) 74:317–20.

70. Tharwat M, Sato H, Kurosawa T, Oikawa S, Nakade T, Koiwa M. Tetralogy of Fallot in a calf: clinical, ultrasonographic, laboratory and postmortem findings. *J Vet Med Sci*. (2004) 66:73–6. doi: 10.1292/jvms.66.73

frontiers | Frontiers in Veterinary Science

TYPE Original Research
PUBLISHED 28 March 2025
DOI 10.3389/fvets.2025.1571850

Check for updates

OPEN ACCESS

EDITED BY
Ryou Tanaka,
Tokyo University of Agriculture and Technology, Japan

REVIEWED BY
Bruno Alberigi,
Federal Rural University of Rio de Janeiro, Brazil
Hyung-Kyu Chae,
Kyungpook National University, Republic of Korea

*CORRESPONDENCE
Ryohei Suzuki
✉ ryoheisuzuki@nvlu.ac.jp

RECEIVED 06 February 2025
ACCEPTED 14 March 2025
PUBLISHED 28 March 2025

CITATION
Saito T, Suzuki R, Yuchi Y, Fukuoka H, Satomi S, Teshima T and Matsumoto H (2025) Post-carvedilol myocardial function in cats with obstructive hypertrophic cardiomyopathy. *Front. Vet. Sci.* 12:1571850.
doi: 10.3389/fvets.2025.1571850



# Post-carvedilol myocardial function in cats with obstructive hypertrophic cardiomyopathy

Takahiro Saito[1,2], Ryohei Suzuki[1]*, Yunosuke Yuchi[1,3], Haru Fukuoka[1], Shuji Satomi[1,4], Takahiro Teshima[1] and Hirotaka Matsumoto[1]

[1]Laboratory of Veterinary Internal Medicine, School of Veterinary Medicine, Faculty of Veterinary Science, Nippon Veterinary and Life Science University, Tokyo, Japan, [2]Sagamihara Animal Medical Center, Kanagawa, Japan, [3]Garden Veterinary Hospital, Tokyo, Japan, [4]Pet Clinic Lusty, Osaka, Japan

**Introduction:** Hypertrophic cardiomyopathy (HCM) is the most prevalent cardiac disease in cats, and one phenotype includes obstructive HCM with dynamic left ventricular outflow tract obstruction (DLVOTO). Myocardial function has been reported to be lower in cats with obstructive HCM than in non-obstructive HCM. Carvedilol, because of its pharmacological action, is expected to reduce the pressure gradient associated with DLVOTO, but no previous reports have studied its effects on myocardial function. This study aimed to evaluate myocardial function in cats with obstructive HCM with left ventricular outflow tract obstruction treated by carvedilol administration.

**Methods:** This retrospective observational study included 16 cats with obstructive HCM and subsequent treatment of DLVOTO with carvedilol. In addition to conventional echocardiography, strain and strain rates in the left ventricular longitudinal and circumferential directions were measured using layer-specific two-dimensional speckle tracking echocardiography. Each variable was then compared before and after carvedilol medication.

**Results:** Systolic anterior motion of the mitral valve disappeared in 14 cats and all cats showed resolved DLVOTO with maximal left ventricular outflow tract blood flow velocity of <2.5 m/s after carvedilol administration ($P < 0.01$). Circumferential strain in the epicardial layer and in the whole layer was significantly increased after carvedilol administration ($P < 0.01$, $P = 0.04$, respectively). In contrast, systolic longitudinal strain showed no significant difference between before and after carvedilol administration.

**Conclusion:** Treatment of obstructive HCM with carvedilol improved DLVOTO and myocardial function without a negative inotropic effect. Carvedilol may be effective in treating cats with obstructive HCM.

KEYWORDS

beta-blocker, feline, left ventricular outflow tract obstruction, myocardium, two-dimensional speckle-tracking echocardiography, strain, systolic anterior motion of the mitral valve leaflet

## 1 Introduction

Hypertrophic cardiomyopathy (HCM), which is characterized by concentric hypertrophy of the left ventricular (LV) wall, is a highly prevalent heart disease in cats (1, 2). In addition, the detection of feline cardiomyopathy appears to have improved in recent years with the improved accuracy of diagnostic equipment, particularly in ultrasound imaging. The age at which HCM is diagnosed in cats varies, and its prognosis ranges from asymptomatic to congestive heart failure, arterial thromboembolism, and sudden death, even at a young age (3–7). HCM also shows diverse phenotypes, with some cases showing dynamic LV outflow tract obstruction (DLVOTO) associated with systolic anterior motion of the mitral valve (SAM). The presence of DLVOTO may cause increased afterload, exacerbation of LV wall thickening, abnormal relaxation, myocardial ischemia, and decreased single-beat output (8). In human patients with obstructive HCM, the presence of DLVOTO with LV outflow tract pressure gradient ≥50 mmHg is considered as a criterion for treatment because of its association with worse outcome (9). We have previously reported that LV myocardial function assessed using two-dimensional speckle-tracking echocardiography (2D-STE) is reduced in feline obstructive HCM with DLVOTO in comparison with that in non-obstructive HCM (10). Therefore, DLVOTO could be a therapeutic target also in feline HCM regardless of the presence of heart failure (2).

Carvedilol, a beta-blocker, blocks the action of catecholamines, resulting in improvement of diastolic dysfunction and suppression of myocardial ischemia associated with an increase in heart rate (11). Although the potential for myocardial function reduction due to the negative inotropic effect of carvedilol remains a concern, no previous report has examined the effect of carvedilol on myocardial function. We hypothesized that LV myocardial function would improve if DLVOTO were reduced by carvedilol administration in cats with obstructive HCM. Therefore, this study aimed to compare myocardial function indices before and after carvedilol treatment in cats with obstructive HCM with DLVOTO.

# 2 Methods

This retrospective observational study adhered to our university's animal care and use guidelines. The study was approved by our university's ethics committee (R2-4), and the owners gave adequate informed consent.

## 2.1 Animals

Medical records were reviewed from May 2015 to August 2022 to enroll cats diagnosed with obstructive HCM showing DLVOTO improvement with carvedilol administration. Each cat received a thorough clinical examination, blood pressure measurements, electrocardiographic evaluations, chest radiographs, and echocardiograms. The diagnostic criterion for HCM was a maximum LV wall thickness measuring ≥6 mm at end-diastole and distinct SAM were included in this study. A cat with SAM was defined as a case in which the anterior mitral leaflet of the mitral valve was in contact with the interventricular septum toward the end of systole in the right parasternal long-axis view. Obstructive HCM was defined as an LV outflow tract maximum blood flow velocity (LVOT $V_{\max}$) >2.5 m/s, based on previous reports (11, 12). In addition, patients were not administered beta-blockers at the time of diagnosis, which was a requirement for inclusion. Cats in this study started on carvedilol after diagnosis and had LVOT $V_{\max}$ <2.5 m/s at the time of the return visit within 1 year. In cats that were already treated with medications other than carvedilol at diagnosis, no medication changes were made. Other types of cardiomyopathies were excluded by assessing the LV systolic function and wall thickness, which were found to be in the normal range using allometric scaling, according to previously published reports (2, 13). Cats with systemic diseases, hypertension, metabolic diseases, neoplastic diseases, or dehydration suggestive of secondary myocardial hypertrophy were excluded from the study. Cats with missing data were also excluded from this study.

## 2.2 Echocardiography

A single researcher (R.S.) performed conventional echocardiography using a Vivid E95 echocardiography scanner and 12S transducer (GE Healthcare, Tokyo, Japan). During the examination, a lead II electrocardiogram was obtained and continuously displayed on the screen. Non-sedated cats were manually restrained in the left and right lateral recumbency. The data were acquired for a minimum of five heartbeats. Subsequently, echocardiographic data analysis was performed by a single researcher (T.S.) using an offline workstation (EchoPAC PC, version 204, GE Healthcare, Tokyo, Japan) on a different day from image acquisition.

Various measurements were taken from the echocardiographic images. To ensure accuracy, each measurement was averaged over three consecutive cardiac cycles before conducting the analysis. The left atrial-to-aortic diameter ratio was determined from the right parasternal short-axis view at the basal heart level. Additionally, end-diastolic interventricular septal thickness (IVSd), LV end-diastolic posterior wall thickness (LVPWd), LV end-diastolic internal diameter (LVIDd), LV end-systolic internal diameter, and fractional shortening (FS) were measured from the right parasternal short-axis view at the level of the chordae tendineae. Relative LV wall thickness (RWT) was calculated using the following formula (14, 15):

$$\mathbf{RWT} = \frac{(\mathbf{IVSd} + \mathbf{LVPWd})}{\mathbf{LVIDd}}$$

Pulsed-wave Doppler was used to measure the transmitral inflow in the left apical four-chamber view, where the peak velocities of the early diastolic wave (E-wave) and late diastolic wave (A-wave) were determined. The E-wave to A-wave velocity ratio (E/A) was calculated.

The pulsed-tissue Doppler technique was used to obtain the velocity of the mitral annular motion in the left apical four-chamber view, specifically from the interventricular septum. Three parameters were measured: Peak velocity of systolic mitral annular motion (s′), peak velocity of early diastolic mitral annular motion (e′), and peak velocity of late diastolic mitral annular motion (a′).

As described previously (12, 16–19), 2D-STE analysis of cats is performed with high-quality images obtained using conventional echocardiography. To evaluate circumferential deformations using 2D-STE, a right parasternal short-axis view of the LV at the level of the chordae tendineae level was used (12, 20). A left apical 4-chamber view was used to analyze the longitudinal deformations.

Peak systolic strain was measured in the longitudinal and circumferential directions (SL and SC, respectively) (21). The SL and SC were measured individually for the endocardial, epicardial, and whole layer. Additionally, early-diastolic and late-diastolic strain rate in the longitudinal and circumferential direction were measured (SrL E, SrL A, SrC E, and SrC A, respectively). The early to late-diastolic strain rate ratio (E/A) was calculated.

Our laboratory has previously reported observer variability in 2D-STE (12, 18, 19, 21).

## 2.3 Statistical analysis

All variables are presented as medians (interquartile ranges). For the statistical analysis, we used commercially available software (R 2.8.1; https://www.r-project.org/). Data were assessed for normality using the Shapiro–Wilk test and compared before and after carvedilol administration. Normally distributed data were evaluated with a paired *t*-test, and non-normally distributed data were evaluated using a Wilcoxon rank-sum test. *P*-values $<0.05$ were considered significantly different.

# 3 Results

## 3.1 Clinical profiles

The demographic characteristics, duration of carvedilol administration and dosage, and physical examination findings before and after carvedilol administration are summarized in Table 1. All cats were given carvedilol twice daily. The duration of carvedilol administration was the same as the duration of the before and after comparisons. Sixteen cats were included in the study, and no cases of severe congestive heart failure, such as pulmonary edema or pleural effusion, were observed. Medications other than carvedilol were angiotensin-converting enzyme inhibitors ($n = 1$), calcium channel blockers ($n = 1$), pimobendan ($n = 1$), and antithrombotic agents ($n = 3$). The heart rate showed a significant decrease before and after carvedilol administration. The systolic blood pressure showed no significant difference after the administration of carvedilol.

TABLE 1 Clinical characteristics in cats with obstructive hypertrophic cardiomyopathy before and after carvedilol administration.

| Variables | | | *P*-value |
|---|---|---|---|
| N (male/female) | 16 (9/7) | | |
| Age (years) | 1.9 (1.0, 3.3) | | |
| ACVIM (B1, B2, C/D) | 11, 5, 0 | | |
| Carvedilol | | | |
| Period of administration (day) | 48 (26, 92) | | |
| Dose (mg/kg/day) | 0.2 (0.1, 0.5) | | |
| Body weight (kg) | 4.0 (3.3, 5.1) | 4.2 (3.7, 5.2) | 0.90 |
| Heart rate (bpm) | 194 (177, 219) | 172 (158, 183)* | <0.05 |
| Systolic blood pressure (mmHg) | 126 (120, 149) | 142 (130, 144) | 0.47 |

Data are presented as median (interquartile range).
*Significantly different values compared to before carvedilol administration.

TABLE 2 Results of conventional echocardiographic variables in cats with obstructive hypertrophic cardiomyopathy before and after carvedilol administration.

| Variables | Pre | Post | *P*-value |
|---|---|---|---|
| LA/Ao | 1.2 (1.1, 1.6) | 1.2 (1.1, 1.3) | 0.12 |
| IVSd (mm) | 6.2 (5.3, 7.2) | 5.8 (4.1, 6.6)* | <0.05 |
| LVPWd (mm) | 6.0 (4.8, 6.5) | 5.2 (4.5, 6.1)* | <0.05 |
| LVIDd (mm) | 12.8 (12.1, 14.2) | 14.0 (12.0, 14.8) | 0.31 |
| LV maximum wall thickness (mm) | 6.8 (6.0, 7.5) | 6.4 (5.7, 7.0)* | <0.05 |
| RWT | 0.9 (0.8, 1.1) | 0.8 (0.7, 0.9)* | 0.08 |
| FS (%) | 51.4 (45.4, 58.8) | 50.0 (43.8, 56.1) | 0.65 |
| *s*′ (cm/s) | 8.1 (6.2, 10.3) | 6.8 (5.7, 7.5) | 0.07 |
| *e*′ (cm/s) | 4.6 (4.2, 5.3) | 4.8 (3.4, 5.7) | 0.12 |
| *a*′ (cm/s) | 9.2 (7.0, 10.6) | 7.0 (6.4, 7.8)* | <0.01 |
| LVOT $V_{max}$ | 3.9 (3.6, 4.8) | 1.2 (1.0, 1.3)* | <0.01 |

LA/Ao, left atrial-to-aortic diameter ratio; IVSd, end-diastolic interventricular septal thickness; LV, Left ventricular; LVPWd, end-diastolic LV free-wall thickness; LVIDd, end-diastolic LV internal diameter; RWT, relative left ventricular wall thickness; FS, fractional shortening; s′, peak velocity of systolic mitral annular motion; e′, peak velocity of early diastolic mitral annular motion; a′, peak velocity of late diastolic mitral annular motion; LVOT $V_{max}$, peak velocity of left-ventricular outflow-tract.
Data are presented as median (interquartile range).
*Significantly different values compared to before carvedilol administration.

## 3.2 Echocardiography

The conventional echocardiographic variables are summarized in Table 2. The IVSd, LVPWd, LV maximum wall thickness, and *a*’ significantly decreased after carvedilol administration. The LVIDd showed no significant difference after administration of carvedilol. Although SAM was present in all cats at the initial evaluation, it disappeared in 14 cats after carvedilol administration. Two cats showing fusion of E- and A-waves were excluded from the analysis. Echocardiographic findings in a representative case of SAM resolved by carvedilol administration are shown in Figure 1.

The myocardial strain results of the analysis using 2D-STE are summarized in Table 3. The SL did not show significant differences before and after carvedilol administration in any of the layers. In the SC, the endocardial layer showed no significant difference after administration of carvedilol. In contrast, the SC in the epicardial layer and in the whole layer increased significantly after carvedilol administration (Figure 2). Myocardial circumferential analysis evaluated by 2D-STE in a representative case of SAM resolved by carvedilol administration is shown in Figure 3. Diastolic myocardial strain rates assessed by 2D-STE are summarized in Table 4. The SrL A decreased significantly after carvedilol administration. On the other hand, there were no significant differences in indices other than SrL before and after carvedilol administration.

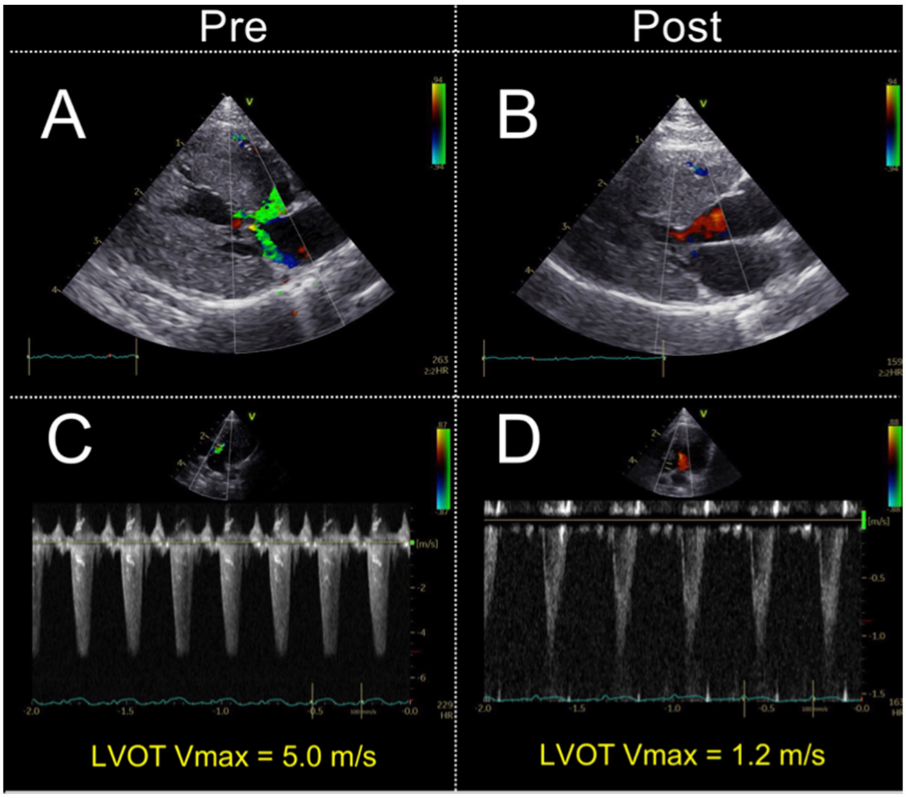


FIGURE 1
Echocardiographic findings in a representative case of systolic anterior motion of the mitral valve resolved by carvedilol administration. Echocardiographic findings on color Doppler. The images show the absence of mosaic on the left ventricular outflow tract and mitral regurgitation **(A, B)**. Doppler echocardiography shows the maximal left ventricular outflow tract blood flow velocity decreased **(C, D)**. LVOT $V_{max}$, left ventricular outflow tract maximum blood flow velocity.

**TABLE 3 The myocardial strain assessed using two-dimensional speckle tracking echocardiography in cats with obstructive hypertrophic cardiomyopathy before and after carvedilol administration.**

| Variables | Pre | Post | *P*-value |
|---|---|---|---|
| SL (%) | | | |
| Whole layer | 19.0 (12.3, 20.4) | 15.3 (14.0, 20.8) | 0.82 |
| Endocardium | 23.6 (19.1, 25.5) | 19.6 (18.3, 25.9) | 0.82 |
| Epicardium | 14.6 (9.7, 17.7) | 12.8 (10.3, 17.1) | 0.85 |
| SC (%) | | | |
| Whole layer | 16.9 (12.3, 21.1) | 17.2 (15.8, 19.3)* | 0.03 |
| Endocardium | 34.0 (28.9, 40.2) | 35.9 (32.3, 40.1) | 0.19 |
| Epicardium | 6.2 (4.1, 8.4) | 7.2 (5.7, 7.8)* | <0.01 |

SL, peak systolic strain in the longitudinal direction; SC, peak systolic strain in the circumferential direction.
Data are presented as median (interquartile range).
*Significantly different values compared to before carvedilol administration.

## 4 Discussion

This is one of the few reports highlighting the effects of carvedilol administration on myocardial function evaluated by 2D-STE in cats with obstructive HCM. Cats with obstructive HCM were found to have improved myocardial function after treatment with carvedilol, without worsening the condition due to negative inotropic effect, which was an initial concern. The results of this study suggest that carvedilol may be useful as a treatment for cats with obstructive HCM.

This study focused on myocardial function in cats with obstructive HCM whose DLVOTO improved with carvedilol. In veterinary medicine, atenolol is the most discussed beta-blocker for treating feline obstructive HCM. Atenolol selectively acts on $\beta_1$ receptors, which inhibits vasodilating effect through $\beta_2$ receptors blockade. However, a recent study has reported that atenolol could not improve 5-year survival in cats (22), although atenolol could improve DLVOTO (11). One concern using atenolol is that this drug is water-soluble, which results in slower gastrointestinal absorption and less transfer to the central nervous system compared to fat-soluble drugs. Therefore, fat-soluble beta-blocker (e.g., carvedilol and bisoprolol) is used preferentially in human obstructive HCM. Carvedilol is one of the fat-soluble, non-selective beta-blockers. As a difference from other beta-blockers, carvedilol has been reported to reduce the risk of developing fatal arrhythmias (23). Additionally, carvedilol has antioxidant and apoptosis-inhibiting effects (24). Although this study could not evaluate these effects in detail, they might contribute to the improvement of myocardial function in cats with obstructive HCM. However, carvedilol also has $\alpha_1$ receptors

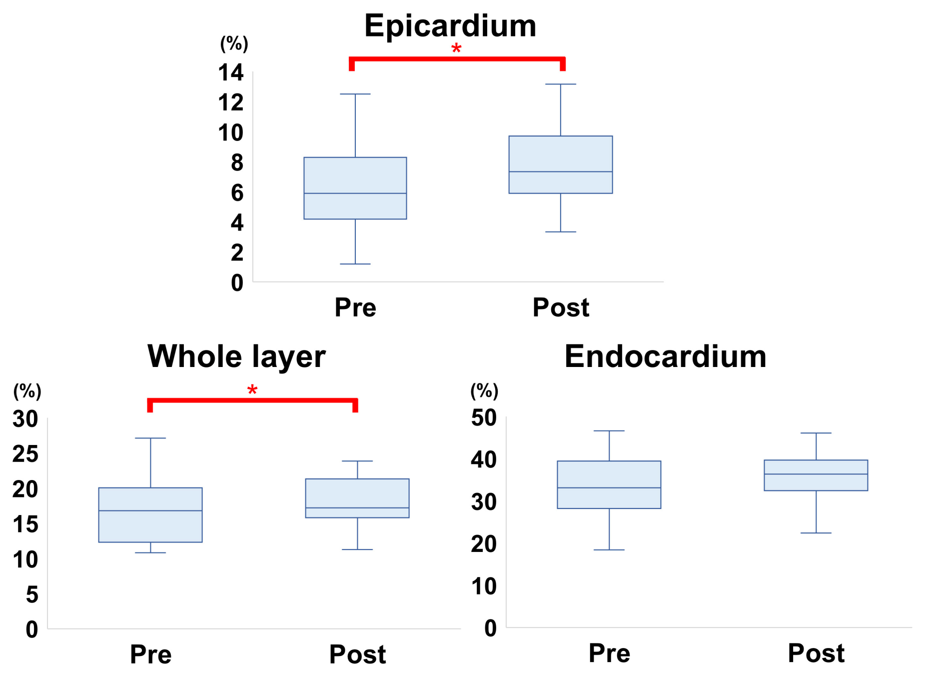


FIGURE 2
Comparison of circumferential strain evaluated by two-dimensional speckle-tracking echocardiography before and after carvedilol administration (box-and-whisker diagram). In the epicardium and whole layer, the circumferential strain shows significant differences before and after carvedilol administration. *Significantly different values compared to before carvedilol administration.

blockade as well as the non-selective $\beta$ receptors blockade. Hence hypotension due to vasodilating effect is a main concern as a side effect. However, systemic blood pressure of this study showed no significant change after carvedilol administration. The main factor attributed to the results was possibly due to increased cardiac output through the alleviation of DLVOTO. Therefore, our results indicate that carvedilol might be a safe treatment option for feline obstructive HCM.

Heart rate of this study was significantly decreased with carvedilol administration. This may be due to the negative chronotropic effects of carvedilol (25, 26). The IVSd, LVPWd, and LV maximum wall thickness were also significantly lower following carvedilol administration. This may be a result of the prolonged LV relaxation time that occurs as the heart rate decreases, which promotes the elongation of the LV wall. Previous reports have shown a significant increase in LVIDd and FS following carvedilol administration in cats with HCM, owing to the negative chronotropic effect of carvedilol (17). In this study, SAM disappeared in many cases, the distinct DLVOTO disappeared in all cases, and the LVOT $V_{\text{max}}$ was significantly lower after carvedilol administration. In previous reports, SAM has been reported to be caused by thickening of the LV wall and elongation of the mitral valve leaflet, resulting in a decrease in the relative distance between the papillary muscle and the mitral valve leaflet (27). In addition, early systolic contact of the mitral valve with the ventricular septum increases the pressure gradient. This gradient is thought to press the mitral valve against the ventricular septum, further narrowing the left ventricular outflow tract and thus increasing the pressure gradient (28). Although this study did not include a morphological evaluation of the mitral valve, the relatively thinner LV wall observed with increased LV volume at end-diastole and decreased heart rate may have reduced the incidence of SAM and improved DLVOTO.

We have previously reported a lower systolic SC in cats with obstructive HCM and DLVOTO (10), and the results of this study were consistent with this observation. This lower SC may have been caused by the increased pressure gradient and decreased cardiac output associated with DLVOTO. In addition, previous studies on HCM in humans reported that survival was shorter in HCM with DLVOTO than in HCM without DLVOTO (29). This may be because an increase in LV pressure owing to obstruction causes increased wall stress, myocardial ischemia, and fibrosis, resulting in diastolic dysfunction and sudden death, thus DLVOTO may worsen cardiac function (29). Furthermore, previous studies have reported that decreased SC in the epicardium of cats with HCM reflects decreased myocardial function due to layer-to-layer compensatory interactions (19, 30). Therefore, the present study can be interpreted as a significant increase in myocardial function, especially in SC on the epicardium after carvedilol administration, resulting in an increase in SC in the whole layer accompanied with an improvement in systolic myocardial function.

In cats with HCM, SL is known to be reduced early and is even lower in cats with more severe HCM (18, 31). In addition to histopathological changes, such as altered myocardial fiber orientation, compensatory mechanisms in the myocardium are thought to be associated with myocardial dysfunction (12, 18, 32). In human patients with HCM, decreased SL in the whole layer has been reported to be a poor prognostic factor, even when FS is normal (33). Although the SL before carvedilol administration in this study was considered to be lower than

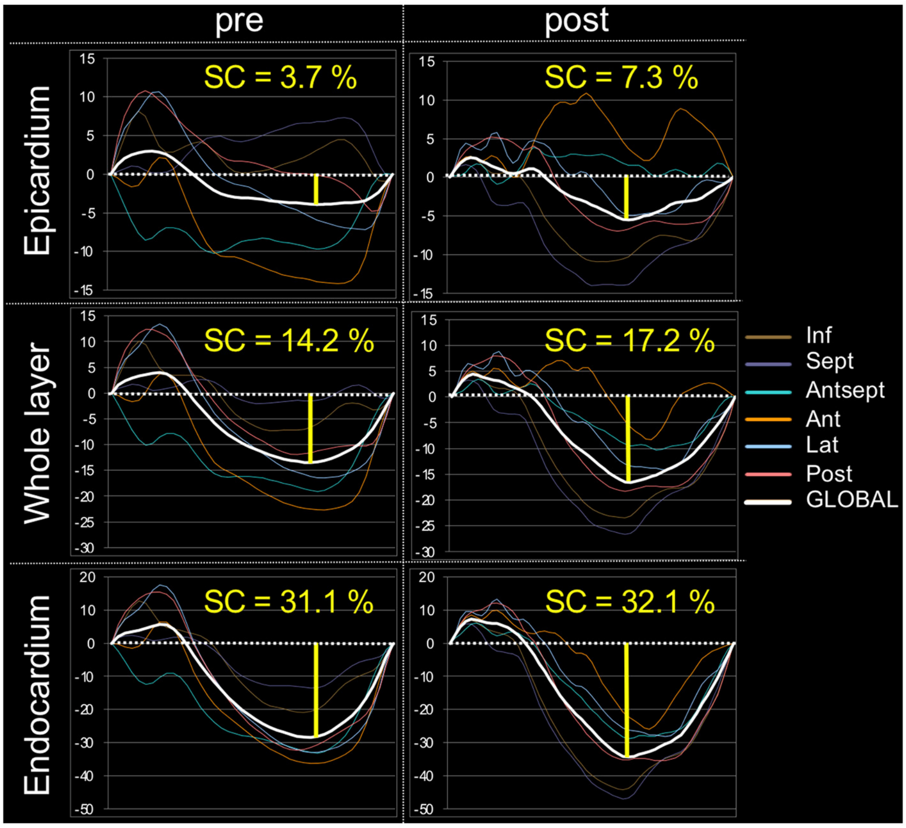


FIGURE 3
Myocardial circumferential analysis evaluated using two-dimensional speckle-tracking echocardiography in a representative case of systolic anterior motion of the mitral valve resolved by carvedilol administration. These are representative data, showing a stronger increase in circumferential strain after carvedilol administration than before in all layers in this case. SC, circumferential strain.

**TABLE 4 The myocardial strain rate assessed using two-dimensional speckle tracking echocardiography in cats with obstructive hypertrophic cardiomyopathy before and after carvedilol administration.**

| Variables | Pre | Post | P-value |
|---|---|---|---|
| SrL E | 1.7 (1.0, 3.3) | 2.6 (1.5, 3.9) | 0.40 |
| SrL A | 3.3 (2.6, 5.0) | 2.2 (1.7, 2.6)* | 0.03 |
| SrL E/A | 0.8 (0.2, 1.2) | 1.4 (0.8, 2.0) | 0.11 |
| SrC E | 2.3 (1.2, 2.6) | 2.5 (1.6, 3.3) | 0.78 |
| SrC A | 2.6 (2.0, 3.2) | 2.0 (1.6, 2.4) | 0.31 |
| SrC E/A | 0.8 (0.3, 1.8) | 1.3 (0.8, 2.0) | 0.58 |

SrL E, early-diastolic strain rate in the longitudinal direction; SrL A, late-diastolic strain rate in the longitudinal direction; SrC E, early-diastolic strain rate in the circumferential direction; SrC A, late-diastolic strain rate in the circumferential direction.
Data is presented as median (interquartile range).
*Significantly different values compared to before carvedilol administration.

that in healthy cats, no significant difference was observed in the SL before and after carvedilol administration. The results of SL indicate that carvedilol did not contribute to the worsening of the disease state.

Unlike the results of SL, SC increased significantly after carvedilol administration. The improvement in DLVOTO after carvedilol administration caused by prolonging the diastolic filling time and LV ejection acceleration time might have improved myocardial function, especially in the circumferential direction, by reducing LV pressure overload and cardiac output failure. The discrepancy in results for SL and SC might be due to compensatory mechanisms of myocardial motion. A previous study reported that circumferential function compensates for impaired longitudinal myocardial function in human patients with cardiovascular risk factors (34). Our results indicate that DLVOTO might be associated with compensatory myocardial motion, particularly in the circumferential direction, also in cats with obstructive HCM. The unchanged loading indices such as LVIDd, LA/Ao, and systemic blood pressure before and after carvedilol administration emphasize that the improvement in SC could reflect the improvement in precise myocardial function. In addition to the alleviation of DLVOTO, the following changes in loading conditions associated with carvedilol administration might have also contributed to the improvement in SC. First, the specific $\alpha_1$ receptors blockade of carvedilol might have contributed to further improvements in SC through the reduction of peripheral vascular resistance. Moreover, the decreased heart rate and prolonged diastole may have also promoted reduced myocardial oxygen consumption and improved coronary blood flow through the sinus of Valsalva. Studies on beta-blocker (metoprolol) treatment of

HCM with DLVOTO in humans have also reported that beta-blockers improve myocardial strain by decreasing DLVOTO at rest and during exercise, prolonging diastolic filling time and increasing myocardial fiber elasticity (35). Overall, carvedilol could theoretically reduce cardiac function due to its negative inotropic effect, but according to the results of this study and previous reports, it may be effective in cats with obstructive HCM with improved DLVOTO.

Among diastolic indices assessed by the 2D-STE, SrL A significantly increased after carvedilol administration. A previous study reported that speckle tracking-derived SrL E and SrL A are significantly decreased in cats with HCM compared to healthy controls (36). Although there was no significant increase in SrL E, the results of this study may suggest that carvedilol administration may have improved diastolic myocardial function, which is already reduced in cats with HCM. In addition, left atrial function is closely linked to LV diastolic function, and enhancement of left atrial function is thought to be a compensatory mechanism for the progression of LV diastolic dysfunction (37, 38). If left atrial pressure is in the normal range, atrial function is considered enhanced to maintain LV filling pressure. Therefore, it is possible that the significant SrL A reduction in this study may have eliminated the compensation for diastolic dysfunction.

In previous studies, tissue Doppler-derived *s*' and *e*' were significantly lower in the HCM cat groups treated with beta-blockers (atenolol) than in those treated with placebo (39). However, in the present study, there was no significant decrease in *s*' and *a*' after carvedilol administration. In addition, the 2D-STE in this study showed no declines in both the longitudinal systolic and diastolic function indices. Although the previous study did not note about DLVOTO, the improvement in DLVOTO by carvedilol administration observed in this study might have prevented the worsening of the tissue Doppler-derived indices through the alleviation of pressure overload. Furthermore, Atenolol is classified as a non-vasodilating beta-blocker and primarily reduces ventricular systolic function and cardiac output. Carvedilol, on the other hand, is classified as a vasodilating beta-blocker that decreases peripheral vascular resistance and increases cardiac output (40). These differences in mechanism of action may have led to the difference in results between atenolol and carvedilol. In addition, the method of 2D-STE overcomes the angle-dependent weakness of tissue Doppler and assesses not only local myocardial function, but also wall motion coordination, dyssynchrony, ischemia, and whole myocardial function (41). The improvement in SC in this study may reflect improved myocardial function for the reasons discussed above.

This study has several limitations. First, this study is a retrospective analysis of clinical cases. Furthermore, this study only included cats with obstructive HCM that had responded to carvedilol treatment. There are a certain number of cats that do not respond to carvedilol treatment. Therefore, the present results may not be applicable in such cases. Further studies are expected to evaluate the response rate of carvedilol to DLVOTO and the resulting improvement in clinical symptoms and survival period in a larger population. Additionally, this study included only cats with asymptomatic obstructive HCM (ACVIM stage B). Further studies are needed to evaluate the efficacy of carvedilol on cats with more progressed HCM. Second, the duration of carvedilol dosing and dosage in the study animals were not consistent and may have influenced the results of the study. In addition, medications already administered at the time of diagnosis could have affected the results. Third, this study did not perform a priori power calculation. A relatively small sample size of this study might affect statistical power. However, this study reported detailed myocardial function analysis in each case using the 2D-STE method. Fourth, this study did not perform the adjustment of statistical analysis. Therefore, there might be some type I error. Finally, this study was based on clinical rather than pathological diagnoses. In some cases, the diagnosis of cardiomyopathy may be incorrect or does not reflect the degree of myocardial damage.

In conclusion, DLVOTO in cats with obstructive HCM may worsen myocardial function assessed by layer-specific 2D-STE analysis. Carvedilol treatment may improve myocardial function, especially in the circumferential direction, without decreasing it. Although larger studies are needed, carvedilol may be a useful drug for improving myocardial function in cats with obstructive HCM.

## Data availability statement

The original contributions presented in the study are included in the article/supplementary material, further inquiries can be directed to the corresponding author.

## Ethics statement

The animal studies were approved by Nippon Veterinary and Life Science University Ethical Committee. The studies were conducted in accordance with the local legislation and institutional requirements. Written informed consent was obtained from the owners for the participation of their animals in this study.

## Author contributions

TS: Conceptualization, Validation, Visualization, Writing – original draft. RS: Conceptualization, Data curation, Funding acquisition, Investigation, Methodology, Project administration, Resources, Software, Supervision, Writing – review & editing. YY: Data curation, Visualization, Writing – review & editing. HF: Formal analysis, Investigation, Writing – original draft. SS: Writing – review & editing. TT: Writing – review & editing. HM: Writing – review & editing.

## Funding

The author(s) declare that financial support was received for the research and/or publication of this article. This research was partially supported by the Japan Society for the Promotion of Science (Grant Numbers: 20K15667 and 22K05995).

## Acknowledgments

This work was conducted at the Laboratory of Veterinary Internal Medicine, School of Veterinary Science, Faculty of Veterinary Medicine, Nippon Veterinary and Life Science University in Tokyo, Japan. We would also like to thank Editage (www.editage.com) for English language editing.

## Conflict of interest

The authors declare that the research was conducted in the absence of any commercial or financial relationships that could be construed as a potential conflict of interest.

## Generative AI Statement

The author(s) declare that no Gen AI was used in the creation of this manuscript.

## Publisher's note

All claims expressed in this article are solely those of the authors and do not necessarily represent those of their affiliated organizations, or those of the publisher, the editors and the reviewers. Any product that may be evaluated in this article, or claim that may be made by its manufacturer, is not guaranteed or endorsed by the publisher.

## References

1. Kittleson MD, Côté E. The Feline Cardiomyopathies: 2. Hypertrophic Cardiomyopathy. *J Feline Med Surg.* (2021) 23:1028–51. doi: 10.1177/1098612X211020162

2. Luis Fuentes V, Abbott J, Chetboul V, Côté E, Fox PR, Häggström J, et al. consensus statement guidelines for the classification, diagnosis, and management of cardiomyopathies in cats. *J Vet Intern Med.* (2020) 34:1062–77. doi: 10.1111/jvim.15745

3. Rush JE, Freeman LM, Fenollosa NK, Brown DJ. Population and survival characteristics of cats with hypertrophic cardiomyopathy: 260 cases (1990-1999). *J Am Vet Med Assoc.* (2002) 220:202–7. doi: 10.2460/javma.2002.220.202

4. Payne JR, Brodbelt DC, Luis Fuentes V. Cardiomyopathy prevalence in 780 apparently healthy cats in rehoming centres (the CatScan study). *J Vet Cardiol.* (2015) 17:S244–57. doi: 10.1016/j.jvc.2015.03.008

5. Paige CE, Abbott JA, Elvinger F, Pyle RL. Prevalence of cardiomyopathy in apparently healthy cats. *J Am Vet Med Assoc.* (2009) 234:1398–403. doi: 10.2460/javma.234.11.1398

6. Fox PR, Keene BW, Lamb K, Schober KA, Chetboul V, Luis Fuentes V, et al. International collaborative study to assess cardiovascular risk and evaluate long-term health in cats with preclinical hypertrophic cardiomyopathy and apparently healthy cats: the REVEAL study. *J Vet Intern Med.* (2018) 32:930–43. doi: 10.1111/jvim.15122

7. Fox PR. Hypertrophic cardiomyopathy. Clinical and pathologic correlates. *J Vet Cardiol.* (2003) 5:39–45. doi: 10.1016/S1760-2734(06)70051-0

8. Nishimura RA, Holmes DR. Clinical practice. Hypertrophic obstructive cardiomyopathy. *N Engl J Med.* (2004) 350:1320–7. doi: 10.1056/NEJMcp030779

9. Authors/Task Force members, Elliott PM, Anastasakis A, Borger MA, Borggrefe M, Cecchi F, et al. 2014 ESC Guidelines on diagnosis and management of hypertrophic cardiomyopathy: the Task Force for the Diagnosis and Management of Hypertrophic Cardiomyopathy of the European Society of Cardiology (ESC). *Eur Heart J.* (2014) 35:2733–79. doi: 10.1093/eurheartj/ehu284

10. Saito T, Suzuki R, Yuchi Y, Fukuoka H, Satomi S, Teshima T, et al. Comparative study of myocardial function in cases of feline hypertrophic cardiomyopathy with and without dynamic left-ventricular outflow-tract obstruction. *Front Vet Sci.* (2023) 10:1191211. doi: 10.3389/fvets.2023.1191211

11. Jackson BL, Adin DB, Lehmkuhl LB. Effect of atenolol on heart rate, arrhythmias, blood pressure, and dynamic left ventricular outflow tract obstruction in cats with subclinical hypertrophic cardiomyopathy. *J Vet Cardiol.* (2015) 17:S296–305. doi: 10.1016/j.jvc.2015.03.002

12. Suzuki R, Mochizuki Y, Yoshimatsu H, Ohkusa T, Teshima T, Matsumoto H, et al. Myocardial torsional deformations in cats with hypertrophic cardiomyopathy using two-dimensional speckle-tracking echocardiography. *J Vet Cardiol.* (2016) 18:350–7. doi: 10.1016/j.jvc.2016.06.004

13. Visser LC, Sloan CQ, Stern JA. Echocardiographic assessment of right ventricular size and function in cats with hypertrophic cardiomyopathy. *J Vet Intern Med.* (2017) 31:668–77. doi: 10.1111/jvim.14688

14. Gomez-Doblas JJ, Schor J, Vignola P, Weinberg D, Traad E, Carrillo R, et al. Left ventricular geometry and operative mortality in patients undergoing mitral valve replacement. *Clin Cardiol.* (2001) 24:717–22. doi: 10.1002/clc.4960241106

15. Dini FL, Capozza P, Donati F, Simioniuc A, Corciu AI, Fontanive P, et al. Patterns of left ventricular remodeling in chronic heart failure: prevalence and prognostic implications. *Am Heart J.* (2011) 161:1088–95. doi: 10.1016/j.ahj.2011.03.027

16. Suzuki R, Mochizuki Y, Yoshimatsu H, Niina A, Teshima T, Matsumoto H, et al. Early detection of myocardial dysfunction using two-dimensional speckle tracking echocardiography in a young cat with hypertrophic cardiomyopathy. *J Feline Med Surg Open Rep.* (2018) 4:205511691875621. doi: 10.1177/2055116918756219

17. Suzuki R, Mochizuki Y, Yuchi Y, Yasumura Y, Saito T, Teshima T, et al. Assessment of myocardial function in obstructive hypertrophic cardiomyopathy cats with and without response to medical treatment by carvedilol. *BMC Vet Res.* (2019) 15:1–8. doi: 10.1186/s12917-019-2141-0

18. Suzuki R, Mochizuki Y, Yoshimatsu H, Teshima T, Matsumoto H, Koyama H. Determination of multidirectional myocardial deformations in cats with hypertrophic cardiomyopathy by using two-dimensional speckle-tracking echocardiography. *J Feline Med Surg.* (2017) 19:1283–9. doi: 10.1177/1098612X17691896

19. Suzuki R, Mochizuki Y, Yoshimatsu H, Niina A, Teshima T, Matsumoto H, et al. Layer-specific myocardial function in asymptomatic cats with obstructive hypertrophic cardiomyopathy assessed using 2-dimensional speckle-tracking echocardiography. *J Vet Intern Med.* (2019) 33:37–45. doi: 10.1111/jvim.15339

20. Suzuki R, Matsumoto H, Teshima T, Koyama H. Noninvasive clinical assessment of systolic torsional motions by two-dimensional speckle-tracking echocardiography in dogs with myxomatous mitral valve disease. *J Vet Intern Med.* (2013) 27:69–75. doi: 10.1111/jvim.12024

21. Suzuki R, Yuchi Y, Kanno H, Teshima T, Matsumoto H, Koyama H. Left and right myocardial functionality assessed by two-dimensional speckle-tracking echocardiography in cats with restrictive cardiomyopathy. *Animals.* (2021) 11:1578. doi: 10.3390/ani11061578

22. Schober KE, Zientek J, Li X, Fuentes VL, Bonagura JD. Effect of treatment with atenolol on 5-year survival in cats with preclinical (asymptomatic) hypertrophic cardiomyopathy. *J Vet Cardiol.* (2013) 15:93–104. doi: 10.1016/j.jvc.2013.03.003

23. Zhou Q, Xiao J, Jiang D, Wang R, Vembaiyan K, Wang A, et al. Carvedilol and its new analogs suppress arrhythmogenic store overload-induced $Ca2+$ release. *Nat Med.* (2011) 17:1003–9. doi: 10.1038/nm.2406

24. Feuerstein G, Yue TL, Ma X, Ruffolo RR. Novel mechanisms in the treatment of heart failure: inhibition of oxygen radicals and apoptosis by carvedilol. *Prog Cardiovasc Dis.* (1998) 41:17–24. doi: 10.1016/S0033-0620(98)80027-3

25. Brunvand H, Kvitting PM, Rynning SE, Berge RK, Grong K. Carvedilol protects against lethal reperfusion injury through antiadrenergic mechanisms. *J Cardiovasc Pharmacol.* (1996) 28:409–17. doi: 10.1097/00005344-199609000-00010

26. Gordon SG, Saunders AB, Hariu CD, Boggess MM, Miller MW. Retrospective review of carvedilol administration in 38 dogs with preclinical chronic valvular heart disease. *J Vet Cardiol.* (2012) 14:243–52. doi: 10.1016/j.jvc.2012.01.007

27. Mochizuki Y, Suzuki R, Yasumura Y, Saito T, Teshima T, Matsumoto H, et al. Left ventricular geometric characteristics predict response to carvedilol in cats with asymptomatic hypertrophic obstructive cardiomyopathy caused by systolic anterior motion of the mitral valve. *J Vet Med Sci.* (2019) 81:734–8. doi: 10.1292/jvms.18-0718

28. Pollick C, Rakowski H, Wigle ED. Muscular subaortic stenosis: the quantitative relationship between systolic anterior motion and the pressure gradient. *Circulation.* (1984) 69:43–9. doi: 10.1161/01.CIR.69.1.43

29. Maron MS, Olivotto I, Betocchi S, Casey SA, Lesser JR, Losi MA, et al. Effect of left ventricular outflow tract obstruction on clinical outcome in hypertrophic cardiomyopathy. *N Engl J Med.* (2003) 348:465–6. doi: 10.1056/NEJMoa021332

30. Okada K, Yamada S, Iwano H, Nishino H, Nakabachi M, Yokoyama S, et al. Myocardial shortening in 3 orthogonal directions and its transmural variation in patients with nonobstructive hypertrophic cardiomyopathy. *Circ J.* (2015) 79:2471–9. doi: 10.1253/circj.CJ-15-0646

31. Wess G, Sarkar R, Hartmann K. Assessment of left ventricular systolic function by strain imaging echocardiography in various stages of feline hypertrophic cardiomyopathy. *J Vet Intern Med.* (2010) 24:1375–82. doi: 10.1111/j.1939-1676.2010.0586.x

32. Carasso S, Yang H, Woo A, Vannan MA, Jamorski M, Wigle ED, et al. Systolic myocardial mechanics in hypertrophic cardiomyopathy: novel concepts and implications for clinical status. *J Am Soc Echocardiogr.* (2008) 21:675–83. doi: 10.1016/j.echo.2007.10.021

33. Liu H, Pozios I, Haileselassie B, Nowbar A, Sorensen LL, Phillip S, et al. Role of global longitudinal strain in predicting outcomes in hypertrophic cardiomyopathy. *Am J Cardiol.* (2017) 120:670–5. doi: 10.1016/j.amjcard.2017.05.039

34. Mizuguchi Y, Oishi Y, Miyoshi H, Iuchi A, Nagase N, Oki T. The functional role of longitudinal, circumferential, and radial myocardial deformation for regulating the early impairment of left ventricular contraction and relaxation in patients with cardiovascular risk factors: a study with two-dimensional strain imaging. *J Am Soc Echocardiogr.* (2008) 21:1138–44. doi: 10.1016/j.echo.2008.07.016

35. Dybro AM, Rasmussen TB, Nielsen RR, Pedersen ALD, Andersen MJ, Jensen MK, et al. Metoprolol improves left ventricular longitudinal strain at rest and during exercise in obstructive hypertrophic cardiomyopathy. *J Am Soc Echocardiogr.* (2023) 36:196–204. doi: 10.1016/j.echo.2022.09.008

36. Sugimoto K, Fujii Y, Sunahara H, Aoki T. Assessment of left ventricular longitudinal function in cats with subclinical hypertrophic cardiomyopathy using tissue Doppler imaging and speckle tracking echocardiography. *J Vet Med Sci.* (2015) 77:1101–8. doi: 10.1292/jvms.14-0354

37. Cioffi G, Mureddu GF, Stefenelli C, De Simone G. Relationship between left ventricular geometry and left atrial size and function in patients with systemic hypertension. *J Hypertens.* (2004) 22:1589–96. doi: 10.1097/01.hjh.0000125454.28861.76

38. Sun JP, Yang Y, Guo R, Wang D, Lee AP-W, Wang XY, et al. Left atrial regional phasic strain, strain rate and velocity by speckle-tracking echocardiography: normal values and effects of aging in a large group of normal subjects. *Int J Cardiol.* (2013) 168:3473–9. doi: 10.1016/j.ijcard.2013.04.167

39. Sugimoto K, Aoki T, Fujii Y. Effects of atenolol on left atrial and left ventricular function in healthy cats and in cats with hypertrophic cardiomyopathy. *J Vet Med Sci.* (2020) 82:546–52. doi: 10.1292/jvms.19-0670

40. Shah NK, Smith SM, Nichols WW, Lo MC, Ashfaq U, Satish P, et al. Carvedilol reduces aortic wave reflection and improves left ventricular/vascular coupling: a comparison with atenolol (CENTRAL Study). *J Clin Hypertens (Greenwich).* (2011) 13:917–24. doi: 10.1111/j.1751-7176.2011.00549.x

41. Voigt JU, Pedrizzetti G, Lysyansky P, Marwick TH, Houle H, Baumann R, et al. Definitions for a common standard for 2D speckle tracking echocardiography: consensus document of the EACVI/ASE/Industry Task Force to standardize deformation imaging. *J Am Soc Echocardiogr.* (2015) 28:183–93. doi: 10.1016/j.echo.2014.11.003

frontiers | Frontiers in Veterinary Science

TYPE Original Research
PUBLISHED 21 May 2025
DOI 10.3389/fvets.2025.1548417



OPEN ACCESS

EDITED BY
Massimo Giunti,
University of Bologna, Italy

REVIEWED BY
Andrea Armenise,
Ultrasonography and Cardiology Advisor, Italy
Mark Dirven,
Ictuscordis, Sweden
Elodie Darnis,
CHV Frégis, France

*CORRESPONDENCE
Nicolas Graziano
✉ nicolas.graziano@uliege.be

RECEIVED 19 December 2024
ACCEPTED 14 April 2025
PUBLISHED 21 May 2025

CITATION
Graziano N, Gommeren K, Valcke A, Burnotte P, Beeston D, Walker T, Gele R, Lekane M and Merveille AC (2025) Retrospective evaluation of left ventricular eccentricity index in the assessment of precapillary pulmonary hypertension in dogs (2017–2021): 145 cases.
*Front. Vet. Sci.* 12:1548417.
doi: 10.3389/fvets.2025.1548417



# Retrospective evaluation of left ventricular eccentricity index in the assessment of precapillary pulmonary hypertension in dogs (2017–2021): 145 cases

Nicolas Graziano[1]*, Kris Gommeren[1], Annelies Valcke[1], Priscilla Burnotte[1], Dave Beeston[2], Tom Walker[3], Rebecca Gele[3], Marine Lekane[1] and Anne Christine Merveille[1]

[1]Department of Small Animal Clinical Science, Faculty of Veterinary Medicine, University of Liège, Liège, Belgium, [2]Willows Veterinary Centre and Referral Services, Solihull, United Kingdom, [3]Emergency and Critical Care, BluePearl Veterinary Specialists, Sandy Springs, GA, United States

**Objective:** To determine interobserver variability of left ventricular eccentricity indices measurements in systole (EIs), diastole (EId) and at maximum flattening (EIm) by emergency and critical care residents on prerecorded cineloops in dogs with or without pulmonary hypertension. To assess whether these EI measurements allow to identify dogs with right heart changes compatible with moderate to severe pulmonary hypertension (PAH).

**Methods:** Multicenter, retrospective, case–control study from 2017 to 2021. Medical records of dogs with stage B1 myxomatous mitral valve disease (MMVD) and dogs diagnosed with precapillary pulmonary hypertension (PCPH) via echocardiograms were reviewed. Dogs were categorized by a cardiologist into five groups (normal, B1 MMVD, mild, moderate, and severe PCPH) based on Doppler pulmonary pressure gradients and right heart morphology. Four blinded emergency and critical care residents measured EIs, EId and EIm.

**Results:** One hundred and forty-five client-owned dogs were included. Interobserver agreement was strong, with an intraclass correlation coefficient (ICC) of 0.737 (95% CI: 0.621–0.852) across all eccentricity indices for the full study population and 0.768 (0.642–0.856) for the PAH group specifically. EIs, EId, and EIm were significantly higher in the PAH group compared to control and MMVD groups ($p < 0.0001$). The differentiation between moderate-to-severe and mild/absent PAH by EIs, EId, and EIm resulted in AUCs of 0.738, 0.834, and 0.766, with cut-off values of 1.40, 1.34, and 1.28, respectively. A gray zone approach identified 90% sensitivity for EIs (1.12), EId (1.15), and EIm (1.23), and specificity for EIs (2.27), EId (1.32), and EIm (2.1) to rule out or diagnose moderate-to-severe PAH.

**Conclusions:** This study showed good inter-observer agreement of EIs, EIm, and EId measurement by ECC residents on prerecorded loops. EI allowed good identification of dogs with moderate to severe PAH by ECC residents.

KEYWORDS

**echocardiography, eccentricity index, pulmonary arterial hypertension, point-of-care ultrasound (POCUS), emergency**

## Introduction

Pulmonary arterial hypertension (PAH) is defined as an abnormally increased arterial pressure within the pulmonary vasculature (1). In human medicine, PAH refers to a pulmonary arterial pressure (PAP) $\geq$ 20 mmHg at rest, ideally measured by direct right heart catheterization (2). PAH may result from various diseases, either due to increased blood flow within the capillaries, increased pulmonary vascular resistance (precapillary PAH), and/or increased downstream resistance [postcapillary pulmonary venous hypertension (PVH)] (3). Precapillary pulmonary hypertension (PCPH) is defined as elevated pulmonary arterial pressure with a normal pulmonary arterial wedge pressure. It can arise because of various underlying conditions, such as parenchymal lung disorders, chronic hypoxia, thromboembolic events, or parasitic infections. In contrast, postcapillary pulmonary hypertension is characterized by both elevated pulmonary arterial pressure and elevated wedge pressure, typically resulting from left-sided heart disease (1–3).

PAH is a complex syndrome that often leads to changes in the right side of the heart, which can progress to right-sided heart failure and death (4). PAH can cause the interventricular septum to flatten and shift toward the left ventricle, affecting left ventricular function, a process referred to as ventricular interdependence. The flattening of the interventricular septum occurs secondary to pressure overload during systole and volume overload during diastole of the right ventricle (5–7). During systole, increased pulmonary arterial pressure leads to right ventricular pressure overload. This elevated pressure causes the septum to bow toward the left ventricle, flattening its normal curvature. In diastole, volume overload due to right ventricular dilation contributes to septal flattening, as the enlarged chamber displaces the septum even when the pressure gradient is lower (5–7). The severity of this septal flattening has been shown to be associated with outcomes in human patients with PAH (1).

EI quantifies the degree of septal flattening (7). EI is calculated as the ratio of the diameter of the left ventricle parallel to the septum to the diameter of the left ventricle perpendicular to the septum.

The EI can be calculated at different time points during the cardiac cycle, namely end-systole (EIs), end-diastole (EId) (8), and at the time of maximal septal flattening (EIm) (9, 10). To capture the maximal septal flattening associated with ventricular interdependence, EI can also be measured at the time when the left ventricle (LV) appears most compressed—that is, when the ratio of the cranio-caudal to latero-lateral LV diameter is greatest, known as EIm (9).

In pulmonary arterial hypertension (PAH), the high resistance of the pulmonary vasculature causes the right ventricle (RV) to contract for a longer period with a smaller ejection volume, impairing LV filling. This results in prolonged RV systole or isovolumic relaxation, leading to a significant delay in RV diastolic inflow compared to the LV (6). Consequently, in PAH, the RV may still be contracting while the LV is already relaxing, causing late maximal septal flattening, with EIm occurring slightly after EIs (9, 10). When there is no additional septal displacement after end-systole, EIs and EIm are (almost) equal (9).

In human medicine, although all EI measurements correlate with invasive hemodynamic parameters, EIm shows the strongest correlation (9). Furthermore, EI correlates with PAH severity and has demonstrated high inter-observer agreement, making it a convenient and reliable non-invasive tool for diagnosing and monitoring PAH (9, 11, 12).

Treatment with sildenafil is recommended for dogs presenting with moderate to severe PAH, underscoring the interest of timely recognition of this condition by emergency clinicians. Cardiac point-of-care ultrasound (POCUS), also called focused cardiac ultrasound (FOCUS), has been proposed as a rapid, bedside method for assessing PAH in dogs without advanced left sided heart disease or other right-sided cardiac conditions (13, 14, 27). A subjective scoring system, utilizing either 8 or 10 points, has been described. These scores evaluate a combination of echocardiographic signs, notably right atrial and ventricular enlargement, right ventricular hypertrophy, interventricular septal flattening, and enlargement of the pulmonary artery and trunk to calculate the composite (PHS8), as well as the presence of peritoneal effusion and/or dilation of the caudal vena cava—(PHS10) (14, 15). FOCUS assesses key aspects of cardiac function through three fundamental views, one of which is the right parasternal short axis at the level of the papillary muscle. EI, measured in this view, necessitates only a single window, as opposed to the 8- or 10-point scoring systems, which require multiple views. EI might therefore serve as a more straightforward and accessible marker of PAH for general practitioners and emergency clinicians.

Our group recently reported EI in dogs with PAH assessed by a single cardiologist (16), but the inter-observer agreement between emergency and critical care (ECC) residents and potential impact of concurrent cardiac morphological changes have not been studied in veterinary medicine. ECC residents were selected due to their role in the initial assessment of critically ill patients and for evaluation of the feasibility of EI measurements by non-cardiologist. Early identification of PAH in emergency settings may enhance patient triage and enable timely initiation of treatment, potentially leading to improved morbidity and mortality. The primary aim of this study was to assess inter-observer agreement of EIs, EId, and EIm among four small animal emergency and critical care residents in dogs with PAH, dogs with ACVIM B1 mitral valve disease without PAH, and dogs without cardiac disease. The secondary aim was to evaluate the ability of EIs, EId, and EIm to predict the presence of moderate to severe PAH.

## Materials and methods

### Population

Medical records of dogs undergoing echocardiography between 2017 and 2021 at a referral hospital and small animal teaching hospital were reviewed. Dogs were included if they had a final diagnosis of precapillary pulmonary hypertension (PCPH) confirmed by a board-certified cardiologist after full diagnostic echocardiography and had available cineloops. Dogs were excluded if they had any left- or right-sided cardiac disease other than ACVIM stage B1 myxomatous mitral valve disease (MMVD) or presumed precapillary pulmonary hypertension (PCPH). These dogs were excluded, as such modifications could have influenced EI measurements. There was no exclusions for missing data or poor image quality.

## Echocardiography

Transthoracic 2D echocardiography, M-mode echocardiography, and conventional Doppler echocardiography was performed by two board-certified veterinary cardiologists according to the recommendations of the Echocardiography Committee of the Specialty of Cardiology, American College of Veterinary Internal Medicine, using two different ultrasound units.[1] Dogs were placed in right and left lateral recumbency, and a simultaneous one-lead echocardiogram was recorded. PAH was diagnosed and categorized retrospectively on cineloops, with cardiologists blinded to other clinical data, based on the presence of an elevated tricuspid regurgitation pressure gradient (TRPG: $> 30$ and $< 50$ mmHg for mild PAH, $\geq 50$ and $< 75$ mmHg for moderate PAH, and $\geq 75$ mmHg for severe PAH) or an elevated pulmonic regurgitation pressure gradient (PRPG: $\geq 20$ and $< 25$ mmHg for mild PAH, $\geq 25$ and $< 35$ mmHg for moderate PAH, and $\geq 35$ mmHg for severe PAH) and indirect echocardiographic evidence of PAH. Indirect parameters were assessed at three different levels, similarly to the approach described in the ACVIM consensus statement. More specifically, pulmonary artery size (main and right branches), right ventricular size and thickness, as well as right atrial dimensions were subjectively and quantitatively evaluated in all dogs (3, 12, 17). Dogs with pulmonary arterial hypertension were included only if no left atrial dilation was present, in order to exclude postcapillary hypertension. Included dogs were divided into different groups according to Doppler echocardiographic evidence of PAH: Mild PAH group, moderate PAH group and severe PAH group. Two control groups were also included: healthy dogs with or without Doppler derived estimates of PA pressure, and dogs with ACVIM B1 MMVD and a normal pulmonary pressure gradient.

The following parameters were recorded: patient age (years), weight (kg), sex, breed, group (control, PAH, MMVD), tricuspid regurgitation pressure gradient in mmHg (TRPG), pulmonic insufficiency pressure gradient in mmHg (PRPG), and severity of the PAH.

## EI assessment

Four small animal ECC with no prior echocardiography experience underwent a short online training course (1.5 h) on EIs, EId, and EIm assessment, delivered by a board-certified cardiologist (ACM). No formal performance assessment was conducted post-training. All residents reviewed the cineloops and were blinded to patient signalment, name, and study group (PH case vs. normal vs. B1 MMVD). Each observer individually and retrospectively performed a single measurement of EIs, EId, and EIm on each case on the transventricular right parasternal short axis cineloop at the level of the papillary muscle, as previously described by Lekane et al. (Figure 1). An electrocardiogram was used to measure EIs (at the end of the T wave) and EId (at the peak of the QRS complex), as ECG-based timing is an objective and standardized method commonly used in cardiology and provides a quality control measure to ensure consistency and reproducibility. EIm was assessed at the subjective maximal downward motion of the interventricular septum.

## Statistical methods

Inter-observer variability was assessed on four measurements for each parameter on all dogs included in the study. To measure the agreement between observers for the EIs, EId, and EIm, the intra-class correlation coefficient was calculated along with its 95% confidence interval. This was done globally and by group, between each pair of observers, and among the four observers. Results were considered significant at the 5% significance level ($P < 0.05$). Receiver operator characteristic curve analyses were performed to determine optimal cut-off values of EId, EIs and EIm to detect moderate and severe PAH. A gray-zone approach was also applied to establish cutoff values with 90% sensitivity and specificity for EId, EIs, and EIm in detecting moderate and severe PAH. Results are presented as means and standard deviations (SD) for normally distributed data, medians and quartiles for non-normally distributed data. Comparisons between groups were done by a Chi-square test for qualitative parameters and with ANOVA for quantitative parameters with the Scheffe *post-hoc* test. All statistical analyses were carried out using SAS version 9.4 (SAS Institute, Cary, NC, USA). Statistical significance was set at $P < 0.05$.

# Results

## Patient population

Cineloops of 145 dogs were available for review and included in the study: 27 dogs without underlying heart disease (normal echocardiogram - control group), 30 dogs with stage B1 MMVD without PAH, and 88 patients with PCPH. The population demographic data is shown in Table 1. In the control group, the most common breeds included the Boxer (3), Chihuahua (2), and Vizsla (2). The median age and weight were 6.0 years (0.25–12) and 23.8 kg (2.0–48.1). The most common breeds with stage B1 MMVD included King Charles Cavalier Spaniel (6), Shih tzu (3), and Dachshund (2), Border collie (2), Australian shepherd (2), and Maltese (2). The median age and weight were 10 years (3.0–18.0) and 9.85 kg (3.3–43.6). The most common breeds with PCPH were Chihuahua (16), Shih tzu (11), Jack Russell Terrier (6), Labrador Retriever (4), Toy Poodle (3), Yorkshire Terrier (3), French Bulldog (3), Pug (3), and mixed breed dogs (6). The median age and weight were 12 years (0.4–18) and 7.2 kg (2.3–37). Dogs in the control group were significantly younger and heavier than dogs in the other groups (PAH and MMVD) ($P < 0.001$). PAH was categorized as

1 GE vivid E95 equipped with 2.2–3.5 and 5.5–7.5 and 1.4–4.6 and 2.4–8.0 MHz phased-array transducers and a Phillips Epiq 7 equipped with 12-4, 8-3, and 5-1 MHz traducers.

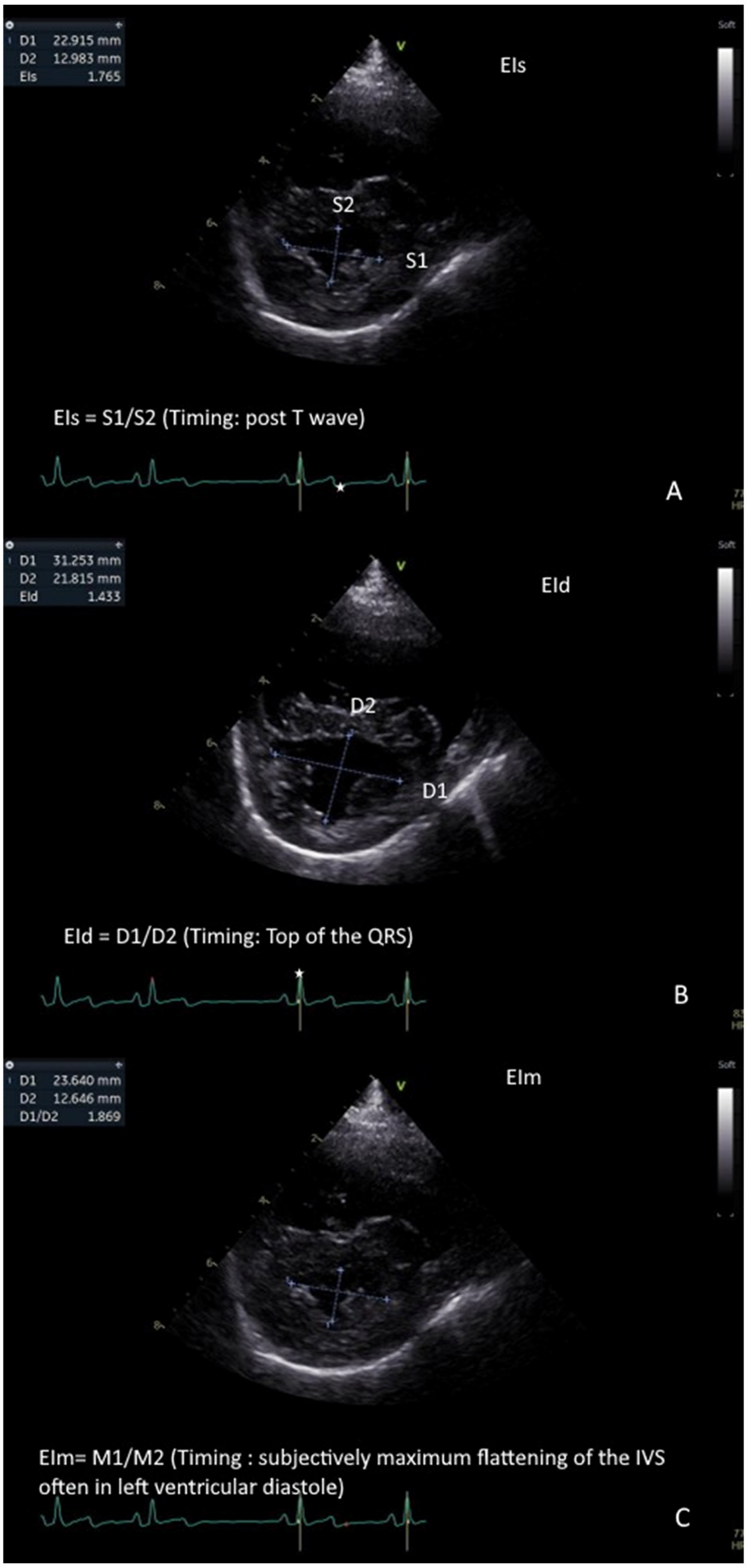


FIGURE 1
Measurement of eccentricity indices: Left ventricular eccentricity index measured at end-systole (EIs) is measured at the end of the T wave (represented as a white star on the ECG). This represents the ratio of the craniocaudal diameter of the left ventricle in systole (S1) on the latero-lateral diameter of the left ventricle in systole (S2). EIs ¼ S1/S2. **(A)**. left ventricular eccentricity index measured at end-diastole (EId) is measured at the peak of the QRS complex wave (represented as a white star on the ECG). This represents the ratio of the cranio-caudal diameter of the left ventricle in diastole (D1) on the latero-lateral diameter of the left ventricle in diastole (D2). EId ¼ D1/D2. **(B)**. Left ventricular eccentricity index measured at maximal septal flattening (EIm) is measured at the maximal interventricular septal flattening. This represents the ratio of the cranio-caudal diameter of the left ventricle (M1) on the latero-lateral diameter of the left ventricle (M2). EIm ¼ M1/M2. **(C)**.

TABLE 1 Represented demographic data for the dogs in the control group, Pulmonary hypertension (PAH) and Myxomatous mitral valve disease group (MMVD).

| | Control | PAH | | | MMVD |
|---|---|---|---|---|---|
| | | Mild | Moderate | Severe | |
| Number of dogs | 27/145 | 17/145 | 33/145 | 38/145 | 30/145 |
| Age [median (range)] | 6.0 (0.25–12.0) | 11.5 (0.4–15) | 12 (4–15.1) | 11.6 (2–18) | 10.0 (6.0–18.0) |
| Weight [median (range)] | 23.8 (2.0–48.1) | 9 (3.3–40) | 6.5 (2.3–30.5) | 7.3 (2.6- 37) | 9.85 (3.3–44.0) |
| Male intact | 6 | 3 | 5 | 4 | 1 |
| Male neutered | 14 | 9 | 14 | 15 | 9 |
| Female intact | 3 | 0 | 7 | 9 | 5 |
| Female neutered | 4 | 5 | 7 | 10 | 15 |

Data are expressed as median and range.

mild in 19.3% (17/88), moderate in 35.2% (31/88), and severe in 45.5% (40/88) of the PAH group.

## Inter-operator agreement

Eccentricity indexes showed consistent agreement between each observer and every other observer in pairs (Figure 2), as well as among all observers for EIs, EId, and EIm, for both the entire population and the PAH group specifically. The median (Q1–Q3) ICC was 0.768 (0.642–0.856) for the whole population and 0.737 (0.621–0.852) for the PAH group. There was a low ICC for all observers in the MMVD group for EIs 0.304 (0.159–0.533), EId 0.530 (0.419–0.711), and EIm 0.281 (0.138–0.504).

## Eccentricity indexes in different groups

EIs, EIm, and EId values were significantly higher ($p$-value $< 0.0001$) in the PAH group for EIs (1.17 ± 0.19), EIm (2.13 ± 1.39), and EId (1.52 ± 0.49) compared to the MMVD [EIs (1.19 ± 0.24), EIm (1.22 ± 0.31), and EId (1.20 ± 0.12)] and control group [EIs (1.17 ± 0.19), EIm (1.18 ± 0.20), and EId (1.18 ± 0.11)] (Figure 3). Patients with moderate to severe PAH had significantly higher ($p$-value 0.0014) EIs, EIm, and EId compared to dogs with mild or absent PAH (Figure 3).

## Receiver operating curves

All EI were significantly correlated with the presence of PAH. Receiver operating curves showed an AUC of 0.738 for Eis, 0.834 for Eid, and 0.766 for EIm. The Youden index values for EIs (1.28), EId (1.40), and EIm (1.34) discriminated moderate-to-severe pulmonary arterial hypertension (PAH) from mild or no PAH, with sensitivity and specificity of 77.3 and 72.7%; 65.2 and 100%; and 77.3 and 77.3% for EIs, EId, and EIm, respectively (see Figure 4). A gray zone approach (Figure 5) indicates a 90% specificity and sensitivity for moderate-to-severe PAH of EIs, EId and EIm at values of 2.27 and 1.12; 1.32 and 1.15; and 2.1 and 1.23, respectively.

# Discussion

This study shows good ICC for EI measurement by ECC residents on prerecorded cineloops of EId, EIs, and EIm. Measures were different in moderate to severe PAH compared to normal dogs and MMVD B1.

Breed distribution was not balanced across our study population, which may have introduced a degree of variability in the measurements. Moreover, dogs in the control group were significantly younger and heavier. This is likely because a significant number of the dogs in the control group were presented for cardiac screening for breeding which probably accounts for the age difference in this group. Cardiac screening for breeding is mainly performed for diseases such as dilated cardiomyopathy, whereas screening for murmur investigation also included dogs with aortic stenosis and tricuspid dysplasia, conditions for which medium to large breed dogs are predisposed, which probably explains the heavier weight of the control group. In human medicine, similar EI cutoff values have been reported for both adult and pediatric patients. However, differences are observed in neonatal patients, suggesting that age and body weight have minimal influence on EI measurements beyond the first year of life (18). A previous veterinary cardiological study does not suggest an impact of age and weight on EI measurements (16). That said, the focus of our study was not to assess whether age and weight impact EI measurements.

The inter-observer agreement was good, with an ICC of 0.737 (0.621–0.852). The ICC for the EI was higher in one human study. The observers in these papers were however cardiologists, whereas our study was conducted by ECC residents. The higher inter-observer agreement between cardiologists could therefore be expected (9). Inter-observer agreement was good in both the PAH and control groups but was only fair in the MMVD group for all eccentricity indexes. Dogs with MMVD B1, even at a mild stage, tend to have a higher median shortening fraction compared to the reference range (19). The authors hypothesize that this increased contractility, or more kinetic profile may have impacted EI measurements. In a different study the Pulmonary Hypertension Score (PHS) appeared to be unaffected by the presence of concurrent cardiac disease when screening for PAH (13). Based on our findings, the EI should probably be interpreted with caution in dogs with

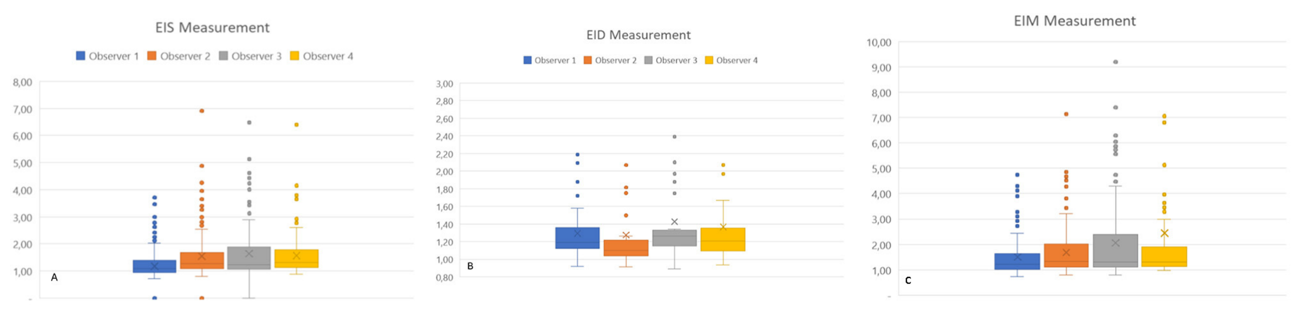


FIGURE 2
Eccentricity index measurements of individual observers for all groups. EIs: left ventricular eccentricity index measured at end-systole **(A)**. EId: left ventricular eccentricity index measured at end-diastole **(B)**; EIm: left ventricular eccentricity index measured at maximal septal flattening **(C)**.

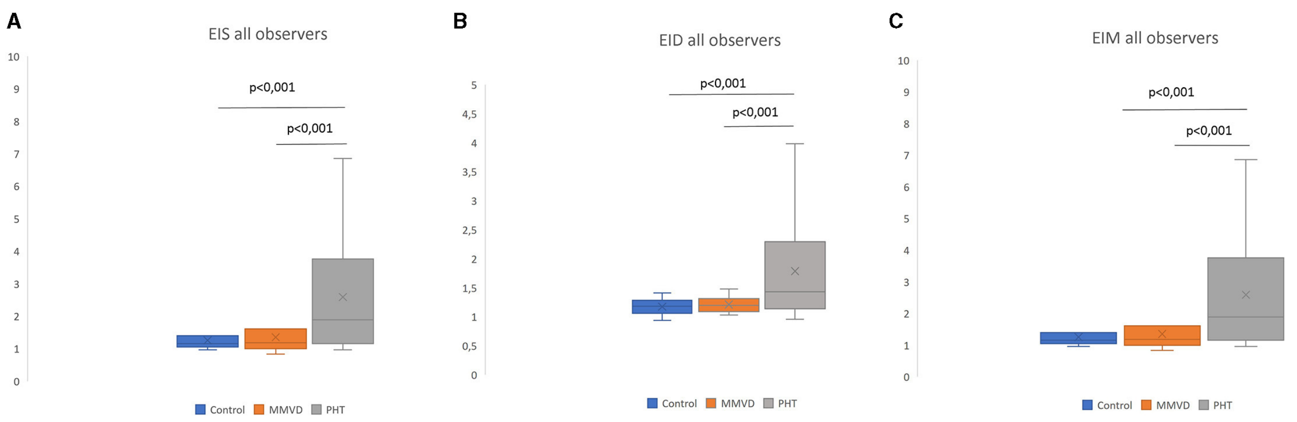


FIGURE 3
Eccentricity index among different groups (average of all observers). EIs: left ventricular eccentricity index measured at end-systole **(A)**. EId: left ventricular eccentricity index measured at end-diastole **(B)**; EIm: left ventricular eccentricity index measured at maximal septal flattening **(C)**.

concurrent cardiac disease, and the PHS may be preferrable in this setting.

Either EId, EIs, or EIm were significantly increased in dogs with PAH compared to dogs without PAH, and these values were significantly higher in dogs with moderate to severe PAH compared to dogs with mild or absent PAH. We did not aim to identify mild cases of PAH compared to the control group, as our primary objective was to support ECC clinicians in the early recognition and management of moderate to severe forms. Mild PAH cases are typically stable enough to undergo a more complete cardiac work-up at a later stage, such as the following day. Importantly, a previous study conducted by cardiologists demonstrated that the left ventricular eccentricity index was not effective in detecting mild pulmonary hypertension, supporting the idea that interventricular septal flattening becomes apparent only in more advanced disease (20).

Furthermore, EId, EIs, and EIm were significantly higher in the PAH group compared to the two control groups. EI was strongly correlated with the presence of PAH, with EId emerging as the best marker. A prior study demonstrated that EId was notably elevated in dogs with severe PAH. EId is measured when the pulmonary valve is closed, reflecting increased RV end-diastolic pressure secondary to RV failure suggesting a more pronounced impairment of right ventricular function with significant diastolic dysfunction (16).

The gray zone approach identified a cut-off of 2.27, 2.1, and 1.27 for EIs, EIm and EId, respectively, to diagnose moderate to severe PAH with 90% specificity. This cut-off may be of clinical relevance in the absence of further cardiological work-up, allowing to commence PAH therapy. Values inferior to 1.12, 1.23, and 1.27 for EIs, EIm and EId, respectively, allow the clinician to rule out moderate to severe PAH with 90% sensitivity suggesting to withhold therapy until further cardiological workup is available. The use of a gray zone approach based on 90% sensitivity and specificity thresholds has been previously used in human studies to define clinically useful diagnostic cut-offs with acceptable levels of uncertainty (15).

The Youden index identified cut-off values of 1.28, 1.40, and 1.34 for EIs, EIm and EId, respectively, to distinguish moderate-to-severe PAH from mild or no PAH. This cut-off value is comparable to those reported in a previous study conducted by cardiologists and to cut-off used in human infant to diagnose PAH (20, 21).

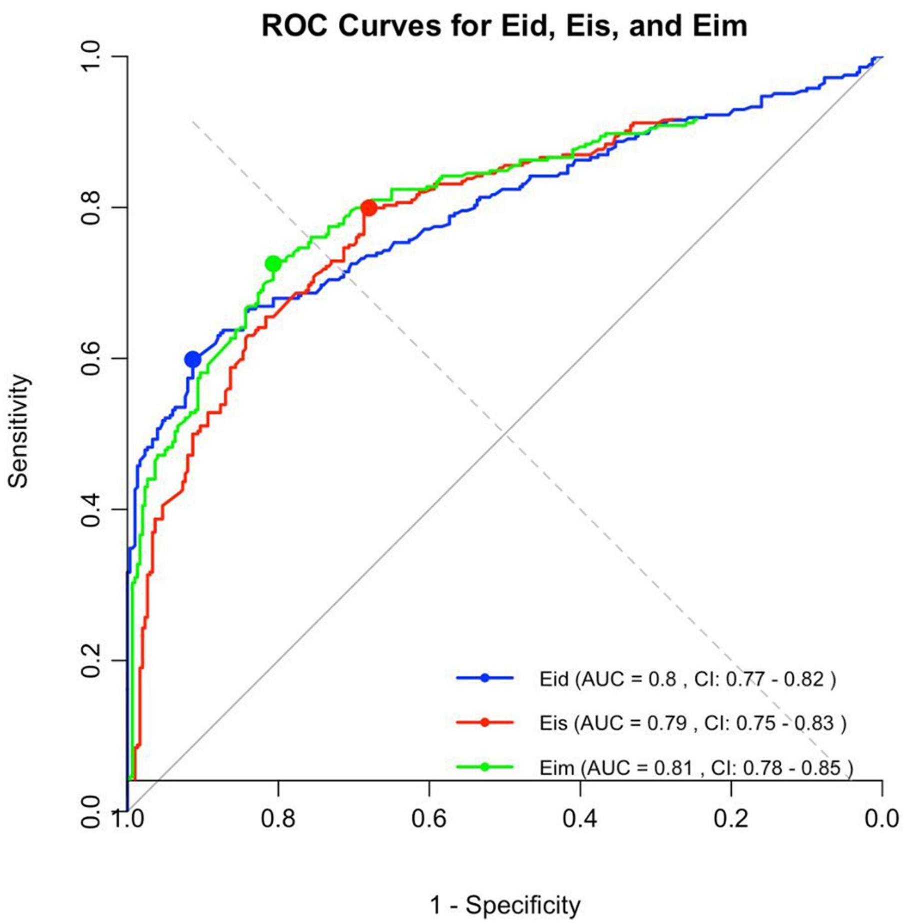


FIGURE 4
The area under the receiving operating characteristic (ROC) curve for the EIs, EId, and EIm. Optimal cutoff values of 1.28 for EIs, 1.40 for EId, and 1.34 for EIm discriminating none/mild to moderate/severe PAH, with a sensitivity of 77.3% for EIs, 65.2% for EId, and 77.3% for EIm, and a specificity of 72.7% for EIs, 100% for EId, and 77.3% for EIm.

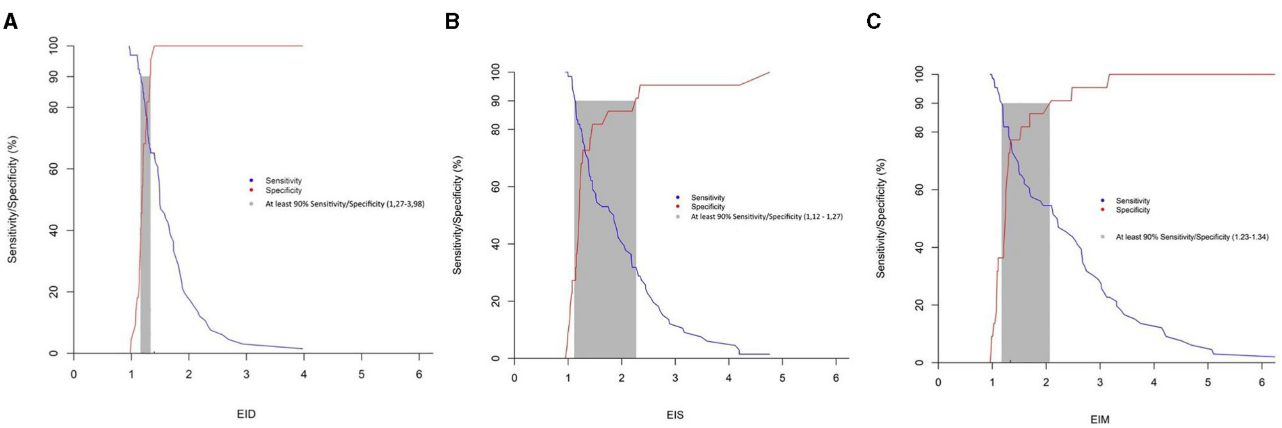


FIGURE 5
Gray zone approach for the eccentricity index **(A)** Eis; **(B)** Eid; **(C)** Eid, the blue line represents sensitivity, whilst the red line represents specificity. The gray zone represents the zone in which sensitivity and specificity are under 90%.

The proposed EI cut-offs may prove to be clinically useful for ECC clinicians in identifying patients with moderate to severe PAH. However, these cut-offs have been identified on a population without significant concurrent left heart disease, and image acquisition was performed by a cardiologist, and therefore this information should be interpreted cautiously.

That said, based on our data, EI appears to show promise in an emergency setting to identify patients with moderate to severe PAH. Especially EIm may represent benefits over EIs and EId in an emergency setting as it does not require simultaneous ECG-recordings.

Our study has several limitations. In this retrospective study, some dogs had received loop diuretics or phosphodiesterase-5 inhibitor prior to echocardiography. These treatments may have influenced measurements. Studies investigating the effect of sildenafil on tricuspid regurgitation (TR) and right heart parameters have been met with variable results (3, 4, 21–23, 25). Furthermore, the severity of PAH was assessed indirectly. Doppler echocardiography-derived estimates of PAP were employed, a common procedure in a clinical setting, despite known discrepancies between non-invasive estimates and invasive measurements. Prior research indicates that while Doppler-derived TRPG can correlate with invasive PAP measurements, the correlation is not perfect (9, 24, 26). The reliance on Doppler-derived TRPG or pulmonic gradients by cardiologists for diagnosing PAH introduces additional challenges. These gradients can be influenced by several factors such as beam alignment, operator skill, sedation, body positioning, and patient respiratory patterns. Specifically, in cases with significant regurgitation, high right atrial pressure, or right ventricular systolic failure, TRPG may not accurately reflect systolic PAP. This study included instances where discrepancies between TR/pulmonic gradients and clinical indicators of right heart function were observed. To enhance diagnostic accuracy for PAH, cardiologists incorporated a comprehensive evaluation of right heart parameters alongside TR/pulmonic gradients, aligning with previously established guidelines. The population included in this study was recruited through the cardiology service, which may differ from the population seen in an emergency setting. To the authors' knowledge, there are no studies in either human or veterinary literature specifically comparing right heart echocardiographic changes between patients presenting to cardiology vs. emergency services. Therefore, whether the findings from our study can be fully extrapolated to emergency populations remains uncertain.

The study population consisted of dogs without left heart remodeling or other right-sided cardiac conditions. Furthermore, some of these cases were recruited through the cardiology service, which may not reflect the spectrum of patients typically encountered in an emergency or critical care setting. Whether ECC clinicians can reliably detect PCPH in the presence of concurrent significant left heart disease or reliably distinguish PCPH from other causes of right-sided heart disease remains an open question. Further work would be needed to assess diagnostic performance in these more complex scenarios.

In addition, the cut-off values proposed for EIs, EId, and EIm were derived from the current dataset and have not yet been validated in an independent population. External validation in a separate cohort will be necessary to confirm their generalizability and clinical applicability.

Furthermore, suboptimal angulation may influence EI measurements. However, in this study, all measurements were based on pre-recorded cineloops obtained by cardiologists. In a prior study on EI conducted by cardiologists, inter-observer variability remained within acceptable limits (7–11%), suggesting that angulation had a limited impact on our results (20).

Additionally, we acknowledge that not all ECC clinicians may be able to obtain a simultaneous ECG tracing during focused cardiac POCUS examinations. As such, the added value of EIm findings may be particularly relevant in situations where ECG monitoring is not readily available or cannot be integrated in real time.

Intra-observer agreement was not assessed in our study, which represents another limitation of our results. However, in a recent study conducted by cardiologists, Intra-observer agreement was evaluated and demonstrated good to excellent repeatability (16). In this study repeatability implied obtaining the image and measuring EI. We do acknowledge future studies in which non-cardiologists performing the measurements should assess intra-observer repeatability.

Finally, echocardiographic cineloops were acquired by board-certified cardiologists or cardiology residents on a dedicated ultrasound device. The recording of high-quality images thanks to well-trained cardiologists on superior devices may have positively impacted inter-rater agreement. Our study did not assess ability of ECC residents to obtain these cineloops, but their capacity to measure EI on these cineloops. Prospective studies in which non-cardiologists record and interpret the images are currently ongoing.

## Conclusion

This study showed good inter-observer agreement of EIs, EIm, and EId measurement by ECC residents on prerecorded loops. EI allowed good identification of dogs with moderate to severe PAH by ECC residents.

## Data availability statement

The raw data supporting the conclusions of this article will be made available by the authors, without undue reservation.

## Author contributions

NG: Writing – original draft, Writing – review & editing. KG: Writing – original draft, Writing – review & editing. AV: Writing – original draft, Writing – review & editing. PB: Writing – original draft, Writing – review & editing. DB: Writing – original draft, Writing – review & editing. TW: Writing – review & editing, Writing – original draft. RG: Writing – review & editing, Writing – original draft. ML: Writing – review & editing, Writing

– original draft. AM: Writing – review & editing, Writing – original draft.

## Funding

The author(s) declare that no financial support was received for the research and/or publication of this article.

## Conflict of interest

The authors declare that the research was conducted in the absence of any commercial or financial relationships that could be construed as a potential conflict of interest.

## Generative AI statement

The author(s) declare that no Gen AI was used in the creation of this manuscript.

## Publisher's note

All claims expressed in this article are solely those of the authors and do not necessarily represent those of their affiliated organizations, or those of the publisher, the editors and the reviewers. Any product that may be evaluated in this article, or claim that may be made by its manufacturer, is not guaranteed or endorsed by the publisher.

## References

1. McMahon P, Saelinger C. Reversal of echocardiographic right-sided heart pathology in a dog with severe pulmonary hypertension: a case report. *VMRR*. (2015) 211:S84181. doi: 10.2147/VMRR.S84181

2. Gelé RR, Burnotte P, Valcke A, Walker TG, Kennedy CR, Merveille A, et al. Retrospective evaluation of a right heart parameter score in the assessment of precapillary pulmonary hypertension in dogs (2017–2021): 135 cases. *J Vet Emergen Crit Care*. (2024) 34:277-84. doi: 10.1111/vec.13394

3. Humbert M, Guignabert C, Bonnet S, Dorfmüller P, Klinger JR, Nicolls MR, et al. Pathology and pathobiology of pulmonary hypertension: state of the art and research perspectives. *Eur Respir J*. (2019) 53:1801887. doi: 10.1183/13993003.01887-2018

4. Haddad F, Guihaire J, Skhiri M, Denault AY, Mercier O, Al-Halabi S, et al. Septal curvature is marker of hemodynamic, anatomical, and electromechanical ventricular interdependence in patients with pulmonary arterial hypertension. *Echocardiography*. (2014) 31:699-707. doi: 10.1111/echo.12468

5. Bach JF, Rozanski EA, MacGregor J, Betkowski JM, Rush JE. Retrospective evaluation of sildenafil citrate as a therapy for pulmonary hypertension in dogs. *Vet Int Med*. (2006) 20:1132-5. doi: 10.1892/0891-6640(2006)20[1132:REOSCA]2.0.CO;2

6. Burkett DA, Patel SS, Mertens L, Friedberg MK, Ivy DD. Relationship between left ventricular geometry and invasive hemodynamics in pediatric pulmonary hypertension. *Circ: Cardiovasc Imaging*. (2020) 13:e009825. doi: 10.1161/CIRCIMAGING.119.009825

7. Friedberg MK. Imaging right-left ventricular interactions. *Cardiovasc Imaging*. (2018) 11:755-71. doi: 10.1016/j.jcmg.2018.01.028

8. Raymond RJ, Hinderliter AL, Willis PW, Ralph D, Caldwell EJ, Williams W, et al. Echocardiographic predictors of adverse outcomes in primary pulmonary hypertension. *J Am Coll Cardiol*. (2002) 39:1214-9. doi: 10.1016/S0735-1097(02)01744-8

9. Brown AJ, Davison E, Sleeper MM. Clinical efficacy of sildenafil in treatment of pulmonary arterial hypertension in dogs: sildenafil in pulmonary hypertension. *J Vet Int Med*. (2010) 24:850-4. doi: 10.1111/j.1939-1676.2010.0517.x

10. Burkett DA, Slorach C, Patel SS, Redington AN, Ivy DD, Mertens L, et al. Impact of pulmonary hemodynamics and ventricular interdependence on left ventricular diastolic function in children with pulmonary hypertension. *Circ Cardiovasc Imaging*. (2016) 9:e004612. doi: 10.1161/CIRCIMAGING.116.004612

11. Hoeper MM, Bogaard HJ, Condliffe R, Frantz R, Khanna D, Kurzyna M, et al. Definitions and diagnosis of pulmonary hypertension. *J Am Coll Cardiol*. (2013) 62:D42-50. doi: 10.1016/j.jacc.2013.10.032

12. Reinero C, Visser LC, Kellihan HB, Masseau I, Rozanski E, Clercx C, et al. ACVIM consensus statement guidelines for the diagnosis, classification, treatment, and monitoring of pulmonary hypertension in dogs. *Vet Int Med*. (2020) 34:549-73. doi: 10.1111/jvim.15725

13. Dong SJ, Smith ER, Tyberg JV. Changes in the radius of curvature of the ventricular septum at end diastole during pulmonary arterial and aortic constrictions in the dog. *Circulation*. (1992) 86:1280-90. doi: 10.1161/01.CIR.86.4.1280

14. Kellum HB, Stepien RL. Sildenafil citrate therapy in 22 dogs with pulmonary hypertension. *Vet Int Med*. (2007) 21:1258-64. doi: 10.1892/07-006.1

15. Cardozo Júnior LCM, Lemos GSD, Besen BAMP. Fluid responsiveness assessment using inferior vena cava collapsibility among spontaneously breathing patients: systematic review and meta-analysis. *Med Intens*. (2023) 47:90-8. doi: 10.1016/j.medin.2021.12.015

16. Kellihan HB, Stepien RL. Pulmonary hypertension in dogs: diagnosis and therapy. *Vet Clin N Am*. (2010) 40:623-41. doi: 10.1016/j.cvsm.2010.03.011

17. Moore CL, Rose GA, Tayal VS, Sullivan DM, Arrowood JA, Kline JA. Determination of left ventricular function by emergency physician echocardiography of hypotensive patients. *Acad Emerg Med*. (2002) 9:186-93. doi: 10.1197/aemj.9.3.186

18. Schweintzger S, Kurath-Koller S, Burmas A, Grangl G, Fandl A, Noessler N, et al. Normal echocardiographic reference values of the right ventricular to left ventricular endsystolic diameter ratio and the left ventricular endsystolic eccentricity index in healthy children and in children with pulmonary hypertension. *Front Cardiovasc Med*. (2022) 9:950765. doi: 10.3389/fcvm.2022.950765

19. Ünlüer E, Karagöz A, Akoglu H, Bayata S. Visual estimation of bedside echocardiographic ejection fraction by emergency physicians. *WestJEM*. (2014) 15:221-6. doi: 10.5811/westjem.2013.9.16185

20. Lekane M, Burnotte P, Gommeren K, Mc Entee K, Merveille AC. Left ventricular eccentricity index to assess precapillary pulmonary hypertension in dogs. *J Vet Cardiol*. (2024) 51:220-31. doi: 10.1016/j.jvc.2023.12.003

21. Abraham S, Weismann CG. Left ventricular end-systolic eccentricity index for assessment of pulmonary hypertension in infants. *Echocardiography*. (2016) 33:910-5. doi: 10.1111/echo.13171

22. Akabane R, Sakatani A, Ogawa M, Nagakawa M, Miyakawa H, Miyagawa Y, et al. The effect of sildenafil on pulmonary haemodynamics in a canine model of chronic embolic pulmonary hypertension. *Res Vet Sci*. (2020) 133:106-10. doi: 10.1016/j.rvsc.2020.08.019

23. Beyar R, Dong SJ, Smith ER, Belenkie I, Tyberg JV. Ventricular interaction and septal deformation: a model compared with experimental data. *Am J Physiol Heart Circ Physiol*. (1993) 265:H2044-56. doi: 10.1152/ajpheart.1993.265.6.H2044

24. Ryan T, Petrovic O, Dillon JC, Feigenbaum H, Conley MJ, Armstrong WF. An echocardiographic index for separation of right ventricular volume and pressure overload. *J Am Coll Cardiol*. (1985) 5:918-24. doi: 10.1016/S0735-1097(85)80433-2

25. Jaffey JA, Leach SB, Kong LR, Wiggen KE, Bender SB, Reinero CR. Clinical efficacy of tadalafil compared to sildenafil in treatment of moderate to severe canine pulmonary hypertension: a pilot study. *J Vet Cardiol*. (2019) 24:7-19. doi: 10.1016/j.jvc.2019.05.001

26. Soydan LC, Kellihan HB, Bates ML, Stepien RL, Consigny DW, Bellofiore A, et al. Accuracy of Doppler echocardiographic estimates of pulmonary artery pressures in a canine model of pulmonary hypertension. *J Vet Cardiol*. (2015) 17:13-24. doi: 10.1016/j.jvc.2014.10.004

27. Lyssens A, Lekane M, Gommeren K, Merveille AC. Focused cardiac ultrasound to detect pre-capillary pulmonary hypertension. *Front Vet Sci*. (2022) 9:830275. doi: 10.3389/fvets.2022.830275

frontiers | Frontiers in Veterinary Science

TYPE Original Research
PUBLISHED 08 July 2025
DOI 10.3389/fvets.2025.1520004

Check for updates

OPEN ACCESS

EDITED BY
Hussein M. El-Husseiny,
Tokyo University of Agriculture and Technology, Japan

REVIEWED BY
Ivayla Danielova Yozova,
Massey University, New Zealand
Jessica Ward,
Iowa State University, United States

*CORRESPONDENCE
Rita Hanel
✉ ritahanel@veg.vet

RECEIVED 30 October 2024
ACCEPTED 23 June 2025
PUBLISHED 08 July 2025

CITATION
Guillaumin J, Cavanagh A, Rechy J Jr, Callahan M and Hanel R (2025) Abdominal, thoracic, and cardiac point-of-care ultrasound skills following an in-person hands-on training course for early-track emergency clinicians.
*Front. Vet. Sci.* 12:1520004.
doi: 10.3389/fvets.2025.1520004



# Abdominal, thoracic, and cardiac point-of-care ultrasound skills following an in-person hands-on training course for early-track emergency clinicians

Julien Guillaumin[1], Amanda Cavanagh[1], Jaime Rechy Jr[2], Morgan Callahan[2] and Rita Hanel[2]*

[1]Department of Clinical Sciences, College of Veterinary Medicine and Biomedical Sciences, Colorado State University, Fort Collins, CO, United States, [2]VEG-ER for Pets, White Plains, NY, United States

**Introduction**: This study was designed to assess baseline compared to three months procedural skills performing abdominal, thoracic, and cardiac point-of-care ultrasound (POCUS) after POCUS training.

**Methods**: A POCUS training was designed as a 3-hour online course, followed by a 2-day in-person course consisting of 3.5 hours of case-based lectures and 4 hours of hands-on laboratory on anesthetized dogs each day. In-person procedural assessment was performed using an anesthetized dog and consisted of identifying 22 anatomical structures in 6 minutes. The assessment was performed pre-course and repeated three months post-course in an identical environment.

**Results**: Fifty-six veterinarians from the Veterinary Emergency Group New ER Doctor program were enrolled. Participants identified an overall 7.8 ± 2.6 structures in the pre-course assessment, compared to 13.8 ± 5.9 in the post-course assessment ($p < 0.0001$). For abdominal POCUS, participants identified 5.9 ± 1.9 structures out of 12 in the pre-course and 9.0±1.5 in the post-course assessment ($p < 0.0001$). For thoracic POCUS, participants identified 1.7 ± 1.2 structures out of 4 in the pre-course and 3.4±0.7 in the post-course assessment ($p < 0.0001$). For cardiac POCUS, participants identified 0.07 ± 0.3 structures out of 6 pre and 1.5±1.6 post-course assessment ($p < 0.0001$). There was no impact of pre-course tested variables on the pre-course score. Survey-based course satisfaction was 100%.

**Discussion**: The Veterinary Emergency Group New ER Doctor POCUS course improved participants' ability to correctly identify anatomical structures on POCUS when assessed three months after the course.

KEYWORDS

**POCUS, focused ultrasound, competency, learning, assessment, performance decay**

## 1 Introduction

Initially designed by trauma surgeons to assess trauma patients bedside, point-of-care ultrasound (POCUS) has evolved to be ubiquitous in emergency medicine in people (1, 2). POCUS is defined as ultrasonography at the patient's bedside that is performed in real-time by a clinician caring for the patient (3). In contrast to traditional comprehensive ultrasound examinations that may involve multiple providers and steps, diagnostic POCUS examinations involve the same clinician determining the need for a focused examination, acquiring and interpreting the images, and incorporating the findings into the immediate management of the patient. POCUS use has increased in emergency medicine, critical care medicine, and internal medicine over the past two decades (4).

In veterinary emergency and critical care medicine, POCUS is similarly an important part of practice and training (1, 2, 5–7). The first report of abdominal POCUS (A-POCUS) was published in 2004 in trauma dogs and the first report of thoracic POCUS (T-POCUS) in 2008 (8, 9). A focused cardiac POCUS (C-POCUS) procedure was also recently described (10). However, incorporation of POCUS training in veterinary medical education is lacking, especially compared to medical schools. Currently, almost 73% of medical schools include POCUS in their preclinical courses as well as clinical education, and a specific C-POCUS curriculum for medical students has been created (11–14). This number is presumably much lower in veterinary medicine. In one survey, veterinarians stated that not having an ultrasound machine in their practice and lack of training or education were the most common reasons for not performing ultrasound exams (6). Recent studies have investigated the feasibility of self-driven POCUS learning, in-person and online video POCUS instructions as well as an hybrid online, in-person didactic training and hands-on training (15–23).

Existing studies vary in scope, target audience and design. The majority of studies investigate veterinary students (15–18, 20, 21). Only two studies investigated canine primary practitioners in the United Kingdom or Australia (21, 23). Most studies focused on a specific organ, such as kidney or heart, one investigated a four quadrant A-POCUS, and only one investigated a more global POCUS approach with A-POCUS, T-POCUS and C-POCUS (16, 20, 22, 23). Published study outcomes also vary, including image quality assessed by an expert (15, 16, 20, 22), comparison to images acquired by board certified specialists (19, 21), and satisfaction survey (18, 23).

In people, studies have demonstrated the effectiveness of POCUS training courses on knowledge and skills acquisition by different learner groups. However, these courses have varied in duration, content, delivery, and target audience (4, 24–26). Similarly, there was heterogeneity in outcome assessment of POCUS competencies. Ideally, a course teaching POCUS should lead to an improvement in ultrasound competency, would lead to students' satisfaction, and students should retain their skills over time.

The aim of our study was to assess the effectiveness of a 2-day POCUS course targeting novice learners in an immersive emergency doctor training program. Our primary objective was to compare baseline skill to a 3-month post-course evaluation assessing learners' ability to correctly identify specific anatomical locations in A-POCUS, T-POCUS, and C-POCUS. We hypothesized that novice learners will improve their POCUS skills globally 3-months after the POCUS course compared to baseline. Our secondary objectives were to determine if any predictors of higher skill levels existed and to assess course feedback, including participants' satisfaction. We hypothesized there would be some predictor(s) of higher skill levels, and that participants would be satisfied with the course and their improved skill level.

Abbreviations: A-POCUS, abdominal point-of-care ultrasound; C-POCUS, cardiac point-of-care ultrasound; ER, emergency room; FAST, abdominal focused assessment with sonography for trauma; NERD, new emergency room doctor; POCUS, point-of-care ultrasound; T-POCUS, thoracic point-of-care ultrasound; VEG, veterinary emergency group.

# 2 Materials and methods

## 2.1 Course design

The POCUS course was designed by Veterinary Emergency Group (VEG) as a 3-prong hybrid approach. First, a 3-h online module consisting of 1-h lectures recorded by experts in their respective fields of A-POCUS, T-POCUS, and C-POCUS was hosted in a learning management system and was accessible remotely at any time by the participants. The lectures included terminology commonly used in POCUS, using terms referring to ultrasound (US) probe location or anatomic site, without any references to trademarked protocols. The lecture content showed participants ways to acquire images of various anatomical structures, including those listed on Table 1, and instructed participants to follow a systemic approach to POCUS of anatomical regions such as starting at the subxiphoid view and making a clockwise or counterclockwise approach around the abdomen, the check-mark sign for T-POCUS and a mushroom view start for C-POCUS (10, 27).

Second, participants were enrolled in a 2-day in-person course consisting of lectures and hands-on training. A total of 3.5 h per day of case-based lectures covering the various aspects of POCUS use in emergency practice (7 h total) was delivered in-person by content experts. The primary learning objective for the lectures was the incorporation of POCUS in case workup and management (e.g., canine spontaneous hemoabdomen for A-POCUS, feline pyothorax for T-POCUS, and feline congestive heart failure for C-POCUS). The cases assumed sufficient knowledge of POCUS techniques based on the supplied pre-course work. Participants also had a 4-h per day, in-person, hands-on POCUS training on anesthetized, purpose-bred, ethically sourced Beagles (8 h total). Due to the number of participants, the hands-on training portion included two groups of participants. For each group of participants, the hands-on training portion had 8-stations divided into two identical groups of four stations.

There were a total of four training stations on each day. On Day 1, there was one A-POCUS in left lateral recumbency, one T-POCUS in sternal recumbency, one C-POCUS in left lateral recumbency and one free scan station in right lateral recumbency where participants could choose any of the three POCUS techniques or a mix of the three. On Day 2, there was one A-POCUS in left lateral recumbency, one T-POCUS in sternal recumbency, and two C-POCUS stations in left lateral and right lateral recumbency. The participants were not allowed to move the dog into a different position unless deemed necessary by the instructor. For C-POCUS views and the right kidney view in right lateral recumbency, students were instructed to slide the probe underneath the dog. Each station had approximately four participants per station, and each group of four participants rotated every 60 min per station. Therefore, each participant had an approximate time of 15 min at four different stations over 2 days, for a total of 120 min of actual ultrasound scanning time.

An instructor was assigned to each of the stations. Instruction was at the discretion of the specific instructor and stations. Each instructor had access and was asked to review in advance the same 3-h online module available to the students, including specific systemic approaches. Most of the instructors were familiar with the hands-on training and had taught it before. No specific effort was made by the instructors to review the list of anatomical structures that were used during the assessment

TABLE 1 Pre and post-POCUS course ability to correctly identify an anatomical local by junior emergency veterinarians ($n$ = 56).

| Anatomical location number | Anatomical location | Pre-course assessment performance (% unless specified) | Post-course assessment performance (% unless specified) |
|---|---|---|---|
| Abdominal point of care ultrasound (A-POCUS) | | | |
| 1 | Liver | 82 | 91 |
| 2 | Gallbladder | 70 | 93* |
| 3 | Heart through the SX view | 48 | 86* |
| 4 | Caudal vena cava | 2 | 20* |
| 5 | Stomach | 32 | 71* |
| 6 | Right kidney | 27 | 75* |
| 7 | Bladder | 96 | 98 |
| 8 | Bladder neck | 57 | 79* |
| 9 | Aortic trifurcation | 0 | 43** |
| 10 | Left kidney | 84 | 96* |
| 11 | Spleen | 80 | 95* |
| 12 | Splenic hilus | 14 | 48* |
| | | | |
| | Systemic approach | 18 | 68* |
| | Time spent in A-POCUS (sec) # | 241.4 ± 58.3 | 184.9 ± 35.3* |
| Thoracic point of care ultrasound (T-POCUS) | | | |
| 13 | A-line | 41 | 85* |
| 14 | Bone-Air in Transverse sign | 34 | 90* |
| 15 | Glide sign | 77 | 90* |
| 16 | Seashore sign | 23 | 56* |
| | | | |
| | Systemic approach | 18 | 54* |
| | Time spent in T-POCUS (sec) # | 65.6 ± 37.9 | 67.5 (30–180) |
| | | | |
| Cardiac point of care ultrasound (C-POCUS) | | | |
| 17 | Right parasternal short-axis ventricular view (i.e., Mushroom view) | 5 | 49* |
| 18 | Right parasternal short-axis heart base view (i.e., Left atrium to Aorta view) | 0 | 24* |
| 19 | Main pulmonary artery | 0 | 7* |
| 20 | Right parasternal long-axis view identifying LA, right atrium, left ventricle and right ventricle view (i.e., Four chambers view) | 2 | 22* |
| 21 | Right parasternal long-axis view identifying LA, Ao, right atrium, left ventricle and right ventricle view (i.e., Five chambers view) | 0 | 10* |
| 22 | Mitral valve in a right parasternal short or long-axis view | 0 | 27* |
| | | | |
| | Systemic approach | 0 | 5 |
| | Time spent in C-POCUS (sec) # | 53.9 ± 44.6 | 101.4 ± 38.3* |

SX, sub-xyphoid; sec, seconds. *$p < 0.05$. #: represents the mean ± standard deviation or median (minimum-maximum) of the individual participant's times.

phase, although individual participants could ask for clarification and help, especially during the free scan station. Instructors were all American board-certified in either cardiology or emergency and critical care, emergency and critical care residents, or experienced academic emergency room doctors with POCUS teaching experience. The course was gamified using rapid rotation between participant and stations (15 min), engaged and present instructors, an individualized bingo sheet that highlighted the 22 anatomical locations assessed during the study, and the occasional use of a spinning wheel with specific anatomical locations to identify in a certain time frame (28).

The course design adopted for the study was based on previous experience by the study team in POCUS training for VEG NERDS for the past 2 years, or approximately six training sessions with similar, but not identical design. Many of the decisions made for the current study design were made due to those previous experiences.

## 2.2 Participant's inclusion criteria

Participants for the study were enrolled in Veterinary Emergency Group's New ER Doctor (NERD) program. NERDs were defined as graduates veterinarians without experience in emergency medicine and were mostly veterinary school graduated within the past 6 months. Prerequisites for the POCUS course included completing the online lectures, answering five quiz questions for each hour of lecture, and having a passing grade of 12 correct answers out of 15 questions.

Participants were excluded if they: were not a VEG NERD, did not complete the required online course, did not have a passing grade for the online course, did not perform both assessments (pre-course and post-course), or were unable to perform a POCUS due to injury.

## 2.3 Study design

Identical in-person pre-course and post-course hands-on assessments were performed. The pre-course assessment was performed on the first morning of the course, as participants were pulled out of lectures or breaks for approximately 10–15 min. The post-course assessment was done in a similar fashion, in-person, 3 months post-course. The same dog was used for each participant for pre-course and post-course assessments.

Participants signed an informed consent prior to the course and were again briefed on the study in-person, the morning of the pre-course assessment, and were provided with the list of anatomical locations (Table 1). They were again briefed on the study in-person the morning of the post-course assessment. Each participant was pre-assigned a time slot (similar for the pre-course and the post-course assessment).

For each of the four anesthesia events, the dog was pre-medicated with butorphanol (0.2–0.4 mg/kg IM, $n = 4$) and dexmedetomidine (5 mcg/kg IM, $n = 2$), or atropine (0.02 mg/kg IM, $n = 2$). After an intravenous catheter was placed, anesthesia induction was performed using ketamine (4 mg/kg IV, $n = 4$) and midazolam (0.2 mg/kg IV, $n = 4$). Maropitant (1 mg/kg SQ) was administered during two of the four anesthesia events. The dog was maintained under light anesthesia with inhaled isoflurane after orotracheal intubation and was breathing spontaneously. Atropine (0.02 mg/kg IV or IM) was used at the anesthesia technician discretion to maintain heart rate above 100 bpm. Dopamine (5–7 mcg/kg/min) was used at the anesthesia technician discretion to maintain blood pressure above 65 mm Hg.

The anesthetized dog was placed in a right lateral recumbency, and the abdomen and left thorax were clipped (Figure 1). A lateral recumbency was chosen due to the anesthesia limiting the ability to maintain sternal recumbency without external holding device which would limit access to the chest of the dog. A right lateral recumbency was chosen for practical reasons, including the dog's abdomen facing the participant's position at the left of the examination table (Figure 1), as well as the authors' experience with shifting of the cardiac axis secondary to atelectasis during the 4 h anesthesia time needed to assess all participants, therefore making C-POCUS image acquisition variable over the course of the assessment. All participants stood left to the dog and performed the ultrasound exam with their right hand. Participants were not allowed to move the dog in a different recumbency side and therefore had to slide their hand underneath the dog in order to acquire C-POCUS images as well as right kidney. In the author's experience, this is performed very easily with the small size dog used in this study.

The participants were given 6 min to perform an A-POCUS, T-POCUS, and C-POCUS and identify as many of the 22 anatomical locations as possible (Table 1). Participants were not allowed to move the dog into a different position. Ultrasound gel was used although alcohol was withheld due to concerns regarding hypothermia. A study support person not involved in the course was present to answer any questions regarding the ultrasound machine[1] (i.e., knobology), switch the machine to a cardiac mode if/when instructed by the participant, and had a physical copy of the list of anatomical locations that the participant could also consult (Table 1). They were not allowed to answer any questions related to the study or the anatomical structure seen on screen. Their default answer was "*do your best*," and they wore a face mask to avoid showing facial expressions. The total study time was 6 min per participant, and the study support person provided a 2 min and four-minute countdown and dismissed the participant after 6 min.

Each participant was equipped with a lapel microphone and instructed to point with their finger on the screen to the specific anatomical location and verbalize the site/sign they identified. The study support person would move the US cursor to the area underneath the participant's finger for redundant video recording purposes. Three video-captures were performed: a bird's-eye view of the dog, a recording of the ultrasound machine input displaying the arrow/cursor (video graphics array cable), and a video recording of the screen displaying hand position (Figure 1).

## 2.4 Data collected and outcome measured

Prior to the study, VEG collected data from the participants, including age, gender/gender identity, dominant hand, veterinary school attended, if the participant received POCUS training during veterinary school, graduation year, and a self-rated POCUS competency using a scale of 0 (i.e., novice) to 5 (i.e., expert). VEG also collected a post-course satisfaction survey that included a second self-rated POCUS competency using the aforementioned scale. The post-course satisfaction survey was submitted at the end of the training course and included two questions, one with a binary answer (i.e., Yes/No) regarding perception of the course benefit for skills improvement, and one using the aforementioned 5-points scale for self-rated POCUS competency.

All data from the 3 videos-captures from both sessions were acquired, then anonymized and labeled by a person not involved in the study design or the course to anonymize the participant and the assessment session (i.e., pre or post). That person was provided with a randomized table and re-labeled each video from 1 to 112. Those randomized, anonymized videos were provided for analysis to one of

1 Sonosite S9, Universal Inc., Bedford Hills, NY, United States.

FIGURE 1
Point-of-care ultrasound (POCUS) course assessment set-up. An ethically-sourced, purpose-bred Beagle was anesthetized, monitored (anesthesia technician visible on the right), and placed in right lateral recumbency. The participant (center) would point on the screen the anatomical location and the assessor (left) would move the ultrasound machine's cursor on the anatomical location pointed by the participant. Three videos-captures were performed: a bird-view of the dog, a recording of the ultrasound machine input displaying the arrow/cursor (video graphics array cable) and a video recording of the screen displaying hand position.

the authors (AC) not involved in the study design or the hands-on lab portion. One point was granted if the participant correctly identified and verbalized the anatomical structure. Correct identification was defined by the image being able appropriate enough to be shown in a lecture or a textbook used by a board-certified emergency and critical care specialist trained in POCUS.

For the purpose of our study, we defined an individual organ (such as the right kidney), an anatomical artifact (such as the bone-air in transverse artifact in T-POCUS) or a specific view (such as a "mushroom view") listed in Table 1 as an "anatomical structure," and we used the term anatomical regions to describe A-POCUS, T-POCUS or C-POCUS. The total number of anatomical structures identified, as well as the total number of anatomical structures by anatomical regions were recorded. Identification of each individual anatomical structure was also recorded (Table 1). If a systematic approach was followed, defined as starting at the subxiphoid view and making a clockwise or counterclockwise approach around the abdomen, the check-mark sign for T-POCUS and a mushroom view start for C-POCUS, it was recorded as a binary outcome (i.e., Yes/No) (10, 27). The time spent by each participant in each region was also recorded.

The study was approved by the Colorado State University Institutional Animal Care and Use Committee (#KP 1258) as well as Institutional Review Board (#KP 5927). Written informed consent was obtained from all study subjects before participation.

## 2.5 Statistical analysis

Preliminary data (not shown) with a group of participants ($n = 77$) not enrolled in the study, but enrolled in an earlier similar, but not identical program, determined they were able to identify 78 ± 15% of anatomical structures that were over 90% similar to the one used in the current study in 5 min 3 months after the POCUS training. Assuming the participant will improve from a baseline score of 60% to a score of 75% with a standard deviation of 15%, 10 students were needed to achieve significance for our primary outcome using a paired samples t-test. A recruitment target of 50 paired assessments was due to the VEG NERDS program coming as cohort of 60 or more doctors, and to mitigate against smaller observed differences.

D'Agostino-Pearson test was used to assess normal distribution. Data were presented in mean ± standard deviation, or median (minimum-maximum), as appropriate. Paired *t*-tests, or Wilcoxon paired tests, as appropriate, were performed to assess differences between numbers of structures identified between the pre and the post-course assessment for the total numbers of structures identified, as well as number of structures identified for each of the regions of A-POCUS, T-POCUS, and C-POCUS.

Factors influencing pre-course scores, and post-course improvement were examined via stepwise multiple regression. Age, pre-course quiz average, dominant hand, veterinary school rank according to the United States news 2023 report,[2] having a POCUS course or hands-on laboratory during veterinary school training (self-disclosed) and pre-course self-rating competency were included as independent variables. The dependent variables tested were pre-course scores and the post-course improvement above the average post-course assessment + one standard deviation. Independent variables were removed if $p > 0.1$. Statistical significance was set at $p < 0.05$. All statistical analyses were performed using commercial software.[3]

# 3 Results

## 3.1 Dogs

Purpose-bred spayed female Beagles between 1 and 2 years of age with a mean weight of 12.0 ± 1.8 kg were ethically sourced. Dogs were acclimated for a minimum of 1 week prior to baseline health assessments. Daily enrichment was provided, and group housing was performed, if possible, according to Colorado State University Laboratory Animal Resources protocols. Free access to water was allowed and a commercial dry kibble was fed twice daily. Food was withheld for 12 h prior to anesthesia. An anesthetized Beagle was used both for the assessment and the hands-on lab (#KP 1258). The same dog was used for both the pre-course assessment and the post-course assessment. All dogs used in the study were ultimately adopted.

## 3.2 Study participants demographics

Sixty-seven participants took the pre-requisites and hands-on course. All participants attended the online lectures and received a 75% or above pass rate on the quiz. Eleven participants were excluded as they graduated veterinary over 6 months prior to the course ($n = 7$), did not perform both pre and post course assessment due to sickness ($n = 2$), a family emergency ($n = 1$) or leaving the NERD program ($n = 1$). Therefore, 56 participants were included in the study for a total of 112 videos. The post-course assessment took place an average of 81 ± 23 days after the pre-course. Median age was 26.0 (25–55) years old. The majority of participants identified as female (n = 54, 96.4%) and two participants identified as male (3.6%). The majority of participants were right-handed (n = 48, 85.7%), while the remaining were left-handed ($n = 8$). All participants graduated in 2022 from the following veterinary schools: University of Florida ($n = 6$), Oklahoma State University ($n = 5$), University of Georgia ($n = 5$), Auburn University ($n = 4$), Tufts University ($n = 3$), Texas A&M University ($n = 3$), St. George's University ($n = 3$), Cornell University ($n = 3$), Colorado State University ($n = 2$), The Ohio State University ($n = 2$), Louisiana State University ($n = 2$), University of Missouri ($n = 2$), University of Illinois ($n = 2$), University College of Dublin (Ireland) ($n = 2$), and 1 of each of the following universities: Kansas State University, Lincoln Memorial University, Mississippi State University, North Carolina State University, Ross University, University of Tennessee, University of Minnesota, University of Pennsylvania, University of Wisconsin, Virginia Maryland University, Western University and the Royal Veterinary College (England). Approximately half of the participants ($n = 31$, 55.3%) did not recall having a POCUS lecture or hands-on lab during veterinary school while 44.7% recalled having one ($n = 25$). The mean self-rated POCUS competency was 1.8 ± 1.0 on a 5-point scale, 0 being an inexperienced user and 5 being a self-rated expert.

## 3.3 Primary objective

When A-POCUS, T-POCUS, and C-POCUS were combined, participants identified 7.8 ± 2.6 out of 22 anatomical structures (35%) in the pre-course assessment, compared to 13.8 ± 5.9 out of 22 anatomical structures (63%) in the post-course assessment. The difference in anatomical structures identified was statistically significant between pre- and post-course assessment ($p < 0.0001$).

The improvement between pre- and post-course assessment was also statistically significant for each of the anatomical regions. For A-POCUS, participants identified 5.9 ± 1.9 out of 12 abdominal anatomical structures (49%) in the pre-course and 9.0 ± 1.5 out of 12 (75%) in the post-course assessment ($p < 0.0001$). For T-POCUS, participants identified 1.7 ± 1.2 out of four thoracic anatomical structures (42%) in the pre-course and 3.4 ± 0.7 out of four (85%) in the post-course assessment ($p < 0.0001$). For C-POCUS, participants identified 0.07 ± 0.3 out of six cardiac anatomical structures (1%) pre- and 1.5 ± 1.6 out of 6 (25%) post-course ($p < 0.0001$).

Each individual structure on A-POCUS, T-POCUS, and C-POCUS was correctly identified on the pre-course assessment in 0–96%, 23–77%, and 0–5%, respectively, depending on the individual structure (Table 1). Most participants did not follow a systematic approach to POCUS in the pre-course assessment (Table 1). Time spent on A-POCUS, T-POCUS, and C-POCUS was 4.0, 1.1, and 0.9 min, respectively, in the pre-course assessment (Table 1). Anatomical structures that were difficult to identify in the pre-course assessment, defined as a score less than 80%, had a significant increase identification in the post-course assessment (Table 1). The range of correctly identifying an anatomical location on the post-course assessment on A-POCUS, T-POCUS, and C-POCUS was 20–96%, 56–90% and 7–49%, respectively (Table 1). Most participants did follow a systematic approach to A-POCUS and T-POCUS, but not C-POCUS in the post-course assessment (Table 1). Time spent on A-POCUS decreased significantly, and time spent on C-POCUS increased significantly in the post-course assessment compared to the pre-course assessment (Table 1).

## 3.4 Secondary objectives

None of the tested variables (i.e., age, pre-course quiz average, dominant hand, vet school rank, having a POCUS course or lab during veterinary school training and self-rating competency) impacted the pre-course score. The only tested variables impacting the post-course improvement was age, with older students performing better, with an estimated odds-ratio of 1.84 (95% CI 1.06–3.19, $p = 0.029$), meaning older students were 84% more likely to perform

2 https://www.usnews.com/best-graduate-schools/top-health-schools/veterinarian-rankings, consulted 5/5/2023.

3 MedCalc® Statistical Software version 20.210. MedCalc Software Ltd., Ostend, Belgium.

better. Receiver operating characteristics curve showed that a cut-off of 26 years was associated with higher likelihood of a post-test score above our threshold criterion, with a sensitivity of 70.0% and a specificity of 58.7% (AUC 0.696, $p = 0.012$) (Figure 2).

Twenty-four post-course surveys were received, 3 being duplicates and one could not be anonymized due to technical issues. Therefore, 20 individual surveys were analyzed (35.7% of participants). To the question "*Do you believe that this POCUS course was beneficial to improve your skill set?*," 100% ($n = 20$) of the participants answered "*Yes*." For the participants who answered the survey, the mean self-assessment score went from 1.9 (1.2) to 3.2 (0.7) ($p < 0.0001$).

## 4 Discussion

Our study found that our POCUS course designed for early career emergency clinicians resulted in a statistically significant improvement in correctly identifying anatomical structures 3 months after the course. The course satisfaction was excellent, and the participants reported an improvement in their self-assessment of POCUS skills. However, the post-course overall result of 63% of correctly identified anatomical structures should be considered a moderate proficiency. This is especially true for C-POCUS, where participants were only able to identify on average 25% of the anatomical structures. A-POCUS and T-POCUS's retention of clinical skills were better, with 75 and 85% of anatomical structures correctly identified, respectively.

This was the first time global POCUS clinical skills training in small animal emergency veterinarians was investigated. Most available studies on veterinary POCUS training involved veterinary students, compared to recent graduates in our study (15–20). Less than 50% of our course participants recalled having some POCUS training, which should be contrasted to the 78% of students recalling having some

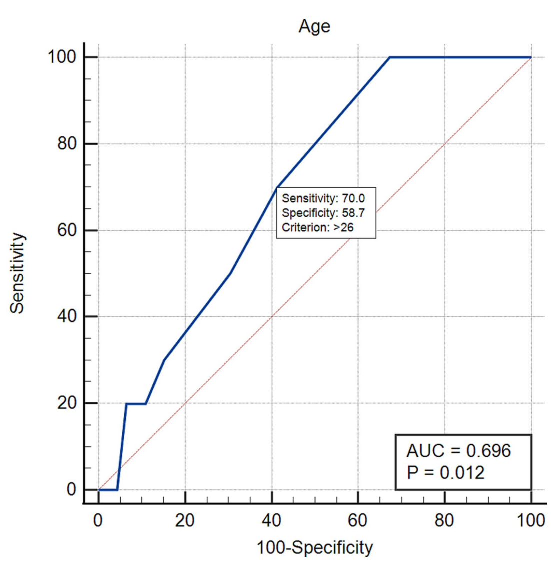


FIGURE 2
Receiving operating characteristics curve for the variable "age," an independent predictor of increased performance in the post-course assessment, defined as average post-course improvement + one standard deviation.

didactic or hands-on training in a study from one US veterinary school (19). This can be due to the heterogeneity of veterinary schools the participants in our study come from.

Participants in our study self-reported an average of 2 out of 5 POCUS competency in our study, corresponding to a low to mild level of proficiency. Although not directly comparable, it seems a higher self-reported proficiency compared to American veterinary students reporting a median comfort level consistent with "*I have no prior training and have not seen them [POCUS study] done before*," or less than 15% Australian practitioners being confident or very confident in various aspects of POCUS (16, 23).

Our primary outcome measurement was A-POCUS, T-POCUS and C-POCUS skills in dogs, with 22 anatomical structures studied and images reviewed by a board-certified emergency and critical care specialist. In A-POCUS, our 12 anatomical structures has to be contrasted with other small animal studies investigating a four quadrant A-POCUS (16), or appropriate identification and orientation on a single kidney view (20). In C-POCUS, our six anatomical structures has to be contrasted with two to four cardiac ultrasound views (19, 21). In previous studies, no clear explanation of how the landmark was identified was provided or reviewed (16), or images were reviewed by cardiologists (19, 21), or radiologists (20).

All other studies were designed for large animals (15, 17, 22), or had participant satisfaction and self-assessment as an outcome (18, 23). Participant satisfaction and self-assessment was also an outcome in the present study. Participant satisfaction of 100% was higher to the published ones of 83–94%, and their self-assessment of skills increased, similar to a previously published study (17, 18, 23).

Currently, there is not a universal-recognized standardized way to perform an A-POCUS, T-POCUS, or C-POCUS, known in people as extended FAST (e-FAST) or FAST-Pleural ultrasound (FAST-PLUS) (29–31). At the time of writing this manuscript, an expert consensus on POCUS protocol is underway and therefore a more standardized list of anatomical sites to evaluate during POCUS examination may be available following the consensus. Another consensus, by The American College of Veterinary Radiology and the European College of Veterinary Diagnostic Imaging has been recently published their consensus on how to perform a full abdominal ultrasound, although it is not relevant to POCUS evaluation (32). For T-POCUS and C-POCUS, clinicians refer to veterinary textbooks for didactic training, online training and/or in-person training (27, 33, 34). Our study design elected to expand the number of POCUS anatomical locations compared to the original abdominal focused assessment with sonography for trauma (FAST), and our course design is relatively similar to one recently published (8, 23). Although arbitrary, the A-POCUS sites were chosen to include important landmarks for specific emergency situations, such as diagnosing a splenic torsion with the "arrow sign" at the splenic hilus, or an aortic thrombus in dogs and cats (35–37). The anatomical locations we used for T-POCUS and C-POCUS have been previously described (10, 33, 38).

Participants had 22 anatomic structures to identify in 6 min, or 16 s per landmark. Pre-course, time allotment was skewed toward A-POCUS, with an average allowance of 20 s per 12 landmarks (more than 16 s), versus C-POCUS, with an average allowance of 9 s per 6 landmarks (less than 16 s). In the pre-course, participants may have spent too much time looking for A-POCUS anatomical structures, leaving less time for the C-POCUS anatomical structures. In the 3-month follow up assessment, the speed of performing A-POCUS decreased by almost 1 min, allowing participants more time to focus on other parts of the POCUS exam. As a result, when the time spent in each area is divided by the number of anatomical locations to identify, all three areas were more evenly distributed with an average of 15 s, 18 s, and 17 s per landmark available for A-POCUS, T-POCUS, and C-POCUS, respectively. This is very close to 16 s per landmark mentioned earlier. This should be contrasted with the aforementioned study in veterinary students, in which students were allotted 6 min to identify the 4 original landmark sites of an abdominal FAST, providing an average allotment of 90 s per site, significantly more than the 16 s in our study (16). The amount of time allocated per site is appropriate for the level of education of the participants, 90 s for veterinary students, compared to 16 s for emergency veterinarians (16). Another study allotted 6 min to veterinary students and veterinarians of various level of training to acquire five standard right-parasternal long- and short-axis C-POCUS views (22). This correspond to 18 s per site, almost identical to the 17 s per site from our study's participants. We conclude that the improved speed in A-POCUS post-course allowed emergency veterinarians to perform A-POCUS, T-POCUS and C-POCUS in a clinically relevant time.

After the POCUS course, participants showed significant improvement, and moderate retention of their ability to correctly identify A-POCUS sites. Eighty percent or more of participants were already able to correctly identify the urinary bladder, left kidney, liver, and spleen on the pre-course baseline assessment. The three least correctly identified A-POCUS sites in the pre-course test were the aortic trifurcation, caudal vena cava, and splenic hilus. After the POCUS course, all of the A-POCUS anatomical locations that scored less than 80% at baseline showed a significant increase in the learners' ability to correctly identify it. Of interest, the liver, right kidney, urinary bladder, and left kidney were identified by 91, 75, 98 and 96% of participants, respectively. The participants in our study performed better compared to the veterinary students investigated in the aforementioned study, where the correct identification of these landmarks within 4 anatomical views were 50, 19, 64, and 22%, respectively (15). This difference could be related to the previously discussed pre-course POCUS comfort scores, the previously discussed level of training and education of participants, or could be due to the course design itself. Regarding the course design differences, in the veterinary students' study, one group of students had a live-animal training session for up to 20 min with one-on-one instruction, and one group had an online tutorial, and found a significant difference between the two groups in the students' ability to identify the subxiphoid view, but not for the other three A-POCUS views, with the one-on-one instruction performing better (15). In our study, participants had both online coursework and 120 min of one-on-one instruction for all participants.

The performance of T-POCUS had a more variable result. Overall, participants showed statistically significant improvement in and retention of their T-POCUS skills. Indeed, the overall average post-course scores were highest in the T-POCUS landmarks. The glide sign was the most likely to be identified in the pre- and post-course assessments, followed by the A-line in the pre-course and the distal acoustic shadow produced by the ribs in the post-course test. There are no published studies to compare from.

Cardiac POCUS had the lowest overall scores, with participants identifying $0.07 \pm 0.3$ structures pre and $1.5 \pm 1.6$ post. For C-POCUS, the right parasternal short-axis view at the left ventricular papillary muscles (mushroom view) and the right parasternal long-axis 4-chamber view were correctly identified in the pre-course assessment by only 5 and 2% of participants, respectively. Direct comparison of our results with published studies cannot be made, as this specific information is not available in the literature (19, 23). After the course, the time spent on C-POCUS increased, and each of the C-POCUS anatomical locations showed an increase in the participants' ability to correctly identify it. However, the most identified anatomic location, the mushroom view, was correctly identified by less than 50% of the learners. Explanation for this finding could be a lack of time, a positioning issue with the dog placed on right lateral recumbency without an echocardiography table, or cardiac anatomical shift due to atelectasis. Interestingly, these findings in our study are comparable to a study performed in a university setting with 23 medical students and one first year physician assistant on motor and cognitive skill retention for novice POCUS learners (39). The authors found that there was a higher rate of decay at 4 weeks for cardiac images than pleural or vascular images and hypothesized that this was due to the higher complexity and difficulty of cardiac imaging.

There were no predictors for performance in the pre-course assessment. Regarding the post-course assessment, however, older students tended to perform better in the post-course assessment. However, the cut-off of 26 years-old identified was identical to the median age of participants. The median age of the participants makes sense, are most of them were young adult learners. It is possible that our finding of older students performing better was due to only a few older participants. Although older adults (i.e., 65 years-old) can be slower and have a lower level of accuracy compared to younger adults (i.e., 24 years-old), it has been shown that the ability to acquire knowledge is largely unaffected by cognitive aging (40). A study in people investigated the neurocognitive mechanisms most important in competence development in performing POCUS (41). In that study, only "relevant knowledge" (i.e., multiple-choice tests, knobology, image interpretation and basic anatomical knowledge) and "visuospatial ability" (i.e., visuospatial manipulation and visuospatial perception), but not "psychomotor ability" were identified as determinants of POCUS competence development (41). If POCUS skills are more related to relevant knowledge and visuospatial ability, and that relevant knowledge is not affected by cognitive aging, it makes sense that older adults may perform POCUS as well as younger adults.

The course satisfaction was excellent, and the participants reported an improvement in their self-assessment of POCUS skills. The post-course survey documenting this had a response rate of 36%, which is consistent with current survey literature (42). There is growing interest and research surrounding the impact of self-assessments, confidence, or self-efficacy, on the competence of a learner (43). Recent surveys showed that the vast majority of primary care veterinarians used POCUS in some form, with the majority of them performing the procedure weekly or daily (6, 7). Competency evaluation was limited in that study with the most common reason cited for limited POCUS use being lack of confidence in performing the procedure (6, 7). Courses such as the one in this study and others in people and veterinary medicine have documented increases in self-efficacy (confidence), and as such, may ultimately improve competence through enhancing confidence (16, 18, 19, 23, 44).

Assuming proficiency was achieved post-course, the amount of decay was significant. In people, there is a growing collection of research, including a meta-analysis, on how to ensure learning retention and prevent decay. This can be done using successive relearning or spaced retrieval of concepts, which involves offering opportunities to retrieve course content beyond the usual short window of time following the initial learning (45–47). This contrasts with the well-established practice of mass learning at a conference or course, such as in this study. Studies specifically looking at retention and decay involving POCUS in human health care recommend retraining of skills at a maximum of 8 weeks from initial training for cardiac and pleural ultrasound in one study, with significant decay noted within 1 month in a second study (39, 48). Similar findings have been documented in other areas of healthcare that rely heavily on psychomotor skills, such as surgery (49). Although it is reasonable to believe that some participants practiced POCUS examination during the 3-month period in between assessments, it was not structured, recorded or formatted into a method involving relearning (testing), so the impact, or lack thereof, on decay cannot be discerned. This represents an area of future research for our group, in which we endeavor to include a post-course assessment, along with successive relearning, in an effort to measure its impact on retention of POCUS skills.

### 4.1 Limitations

Our study has some limitations. Some of them have already been discussed, such as the unknown clinical relevance of older participants performing better or the time limitation to identify 22 anatomical structures in 6 min. This timeframe was chosen because it is not only clinically relevant, but consistent with other studies (16, 22).

We did not perform an immediate post-course assessment, which limits our ability to accurately document an immediate post-course level of proficiency, and therefore proficiency decay over time. This was mainly due to not having time with the participants immediately after the course, as well as finances. The authors were also comfortable to forgo the immediate post-assessment because they believe, based on previous experience teaching this course and performing unrecorded mock tests similar to the one performed in our study, that the majority of participants should be able to identify the 22 anatomic locations within 6 min at the end of the 2-day course. This belief was confirmed by a study showing 100% success in obtaining C-POCUS images in horses after a 1-day course, and another study in medical students showing 100% in obtaining T-POCUS and C-POCUS images after a 1-h didactic and 1-h hands-on training (22, 39).

Because of the need for a standardized setup due to camera placements, the use of the non-dominant hand for a small percentage of the participants could have swayed the results, although it did not appear to affect the pre-course or post-course proficiency. Although limited, existing evidence suggests that using the non-dominant hand for ultrasound image acquisition or guidance has minimal impact on performance (50–53).

Unlike other veterinary studies, our study did not define specific image quality criteria for correct anatomical identification. However, previous studies focused on much fewer structures (e.g., 1–4), while our study examined 22 (20, 22). Our decision not to include strict criteria was based on logistical constraints creating 22 strict criteria for three anatomical regions.

## 5 Conclusion

New ER doctors significantly improved their skills in A-POCUS, T-POCUS, and C-POCUS when assessed 3 months after their POCUS course, meaning the course appears to be effective at teaching global POCUS skills. They reached moderate proficiency in A-POCUS and T-POCUS, but not C-POCUS.

## Data availability statement

The raw data supporting the conclusions of this article will be made available by the authors, without undue reservation.

## Ethics statement

The studies involving humans were approved by Colorado State University Institutional Review Board. The studies were conducted in accordance with the local legislation and institutional requirements. The participants provided their written informed consent to participate in this study. The animal study was approved by Colorado State University IACUC. The study was conducted in accordance with the local legislation and institutional requirements.

## Author contributions

JG: Conceptualization, Funding acquisition, Investigation, Project administration, Writing – original draft, Writing – review & editing. AC: Formal analysis, Methodology, Writing – original draft, Writing – review & editing. JR: Writing – original draft, Writing – review & editing. MC: Writing – original draft, Writing – review & editing, Investigation. RH: Writing – original draft, Writing – review & editing, Funding acquisition, Project administration, Resources.

## Funding

The author(s) declare that financial support was received for the research and/or publication of this article. This manuscript were funded by Veterinary Emergency Group.

## Acknowledgments

The authors wanted to thank Jeff Ullmer and the Colorado State University Translational Medical Institute Continuing education team for their support and assistance.

## Conflict of interest

AC and JG received honorarium from the Veterinary Emergency Group for teaching and consulting.

The remaining authors declare that the research was conducted in the absence of any commercial or financial relationships that could be construed as a potential conflict of interest.

## Generative AI statement

The authors declare that no Gen AI was used in the creation of this manuscript.

## Publisher's note



## References

1. Lisciandro GR. Abdominal and thoracic focused assessment with sonography for trauma, triage, and monitoring in small animals. *J Vet Emerg Crit Care*. (2011) 21:104–22. doi: 10.1111/j.1476-4431.2011.00626.x

2. Kirkpatrick AW. Clinician-performed focused sonography for the resuscitation of trauma. *Crit Care Med*. (2007) 35:S162–72. doi: 10.1097/01.CCM.0000260627.97284.5D

3. Moore CL, Copel JA. Point-of-care ultrasonography. *N Engl J Med*. (2011) 364:749–57. doi: 10.1056/NEJMra0909487

4. Yamada T, Minami T, Soni NJ, Hiraoka E, Takahashi H, Okubo T, et al. Skills acquisition for novice learners after a point-of-care ultrasound course: does clinical rank matter? *BMC Med Educ*. (2018) 18:202. doi: 10.1186/s12909-018-1310-3

5. Restrepo D, Heyne TF, Schutzer C, Dversdal R. "Teaching old dogs new tricks" - POCUS education for senior faculty. *POCUS J*. (2023) 8:9–12. doi: 10.24908/pocus.v8i1.16145

6. Pelchat J, Chalhoub S, Boysen SR. The use of veterinary point-of-care ultrasound by veterinarians: a nationwide Canadian survey. *Can Vet J*. (2020) 61:1278–82.

7. Zelachowski KA, Rishniw M, DeFrancesco TC. A survey of the use of ultrasound by small animal veterinary clinicians. *Vet Radiol Ultrasound*. (2024) 65:429–36. doi: 10.1111/vru.13377

8. Boysen SR, Rozanski EA, Tidwell AS, Holm JL, Shaw SP, Rush JE. Evaluation of a focused assessment with sonography for trauma protocol to detect free abdominal fluid in dogs involved in motor vehicle accidents. *J Am Vet Med Assoc*. (2004) 225:1198–204. doi: 10.2460/javma.2004.225.1198

9. Lisciandro GR, Lagutchik MS, Mann KA, Voges AK, Fosgate GT, Tiller EG, et al. Evaluation of a thoracic focused assessment with sonography for trauma (TFAST) protocol to detect pneumothorax and concurrent thoracic injury in 145 traumatized dogs. *J Vet Emerg Crit Care*. (2008) 18:258–69. doi: 10.1111/j.1476-4431.2008.00312.x

10. DeFrancesco TC, Ward JL. Focused canine cardiac ultrasound. *Vet Clin North Am Small Anim Pract*. (2021) 51:1203–16. doi: 10.1016/j.cvsm.2021.07.005

11. Johri AM, Durbin J, Newbigging J, Tanzola R, Chow R, de S, et al. Cardiac point-of-care ultrasound: state-of-the-art in medical school education. *J Am Soc Echocardiogr*. (2018) 31:749–60. doi: 10.1016/j.echo.2018.01.014

12. Russ BA, Evans D, Morrad D, Champney C, Woodworth AM, Thaut L, et al. Integrating point-of-care ultrasonography into the osteopathic medical school curriculum. *J Am Osteopath Assoc*. (2017) 117:451–6. doi: 10.7556/jaoa.2017.091

13. Díaz-Gómez JL, Mayo PH, Koenig SJ. Point-of-care ultrasonography. *N Engl J Med*. (2021) 385:1593–602. doi: 10.1056/NEJMra1916062

14. Nicholas E, Ly AA, Prince AM, Klawitter PF, Gaskin K, Prince LA. The current status of ultrasound education in United States medical schools. *J Ultrasound Med*. (2021) 40:2459–65. doi: 10.1002/jum.15633

15. Williams ZJ, Sage A, Valberg SJ. Hand-held point-of-care ultrasound: a new tool for veterinary student self-driven learning in the time of COVID-19. *J Vet Med Educ*. (2022) 49:306–11. doi: 10.3138/jvme-2020-0131

16. Davy RB, Hamel PE, Su Y, Berry CR, Conner BJ. Evaluation of two training methods for teaching the abdominal focused assessment with sonography for trauma technique (A-FAST) to first- and second-year veterinary students. *J Vet Med Educ*. (2019) 46:258–63. doi: 10.3138/jvme.0517-059r1

17. Navas De Solis C, Stefanovski D, Johnson AL, Reef VB, Underwood C. Evaluation of a self-driven large animal point of care ultrasound learning program for veterinary students. *J Vet Med Educ*. (2023):e20230009. doi: 10.3138/jvme-2023-0009

18. Ward JL, Carnevale J, Collins B, Langel J, McQuinn E, Riha J, et al. Development and implementation of a basic veterinary ultrasound curriculum. *J Vet Med Educ*. (2024):e20230180. doi: 10.3138/jvme-2023-0180

19. Huh T, Achilles EJ, Massey LK, Loughran KA, Larouche-Lebel É, Convey V, et al. Utility of focused cardiac ultrasonography training in veterinary students to differentiate stages of subclinical myxomatous mitral valve disease in dogs. *J Vet Intern Med*. (2024) 38:1325–33. doi: 10.1111/jvim.17056

20. Cheney DM, Voges AK, Ritter N, Scallan E, Chaney K. Modified B-QUIET scoring of kidney images acquired by veterinary students in live canines with versus without sequential practice on ultrasound phantoms. *Vet Radiol Ultrasound*. (2023) 64:511–20. doi: 10.1111/vru.13197

21. Dickson D, Harris J, Chang CH, Patteson M, Hezzell MJ. Validation of a focused echocardiographic training program in first opinion practice. *J Vet Intern Med*. (2022) 36:1913–20. doi: 10.1111/jvim.16539

22. Eberhardt C, Schwarzwald CC. Focused cardiac ultrasound examination in the emergency and critical care horse: training for non-specialist veterinarians and evaluation of proficiency. *J Vet Intern Med*. (2022) 36:1471–80. doi: 10.1111/jvim.16446

23. Valcke A, Manning P, Boysen S, Gommeren K. Confidence level of Australian veterinarians with point-of-care ultrasound before and after a training course. *Can Vet J*. (2024) 65:910–9.

24. Alba GA, Kelmenson DA, Noble VE, Murray AF, Currier PF. Faculty staff-guided versus self-guided ultrasound training for internal medicine residents. *Med Educ*. (2013) 47:1099–108. doi: 10.1111/medu.12259

25. Greenstein YY, Littauer R, Narasimhan M, Mayo PH, Koenig SJ. Effectiveness of a critical care ultrasonography course. *Chest*. (2017) 151:34–40. doi: 10.1016/j.chest.2016.08.1465

26. Maw A, Jalali C, Jannat-Khah D, Gudi K, Logio L, Evans A, et al. Faculty development in point of care ultrasound for internists. *Med Educ Online*. (2016) 21:33287. doi: 10.3402/meo.v21.33287

27. Boysen SR, Gommeren K, Chalhoub S. The essentials of veterinary point of care ultrasound: pleural space and lung Edra. US LLC, Palm Beach Gardens, FL: Edra Publishing (2002).

28. Russell FM, Lobo D, Herbert A, Kaine J, Pallansch J, Soriano P, et al. Gamification of POCUS: are students learning? *West J Emerg Med*. (2023) 24:243–8. doi: 10.5811/westjem.2022.11.57730

29. Montoya J, Stawicki SP, Evans DC, Bahner DP, Sparks S, Sharpe RP, et al. From FAST to E-FAST: an overview of the evolution of ultrasound-based traumatic injury assessment. *Eur J Trauma Emerg Surg*. (2016) 42:119–26. doi: 10.1007/s00068-015-0512-1

30. Ianniello S, Conte P, Di Serafino M, Miele V, Trinci M, Vallone G, et al. Diagnostic accuracy of pubic symphysis ultrasound in the detection of unstable pelvis in polytrauma patients during e-FAST: the value of FAST-PLUS protocol. A preliminary experience. *J Ultrasound*. (2021) 24:423–8. doi: 10.1007/s40477-020-00483-6

31. Savoia P, Jayanthi SK, Chammas MC. Focused assessment with sonography for trauma (FAST). *J Med Ultrasound*. (2023) 31:101–6. doi: 10.4103/jmu.jmu_12_23

32. Seiler GS, Cohen EB, d'Anjou MA, French J, Gaschen L, Knapp S, et al. ACVR and ECVDI consensus statement for the standardization of the abdominal ultrasound examination. *Vet Radiol Ultrasound*. (2022) 63:661–74. doi: 10.1111/vru.13151

33. Boon JA. Veterinary echocardiography. *2nd* ed. Hoboken, NJ: Wiley-Blackwell (2011).

34. Lisciandro GR ed. Point-of-care ultrasound techniques for the small animal practitioner. *2nd* ed. Hoboken, NJ: Wiley-Blackwell (2021).

35. Eberlé O, Pouzot-Nevoret C, Thomas-Cancian A, Lurier T, Nectoux A, Ségard-Weisse E. Ultrasonographic findings of feline aortic thromboembolism. *J Feline Med Surg*. (2022) 24:e588–94. doi: 10.1177/1098612X221123770

36. Ruehl M, Lynch AM, O'Toole TE, Morris B, Rush J, Couto CG, et al. Outcome and treatments of dogs with aortic thrombosis: 100 cases (1997-2014). *J Vet Intern Med*. (2020) 34:1759–67. doi: 10.1111/jvim.15874

37. Mai W. The hilar perivenous hyperechoic triangle as a sign of acute splenic torsion in dogs. *Vet Radiol Ultrasound*. (2006) 47:487–91. doi: 10.1111/j.1740-8261.2006.00169.x

38. Armenise A, Boysen RS, Rudloff E, Neri L, Spattini G, Storti E. Veterinary-focused assessment with sonography for trauma-airway, breathing, circulation, disability and exposure: a prospective observational study in 64 canine trauma patients. *J Small Anim Pract*. (2019) 60:173–82. doi: 10.1111/jsap.12968

39. Rappaport CA, McConomy BC, Arnold NR, Vose AT, Schmidt GA, Nassar B. A prospective analysis of motor and cognitive skill retention in novice learners of point of care ultrasound. *Crit Care Med*. (2019) 47:e948–52. doi: 10.1097/CCM.0000000000004002

40. Clark R, Freedberg M, Hazeltine E, Voss MW. Are there age-related differences in the ability to learn Configural responses? *PLoS One*. (2015) 10:e0137260. doi: 10.1371/journal.pone.0137260

41. Mulder TA, van de Velde T, Dokter E, Boekestijn B, Olgers TJ, Bauer MP, et al. Unravelling the skillset of point-of-care ultrasound: a systematic review. *Ultrasound J*. (2023) 15:19. doi: 10.1186/s13089-023-00319-4

42. Fincham JE. Response rates and responsiveness for surveys, standards, and the journal. *Am J Pharm Educ*. (2008) 72:43. doi: 10.5688/aj720243

43. Hayat AA, Shateri K, Amini M, Shokrpour N. Relationships between academic self-efficacy, learning-related emotions, and metacognitive learning strategies with academic performance in medical students: a structural equation model. *BMC Med Educ*. (2020) 20:76. doi: 10.1186/s12909-020-01995-9

44. Mori T, Nomura O, Takei H, Fukuhara S, Ichihashi K. Implementation and assessment of a pediatric point-of-care ultrasound training course in Japan: a pilot study. *J Med Ultrason*. (2001) 49:85–93. doi: 10.1007/s10396-021-01155-6

45. Cepeda NJ, Pashler H, Vul E, Wixted JT, Rohrer D. Distributed practice in verbal recall tasks: a review and quantitative synthesis. *Psychol Bull*. (2006) 132:354–80. doi: 10.1037/0033-2909.132.3.354

46. Rawson KA, Dunlosky J, Sciartelli SM. The power of successive relearning: improving performance on course exams and long-term retention. *Educ Psychol Rev*. (2013) 25:523–48. doi: 10.1007/s10648-013-9240-4

47. Hopkins RF, Lyle KB, Hieb JL, Ralston PAS. Spaced retrieval practice increases college students' short- and long-term retention of mathematics knowledge. *Educ Psychol Rev*. (2016) 28:853–73. doi: 10.1007/s10648-015-9349-8

48. Yamamoto R, Clanton D, Willis RE, Jonas RB, Cestero RF. Rapid decay of transthoracic echocardiography skills at 1 month: a prospective observational study. *J Surg Educ*. (2018) 75:503–9. doi: 10.1016/j.jsurg.2017.07.011

49. Cecilio-Fernandes D, Cnossen F, Jaarsma DADC, Tio RA. Avoiding surgical skill decay: a systematic review on the spacing of training sessions. *J Surg Educ*. (2018) 75:471–80. doi: 10.1016/j.jsurg.2017.08.002

50. Yoosaf SS, Mohamed UZ, Sugashini V, Ravindran GC, Kumar L. Role of handedness in conducting an ultrasound-guided procedure: a comparative study. *J Diagn Med Sonogr*. (2022) 38:438–45. doi: 10.1177/87564793221092975

51. Tetteh E, Wang T, Norasi H, Bremer M, Schmida E, Kim H, et al. Comparison of physical workload in upper extremities between left- and right-hand ultrasound scanning: 66th international annual meeting of the human factors and ergonomics society, HFES 2022. *Proc Hum Factors Ergon Soc*. (2022) 66:651–5. doi: 10.1177/1071181322661144

52. Jones N, Handel IG, Llewellyn E. Comparison of success rate and time to obtain venous cannulation by cutdown technique at 3 locations using canine cadavers. *J Vet Emerg Crit Care (San Antonio)*. (2022) 32:356–364. doi: 10.1111/vec.13183

53. Seto E, Biclar L. Ambidextrous sonographic scanning to reduce sonographer repetitive strain injury. *J Diagn Med Sonogr*. (2008) 24:127–35. doi: 10.1177/8756479308315230

# Frontiers in
# Veterinary Science

## Transforms how we investigate and improve animal health

The third most-cited veterinary science journal, bridging animal and human health with a comparative approach to medical challenges. It explores innovative biotechnology and therapy for improved health outcomes.

---

## Discover the latest Research Topics

See more →


**Frontiers**

Avenue du Tribunal-Fédéral 34
1005 Lausanne, Switzerland
frontiersin.org

**Contact us**

+41 (0)21 510 17 00
frontiersin.org/about/contact